MCEER
EARTHQUAKE ENGINEERING TO EXTREME EVENTS

Seismic Response Modeling of Water Supply Systems

by

Peixin Shi and Thomas D. O'Rourke

NOTICE

1   Geotechnical Engineer, PB Americas, Inc., Geotechnical and Tunneling Group; former Ph.D. Candidate, School of Civil and Environmental Engineering, Cornell University
2   Thomas R. Briggs Professor of Engineering, School of Civil and Environmental Engineering, Cornell University

NTIS DISCLAIMER

❖   This document has been reproduced from the best copy furnished by the sponsoring agency.

Preface

The Multidisciplinary Center for Earthquake Engineering Research (MCEER) is a national center of excellence in advanced technology applications that is dedicated to the reduction of earthquake losses nationwide. Headquartered at the University at Buffalo, State University of New York, the Center was originally established by the National Science Foundation in 1986, as the National Center for Earthquake Engineering Research (NCEER).

Comprising a consortium of researchers from numerous disciplines and institutions throughout the United States, the Center's mission is to reduce earthquake losses through research and the application of advanced technologies that improve engineering, pre-earthquake planning and post-earthquake recovery strategies. Toward this end, the Center coordinates a nationwide program of multidisciplinary team research, education and outreach activities.

MCEER's research is conducted under the sponsorship of two major federal agencies: the National Science Foundation (NSF) and the Federal Highway Administration (FHWA), and the State of New York. Significant support is derived from the Federal Emergency Management Agency (FEMA), other state governments, academic institutions, foreign governments and private industry.

MCEER's NSF-sponsored research objectives are twofold: to increase resilience by developing seismic evaluation and rehabilitation strategies for the post-disaster facilities and systems (hospitals, electrical and water lifelines, and bridges and highways) that society expects to be operational following an earthquake; and to further enhance resilience by developing improved emergency management capabilities to ensure an effective response and recovery following the earthquake (see the figure below).
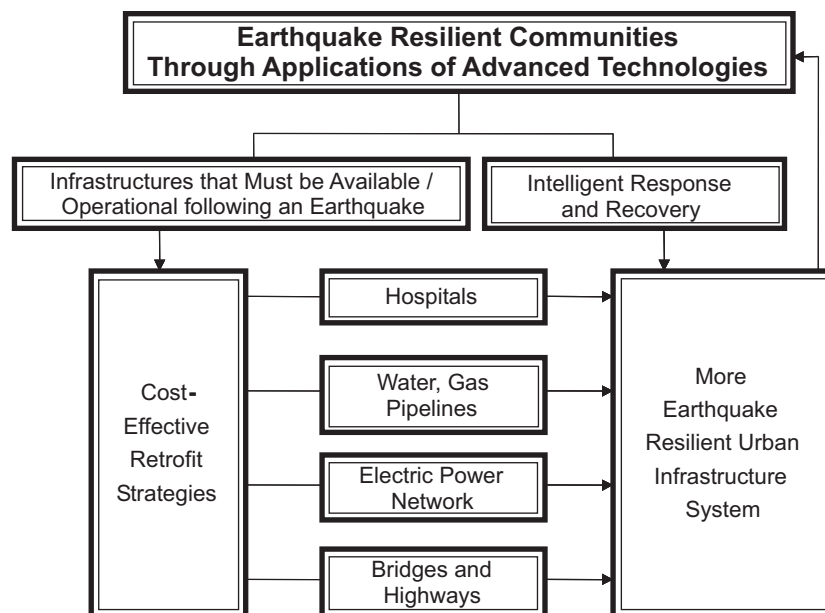
A cross-program activity focuses on the establishment of an effective experimental and analytical network to facilitate the exchange of information between researchers located in various institutions across the country. These are complemented by, and integrated with, other MCEER activities in education, outreach, technology transfer, and industry partnerships.

This report presents a comprehensive model for simulating the earthquake performance of water supply systems. The model is developed in conjunction with the water system operated by the Los Angeles Department of Water and Power (LADWP) and validated through comparisons to observations and flow measurements for the heavily damaged LADWP water supply after the 1994 Northridge earthquake. The earthquake performance of damaged water supply systems is simulated using hydraulic network analysis that uses an iterative approach to isolate the network nodes with negative pressures. The isolation process accounts accurately for reliable flows and pressures in the damaged water networks by removing unreliable flows and identifying those portions of the system requiring mitigation. An analytical model is developed to predict the effect of seismic waves on underground pipelines. The seismic performance of the LADWP system is simulated using a multi-scale technique in which the LADWP trunk system is explicitly accounted for, while the remaining distribution lines are simulated through fragility curves relating demand to repair rate. The repair rate, in turn, is correlated with peak ground velocities, and fragility curves are developed on the basis of distribution network simulations. The proposed model is integrated into computer code, Graphical Iterative Response Analysis for Flow Following Earthquakes (GIRAFFE) developed by the authors, which presents the simulation results in GIS format.

ABSTRACT

This report describes a comprehensive model for simulating the earthquake performance of water supply systems. This model is developed in conjunction with the water supply system operated by the Los Angeles Department of Water and Power (LADWP) and validated by a favorable comparison of simulation results with observations and flow measurements for the heavily damaged LADWP water supply after the 1994 Northridge earthquake.

Earthquake performance of water supply systems is simulated using hydraulic network analysis. Hydraulic simulation procedures for heavily damaged water supply systems are developed on the basis of an iterative approach to isolate the network nodes with negative pressures step by step, starting with the one of highest negative pressure. The isolation approach accounts accurately for reliable flows and pressures in the damaged system. The isolation approach removes unreliable flows, and identifies vulnerable parts of the damaged system for mitigation.

To predict earthquake damage to underground water supply pipelines, an analytical model is developed for surface wave interaction with jointed concrete cylinder pipelines (JCCPs). A dimensionless chart is developed for estimating the joint pullout of JCCPs under the action of seismic waves. This model is applied to analyze seismic wave interaction with other jointed pipelines, such as cast iron (CI) pipelines with lead-caulked joints. Dimensionless reduction curves are developed for estimating joint pullout associated with brittle and ductile joint performance.

Pipeline damage in hydraulic simulations is classified as breaks and leaks. A break is simulated by disconnecting the original pipeline completely and opening the broken ends into the atmosphere; a leak is simulated as an orifice in the pipe wall. Energy loss from the leak is accounted for as minor losses. Five different scenarios of leakage are simulated as a function of pipe diameter.

Seismic performance of the LADWP system is simulated using a multi-scale technique. This technique explicitly accounts for 2,200 km of pipelines, associated with the LADWP trunk system, and simulates the remaining 9,800 km of distribution lines by fragility curves relating demand to repair rate in the distribution network. Repair rate, in turn, is correlated with peak ground velocity. The fragility curves are developed on the basis of LADWP distribution network simulations.

A computer code, GIRAFFE, is developed for the implementation of the model. GIRAFFE builds on an open source hydraulic network analysis engine, EPANET, and works in conjunction with Geographical Information Systems (GIS) for simulation result presentations.

ACKNOWLEDGMENTS

TABLE OF CONTENTS

LIST OF FIGURES

LIST OF FIGURES (Cont'd)

LIST OF FIGURES (Cont'd)

LIST OF TABLES

CHAPTER 1

INTRODUCTION

1.1 BACKGROUND

Water supplies constitute a key component of critical civil infrastructure that supports fire protection and provide water for potable household consumption as well as industrial and commercial uses. Water is conveyed mostly in underground pipelines. Thus, ground movements triggered by earthquakes have a direct effect on the integrity and reliability of water distribution networks. Water supplies are vulnerable to earthquakes. This vulnerability has been demonstrated by extensive damage sustained during previous earthquakes, such as the 1906 San Francisco (e.g., Schussler, 1906; Manson, 1908; Lawson, 1908; Scawthorn, et al., 2006), 1971 San Fernando (e.g., Steinbrugge, et al., 1971; Subcommittee on Water and Sewerage Systems, 1973; Eguchi, 1982), and 1994 Northridge (e.g., Lund and Cooper, 1995; Hall, 1995; Eguchi and Chung, 1995; O'Rourke, et al., 2001) earthquakes. Earthquake damage to water supply systems may disrupt residential, commercial, and industrial activities; impair fire-fighting capacities; and prolong local community recovery in the aftermath of earthquakes. It is very important, therefore, to model the earthquake performance of water supply systems in a robust and reliable way for emergency planning, community restoration, and assessment of regional economic impacts.

There has been extensive work performed on the seismic modeling of water supply systems. Early studies focused on component behavior and simple system

models (e.g., Hall and Newmark, 1977; Wright and Takada, 1980; Hwang and Lysmer, 1981; O'Rourke, 1998). As more advanced experimental and computational modeling was developed, network simulations were explored to assess system reliability and serviceability (e.g., Eguchi, et al., 1983; Ballantyne, et al., 1990; Khater and Grigoriu, 1989; Markov, et al., 1994; Shinozuka, et al., 1981, 1992, 1998; Hwang, et al., 1998; Chang, et al., 2000).

Water supplies are large, geographically dispersed systems that are composed of many different types of pipelines as well as other supporting facilities, such as tanks, reservoirs, pumping stations, and regulator stations. Moreover, water supplies are subject to seismic and geotechnical loading conditions associated with spatially variable ground conditions, seismic sources, and source to site pathways for seismic waves. It is not possible to model such systems in a deterministic manner, and thus probabilistic methods have been developed to characterize system performance. Scenario earthquakes for evaluating system performance are often chosen on the basis of recurrence interval so that the seismic hazard can be linked with the probability of exceedance within a certain time span, often taken as 50 years (Frankel, et al., 1996). The response of a lifeline system to various seismic hazards is often assessed in a probabilistic way because it is not possible *a priori* to predict where damage will occur, although it is possible to estimate average rates of repair under various extreme event conditions. Monte Carlo simulations are performed to predict system response, followed by the probabilistic characterization of system reliability and serviceability. The probabilistic approach has been applied to evaluate the seismic performance of the water supply system operated by Memphis Light, Water and Gas (MLWG) in Memphis and Shelby County, TN, by Shinozuka, et al. (1998) and Chang, et al. (2000),

2

as well as the Auxiliary Water Supply System (AWSS) in San Francisco by Khater and Grigoriu (1989) and Markov, et al. (1994).

A key feature of modern water supply system modeling is the use of geographic information systems (GIS). The rapid development of computer mapping and visualization tools, embodied in GIS, provides a powerful basis for evaluating earthquake effects on water supplies. GIS has become an engine for driving new methodologies and decision support tools focused on the spatial variation of earthquake effects. The Japan Water Works Association (1996) developed a very large GIS database of 7 water distribution networks with 12,000 km of pipelines and 2885 damage-related repairs collected after the 1995 Kobe earthquake. In U.S., the Cornell research group (Topark, 1999; Jeon, 2002; O'Rourke, et al., 2001) developed similar GIS databases for the water supply system operated by the Los Angeles Department of Water and Power (LADWP). The Cornell GIS databases include more than 11,000 km of distribution (pipe diameter < 610 mm) and 1000 km of trunk lines (pipe diameter ≥ 610 mm), as well as over 1000 distribution and 100 trunk line repairs collected after the 1994 Northridge earthquake.

More recently, the economic and community consequences of earthquake damage have been integrated with network simulations to create models and a modeling process that link component behavior through system reliability and serviceability assessments to regional economic impacts (Bruneau, et al., 2003; Chang, et al., 1996, 2000, 2002; Rose and Liao, 2003; Shinozuka, et al., 1998). For example, Chang, et al. (1996, 2000, 2002) linked the MLWG water delivery damage with economic consequences through a methodology that correlates water losses with areas of economic activity, adjusts for business resiliency, and accounts for direct and

indirect economic losses. Indirect economic losses were initially estimated with Input-Output analysis (Rose, et al., 1997) and were recently estimated by employing Computable General Equilibrium methods (Rose and Liao, 2003).

Early water supply network simulations (Eguchi, et al., 1983) focused on connectivity analyses, which trace the connectivity of customers to water sources and identify water outage areas. Recent system network simulations have been improved by using hydraulic network analyses, which utilize the physical and operational properties, topology, and demands of a water supply system as basic input data, and calculate pressure and flow distributions (e.g., Jeppson, 1976; Thomas, 1984; Walski, et al., 2001). Hydraulic network analyses automatically take the network connectivity into account and incorporate system dynamics and operational characteristics into the simulation.

Many researchers have applied hydraulic network analysis to evaluate the reliability and serviceability of existing water supply systems in areas vulnerable to earthquakes. Ballantyne, et al. (1990) developed an earthquake loss estimation model and applied this model to the Seattle water supply system. In their model, earthquake damage to water supply components was evaluated and hydraulic network analysis was performed to the damaged system for system serviceability prediction. Shinozuka and coworkers (Okumura and Shinozuka, 1991; Shinozuka, et al., 1981, 1992; Hwang, et al., 1998) evaluated the seismic serviceability of the MLGW water supply system using hydraulic network analysis in conjunction with GIS.

Of particular interest is the work performed on modeling the AWSS in San Francisco. Khater and Grigoriu (1989) and Markov, et al. (1994) developed a

computer program, GISALLE, which has a special algorithm for negative pressure treatment in the hydraulic simulation of heavily damaged water supply systems. This program was applied to evaluate the fire fighting capability of the AWSS under various supply, fire, and damage scenarios. The AWSS, which was developed after the 1906 San Francisco earthquake, serves as the backbone of city fire protection in San Francisco (O'Rourke, et. al., 1985; Scawthorn, et al., 2006). Research conducted by Khater and Grigoriu (1989) and Markov, et al. (1994) showed that the seismic serviceability of the AWSS is very sensitive to pipe breaks.

To develop an improved model for simulating water supply system performance in response to earthquakes, this work uses the LADWP water supply as a test bed. The LADWP water supply represents a very large and complex system, which covers a service area of 1,200 km^2 and consists of more than 12,000 km of pipelines with diameters ranging from 50 (2) to 3850 mm (152 in.). If simulation models and/or modeling procedures can be developed for successful application in such a complex system, they can be readily applied to less complex systems. Moreover, the damage sustained by the LADWP network during the 1994 Northridge earthquake provides a valuable resource for the validation of new models and decision support systems to improve emergency planning and community restoration.

Previous research at Cornell University (Jeon, 2002; Jeon and O'Rourke, 2005; O'Rourke, et al., 2004b) has led to empirical regression relationships, which correlate repair rate with peak ground velocity for trunk and distribution pipelines. These regressions apply to different types of pipelines, including cast iron, ductile iron, concrete, riveted steel, and steel with welded slip joints. In combination with GIS, pre- and post- earthquake air photo measurements were used to evaluate the effects of

permanent ground deformation on buried pipelines during the Northridge earthquake (Sano, et al., 1999; O'Rourke, et al., 1998). The research described in this report, in combination with the research performed by Wang (2006), represents an extension of previous work to develop a comprehensive model for simulating earthquake effects on water supply systems and to provide a methodology for planning and management to reduce the detrimental effects of future earthquakes.

Soil-structure interaction triggered by seismic waves has an important effect on pipeline behavior, and when integrated over an entire network of pipelines, on system performance. Surface waves are generated by the reflection and refraction of body waves at the ground surface. Surface waves can be more destructive to buried pipelines than body waves by generating larger ground strain driven by their low phase velocity. Papageorgiu and coworkers (e.g., Papageorigu and Kim, 1993; Pei and Papageorigu, 1996) analyzed the strong motion records collected in Santa Clara Valley during the 1989 Loma Prieta earthquake and demonstrated clear evidence of surface waves. Ayala and O'Rourke (1989) reported severe damage to water supply pipelines related to surface wave effects during the 1985 Michoacan earthquake in Mexico City.

Analytical models of surface wave effects on buried pipelines have practical significance for both pipe damage estimation and system response evaluation. Analytical models for surface wave effects on underground pipelines are developed in this work, and are complementary to the development of similar models for body wave effects by Wang (2006).

6

1.2 OBJECTIVES

The general goal of this work is to develop a comprehensive model for the seismic response simulation of water supply systems. This model is developed in conjunction with the LADWP water supply system. This model needs to: 1) account accurately for reliable hydraulic flows and pressures in heavily damaged water supply systems; 2) provide analytical models for analyzing surface wave interaction with underground pipelines; 3) incorporate a comprehensive method for simulating pipeline damage; 4) provide an effective way to simulate complex water supply systems; 5) be implemented into a computer code and validated by a case history. The general goal of this report is addressed by focusing on five specific objectives as described briefly under the subheadings that follow:

1.2.1 Hydraulic Network Analysis for Damaged Systems

Earthquake performance of a water supply system depends on the available flows and pressures in the damaged system. The flows and pressures can be predicted using hydraulic network analysis, which involves solving a set of linear and/or nonlinear algebraic equations, normally by means of computer programs. Commercial hydraulic network analysis software packages are designed for undamaged systems, and may predict unrealistically high negative pressures when used for damaged systems. Real water supply systems are not air tight, and thus their ability to support negative pressures is limited. In this study, simulation procedures for hydraulic network analyses are developed on the basis of an iterative approach to isolate the nodes with negative pressures step by step, starting with the one of highest negative pressure. The isolation process removes the unreliable portions of the system to

7

display the remaining part of the network that meets threshold serviceability requirements for positive pressure. The approach followed in this work is similar to that described by Khater and Grigoriu (1989) and Markov, et al. (1994). Improvements in the previous methodology are introduced by linking the algorithm for eliminating negative pressure nodes with a robust hydraulic analysis engine, removing nodes with partial flow to improve numerical stability, and providing the analysis package as open source software.

1.2.2   Seismic Response of Buried Pipelines to Surface Wave Effects

This work presents an analytical model for analyzing the joint pullout of buried pipelines affected by surface waves. By accounting for the mechanism of shear transfer and relative joint movement as a result of soil-structure interaction, substantial insight about potential joint pullout is obtained. By accounting for different joint tensile behaviors, this model is able to analyze pipelines caulked with different types of joints. Finite element results of the joint pullout for jointed concrete cylinder pipelines (JCCPs) are consistent with the field observations from previous earthquakes. In conjunction with the work conducted by Wang (2006) on body wave effects, this work develops a dimensionless plot for estimating the relative joint slip of JCCPs. The application of the dimensionless plot is expanded to other types of pipelines composed of joints exhibiting ductile tensile failure, such as cast iron (CI) pipelines with lead-caulked joints, by incorporating a dimensionless reduction factor to consider the joint ductility.

1.2.3   Pipe Damage Modeling

To simulate the seismic performance of water supply systems, earthquake damage to pipelines needs to be added in the network and then hydraulic simulation is performed to the damaged network. This work presents a comprehensive model for pipeline damage simulation in hydraulic network analysis. Pipe damage is classified into breaks and leaks according to the extent of pipe functionality loss for water transportation purposes. A pipe break is modeled by disconnecting the original pipe completely and opening the disconnected ends to the atmosphere. A pipe leak is modeled as an opening in the pipe wall, and energy loss from the leak is accounted for as minor losses. Five leak scenarios with different rupture states are identified based on pipe material properties, joint characteristics, and seismic damage mechanisms. Leakage is then characterized as a function of pipe diameter.

1.2.4   Multi-Scale Technique for Water Supply System Modeling

Water supply systems are characterized by broad coverage and a high level of detail. The broad coverage is associated with large service area. The high level of detail is related to the large amount of different pipelines and facilities in the system. A hydraulic network model, which models both broad coverage and component details, would be difficult to manage and trouble shoot. In this study, a multi-scale technique is proposed to model the LADWP water supply system. The system response is simulated by a system-wide hydraulic network model, which includes 2200 km of pipelines, ranging in diameters from 300 (12) to 3850 mm (152 in.), associated with the LADWP trunk system. The other 9800 km of small diameter distribution lines are modeled as demand nodes in the trunk system. When using the trunk system model

9

for earthquake simulations, damage to trunk lines is explicitly accounted for by adding breaks and leaks. Damage to distribution lines is simulated implicitly by increasing the demands at nodes in the trunk system. The increased demands are characterized by fragility curves that relate demand to repair rate in the distribution network. Repair rate, in turn, is correlated with peak ground velocity and permanent ground deformation. The fragility curves are developed on the basis of LADWP distribution network simulations.

1.2.5 Evaluation of Northridge Earthquake Performance

As part of the study, a software package, GIRAFFE, is developed for the hydraulic network modeling of heavily damaged water supply systems. GIRAFFE stands for Graphical Iterative Response Analysis for Flow Following Earthquakes. It has specific features to eliminate negative pressures, represent different damage states, assess earthquake demands from local distribution networks, and perform Monte Carlo simulations. To assess the GIRAFFE simulation capabilities, the seismic response of the LADWP system to the 1994 Northridge earthquake is used as a case history. The GIRAFFE simulation results of the LADWP system during the 1994 Northridge earthquake are shown to produce water outages and flows at key locations that compare favorably with the documented water outages and flows monitored by LADWP.

1.3 SCOPE

This work is divided into eight chapters, the first of which provides the background and objectives of this study. Chapter 2 describes hydraulic network

analyses for undamaged water supply systems. The basic components in a hydraulic network, fundamentals of fluid mechanics, and principle laws governing water flow in the hydraulic network are introduced. Four types of flow equations and their numerical solution procedures are discussed. Hydraulic network analysis software packages, EPANET and H2ONET, are introduced. Common limitations of these software packages, when used to simulate heavily damaged systems during earthquakes, are also discussed.

Chapter 3 presents an algorithm for the hydraulic network analysis of heavily damaged water supply systems, with special treatment of negative pressures. The generation of negative pressures is illustrated using a simple hydraulic network. Previous research on this subject is briefly reviewed and discussed.

Chapter 4 presents an analytical model for buried pipeline response to surface wave effects. The seismic wave propagation hazards to buried pipelines are briefly discussed. An analytical model is developed for surface wave interaction with JCCPs, and a dimensionless chart is constructed to estimate the joint pullout of JCCPs under the action of seismic waves. This model is applied to analyze seismic wave interaction with other jointed pipelines, such as CI distribution and trunk mains with lead-caulked joints. Dimensionless reduction curves are developed for estimating joint pullout associated with brittle and ductile joint performance.

Chapter 5 describes a comprehensive method for pipe damage simulation in hydraulic network analysis. Hydraulic models for pipe leaks and breaks are developed. The methodology and its verification for the leak simulation are discussed. A brief review of material properties, joint characteristics, and seismic damage mechanisms is

11

provided for various types of pipelines. A classification for leak scenarios is proposed, and mathematical formulations are developed to estimate leakage for each scenario. A description is provided for the implementation of the pipe damage model in association with Monte Carlo simulations to evaluate network performance.

Chapter 6 describes a multi-scale technique for modeling complex water supply systems, with application to the LADWP system. The LADWP system, including its trunk and distribution networks, is described. Procedures for constructing fragility curves that relate demand to repair rate in local distribution networks, based on the Monte Carlo simulations, are described.

Chapter 7 describes the computer code, GIRAFFE. The major functions, input parameters, and output results of each GIRAFFE module are explained. The observed performance of the LADWP system during the 1994 Northridge earthquake is discussed. The GIRAFFE simulated flows at key locations of LADWP system during the Northridge earthquake are compared with flows measured by LADWP before and after the earthquake.

The final chapter summarizes the research findings. It presents conclusions pertaining to the research, and recommendations for future investigations.

CHAPTER 2

HYDRAULIC NETWORK ANALYSIS FOR UNDAMAGED SYSTEMS

2.1 INTRODUCTION

The basic function of a water supply system is to deliver water from sources to customers. Moving water from source to customer requires a network of pipes, pumps, valves, and other appurtenances. Storing water to accommodate fluctuations in demand due to varying rates of usage or fire protection requires storage facilities, such as tanks and reservoirs. Pipes, pumps, valves, storages, and the supporting infrastructures together comprise a water supply system. A hydraulic network is a mathematical model of a water supply system, in which the water supply physical components are represented as nodes and links. Hydraulic network analysis utilizes the physical and operational properties, topology, and demands of a water supply system as basic input data, and calculates pressures at nodes and flows in links. Hydraulic network analysis can be used to predict pressure and flow conditions in a water supply system under different operational scenarios to ensure that sound, cost-effective engineering solutions can be accomplished in the design, planning, and functioning of the water supply system.

This chapter provides a brief introduction to hydraulic network analyses for undamaged water supply systems. The basic components in a hydraulic network, fundamentals of fluid mechanics, and principle laws governing water flow in the

hydraulic network are introduced. Four types of flow equations and their numerical solution procedures are discussed. Hydraulic network analysis software packages, EPANET and H2ONET, are described. Common limitations of these software packages, when used to simulate heavily damaged systems during earthquakes, are also discussed.

2.2   COMPONENTS IN HYDRAULIC NETWORKS

In general, a hydraulic network consists of two basic classes of elements, nodes and links. The nodes represent facilities at specific locations in a water supply system, and the links define relationships between nodes. Typical nodal elements include junctions and storage nodes, and typical link elements are pipes. Other components, such as valves and pumps, can be modeled as either links or nodes, depending on different modeling techniques. The primary modeling purpose of each physical element is briefly described below.

1. *Junctions*: represent locations where links intersect and where water enters or leaves the network.

2. *Storage nodes*: represent locations of storage reservoirs and tanks. The pressures at storage nodes are known and treated as boundary conditions to solve flow equations. In contrast to tanks, which have limited storage capacity and for which the volume of stored water varies with simulation time, reservoirs represent external water sources with unlimited storage capacity, such as sources from lakes, rivers, or ground aquifers.

3. *Pipes*: represent links conveying water from one node to another.

4. *Pumps*: represent elements adding energy to flowing water in the form of an increased hydraulic grade. A pump can be modeled as either a node or link.

5. *Valves*: represent elements controlling water flow or pressure from one node to another. A valve can be modeled as either a node or link. There are different types of valves with different functions, such as check, pressure reducing, flow control, throttle control, air release, and vacuum breaking valves.

These physical components are interconnected to form a network and operate together under some operational rules. Typical operational rules include the change of the status of pipes, pumps, and valves under certain conditions. For example, the status of a pump is typically controlled by the water level of the tank it serves. When water in the tank is lower than a certain level, the pump is open to boost water to the tank. When water in the tank is higher than a certain level, the pump is closed and the tank supplies water to customers. The operational rules give a water supply system the ability to work efficiently under different operation scenarios.

2.3   FUNDAMENTALS OF FLUID MECHANICS

Hydraulic network analysis solves water flow and pressure conditions in a pressurized pipeline network using fluid mechanics. The fundamentals of fluid mechanics, including fluid properties, flow regime, fluid energy, and the principle laws governing fluid flow, are briefly introduced in this section.

2.3.1 Fluid Properties

The most important fluid properties taken into consideration in hydraulic network analysis are fluid density and unit weight, viscosity, and compressibility (Jeppson, 1976; Armando, 1987; Walski, et al., 2001).

Density and Unit Weight

The density of a fluid is the mass of the fluid per unit volume. The density of water is 1000 kg/m^3 at standard pressure of 1 atm and standard temperature of 0 $^{\text{o}}$C. Although it varies with pressure and temperature, the variation is minor and not considered within the normal conditions for hydraulic network modeling. The unit weight of a fluid is the weight of the fluid per unit volume. The unit weight is related to density by gravitational acceleration as

$$\gamma = \rho\, g \qquad\qquad (2.1)$$

in which γ is the unit weight, ρ is the density, and g is the gravitational acceleration. The unit weight of water, γ_w, at standard pressure and temperature is 9806 N/m^3, which is treated as constant in hydraulic network modeling.

Viscosity

The fluid viscosity is the property that controls fluid resistance to flow. This resistance results from shear stresses both within a moving fluid and between the fluid and its container (Jeppson, 1976). Viscosity is defined as the ratio of the shear stress

to the rate of change in velocity. This definition results in the following equation for fluid shear stress

$$\tau = \mu \frac{d\text{v}}{dy} \qquad (2.2)$$

where τ is the shear stress, μ is the absolute (dynamic) viscosity, and $d\text{v}/dy$ is the derivative of the flow velocity, v, with respect to the distance, y, normal to the flow direction.

For hydraulic formulas related to fluid motion, the relationship between fluid viscosity and fluid density is often expressed as a single parameter, kinematic viscosity, which is expressed as

$$\upsilon = \frac{\mu}{\rho} \qquad (2.3)$$

where υ and ρ are the kinematic viscosity and density of the fluid, respectively.

The viscosity of many common fluids, such as water, is a function of temperature, but not the shear stress, τ, or the rate of change in velocity, $d\text{v}/dy$. Such fluids are called Newtonian fluids to distinguish them from non-Newtonian ones, for which the viscosity depends on $d\text{v}/dy$. The viscosity of water leads to the development of shear stresses between the pipe wall and flowing water, and therefore energy losses along the path of water flow. This energy loss is called frictional loss, and the viscosity is an input parameter for estimating the frictional loss in hydraulic

17

network analysis. The absolute and kinematic viscosities of water over the typical range of temperature for water supply operation can be found in the literature (e.g., Jeppson, 1976; Armando, 1987; Philip, et al., 1992).

Compressibility

Compressibility is a physical property of fluid that relates the volume occupied by a fixed mass of fluid to its internal pressure. Compressibility is described by defining the fluid bulk modulus of elasticity as

$$E_V = -V \frac{dp}{dV} \qquad (2.4)$$

where E_V is the bulk modulus of elasticity, p is the internal pressure, and V is the volume of fluid.

All fluids are compressible to some extent. The effects of compression in a water distribution system are very small, and thus the flow equations used in hydraulic network analysis are based on the assumption that water is incompressible. With a bulk modulus of elasticity of 2.83×10^6 kPa at 20 $^\circ$C (Walski, et al., 2001), water can safely be treated as incompressible.

2.3.2   Flow Regime

Observation shows that there are three types of fluid flow. This was demonstrated by Ostorne Reynolds in 1883 (Douglas, et al., 1985; Walski, et al.,

2001) through an experiment in which water was discharged from a tank through a glass tube, as shown in Figure 2.1. The flow rate could be controlled by a valve at the outlet, and a fine dye filament was injected at the entrance to the tube. It was noticed that at very low flow rates, the dye stream remained intact with a distinct interface between the dye stream and the fluid surrounding it. This condition is referred as laminar flow by Reynolds. At slightly higher flow rates, the dye stream began to waver a bit, and there was some blurring between the dye stream and surrounding fluid. Reynolds called this condition transitional flow. At even higher flow rates, the dye stream was completely broken up, and the dye mixed thoroughly with the surrounding fluid. Reynolds referred to this regime as turbulent flow.

Based on experimental evidence gathered by Reynolds and dimensional analysis, a dimensionless number, Reynolds Number, is defined for pressurized circular pipes to characterize flow regimes.

$$R_e = \frac{\mathrm{v}d\rho}{u} = \frac{\mathrm{v}d}{\upsilon} \tag{2.5}$$

where R_e is Reynolds Number, d is the pipe diameter, ρ is the fluid density, u is the fluid absolute viscosity, v is the fluid velocity, and υ is the fluid kinematic viscosity. Conceptually, Reynolds Number can be thought as the ratio between inertial and viscous forces in a fluid. The ranges of Reynolds Number that define the three flow regimes are shown in Table 2.1. The water flow through municipal water supply systems is almost always turbulent, except in peripheral piping, where water demand is low and intermittent, and may result in laminar flow conditions.
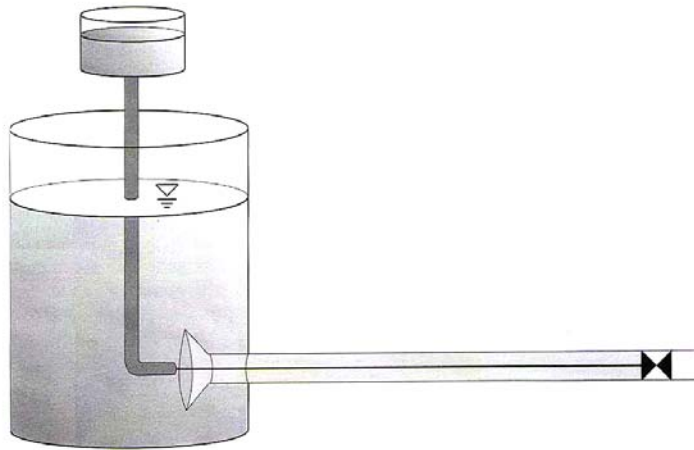
Figure 2.1 Experimental Apparatus Used to Determine Reynolds Number

(after Walski, et al., 2001)

Turbulence in a fluid is manifested by the irregular state of flow in which fluid particle motion varies randomly in space and time. However, it is statistically possible to establish mean values for the parameters used to characterize the particle motion. That is to say, in turbulent flow, fluid particles do not remain in layers, but move in a heterogeneous fashion. Fluid particles collide with each other in an entirely random manner, but with a degree of regularity in time. At a given movement, the flow pattern is repeated with some regularity in space (Armando, 1987). Thus, the time-averaged parameters of flow may be constant, in which case the flow is called steady state flow. In contrast, unsteady state flow occurs when the averaged parameters change with time.

The two most important applications of steady state flow are the water flow in closed and open conduits. A closed conduit is a pipe or duct through which water flow completely fills the cross-section. Since the water has no free surface, the conduit is pressurized and the pressure may vary from cross-section to cross- section

Table 2.1 Reynolds Number for Various Flow Regimes

Flow Regime	Reynolds Number
Laminar	< 2000
Transitional	$2000 - 4000$
Turbulent	> 4000

along its length. An open conduit is a duct or open channel along which water flows with a free surface. At all points along the length of the open conduit, the pressure at the free surface is the same, usually atmospheric. An open conduit may be covered providing that it is not running full and the water retains a free surface. A partly filled pipe will, for example, be treated as an open channel. Hydraulic network analysis assumes pipes are completely filled and pressurized with water while steady state flow is reached.

2.3.3 Fluid Energy

Fluids possess energy in three forms. The amount of energy depends on the fluid movement (kinetic energy), elevation (potential energy), and pressure (pressure energy) (Jeppson, 1976; Armando, 1987; Douglas, et al., 1985; Walski, et al., 2001). In a hydraulic network, a fluid can have all three types of energy simultaneously. The total energy per unit weight of fluid is called total head, which consists of the velocity head ($v^2/2g$) from kinetic energy, elevation head (*z*) from potential energy, and pressure head (p/γ) from internal pressure energy:

$$H = z + \frac{p}{\gamma} + \frac{v^2}{2g} \tag{2.6}$$

where H is the total head, z is the elevation above datum, p is the fluid internal pressure, γ is the fluid unit weight, v is the fluid velocity, and g is the gravitational acceleration constant.

In most water distribution applications, the velocity head, $v^2/2g$, is relatively small compared with both the elevation head, z, and pressure head, p/γ, and is generally neglected. The total head in hydraulic network analysis typically refers to the sum of the elevation and pressure heads.

2.3.4 Energy Losses

Whenever water flow passes a fixed wall or boundary, friction exists due to the viscosity of water. The friction transforms part of the useful energy into heat or other forms of non-recoverable energy, which results in frictional head losses. A number of appurtenances, such as inlets, bends, elbows, contractions, expansions, valves, meters, and pipe fittings, commonly occur in water supply systems. These devices alter the flow pattern in pipes by creating additional turbulence, which leads to head losses in excess of frictional head losses. These additional head losses are called minor or local losses.

2.3.4.1 Frictional Loss

The frictional loss results from the shear stress developed between water and the pipe wall. Its magnitude depends on the density, viscosity, and moving velocity of water, as well as the internal roughness, length, and size of the pipe (Jeppson, 1976).

There are various formulations to evaluate frictional head losses, and all formulations can be generalized into the following form (Walski, et al., 2001)

$$h_{fk} = K_{fk} Q_k^{n_k} \tag{2.7}$$

in which h_{fk} is the frictional head loss along pipe k, Q_k is the flow rate through the pipe, K_{fk} is a resistance coefficient, and n_k is a constant flow exponent.

The most widely used formulations to calculate frictional head losses in hydraulic network analysis are the Darcy-Weisbach, Hazen-Williams, and Chezy-Manning equations. The resistance coefficient, K_{fk}, and flow exponent, n_k, associated with each formulation are listed in Table 2.2. The Darcy-Weisbach equation is physically-based, as it is derived from the basic equations of Newton's Second Law. The main disadvantage associated with the Darcy-Weisbach equation is that the frictional factor, f, and thus the resistance coefficient, K_{fk}, is a function of flow rate, Q_k. When Equation 2.7 is used to solve flow rate, Q_k, with known head loss, h_{fk}, the equation is an implicit expression of the flow rate. Trial-and-error or numerical methods must be applied to solve it. The Hazen-Williams and Manning formulas are empirically-based expressions developed from experimental data. The Hazen-Williams formula is the most frequently used formulation for hydraulic network analysis in the U.S. Jeppson (1976) provides a detailed discussion of the three formulas.

Table 2.2 Frictional Head Loss Evaluation Formulas

Equation	Resistance Coefficient K_{fk}	Flow Exponent n^k
Darcy-Weisbach	$\dfrac{8fl_k}{gd_k^5\pi^2}$	2
Hazen-Williams	$\dfrac{Bl_k}{C^{1.852}d_k^{4.87}}$	1.852
Chezy-Manning	$\dfrac{Al_k\mu^2}{d_k^{5.333}}$	2

Notes:

g: Acceleration of gravity

f: Friction factor in Darcy-Weisbach formulation, a function of the flow rate and physical properties of the pipeline. The friction factor, f, can be determined using the Colebrook-White equation (Jeppson, 1976), Moody diagram (Moody, 1944), or Swamee-Jian formula (Swamee and Jian, 1976).

l_k: Length of pipe

d_k: Diameter of pipe

B: Dimensional constant in Hazen-Williams formulation, equal to 4.73 and 10.70 in British and SI units, respectively.

C: Hazen-Williams roughness coefficient, a function of the pipe physical properties. The values of C for different types of pipeline are available in the literature (e.g., Jeppson, 1976; Armando, 1987; Walski, et al., 2001).

A: Dimensional constant in Chezy-Manning formulation, equal to 4.64 and 10.29 in British and SI units, respectively.

μ: Manning roughness coefficient, a function of the pipe physical properties. The values of μ for different types of pipeline are available in the literature (e.g., Jeppson, 1976; Armando, 1987; Walski, et al., 2001).

2.3.4.2   Minor Loss

Minor losses (also called local losses) are induced by local turbulence. The importance of such losses depends on the geometric dimension of the hydraulic network and the required simulation accuracy. If pipelines are relatively long, these minor losses may be truly minor compared with frictional losses and can be neglected. In contrast, if pipelines are short, the minor losses may be large and should be considered. If devices, such as a partly closed valve, cause large losses, the minor losses can have an important influence on the flow rate. In practice, some engineering judgment is required to decide if the minor losses need to be considered or not. The minor losses are generally expressed as

$$ h_{mk} = \frac{K_{mk}}{2gA_k^2} Q_k^2 = K_{mk}^{'} Q_k^2 \tag{2.8} $$

in which $K_{mk}^{'} = K_{mk} / (2gA_k^2)$, g is the acceleration of gravity, Q_k is the flow rate, K_{mk} is the minor loss coefficient, and A_k is the pipe cross-sectional area. The values of K_{mk} for different types of minor losses have been determined from experiments, and are available in the literature (e.g., Crane Company, 1972; Miller, 1978; Armando, 1987; Idelchik, 1999; Waskli, et al., 2001). Sometimes, it is more convenient to equate the minor losses to frictional losses caused by a fictitious length of pipe, known as an equivalent pipe length. This length can be derived from Equations 2.7 and 2.8, with the substitution of the selected resistance coefficient K_{fk} and flow exponent n_k.

2.3.5   Energy Gains

There are many occasions when energy needs to be added into a hydraulic system to overcome elevation difference, as well as frictional and minor losses. A pump is a device to which mechanical energy is applied and transferred to water as hydraulic head. The head added to water is called pump head, and is a function of discharge through the pump. The relationship between pump head and discharge rate is called a pump head characteristic curve, as shown in Figure 2.2. The pump characteristic curve is nonlinear, and as expected, the more water that passes through the pump, the less head it can add.

The head that is plotted in the head characteristic curve is the head difference across the pump, called the total dynamic head. This curve needs to be described as a mathematical equation to be used in hydraulic simulation. Some models fit a polynomial curve to selected data points, but a more common approach is to describe the curve using a power function in the form of

$$h_P = h_o - cQ_P^m \tag{2.9}$$

where h_P is the pump head, h_o is the cutoff (shutoff) head (pump head at zero flow), Q_P is the pump discharge, and c and m are the coefficients describing the curve shape.

The purpose of a pump is to overcome elevation differences and head losses due to pipe friction and obstructed flow at fittings. The amount of head, which a pump must add to overcome elevation differences, is referred to as static head or static lift, which is dependent on system topology, but independent of the pump discharge.
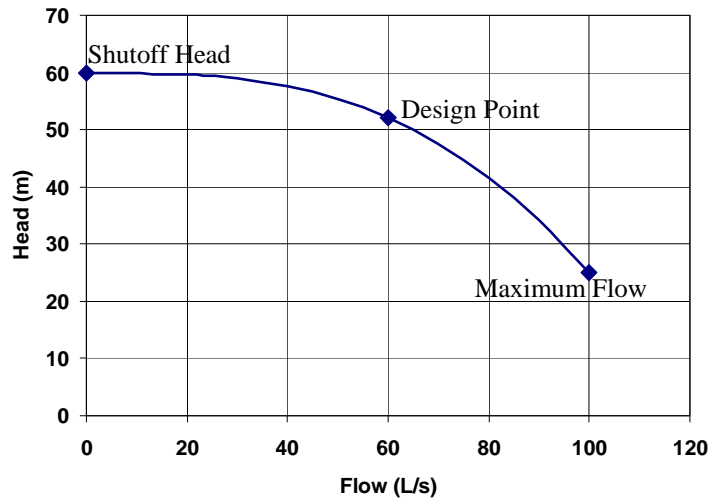
Figure 2.2 General Shape of Pump Characteristic Curve

Frictional and minor losses, however, are highly dependent on the pump discharge rate. When these losses are added to the static head for a series of discharge rates, the resulting plot is called a system head curve. The pump characteristic curve is a function of the pump and independent of the system, while the system head curve is dependent on the system and independent of the pump. When a pump characteristic curve and a system head curve are plotted on the same axes, there is only one point that lies on both of them. This intersection, as shown in Figure 2.3, defines the pump operation point, which represents the discharge that passes through the pump and the head that the pump adds in hydraulic network simulations.

2.3.6   Principle Laws of Flow Analysis

Many analytical computations in engineering and the physical sciences are based on relatively few fundamental principles and concepts. Most important among them are the laws of mass and energy conservation, which are also the governing laws for flow analyses in hydraulic networks.

27
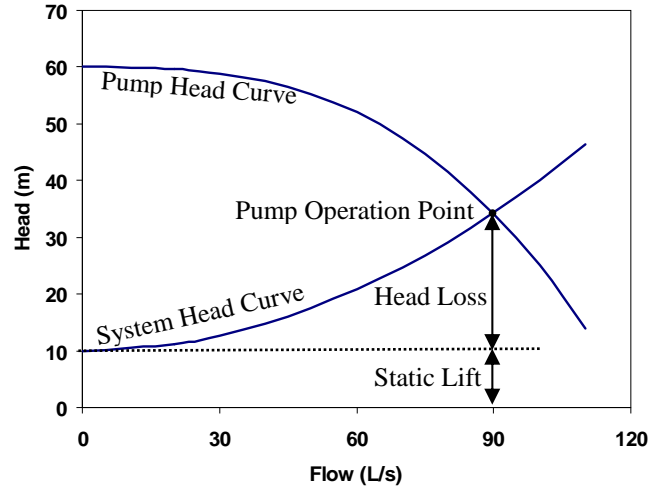
Figure 2.3 Pump Operation Point

2.3.6.1 Equation of Continuity

In hydraulic network analyses, conservation of mass is typically expressed as equation of continuity, which simply states that the algebraic sum of flows into and out of any node should be zero (Jeppson, 1976). Consider a node i, for which the continuity equation can be expressed as

$$\sum_{k=1}^{n_{pi}} Q_{ik} = \tilde{Q}_i \tag{2.10}$$

in which $\tilde{Q}_i$ is the external flow at node i, (normally called demand), n_{pi} is the number of pipes connected to node i, k is an index for pipes, and Q_{ik} is the flow rate in pipe k to node i. Typically, Q_{ik} is positive for flows coming into the node and negative going out. In contrast, $\tilde{Q}_i$ is positive for flows going out of the node and negative coming into.

28

2.3.6.2 Bernoulli Equation

The conservation of energy between two cross-sections, i and j, within a flow is expressed by the Bernoulli equation (Jeppson, 1976) in the form of hydraulic heads as

$$z_i + \frac{p_i}{\gamma_w} + \frac{\mathrm{v}_i^2}{2g} + h_p = z_j + \frac{p_j}{\gamma_w} + \frac{\mathrm{v}_j^2}{2g} + h_f \qquad (2.11)$$

where z is the elevation of nodes relative to the datum, p is the internal pressure measured from atmospheric levels, v is the flow velocity, γ_w is the unit weight of water, h_p is the head gain from external mechanical energy, such as pumps, and h_f is the head losses including frictional and minor losses.

A fundamental aspect of the Bernoulli equation is that there is only one hydraulic head at each node in a hydraulic network. The algebraic sum of the head losses and gains around any closed loop should be zero, which is expressed as

$$\sum_{k=1}^{n_L} h_k = 0 \qquad (2.12)$$

where n_L is the number of pipes in the loop and h_k is the head gain or loss in pipe k.

2.4 FLOW EQUATIONS

Hydraulic network analysis is governed by the laws of mass (continuity equation) and energy (Bernoulli equation) conservation. The major unknowns that need to be solved for are flows in links and hydraulic heads at nodes. The flows and hydraulic heads are linked with each other by the head loss equations, Equations 2.7 and 2.8. Based on different primary unknowns used in the equations, four types of flow equations can be developed, which are Q-, H-, ΔQ - and hybrid equations (Jeppson, 1976), to express the laws of mass and energy conservation. The four types of flow equations are discussed in the following sections. For simplicity, the following equations are constructed for networks only with pipes and nodes, and all energy losses occur as frictional losses since minor losses can be expressed as frictional losses of an equivalent pipe. All the symbols used in these equations, if not explained, have the same meaning as those used in the previous sections.

2.4.1 Q-equations

In this system of formulations, the flow rate, Q, in each pipe is taken as the primary unknown and solved first. The hydraulic head, H, is solved successively according to the head loss equation, Equation 2.7, from a node with known head, such as a tank or reservoir, in the network. For a network containing n_n nodes, n_p pipes, and n_L loops, the system of formulations consists of two separate sets of equations:

$$\sum_{k=1}^{n_{pi}} Q_{ik} = \tilde{Q}_i \qquad i = 1, 2, \cdots, n_n\text{-}1 \tag{2.13}$$

30

$$\sum_{k=1}^{n_L(I)} K_{fk} Q_k^{n_k} = 0 \qquad I = 1, 2, \cdots, n_L \qquad (2.14)$$

Equation 2.13 follows directly from the continuity equation, Equation 2.10. There are n_n-1 independent continuity equations. The n_n^{th} continuity equation is satisfied automatically if the former n_n-1 ones are satisfied. Equation 2.14 results from substituting the frictional loss equation, Equation 2.7, into the loop energy conservation equation, Equation 2.12. The script I represents the loop index, and k represents the pipe index in the loop. The number of Equation 2.14 is equal to the number of loops, n_L. The n_n-1 continuity equations are linear and the n_L loop energy equations are nonlinear with respect to the flow rate, Q. For the network with n_n nodes, n_L loops, and n_p pipes, the following expression is true (Jeppson, 1976)

$$n_p = n_n + n_L - 1 \qquad (2.15)$$

As such, the number of unknowns is exactly equal to the number of independent equations in this system of formulations. All flows can be solved directly. Since a large network may consist of thousands of pipes, this system of equations is best solved by systematic methods using computers. Such techniques will be discussed in Section 2.5.

2.4.2   H-equations

In this system of formulations, the hydraulic head, H, at each node is set as the primary unknown and solved first. The flow rate, Q, in each pipe is solved next from

the head loss equation, Equation 2.7. Reformatting Equation 2.7 for a pipe k connected to nodes i and j results in

$$Q_k = \left(h_{fk} / K_{fk}\right)^{1/n_k} = \left(\frac{H_i - H_j}{K_{fk}}\right)^{1/n_k} \tag{2.16}$$

Substituting Equation 2.16 into the nodal continuity equation, Equation 2.10, there is the following set of equations:

$$\sum_{k=1}^{n_{pi}} \left(\frac{H_i - H_j}{K_{fk}}\right)^{\frac{1}{n_k}} = \tilde{Q}_i \qquad i = 1, 2, \cdots, n_n - 1 \tag{2.17}$$

For a network with n_n nodes, a system of n_n-1 nonlinear equations with respect to hydraulic head, H, can be developed. The solution of these equations gives the head at each node with at least one known head, such as the head at a tank or reservoir, in the network. The number of the H-equations is less than that of the Q-equations because no loop equations need to be solved. However, all the H-equations are nonlinear.

2.4.3 ΔQ-equations

In this system of formulations, a corrective flow, ΔQ, in each loop is set as the primary unknown. To construct the ΔQ-equations, a network is divided into n_L loops first. An initial flow in each pipe is then assumed, which satisfies the n_n-1 nodal continuity equations. To satisfy the n_L loop energy equations, Equation 2.12, a corrective flow is added into each loop. Assuming the initial flow in pipe k as Q_{ok} and

the corrective flow in loop I as ΔQ_I, a set of loop energy equations can be expressed as

$$\sum_{k=1}^{n_L(I)} K_{fk}(Q_{ok} + \Delta Q_I)^{n_k} = 0 \qquad I = 1, 2, \cdots, n_L \qquad (2.18)$$

The system of Equation 2.18 consists of n_L equations and n_L unknowns, ΔQ_I, such that all unknowns can be solved. The final flow in each pipe is equal to the initial flow, Q_{ok}, plus the corrective flow, ΔQ_I. The hydraulic head can, thereafter, be solved using the head loss equation, Equation 2.7, successively from a node with known head in the network.

Obviously, there are fewer loops than either pipes or nodes in a network, so the matrix developed by the ΔQ-equations is smaller than that by the Q- and H-equations. However, all the ΔQ-equations are nonlinear and this method is difficult to address in a computer solution because it involves cumbersome record keeping of loops and pipes.

2.4.4 Hybrid Equations

In this system of formulations, both flow rates in pipes and hydraulic heads at nodes are set as the primary unknowns and solved simultaneously. Combining the head loss equations, Equation 2.16, and the continuity equations, Equation 2.10, results in

$$H_i - H_j = K_{kf}Q_k^{n_k} \qquad\qquad k = 1, 2, \cdots, n_p \qquad (2.19)$$

$$\sum_k^{n_{pi}} Q_{ik} = \tilde{Q}_i \qquad\qquad i = 1, 2, \cdots, n_n \qquad (2.20)$$

Equations 2.19 and 2.20 can be assembled as a system of $n_p + n_n$ equations with $n_p + n_n$ unknowns; therefore, all flows and heads can be solved simultaneously. Although there are more equations in the hybrid equations than the previous three systems of equations, the matrix formulated by Equations 2.19 and 2.20 are sparse, and the convergence rate is fast when solved by appropriate algorithms. The details on how to solve the hybrid equations are discussed in Section 2.5.4, Gradient Method.

2.5   NUMERICAL METHODS FOR FLOW EQUATIONS

In the last section, four types of flow equations are described. The solution to these equations involves solving a set of linear and/or nonlinear equations. For networks with a large number of components, numerical methods have to be applied. Four widely used numerical methods are Hardy-Cross, Newton-Rapshon, linear theory, and gradient method.

2.5.1   Hardy-Cross Method

The Hardy-Cross method is the oldest and most widely used numerical method for analyzing pipe networks (Cross, 1936). The Hardy-Cross method is most frequently used to solve ΔQ-equations, and the H- and Q-equations can also be solved by this method. The procedures for Hardy-Cross method applied to ΔQ-equations are:

1. Divide the network into n_L closed loops.

2. Assume initial value of flow in each pipe Q_{ok}, with the continuity equation satisfied at each node.

3. Compute the sum of head losses around a loop, keeping track of signs. If the direction of movement (clockwise and counterclockwise) around the loop is opposite to the direction of flow in the pipe, the head loss, h_{fk}, is negative, otherwise positive. The sum of the head losses, F_I, along the loop I, can be expressed as

$$F_I = \sum_{k=1}^{n_L(I)} h_{fk} = \sum_{k=1}^{n_L(I)} K_{fk} Q_{ok}^{n_k} \tag{2.21}$$

4. Compute ΔQ_I for loop I using

$$\Delta Q_I = -\frac{\displaystyle\sum_{k=1}^{n_L(I)} K_{fk} Q_{ok}^{n_k}}{\displaystyle\sum_{k=1}^{n_L(I)} \left| n_k K_{fk} Q_{ok}^{n_k-1} \right|} \tag{2.22}$$

The mathematical basis of Equation 2.22 is explained by Cross (1936) or Jeppson (1976).

5. Correct Q_{ok} as $Q_{ok} + \Delta Q_I$ for loop I.

6. Repeat steps 3 through 5 for each loop in the network.

7. Perform steps 3 through 6 iteratively until the sum of head losses, F_I, along all loops, is small enough to satisfy the required accuracy. The final flow in each

pipe is equal to the flow in the previous iteration step plus the final corrective flow.

8. Solve the hydraulic head at each node, using the head loss equation, Equation 2.7, successively from a node with known head in the network.

For this application of the Hardy-Cross method, the number of equations is equal to the loop number in the network. It is typically small. However, the convergence rate of the Hardy-Cross method is generally slow and strongly depends on the initial estimates of the iteration. Thus, the Hardy-Cross method is more suitable for solving small systems by hand calculations.

2.5.2 Newton-Raphson Method

The Newton-Raphson method is probably the most widely used numerical method for solving implicit or nonlinear equations. The main advantage associated with this method lies in its rapid convergence rate to the solution. The mathematical principle of this method is that a solution to the equation $F(x) = 0$ can be obtained by the iterative formula $x^{(m+1)} = x^{(m)} - F(x^{(m)})/F'(x^{(m)})$, in which the $m+1$ and m are indices for the iterative steps and $F'(x^{(m)})$ is the derivative of $F(x)$ with respect to x at the mth iteration. Mathematically, the error of the $(m+1)^{th}$ iteration is proportional to the square of the error in the mth; accordingly, it has a quadratic convergence rate. The Newton-Raphson method can be applied to any of the four types of flow equations. Its application to the H-equations is described below as an example.

1. Express Equation 2.17 for node i in the form of

$$F_i = \left[\sum_{k=1}^{n_{pi}} \left(\frac{H_i - H_j}{K_{fk}} \right)^{\frac{1}{n_k}} \right] - \tilde{Q}_i \qquad (2.23)$$

in which F_i is a function of the hydraulic head, H_i, at node i, and all the hydraulic heads, $H_j's$, at the nodes having connection with node i. The n_{pi} is the number of pipes connected to node i.

2. Assemble a system of nonlinear equations with Equation 2.23 applied to all nodes.

$$\underline{F}(\underline{H}) = 0 \qquad (2.24)$$

in which $\underline{F}$ is a vector of continuity for all nodes, $i = 1, 2, ..., n_n$, and $\underline{H}^T = \{H_1, \cdots, H_{n_n}\}$ is a vector of hydraulic heads.

3. Solve Equation 2.24 iteratively using the Newton-Raphson formula as

$$\underline{H}^{(m+1)} = \underline{H}^{(m)} - \underline{D}^{-1}(\underline{F}(\underline{H}^{(m)}))\underline{F}(\underline{H}^{(m)}) \qquad (2.25)$$

in which $\underline{H}^{(m)}$ is the estimate of the head vector at the mth iteration, and $\underline{D}^{-1}(\underline{F}(\underline{H}^{(m)}))$ is the inverse of Jacobian matrix $\underline{D}$ at $\underline{F}(\underline{H}^{(m)})$.

$$\underline{D} = \begin{vmatrix} \dfrac{\partial F_1}{\partial H_1} & \cdots & \dfrac{\partial F_1}{\partial H_n} \\ \vdots & & \vdots \\ \dfrac{\partial F_n}{\partial H_1} & \cdots & \dfrac{\partial F_n}{\partial H_n} \end{vmatrix} \qquad (2.26)$$

The iteration begins with an initial estimate of the head vector $\underline{H}^{(0)}$. Then the matrix $\underline{F}(\underline{H}^{(0)})$ is developed, and the inverse of the Jacobian matrix $\underline{D}^{-1}(\underline{F}(\underline{H}^{(0)}))$ is calculated. Thereafter $\underline{H}^{(1)}$ can be derived by Equation 2.25. The above steps iterate until the difference between two successive iterations is within the required accuracy, after which the hydraulic head at each node is solved.

4. Solve the flow rate in each pipe according to the head loss equation, Equation 2.7, from the known head at each node.

2.5.3 Linear Theory Method

The linear theory method has several distinct advantages compared with the Hardy-Cross and Newton-Raphson methods (Wood and Carl, 1972). It does not necessarily require an initialization, and it always converges in relatively few iterations. It is most suitable for solving the Q-equations. Its application to solve the H- and ΔQ-equations is not recommended. The mathematical basis for this method is to transform the n_L nonlinear Q-equations into linear equations as

$$h_{fk} = K_{fk}Q_k^{n_k} = [K_{fk}Q_{ko}^{n_k-1}]Q_k = K'_{fk}Q_k \qquad (2.27)$$

in which, the coefficient K_{fk}' is defined as the product of K_{fk} multiplied by $Q_{ko}^{n_k-1}$, an initial estimate of the flow rate in pipe k.

The procedures of applying the linear theory method to Q-equations are:

1. Express the continuity equation at each node as Q-equations:

$$\sum_{k=1}^{n_{pi}} Q_{ik} = \tilde{Q}_i \qquad i = 1, 2, \cdots, n_n\text{-}1 \qquad (2.28)$$

2. Express the energy conservative equation in each loop as Q-equations:

$$\sum_{k}^{n_L(I)} K_{fk} Q_k^{n_k} = 0 \qquad I = 1, 2, \cdots, n_L \qquad (2.29)$$

3. Estimate the initial flow, Q_{ko}, and calculate $K_{fk}' = K_{fk} Q_{ko}^{n_k-1}$ for each pipe. Typically, Q_{ko} is set as 1 and $K_{fk}' = K_{fk}$.

4. Substitute K_{fk}' into Equation 2.29, and transform it into a linear equation of form:

$$\sum_{k}^{n_L(I)} K_{fk}' Q_k = 0 \qquad I = 1, 2, \cdots, n_L \qquad (2.30)$$

5. Solve the system of linear equations, Equations 2.28 and 2.30, simultaneously, and update the coefficient of K_{fk}' using the solved flow rate in each pipe. This iteration continues until the difference between the flow rate in each pipe in two successive steps is within the required accuracy.

6. Solve the hydraulic head at each node, using the head loss equation, Equation 2.7, successively from a node with known head in the network.

2.5.4   Gradient Method

The gradient method is among the most efficient methods for solving flow equations because it solves for both flows and hydraulic heads simultaneously. This method is utilized as the solver of many commercial hydraulic network analysis computer programs. The gradient method is applied to solve the hybrid equations in which the hydraulic head at each node and the flow rate in every pipe are the unknowns. The hybrid equations, Equations 2.19 and 2.20, can be written in the matrix format (Todini and Pilati, 1987) of

$$
\begin{bmatrix} A_{11} & A_{12} \\ A_{21} & 0 \end{bmatrix} * \begin{bmatrix} \underline{Q} \\ \underline{H} \end{bmatrix} = \begin{bmatrix} -A_{10}\underline{H0} \\ \underline{\tilde{Q}} \end{bmatrix}
\tag{2.31}
$$

in which, $A_{11} = \begin{bmatrix} K_{1f}|Q_1|^{n_1-1} & & & \\ & K_{2f}|Q_2|^{n_2-1} & & \\ & & \ddots & \\ & & & K_{nf}|Q_{n_p}|^{n_n-1} \end{bmatrix}$ is a (n_p, n_p) diagonal matrix.

$A_{12} = A_{21}{}^T$ $\qquad\qquad$ (n_p, n_n) unknown head nodes incidence matrix.

$A_{10} = A_{01}{}^T$ $\qquad\qquad$ (n_p, n_o) fixed head nodes incidence matrix.

$\underline{Q}^T = \begin{bmatrix} Q_1, Q_2, \cdots, Q_{n_p} \end{bmatrix}$ $\qquad$ $(1, n_p)$ flow rates in each pipe.

$\underline{\tilde{Q}}^T = \begin{bmatrix} \tilde{Q}_1, \tilde{Q}_2, \cdots, \tilde{Q}_{n_n} \end{bmatrix}$ $\qquad$ $(1, n_n)$ nodal demands.

$\underline{H}^T = \begin{bmatrix} H_1, H_2, \cdots, H_{n_n} \end{bmatrix}$ $\qquad$ $(1, n_n)$ unknown nodal heads

$\underline{H0}^T = \begin{bmatrix} H0_1, H0_2, \cdots, H0_{n_o} \end{bmatrix}$ $\quad$ $(1, n_o)$ fixed nodal heads

with

n_n $\qquad\qquad\qquad\qquad\qquad$ number of nodes with unknown head

n_o number of nodes with fixed head

n_p number of pipes with unknown flow

$$A_{12}(i,j) = \begin{cases} +1 & \text{if flow of pipe } i \text{ enters node } j \\ 0 & \text{if pipe } i \text{ and node } j \text{ are not connected} \\ -1 & \text{if flow of pipe } i \text{ leaves node } j \end{cases}$$

The upper part of Equation 2.31 represents the relationship between head loss and flow rate for pipes, while the lower part corresponds to the continuity of flow at nodes. The matrix A_{11} is the head loss-flow relationship being used and A_{12} is a topological matrix containing the connectivity information between pipes and nodes. A_{12} is a ($n_p \times n_n$) matrix with just two nonzero elements in each row: a "-1" in the column corresponding to the starting node of a pipe, and a "$+1$" corresponding to the ending node. A_{21} is the transpose of A_{12}. A_{10} is defined similarly to A_{12} for fixed head nodes. Since A_{11} depends on the flows, the upper part of Equation 2.31 is a set of nonlinear equations. In contrast, the lower part of Equation 2.31 is a set of linear equations.

To solve the system of partly linear and partly nonlinear equations, one starts with the minimization of a slightly modified Content Model (Collins et al. 1978) to prove the existence and uniqueness of the solution. Then the Newton-Raphson technique is applied in the enlarged space of flows and heads where the proof of the existence and uniqueness of the solution holds, and the problem is algebraically reconstructed to the recursive solution of a system of linear equations. The solution to the system of linear equations is then efficiently obtained using the Incomplete Choleski Factorization/Modified Conjugate Gradient (ICF/MCG) algorithm proposed by Kershaw (1978). A detailed derivation of the solution for Equation 2.31 is provided by Todini and Pilati (1987).

2.6   HYDRAULIC NETWORK ANALYSIS SOFTWARE

Typically, a set of linear and/or nonlinear equations needs to be solved simultaneously in hydraulic network analysis. The flow equations are best solved by computer programs. Many commercial software packages are available in the market for hydraulic network analysis. Among them, EPANET, developed and distributed by the US Environmental Protection Agency (EPA), (Rossman, 2000) is one of the earliest and most widely used. Because EPANET contains a state-of-the-art hydraulic analysis engine and its source code is open freely to public, a family of software packages, including WaterCAD (WaterCAD, 2005), MIKENET (MIKENET, 2005), H2ONET (MWH Soft Inc., 1999), and so on, use the EPANET analysis engine and develop their own products on top of it. The LADWP hydraulic network model works with the software package H2ONET, which is fully compatible with EPANET.

2.6.1   EPANET

EPANET was designed to be a research tool for improving the understanding of the movement and fate of drinking water constituents in water distribution systems (Rossman, 2000). It has two major capabilities, hydraulic and quality modeling for water in a pressurized pipeline network. The water quality modeling is beyond the scope of this study, and therefore, only the hydraulic modeling capabilities of EPANET are discussed. The following discussion is based on, but not limited to, the information provided in the EPANET user manual by Rossman (2000).

EPA released two versions of EPANET, DOS and Windows versions. The DOS version is an analysis engine, coded in the C language. The Windows version

includes the C coded engine and a graphical user interface (GUI) written with the Daphi language. To run EPANET in the DOS environment, all network input data are stored in an input text file and analysis results are written into an output text file. To run EPANET in the Windows environment, users can use the GUI to construct a hydraulic network model and input network attributes graphically. The GUI compiles the input information into a text file, and calls on the engine to do the analysis. After finishing the analysis, the GUI retrieves data from the text output file generated by the engine and displays the results graphically for visualization. The source codes and executable files of both the analysis engine and GUI are available from the Internet free of charge. Thus, users can use EPANET to perform hydraulic network analyses, and can also modify the source codes for their own product development.

2.6.1.1 EPANET Hydraulic Network Components

An EPANET hydraulic network model consists of various physical components, which are the mathematical representations of physical objects in a real water supply system. Mathematical representations are also used for operational components that control the behavior and operational properties of the physical components.

2.6.1.1.1 Physical Components

EPANET models a water supply system as a collection of links connected to nodes. The nodes represent junctions and storage nodes, including tanks and reservoirs. The links represent pipes, pumps, and control valves. Figure 2.4 illustrates how these objects can be connected to one another to form a network. Each reservoir,
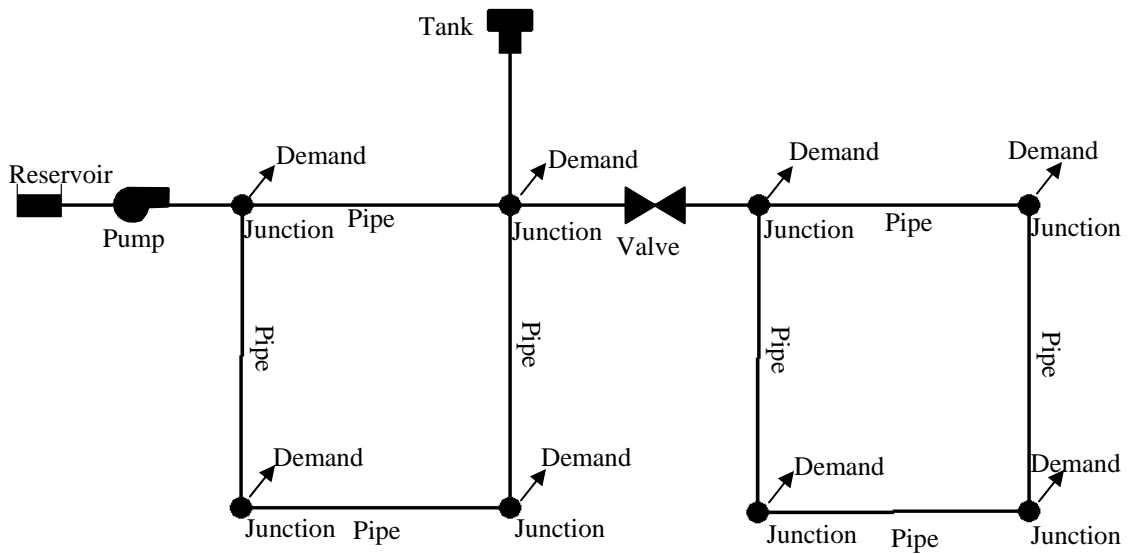
Figure 2.4 Physical Components in an EPANET Hydraulic Network

tank, pump, and valve, because of its different physical properties and/or functions, can have different modeling options. Table 2.3 lists all the physical components that EPANET can model. In total, there are 17 different components, including 1 junction, 4 storage nodes, 1 pipe, 4 pumps, and 7 valves. Table 2.3 provides a brief description of the functions and basic input and output parameters, associated with hydraulic simulations of each physical component.

2.6.1.1.2   Operational Components

In addition to the physical components, EPANET employs three types of operational components: curves, patterns, and controls that describe the operational aspects of the physical components.

Table 2.3 Summary Table for Physical Components in an EPANET Hydraulic Network Model

Components			Descriptions	Inputs	Outputs
Junction			Points where links join together and where water enters or leaves the network	Coordinates; elevation; demand	Hydraulic head; pressure
Storage Node	**Reservoir**	**Constant Level**	Unlimited capacity water sources with constant water level during simulation time	Coordinates; hydraulic head (a constant value)	Hydraulic head
		Variable Level	Unlimited capacity water sources with water level varying with simulation time	Coordinates; hydraulic head curve (hydraulic head vs. time)	
	Tank	**Cylindrical**	Limited capacity water sources with cylindrical shape	Coordinates; bottom elevation; diameter; initial, minimum, and maximum water level	Hydraulic head
		Variable Area	Limited capacity water sources with variable cross-sectional area	Coordinates; volume vs. hydraulic grade curve	Hydraulic head
Pipe			Links conveying water from one node in the network to another	Start and end node; diameter; length; roughness and minor loss coefficients; status (open, closed, or containing check valve)	Flow rate; head loss
Pump	**Constant Power**		Pumps which supply constant amount of energy to water	Start and end node; diameter; energy; status (open or closed)	
	One-Point		Pumps with characteristic curves defined by one point	Start and end node; diameter; operation flow and head gain; status (open or closed)	Flow rate; head gain
	Three-Point		Pumps with characteristic curves defined by three points	Start and end node; diameter; pump curve; status (open or closed)	
	Multiple-Point		Pumps with characteristic curves defined by multiple points	Start and end node; diameter; pump curve; status (open or closed)	

45

Table 2.3 (Continued)

Component	Description	Input	Output
Check (CVs)	Allow water through one direction (built in pipe)		
Pressure Reducing Valves (PRVs)	PRVs limit the pressure on their downstream end to not exceed a pre-set value when the upstream pressure is above the setting. If the upstream pressure is below the setting, then flow through the valve is unrestricted. If the downstream pressure exceeds the upstream pressure, the valve closes to prevent reverse flow.	Start and end node; diameter; minor loss coefficient; downstream pressure setting; status (open or closed)	
Pressure Sustaining Valves (PSVs)	PSVs attempt to maintain a minimum pressure on their upstream end when the downstream pressure is below the setting. If the downstream pressure is above the setting, then flow through the valve is unrestricted. If the downstream pressure exceeds the upstream pressure, the valve closes to prevent reverse flow.	Start and end node; diameter; minor loss coefficient; downstream pressure setting; status (open or closed)	Flow rate; head loss
Pressure Breaker Valves (PBVs)	PBVs force a specified pressure loss to occur across the valve. Flow through the valve can be in either direction.	Start and end node; diameter; minor loss coefficient; pressure setting; status (open or closed)	
Flow Control Valves (FCVs)	FCVs limit the flow to a specified amount.	Start and end node; diameter; minor loss coefficient; flow setting; status (open or closed)	
Throttle Control Valves (TCVs)	TCVs simulate a partially closed valve by adjusting the minor head loss coefficient of the valve.	Start and end node; diameter; minor loss coefficient; status (open or closed)	
General Purpose Valves (GPVs)	GPVs are used to represent a link where the user supplies a special flow-head loss relationship instead of following one of the standard hydraulic formulas.	Start and end node; diameter; head loss vs. flow rate curve; status (open or closed)	

*(Far-left column spanning valve rows: **Valve**)*

46

Curves

Curves are objects that contain data pairs representing a relationship between two quantities. An EPANET model can utilize four types of curves, which are pump characteristic, efficiency, volume, and head loss curves. A pump characteristic curve represents the relationship between the head and flow rate that a pump can deliver. EPANET can model three different shapes of pump curves, which are single-, three-, and multi-point curves, dependent on the number of points used to calibrate the pump characteristics. An efficiency curve describes pump efficiency as a function of pump flow rate. The efficiency curve is used for energy consumption and cost calculation associated with pump operations. These calculations are not considered in this project. A volume curve describes how storage tank volume varies as a function of water level. It is used when it is necessary to accurately represent tanks, for which the cross-sectional area varies with water height. A head loss curve is used to describe the head loss through a general purpose valve as a function of flow rate. It provides the capability to model devices and situations with unique head loss-flow relationships, such as reduced flow-backflow prevention valves, turbines, and well draw-down behavior.

Time Patterns

A time pattern is a collection of multipliers that can be applied to a quantity to allow it to vary over simulation time. Nodal demands, reservoir heads, and pump schedules can all have time patterns associated with them. When applying time pattern to a quantity, the hydraulic simulation time is divided into different time intervals, which are set by users. Within each time interval the quantity remains at a

constant level, equal to the product of its nominal value and the pattern's multiplier for that time period.

Controls

Controls are statements that determine how the network is operated over time. They specify the status of selected links as a function of time, tank water levels, and pressures at select junctions within the network. There are two types of controls, simple and rule-based, in EPANET hydraulic network hydraulic simulations. Simple controls change the status or setting of a link based on one control condition, such as water level in a tank, pressure at a junction, time into the simulation, or the time of day. Rule-based controls change the link status or settings based on a combination of conditions that might exist in the network.

2.6.1.2   EPANET Input File

EPANET stores all input data in a text file with the extension of file name, *.inp*. The *inp* file is organized into sections, where each section begins with a key word enclosed in brackets. The various sections are listed in Table 2.4. A detailed example of the input file is shown in Table 2.5 in Section 2.6.1.5. In general these sections can be classified into five categories, Network Components, System Operation, Water Quality, Options and Reporting, and Network Map/Tags.

The Network Components category stores information about the hydraulic properties of network physical components, including junctions, reservoirs, tanks, pipes, pumps, and valves. The System Operation category mainly stores information

Table 2.4 Sections in an EPANET Input File

Network Components	System Operation	Water Quality	Options and Reporting	Network Map/Tags
[TITLE]	[CURVES]	[QUALITY]	[OPTIONS]	[COORDINATES]
[JUNCTIONS]	[PATTERNS]	[REACTIONS]	[TIMES]	[VERTICES]
[RESERVOIRS]	[ENERGY]	[SOURCES]	[REPORT]	
[TANKS]	[STATUS]	[MIXING]		
[PIPES]	[CONTROLS]			
[PUMPS]	[RULES]			
[VALVES]	[DEMANDS]			

of system operational properties, such as curves, patterns, initial status, controls, rules, and demand. The Water Quality category stores information for water quality simulation. The Options and Reporting category stores information of simulation and report options, and times for extended period simulation. The Network Map/Tags category stores information on the coordinates of each node and coordinates of each vertex of links.

Users can use the GUI provided by EPANET to construct a hydraulic model and export the *inp* file. Because EPANET is one of the most widely used hydraulic software programs, most of the commercial hydraulic network analysis software packages can export EPANET input files for data exchange. For example, a network model constructed by H2ONET can be directly exported with the EPANET input file format and analyzed by the EPANET engine. Furthermore, because the EPANET input file is well organized with different sections, it provides an easy way to modify the input file by programming.

2.6.1.3   EPANET Hydraulic Simulation Methodology

EPANET hydraulic engine can perform either steady state or extended period simulation. During a steady state simulation, EPANET computes junction heads and link flows for a fixed set of reservoir levels, tank levels, and water demands at a fixed point of time. For extended period simulation, EPANET computes junction heads and link flows for a fixed set of reservoir levels, tank levels, and water demands over a succession of points in time. From one time step to the next, reservoir levels and junction demands are updated according to their prescribed time patterns while tank levels are updated using the current flow solution. The solution for heads and flows at a particular time involves simultaneously solving a set of hybrid equations using the gradient method. The hybrid equations and gradient method are discussed in Section 2.4.4 and 2.5.4, respectively.

2.6.1.4   EPANET Output File

The outputs from the EPANET engine are generated in a text file with the extension of file name, *.rpt*. An output file can contain four sections, Status, Energy, Nodes, and Links. Users can apply the control parameters in the input file to specify the interested sections and the quantities associated with each section to be reported.

The Status section lists the initial status of all reservoirs, tanks, pumps, valves, and pipes, as well as any changes in the status of these components as they occur over time in an extended period simulation. The Energy section lists the energy consumption and cost for the operation of each pump in the network. The Nodes section lists simulation results for nodes with the quantities specified by the user. The

default quantities reported for each node include demand, hydraulic head, and pressure. Results are listed for each reporting time step of an extended period simulation. The Links section lists simulation results for links with quantities specified by the user. The default quantities reported for each link include flow, velocity, and head loss. Diameter, length, water quality, status, setting, reaction rate, and friction factor can also be reported if required by the user.

2.6.1.5 An Example of EPANET Simulation

Figure 2.5 shows the same water distribution network as the one in Figure 2.4, with component IDs and nodal demands. The network contains 1 reservoir with ID 1, 1 tank with ID 7, 1 pump with ID 2, 1 PRV with ID 14, and 9 pipes. Eight demand nodes are distributed around the network. Each demand node has a demand of 6 liters per second (100 gpm). All network information for hydraulic simulation is stored in the input file shown in Table 2.5. In general, water flows from the tank and reservoir in the northwest towards the southeast to satisfy the demands. The steady state flow analysis was performed using EPANET, and results of nodes and links are reported in the output file shown in Table 2.6. The analytical results are further visualized using the GUI of EPANET shown in Figure 2.6. In this figure, the node and link IDs are shown as black numbers. The link flows in units of liter per second and nodal pressures in units of meter of water height are coded using the colors indicated in the legends. To verify the correctness of the results, the mass and energy conservations were checked for each node and link by hand calculations. It was found that all mass and energy conservations are satisfied.
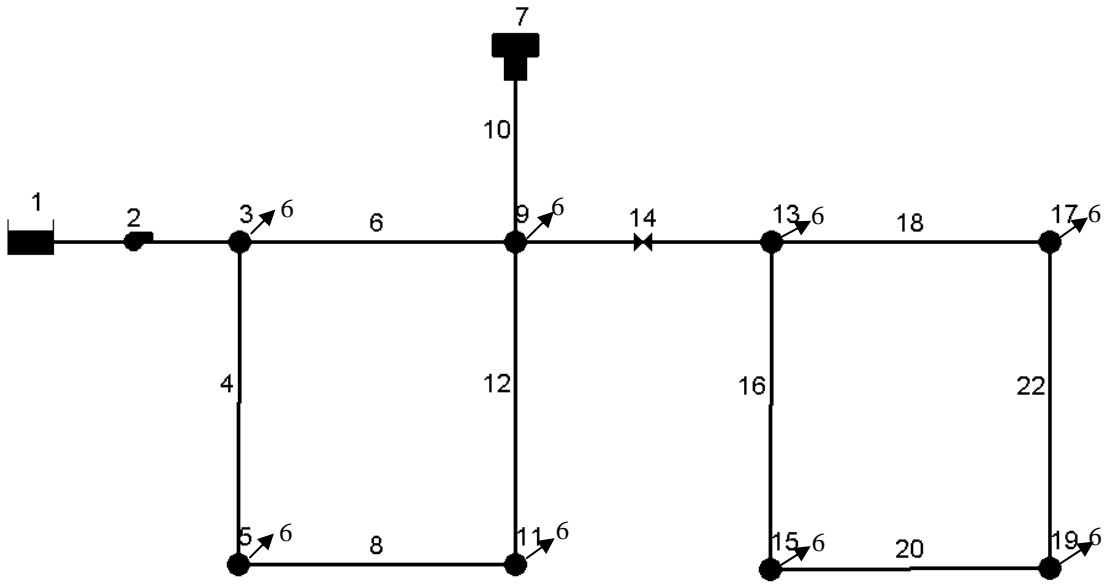
Figure 2.5 Hydraulic Network with Component IDs and Demands (unit: L/s)
(6 L/s = 100 gpm)

2.6.2   H2ONET

H2ONET is developed and distributed by MWH Soft, Inc (1999). H2ONET utilizes the EPANET analysis engine in conjunction with the AutoCAD environment to create network model drawings and display analysis results. There are three major modules in H2ONET: graphical model creation (pre-processor), network analysis (analyzer), and model result presentation (post-processor). The major improvement of H2ONET over EPANET is that H2ONET takes full advantage of the capabilities of AutoCAD to create the network model and display analytical results. Since H2ONET and EPANET are using the same engine, they are completely compatible for hydraulic network analysis. All physical and operational components in an EPANET hydraulic network model are supported by H2ONET. A H2ONET hydraulic network model can be imported directly into EPANET to perform hydraulic analysis.

Table 2.5 EPANET Input File

```
[TITLE]
EPANET Example Network 1

[JUNCTIONS]
ID        Elevation(m)       Pattern
3          100.00
5          100.00
9          100.00
11         100.00
13         50.00
15         50.00
17         50.00
19         50.00

[RESERVOIRS]
ID         Head(m)
1           150.00

[TANKS]
ID     Elev(m)   InitialLevel(m)   MinLevel(m)   MaxLevel(m)   Dia.(m)   MinVol(m³)   VolCurve
7      150.00    40.00             0.00          40.00         10.00     0.00

[PIPES]
ID    FromNode    ToNode    Length(m)    Diameter(mm)   Roughness   MinorLoss   CheckValve
10      7           9        100.00       100.00         100.00      0.00
12      9           11       100.00       100.00         100.00      0.00
16      13          15       100.00       100.00         100.00      0.00
18      13          17       100.00       100.00         100.00      0.00
20      15          19       100.00       100.00         100.00      0.00
22      17          19       100.00       100.00         100.00      0.00
4       3           5        100.00       100.00         100.00      0.00
6       3           9        100.00       100.00         100.00      0.00
8       5           11       100.00       100.00         100.00      0.00

[PUMPS]
ID     FromNode    ToNode     Parameter(kw)
2        1           3        POWER 10.00

[VALVES]
ID     FomNode     ToNode      Diameter(mm)     Type     Setting(m)     MinorLoss
14       9           13         100.00          PRV      80.00          0.00

[DEMANDS]
ID     Demand(L/s)
3        6.00
5        6.00
9        6.00
11       6.00
13       6.00
15       6.00
17       6.00
19       6.00
```

Table 2.5 (Continued)

```
[CURVES]

[PATTERNS]
PATN1    1.00        1.00        1.00        1.00        1.00        1.00

[STATUS]

[CONTROLS]

[SOURCES]

[QUALITY]

[REACTIONS]
GLOBAL BULK 0.00
GLOBAL WALL 0.00

[ENERGY]

[OPTIONS]
UNITS LPS
HEADLOSS H-W
VISCOSITY 1e-006
DIFFUSIVITY 1.21e-009
SPECIFIC GRAVITY 1.00
TRIALS 40
ACCURACY 0.001
DEMAND Multiplier 1.00

[REPORT]
PAGESIZE 30
STATUS NO
NODE ALL
LINK ALL

[COORDINATES]
ID    x(m)           y(m)
1     141.17         174.43
3     169.66         174.43
5     169.57         130.59
7     207.22         199.58
9     207.22         174.45
11    207.25         130.57
13    242.03         174.45
15    241.99         129.94
17    280.01         174.43
19    280.01         130.04

[VERTICES]

[End]
```

Table 2.6 EPANET Output File

```
*******************************************
*                E P A N E T              *
*        Hydraulic and Water Quality       *
*         Analysis for Pipe Networks       *
*              Version 2.0                  *
*******************************************


Input Data File ...................Example.inp
Number of Junctions...........8
Number of Reservoirs.........1
Number of Tanks ................1
Number of Pipes .................9
Number of Pumps ...............1
Number of Valves ...............1
Headloss Formula ...............Hazen-Williams
Hydraulic Timestep .............4.00 hrs
Hydraulic Accuracy .............0.001
Maximum Trials .................40
Quality Analysis ..................None
Specific Gravity ..................1.00
Relative Kinematic Viscosity ......0.98
Relative Chemical Diffusivity .....1.00
Demand Multiplier ......................1.00
Total Duration ............................0.00 hrs

Reporting Criteria:
All Nodes
All Links

Analysis begun Sun April 3 17:33:05 2005


Node Results:
--------------------------------------------------
Node      Demand    Head    Pressure
            L/s       m         m
--------------------------------------------------
3          6.00      184.74   84.74
5          6.00      181.02   81.02
9          6.00      180.19   80.19
11         6.00      180.15   80.15
13         6.00      130.00   80.00
15         6.00      127.45   77.45
17         6.00      127.45   77.45
19         6.00      127.12   77.12
1         -29.36     150.00    0.00    Reservoir
7         -18.64     190.00   40.00    Tank
```

Table 2.6 (Continued)

```
Link Results:
-------------------------------------------------------
Link        Flow      Velocity    Headloss
            L/s         m/s        /1000m
-------------------------------------------------------
10         18.64       2.37        98.13
12          0.95       0.12         0.40
16          9.00       1.15        25.49
18          9.00       1.15        25.49
20          3.00       0.38         3.33
22          3.00       0.38         3.33
4          11.05       1.41        37.24
6          12.32       1.57        45.57
8           5.05       0.64         8.73
2          29.36       0.00       -34.74      Pump
14         24.00       3.06        50.19      PRV

  Analysis ended Sun April 3 17:33:05 2005
```
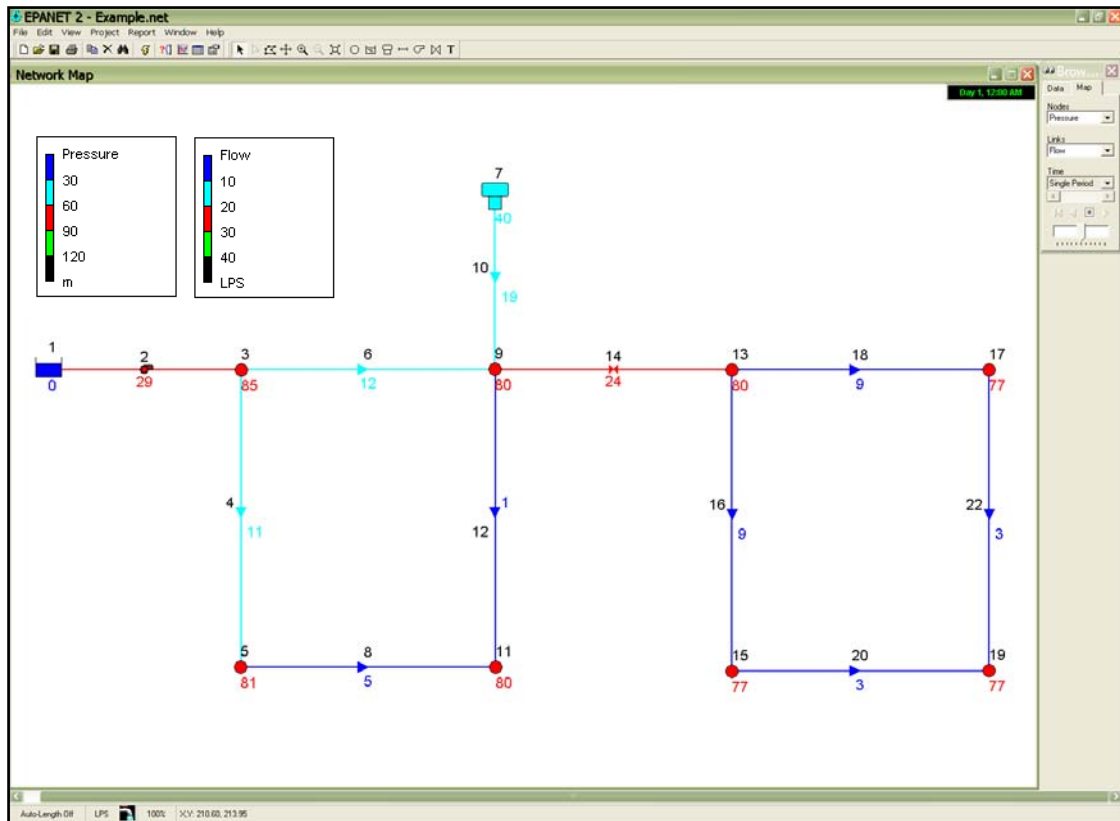

Figure 2.6 Hydraulic Network Analysis Results from EPANET

56
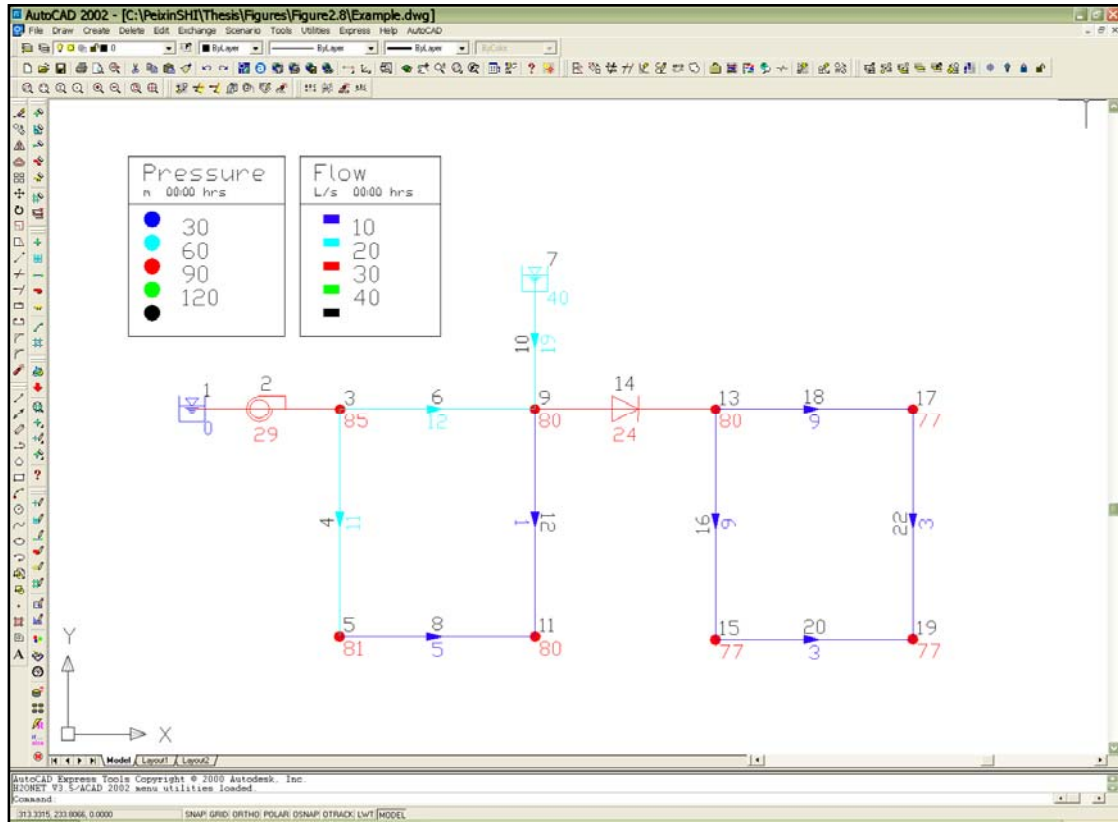
Figure 2.7 Hydraulic Network Analysis Results from H2ONET

Figure 2.7 shows the hydraulic network analysis results from H2ONET for the same network as the one shown in Figure 2.5. This figure shows that all the results, rounded to integers, are the same as those shown in Figure 2.6. The difference between Figures 2.6 and 2.7 is the graphical interfaces used by the two software packages. Tables 2.7 and 2.8 present a detailed comparison of the flow rates and pressures between EPANET and H2ONET results. These tables show that all the relative differences of flows and pressures are smaller than 0.12%. The reason for these small differences may be associated with the different convergence criteria used by EPANET and H2ONET during hydraulic balancing, which is a highly nonlinear process. Both EPANET and H2ONET are capable of analyzing the hydraulic network correctly.

57

Table 2.7 Comparison of Link Flow Rates Between EPANET and H2ONET Results

ID	From Node	To Node	EPANET Flow (L/s)	H2ONET Flow (L/s)	Difference (L/s)	Relative Difference (%)
10	7	9	18.64	18.62	0.02	0.11
12	9	11	0.95	0.95	0.00	0.00
16	13	15	9.00	9.00	0.00	0.00
18	13	17	9.00	9.00	0.00	0.00
20	15	19	3.00	3.00	0.00	0.00
22	17	19	3.00	3.00	0.00	0.00
4	3	5	11.05	11.05	0.00	0.00
6	3	9	12.32	12.33	-0.01	-0.08
8	5	11	5.05	5.05	0.00	0.00
2	1	3	29.36	29.38	-0.02	-0.07
14	9	13	24.00	24.00	0.00	0.00

Table 2.8 Comparison of Nodal Pressures Between EPANET and H2ONET Results

ID	EPANET Pressure (m)	H2ONET Pressure (m)	Difference (m)	Relative Difference (%)
11	80.15	80.07	0.08	0.10
13	80.00	80.00	0.00	0.00
15	77.45	77.42	0.03	0.04
17	77.45	77.42	0.03	0.04
19	77.12	77.09	0.03	0.04
3	84.74	84.72	0.02	0.02
5	81.02	80.96	0.06	0.07
9	80.19	80.11	0.08	0.10

2.6.3 Limitations of Commercial Software Packages

Today, fast computers and efficient computational algorithms liberate users from the cumbersome hand calculations required for hydraulic network analysis. The integration of hydraulic network engines with CAD or GIS makes the network construction and analysis point-and-click simple. These software packages provide a good tool to predict flow and pressure conditions in an undamaged water supply system. However, when used for a damaged system during earthquakes, these software packages have serious limitations.

2.6.3.1 Negative Pressure Prediction

Hydraulic network analysis assumes a pipeline network is always full and pressurized with water. The incompressible flow is then governed by the laws of mass and energy conservation. The law of mass conservation can be expressed as the equation of continuity, which assumes that all demands must be satisfied. The forced satisfaction of all demands may lead to the prediction of unrealistically high negative pressures, especially in an earthquake-damaged system, in which earthquake demands from pipe breaks and leaks may be much higher than the supply from reservoir and transmission sources. The prediction of negative pressures contradicts the field evidence that water supply systems are not air tight and not all demands can be satisfied. Hydraulic network analysis results with negative pressures are inaccurate.

2.6.3.2 Pipe Damage Simulation

To simulate the response of a water supply system during earthquakes, it may be necessary to damage the system first and then perform a hydraulic network simulation of the damaged system. Previous research shows that buried pipelines in a water supply system are the most vulnerable components (ATC, 1991). They can either break or leak during earthquakes. There are no pipe break or leak simulation algorithms in EPANET, H2ONET, or any other commercial software packages. It is therefore important to develop an algorithm to model pipe breaks and leaks, and integrate this algorithm into a computer program for simulation purposes.

CHAPTER 3

HYDRAULIC NETWORK ANALYSIS FOR DAMAGED SYSTEMS

3.1 INTRODUCTION

Earthquake performance of a water supply system depends on the available flows and pressures in the damaged system. The flows and pressures can be predicted using hydraulic network analysis. Commercial hydraulic network analysis computer software packages are designed for undamaged systems. When used for damaged systems, they may predict unrealistically high negative pressures. Water distribution systems are not air tight so that their ability to support negative pressures is very limited. Hydraulic network analysis results with negative pressures tend to over predict the available flows in the system, and result in unconservative estimates of system serviceability.

This chapter describes an algorithm for the hydraulic network analysis of a heavily damaged water supply system with special treatment of negative pressures. After the introduction, the generation of negative pressures is illustrated using a simple hydraulic network in Section 3.2. Thereafter, previous research on this subject is reviewed briefly in Section 3.3. Section 3.4 presents the algorithm applied to treat negative pressures in this study.

3.2   NEGATIVE PRESSURE GENERATION

Hydraulic network analysis solves incompressible water flow in a pressurized pipeline network based on two principle laws, the laws of mass and energy conservation. The law of mass conservation can be expressed as the equation of continuity, which assumes that all demands in a system must be satisfied. The law of energy conservation indicates that water can only flow from nodes with high energy to nodes with low energy. The energy of water is expressed as hydraulic head, which is the summation of elevation and pressure heads. Hydraulic head neglects velocity, which is typically small and does not contribute significantly to the energy balance. The conventional hydraulic network analysis algorithm does not differentiate positive and negative pressures, and only uses the total head difference to drive water flow to satisfy demands. The forced satisfaction of all demands, with no differentiation of positive and negative pressures, may lead to the prediction of unrealistically high negative pressures at some nodes. This outcome is especially true in an earthquake-damaged system, in which demands due to water losses from pipeline breaks and leaks may be much higher than the supply from reservoir and transmission pipeline sources.

The negative pressure generation in a damaged system can be illustrated using a simple example. Consider the hydraulic network in Figure 3.1, consisting of two pipes and three nodes. Node *A* is a tank with a water level of 40 m measured from the datum. Node *B* has an elevation of 50 m. Node *C* is a fixed grade node, which has an elevation of 0 m and is open to the atmosphere to simulate a broken end of a pipeline. Pipe *a* connects nodes *A* and *B*, and pipe *b* connects nodes *B* and *C*. For simplicity, it is assumed that pipes *a* and *b* have a same length of 100 m and diameter of 300 mm. It is further assumed that there are no minor losses in the system and frictional losses
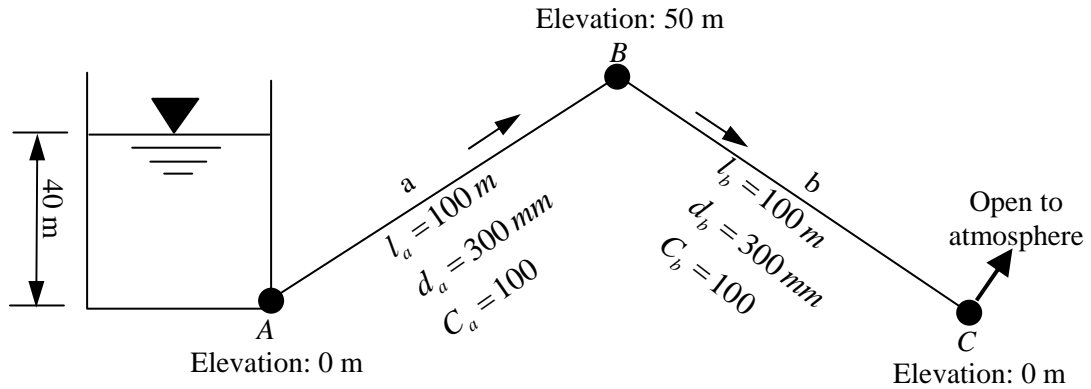
Figure 3.1 Hydraulic Network Analysis with Negative Pressures

can be calculated using the widely-used empirical Hazen-William equation. The Hazen-William roughness coefficient of pipes a and b is assumed to be 100. Node A has a hydraulic head of 40 m, which is higher than the hydraulic head at node C of 0 m. The head difference between nodes A and C will drive water to flow from nodes A through B down to C. Node C can be treated as a node with earthquake demand, the value of which is decided by the system topology and hydraulic properties.

Applying the Hazen–William equation to pipes a and b, respectively, results in the following equations

$$H_A - H_B = \frac{10.7 l_a}{C_a^{1.852} d_a^{4.87}} * Q_a^{1.852} \tag{3.1}$$

$$H_B - H_C = \frac{10.7 l_b}{C_b^{1.852} d_b^{4.87}} * Q_b^{1.852} \tag{3.2}$$

where H_A, H_B, and H_C are the hydraulic heads at nodes A, B, and C, respectively. The l_a, d_a, and C_a are the length, diameter, and Hazen-William roughness coefficient of pipe a, respectively. The l_b, d_b, and C_b are the length, diameter, and Hazen-William roughness coefficient of pipe b, respectively. The Q_a and Q_b are the flow rates in pipes a and b, respectively.

To satisfy the continuity condition at node B, the following equation is applied:

$$Q_a = Q_b \tag{3.3}$$

Comparing the right side of Equations 3.1 and 3.2 and noting that, $l_a = l_b$, $C_a = C_b$, $d_a = d_b$, and $Q_a = Q_b$, result in

$$H_A - H_B = H_B - H_C \tag{3.4}$$

From which the hydraulic head at node B can be solved as

$$H_B = 1/2(H_A - H_C) = 1/2 \times (40 - 0) = 20(m) \tag{3.5}$$

The hydraulic head at node B is the summation of the elevation head H_{BE} and pressure head H_{BP}. With the known total head H_B and elevation head H_{BE}, the pressure head H_{BP} can be solved as

$$H_{BP} = H_B - H_{BE} = 20m - 50m = -30m \tag{3.6}$$

The pressure, p_B, at node B can be calculated as

$$p_B = H_{BP} \times \gamma_w = -0.3 MPa \qquad (3.7)$$

where γ_w is the unit weight of water.

Substituting H_A equal to 40 m and H_B equal to 20 m into Equation 3.1 and reformatting Equation 3.1, the flow along pipe a can be solved as

$$Q_a = \left(\frac{C_a^{1.852} d_a^{4.87} (H_A - H_B)}{10.7 l_a} \right)^{1/1.852} = \left(\frac{100^{1.852} 0.3^{4.87} * 20}{10.7 * 100} \right)^{1/1.852} = 491.8(L/s) \qquad (3.8)$$

The flow in pipe b can be solved as 491.8 L/s using either the energy equation, Equation 3.2, or the continuity equation, Equation 3.3. Conventional hydraulic analysis solves a flow rate of 491.8 L/s in pipes a and b and a negative pressure, -0.3 MPa, at node B. The same results can be obtained from hydraulic network analysis software packages, such as EPANET and H2ONET. Given the damaged system is not air tight and that vacuum release valves exist in water delivery systems, the pressure at node B is better represented by zero pressure than -0.3 MPa. The results from the hydraulic network analysis are thus inaccurate.

After setting the pressure at node B to zero, the total hydraulic head at node B is 50 m, which is higher than 40 m, the hydraulic head at node A. Water cannot flow from the low head to high head and therefore, there is no flow in pipes a and b. The correct solution for this network should be, pressure at node B is 0 and flow rate in pipes a and b is zero too. Conventional hydraulic network analysis over predicts a

491.8 L/s flow rate in the system. In this example, node B can be called a no-flow node, because water cannot flow through it.

In the same network as shown in Figure 3.1, let the elevation of node B be 30 m, then the hydraulic head, H_B, at node B can be calculated using Equations 3.1 to 3.5. It is noted that H_B is always 20 m, the average of heads at nodes A and C, and does not vary with the elevation at node B. With the known total and elevation heads at node B, the pressure head can be calculated as

$$H_{BP} = H_B - H_{BE} = 20m - 30m = -10m \qquad (3.9)$$

The pressure, p_B, at node B can be calculated as

$$p_B = H_{BP} \times \gamma_w = -0.1(MPa) \qquad (3.10)$$

The flow rate in pipes a and b can be calculated as 491.8 L/s using Equation 3.8. The increase in elevation at node B only causes the decrease of pressure at node B, but does not change the flow in the network because the water flow is driven by the head difference between nodes A and C.

In this latter case, node B is still a negative pressure node. After setting the pressure at node B to zero, the total hydraulic head at node B is 30 m, which is 10 m lower than 40 m, the head at node A. Water can thus flow from nodes A through B down to C.

66

With the known hydraulic heads at nodes A and B, which are 40 m and 30 m, respectively, the flow rate in pipe a can be solved using the energy loss equation, Equation 3.8, as

$$Q_a = \left(\frac{C_a^{1.852} d_a^{4.87} (H_A - H_B)}{10.7 l_a} \right)^{\frac{1}{1.852}} = \left(\frac{100^{1.852} 0.3^{4.87} \cdot 10}{10.7 \cdot 100} \right)^{\frac{1}{1.852}} = 338.3 (L/s) \quad (3.11)$$

With the known hydraulic head at nodes B and C, 30 m and 0 m, respectively, the flow rate in pipe b can be calculated as

$$Q_b = \left(\frac{C_b^{1.852} d_b^{4.87} (H_B - H_C)}{10.7 l_b} \right)^{\frac{1}{1.852}} = \left(\frac{100^{1.852} 0.3^{4.87} \cdot 30}{10.7 \cdot 100} \right)^{\frac{1}{1.852}} = 612.2 (L/s) \quad (3.12)$$

Comparing Equations 3.11 & 3.12 shows that the flow rates in pipes a and b are different. The continuity condition at node B cannot be satisfied since there are no demands and additional water sources at node B.

The violation of continuity at node B indicates that flow conditions in the network cannot be solved using the same equations as those used in hydraulic network analysis, even after correcting for negative pressure at node B. This is because hydraulic network analysis is based on the assumption that pipes are always full and pressurized with water. The analyzed network in this example is not pressurized around node B. Open-channel flow may occur under these conditions. This type of flow is characterized by a free water surface and gravity driven flow.

A sketch of the flow profile in the network is shown in Figure 3.2, in which water flow starts from node *A* with full pressurized flow, and transfers to open-channel flow around node *B*. The solution for flow in this case involves full pressurized flow in part of pipe *a*, transitional flow from pressurized to open-channel around node *B*, and open-channel flow in pipe *b*. The solution for open-channel flow is more complicated than pressurized flow because it involves the determination of a free water surface. The transition from pressurized to open-channel flow may result in unsteady flow. Currently, commercial software packages are not configured to solve these types of flow conditions.

For the conditions illustrated in Figure 3.1, there will be no open-channel flow because the hydraulic head at node *B* exceeds that of node *A*. There will be temporary flow from node *C* until the contents of pipe *b* are discharged.

Negative pressure generation is of practical concern. When negative or low pressures occur, contaminants may be drawn into the pipelines. Negative or low water pressure in water distribution systems is a well-known risk factor for outbreaks of waterborne disease (Hunter, 1997).

Another concern of negative or low pressure involves fire protection after an earthquake. Fire following earthquakes is a well-known hazard. For example, the fires following the 1906 San Francisco earthquake destroyed roughly 90% of the city (Gilbert, et al., 1907), and much of the loss in fire fighting capacity at that time can be attributed to water distribution pipelines damaged by earthquake effects (e.g., O'Rourke, et al., 2006; Scawthorn, et al., 2006). A minimum operational pressure is generally required at hydrants for fire fighting purposes. Water supply systems are
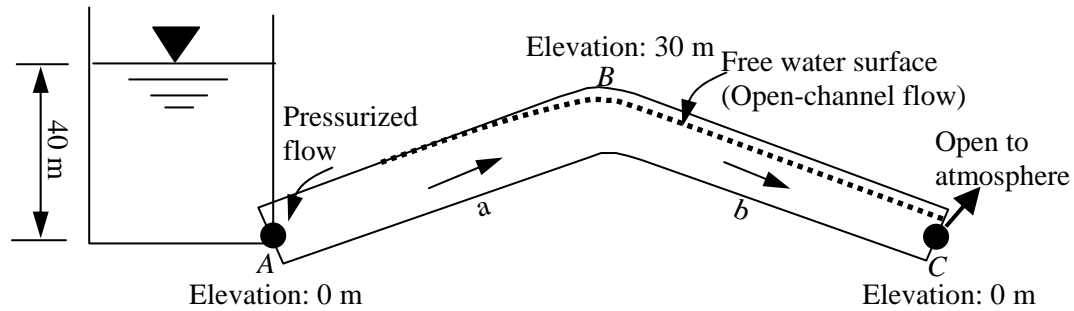
Figure 3.2 Water Profile Around Partial-Flow Node

tested locally, and documentation of minimum pressure is often required by insurance underwriters. Trautmann, et al. (1986), for example, reported on minimum pressure requirements of 0.14 MPa (20 psi) to prevent collapse of fire hoses that connect hydrants to pumper trucks.

3.3   PREVIOUS RESEARCH

Various researchers have engaged in the modeling of water supply systems (e.g., Ballantyne, et al., 1990; Okumura and Shinozuka, 1991; Shinozuka, et al., 1981, 1992; Hwang, et al., 1998; Khater and Grigoriu, 1989; Markov, et al., 1994) by using hydraulic network analyses for heavily damaged systems, in which negative pressures are specially treated.   The methods for negative pressure treatment are briefly reviewed and discussed below.

3.3.1   Ballantyne et al. Approach

Ballantyne, et al. (1990) performed hydraulic network analyses to evaluate the earthquake effects on the Seattle water supply system using the software KYPipe

(KYPipe Company, 2005). This program employs a conventional hydraulic network analysis algorithm, which assumes all demands must be satisfied so that negative pressures are generated at nodes in the damaged system. Ballantyne, et al. noted that the KYPipe gave inaccurate results when negative pressures occurred in the system. When they performed loss estimation, they assumed that there is no water available at the nodes where negative pressures were generated.

3.3.2   Shinozuka et al. Approach

Shinozuka and coworkers (Okumura and Shinozuka, 1991; Shinozuka, et al., 1981, 1992; Hwang, et al., 1998) performed hydraulic network analysis to evaluate the effects of earthquake damage to the water supply system operated by the Memphis Light, Gas, and Water, using KYPipe. In their approach, negative pressure nodes were eliminated from the network, together with the links connected to them. After the elimination, hydraulic network analysis was performed again to update the flow and pressure conditions in the remaining system.

3.3.3   Markov et al. Approach

Researchers at Cornell University (Markov, et al. 1994; Khater and Grigoriu, 1989) performed hydraulic network analysis to the damaged San Francisco Auxiliary Water Supply System, using the computer program GISALLE that was developed for their work. To address negative pressures, Markov et al. assumed that the water distribution network is not air tight when internal pressures fall below atmospheric levels, and developed rules for the elimination of negative pressure nodes.

Consider node i, shown in Figure 3.3, of a water supply system with pressure $p_i < 0$, where zero stands for atmospheric pressure. The hydraulic head at node i is $H_i = H_{iE} + p_i/\gamma_w$, where H_{iE} is the elevation head of node i and γ_w is the unit weight of water. It is assumed that air enters the system such that $p_i = 0$ and $H_i = H_{iE} + p_i/\gamma_w = H_{iE}$. The flow in the pipes connected with node i can be analyzed under $p_i = 0$ condition. Let Q_k be the flow in pipe k connected to nodes i and j. The flow, Q_k, will be zero if the hydraulic head at node i is higher than that at node j (i.e., $H_i = H_{iE} > H_j$). If this is the case for all pipes connected to node i, the node is considered as a no-flow node. If there are pipes where this condition is not satisfied, the node is considered as a partial-flow node.

The solution for a damaged pipeline network involves several phases. First, nodes with negative pressures are identified and divided into two categories: no-flow and partial-flow nodes. The no-flow nodes and pipes connected to them are eliminated sequentially, starting with the node of highest negative pressure. Flows and pressures are recalculated after each step of elimination. The no-flow nodes may isolate a part of the network, in which case that part is taken out of the system. Partial-flow nodes are considered next. The effect of partial-flow is approximated by changing the roughness of the pipes connected to the partial-flow node until $p_i = 0$. This is a heuristic approach. Thus, the explicit calculation of an open-channel flow profile is avoided. While adjusting any no-flow or partial- flow node, the previously adjusted nodes are checked to ensure that they continue to meet the criteria for no-flow and partial-flow nodes. Markov, et al. (1994) performed a sensitivity analysis of the elimination sequence on the final results, and found that the elimination sequence
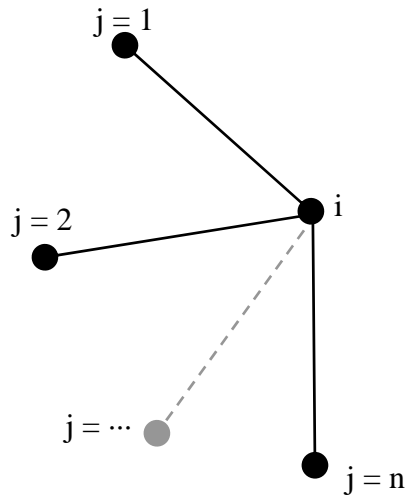
Figure 3.3 Negative Pressure Node Demonstration (after Markov, et al., 1994)

does not have significant impacts on the final simulation results. The elimination sequence, starting with the node of highest negative pressure, provides a rational and easy-to-program way for negative pressure elimination.

3.3.4   Discussions of the Three Approaches

Among the three approaches, the approach adopted by Ballantyne et al. is the simplest one with least computational efforts. It only performs hydraulic network analysis once, and then assumes there is no water flow through the negative pressure nodes. This assumption is valid for no-flow nodes as defined by Markov, et al. (1994). This assumption is also valid for partial-flow nodes as defined by Markov et al. (1994), if the system operator isolates the nodes with negative pressures promptly to prevent contamination, as well as water and pressure losses. However, this approach does not consider the flow and pressure redistributions after the isolation. Shinozuka et al.

made improvements at this point by updating the pressure and flow conditions after the isolation of negative pressure nodes.

Markov et al. provided an alternate approach by differentiating negative pressure nodes into no-flow and partial-flow nodes, and treating them differently. The differentiation of no-flow and partial-flow nodes is consistent with real situations, in which some nodes with negative pressures have flow through them. The heuristic approach of Markov et al. (1994) that adjusts the roughness of pipelines connected to the partial-flow nodes is hard to justify since an accurate solution for partial-flow nodes is not available. Furthermore, adjusting the roughness coefficient will not eliminate negative pressures in many circumstances, which can be explained with the example in Section 3.2.

Combining Equations 3.1 and 3.6, the pressure at node B, p_B, can be expressed as

$$p_B = H_A - \frac{10.7 l_a}{C_a^{1.852} d_a^{4.87}} \cdot Q_a^{1.852} - H_{BE} = H_A - \left(\frac{Q_a}{C_a}\right)^{1.852} \frac{10.7 l_a}{d_a^{4.87}} - H_{BE} \qquad (3.13)$$

Given the hydraulic head H_A at node A, pipe length l_a, diameter d_a, and elevation H_{BE} at node B, the pressure at node B is a function of the roughness coefficient C_a and flow rate Q_a. In the Hazen-William equation, decreasing the roughness coefficient means increasing the resistance to water flow and therefore results in a smaller flow rate Q_a in the pipeline. The overall effects of decreasing C_a and Q_a simultaneously may either increase or decrease the pressure p_B at node B. In contrast, increasing the roughness coefficient means decreasing the resistance to water flow, thereby causing a larger

flow rate Q_a in the pipeline. The overall effects of increasing C_a and Q_a simultaneously may either increase or decrease the pressure p_B at node B. The effect of adjusting the roughness coefficient on the pressure at a partial-flow node depends on the system dynamics, which are further related to the hydraulic properties and topology of the network.

The modeling approach adopted in GISALLE did not account for situations in which pipe roughness adjustments are not be able to eliminate negative pressures, thereby leading to a numerical convergence problem when adjusting the roughness coefficient to eliminate the negative pressures at partial-flow nodes. Based on simulations with many hydraulic networks, when the negative pressure is lower than - 0.07 MPa (-10 psi), it is generally not possible to eliminate negative pressures by adjusting the pipe roughness. The algorithm in GISALLE can be improved by treating the partial-flow nodes as no-flow nodes if adjusting the roughness coefficient cannot eliminate the negative pressure. The approach, however, still begs the question of whether reducing flow by roughness adjustment is a suitable approach to modeling the open-channel conditions associated with certain partial flow nodes.

3.4   CURRENT APPROACH

In this study, an isolation approach is applied to treat the negative pressures. After conventional hydraulic network analysis of the damaged system, nodes with negative pressures are identified and isolated step by step, starting with the one of highest negative pressure. The isolation is simulated by eliminating the node and all connected links. After each elimination, network connectivity is checked. If part of the system is isolated from the main system without water sources, it is taken out of

the system. Flow analysis and the elimination process continue until no negative pressure nodes exist in the system.

By discounting water conveyance through partial-flow nodes, the approach removes flow under atmospheric conditions as well as transitional pressures approaching atmospheric. Such flow will generally occur at relatively low rates and is not reliable for fire protection after an earthquake. Hence, the model eliminates piping with uncertain and/or unreliable flows, thus concentrating on those parts of the system that can be effective during emergency response.

The modeling approach adopted in this study, in effect, expresses a damage state as an operational state by converting the damaged network into one that meets the requirements of positive pressure and flow in all pipes. By eliminating pipelines with unreliable flow, it has the practical advantage of showing the system operator what parts of the network are no longer functional, and thus provides information about the most vulnerable distribution sectors and potential strategies for mitigation. The model does not account explicitly for water delivery and pressure losses associated with unsteady flow because accurate network analyses for this condition are not available. Instead, the model removes the unreliable portions of the system to display the remaining part of the network that meets threshold serviceability requirements for positive pressure.

CHAPTER 4

SEISMIC RESPONSE OF BURIED PIPELINES
TO SURFACE WAVE EFFECTS

4.1   INTRODUCTION

The seismic performance of a water supply system is closely related to the performance of its components (O'Rourke, et al., 2004b). In general, water supply pipelines can be damaged by permanent ground deformation (PGD) and transient ground deformation (TGD) (e.g., O'Rourke, 1998). PGD hazards are usually limited to small regions with high damage rates due to the large deformation imposed on pipelines. In contrast, the TGD hazards typically affect the whole pipeline network, but with lower damage rates. The TGD hazards are mostly related to the propagation of seismic waves, including body and surface waves. Compared with body waves, surface waves have a much lower apparent wave propagation velocity, which drives higher ground strain. Under the appropriate conditions, therefore, surface waves can be more hazardous to buried pipelines than body waves.

In this chapter, an analytical model is developed to analyze the joint pullout movement of buried pipelines to surface wave effects. Such a model is an important adjunct for comprehensive simulation of buried pipeline response to TGD, and provides a rational basis for evaluating soil-structure interaction caused by traveling ground waves. Seismic wave propagation hazards to buried pipelines are briefly discussed, with special attention to the characteristics of surface waves. An analytical

77

model is developed for analyzing the interaction of surface waves with jointed concrete cylinder pipelines (JCCPs). The model is expanded to analyze surface wave interaction with cast iron (CI) pipelines composed of lead-caulked joints having ductile pullout characteristics.

4.2 SEISMIC HAZARDS TO BURIED PIPELINES

An important characteristic of buried pipelines, which distinguishes them from above-ground structures, is that the relative movement of the pipeline with respect to the surrounding soil is small, and the inertial forces due to the weight of the pipeline and its contents are not significant. Seismic analysis of buried pipelines therefore focuses on the free field deformation of the ground and associated soil-structure interaction. The seismic loads are characterized, generally, in terms of the deformations and/or strains imposed on the pipeline by the surrounding soil.

4.2.1 Seismic Wave Hazards

In general, there are two types of seismic waves, body and surface waves. The body waves include compression (P-) and shear waves (S-waves). For P-waves, the ground moves parallel to the direction of propagation, which generates alternating compressive and tensile strain. For S-waves, the ground moves perpendicular to the direction of propagation. Compared with P-waves, the S-waves are more hazardous to buried pipelines because they carry more energy.

Surface waves are generated by the reflection and refraction of body waves, and travel along the ground surface. They generally decay quickly below the ground

surface. Two major types of surface waves are Love (L-) and Rayleigh waves (R-waves). For L-waves, the particle motion is along a horizontal line perpendicular to the direction of propagation, while for R-waves, the particle motion traces a retrograde ellipse in a vertical plane, with the horizontal component of motion parallel to the direction of propagation. Figure 4.1 shows the propagation and particle motion of R-waves, which generate alternating compressive and tensile axial strains along pipelines. The L-waves generate bending strains in buried pipelines that are substantially smaller than the axial strains induced by R-waves. The bending strains generated by L-waves with phase velocities comparable to those of R-waves are typically 2 to 3 orders of magnitude less than the axial strains induced by R-waves (St. John and Zahrah, 1987). As such, only the effects of R-waves are considered in this study.

The seismic loads on buried pipelines imposed by wave propagation are typically characterized by ground strains. The ground strain, ε_g, can be calculated as the ratio of ground particle velocity, V, to apparent wave propagation velocity, C_a, as

$$\varepsilon_g = \frac{V}{C_a} \tag{4.1}$$

For surface waves, the apparent wave propagation velocity, C_a, depends on the phase velocity, C_{Ph}. The phase velocity, C_{Ph}, is defined as the velocity at which a transient vertical disturbance at a given frequency propagates across the ground surface (O'Rourke and Liu, 1999).
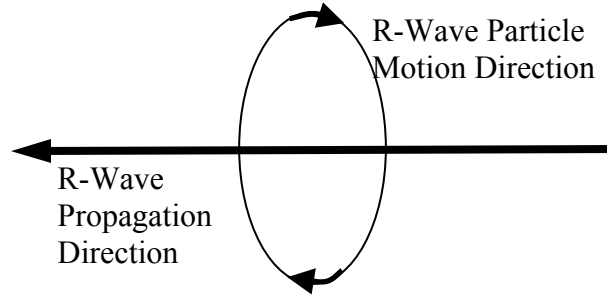
Figure 4.1 R-Wave Propagation and Particle Motion Directions

To calculate the ground strain along the axial direction of a pipeline, it is necessary to resolve the particle and apparent wave propagation velocities into components parallel to the pipeline. In Figure 4.2, WV and PV are the directions of phase and particle velocities of surface waves, respectively. Assuming a pipeline orientated at an angle, α, with respect to the particle velocity, V, the ground strain along the axial direction of the pipeline can be calculated as

$$\varepsilon_g = \frac{V \cos\alpha}{C_{Ph}/\cos\alpha} = \frac{V}{C_{Ph}}\cos^2\alpha \qquad (4.2)$$

where $V\cos\alpha$ and $C_{Ph}/\cos\alpha$ are the particle and phase velocities parallel to the pipe axis, respectively. The ground strain along the pipe axis reaches its maximum value, V/C_{Ph}, when the pipeline is parallel to the particle and phase velocities. For a treatment of body wave effects on axial pipeline strain, reference should be made to Wang (2006).

Equation 4.2 shows that the ground strain along the pipeline is controlled by three factors, ground particle velocity, V, phase velocity, C_{Ph}, and the intersection angle, α, of the pipeline with respect to particle velocity. Either high V or low C_{Ph}

80
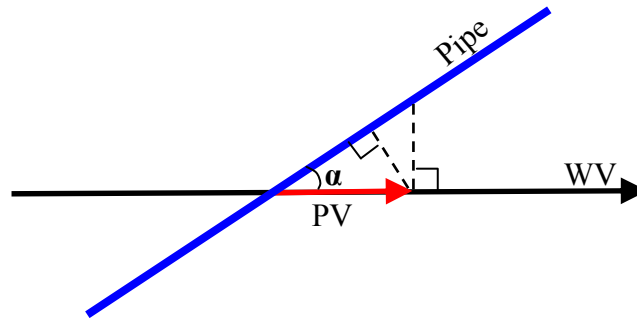
Figure 4.2 Resolution of Particle and Phase Velocities Along the Pipeline Axial
Direction for R-Waves

can generate large ground strain. For body waves, large ground strain is normally
driven by high V. Strong motion records from previous earthquakes show PGV for
body waves as high as 177 cm/sec (Trifunac, et. al., 1998). In contrast, for surface
waves, large ground strain typically results from low phase velocity. Ayala and
O'Rourke (1989) reported that the phase velocity of R-waves, generated in the Lake
Zone in Mexico City during the 1985 Michoacan earthquake was as low as 120 m/sec.
The strong motion recording shows that the PGV of the R-waves was higher than 30
cm/sec at the same location during the same earthquake. Combining the PGV of 30
cm/sec and C_{Ph} of 120 m/sec results in a ground strain of 0.0025, which may exceed
the yield capacity of steel. Under conditions of very low phase velocity and relatively
high particle velocity, therefore, surface waves can be more destructive to buried
pipelines than body waves.

4.2.2 Surface Wave Characteristics

Surface waves are generated by the reflection and refraction of body waves at
the ground surface. In particular, body wave reflection and refraction in large,

sedimentary basins (several km wide with soil depths ≤ 1 km) can cause R-waves that amplify the ground motion significantly (O'Rourke, 1998). The amplification effects associated with R-wave propagation in sedimentary basins have been studied by Papageorgiu and coworkers (e.g., Papageorigu and Kim, 1993; Pei and Papageorigu, 1996), who demonstrated that sedimentary basins can trap and focus wave energy, thus increasing peak amplitudes and prolonging the duration of TGD. Their analyses of recorded motions in the Santa Clara Valley during the Loma Prieta earthquake provide clear evidence of first and second mode R-waves (Pei and Papageorigu, 1996). Similar patterns of R-waves were shown by numerical simulations of incident SV and P-wave interaction with the sedimentary basin underlying Caracas, VZ (Pei and Papageorigu, 1996).

Figure 4.3 shows the north-south ground velocity records from two strong motion stations, Ciudad Universitaria - Lab and Central de Abastos - Oficinas in Mexico City during the 1985 Michoacan earthquake (Ayala and O'Rourke, 1989). The Ciudad Universitaria - Lab Station is located in the Hill Zone, outside the sedimentary basin. The Central de Abastos - Oficinas Station is located in the Lake Zone, inside the sedimentary basin.

In the Hill Zone record, the PGV is about 10 cm/sec (Figure 4.3a), which occurred roughly at 20 to 30 seconds after initial measurement triggering. In the Lake Zone record (Figure 4.3b), the PGV associated with surface waves higher than 30 cm/sec occurred about 60 and 90 seconds after initial triggering.

The surface waves were similar to sinusoidal waves with similar amplitude and predominant period. The predominant period of the surface waves can be estimated
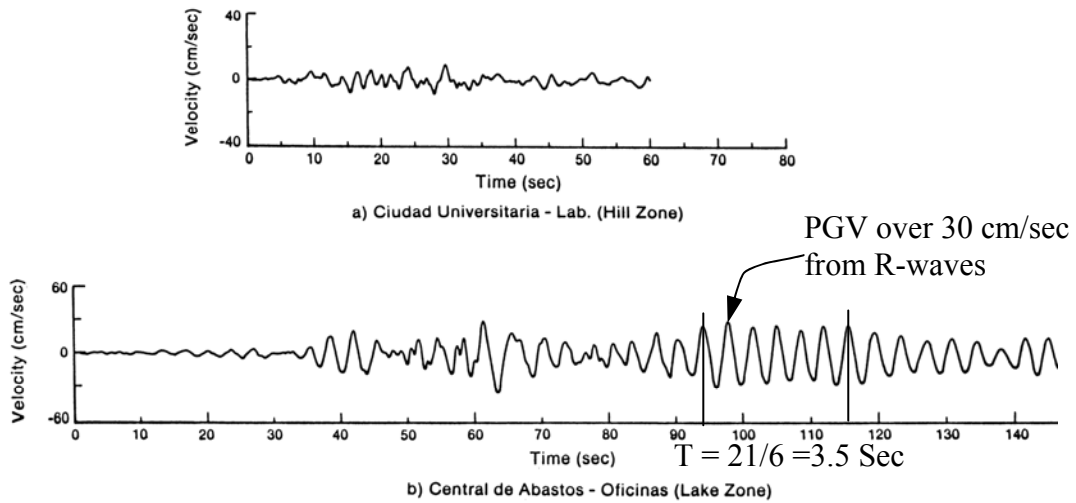
Figure 4.3 North-South Velocity Histories in Hill and Lake Zones in Mexico City during the 1985 Michoacan Earthquake (after Ayala and O'Rourke, 1989)

from the velocity records. Figure 4.3b shows 6 cycles of R-waves that occurred over 21 seconds, with a predominant period of 3.5 seconds.

Analytical and numerical solutions are available in the literature to generate dispersion curves for layered soil profiles (e.g., Haskell, 1953; Schwab and Knopff, 1977). O'Rourke, et al. (1984) developed a simple procedure for determining the dispersion curve for layered soil profiles in which the shear wave velocity increases with depth. Figures 4.4 and 4.5 show the soil profile at Central de Abastos - Oficinas and the corresponding dispersion curves at this location for R-waves. From Figure 4.5, the R-waves have a phase velocity of roughly 120 m/sec corresponding to a predominant period of 3.5 seconds.
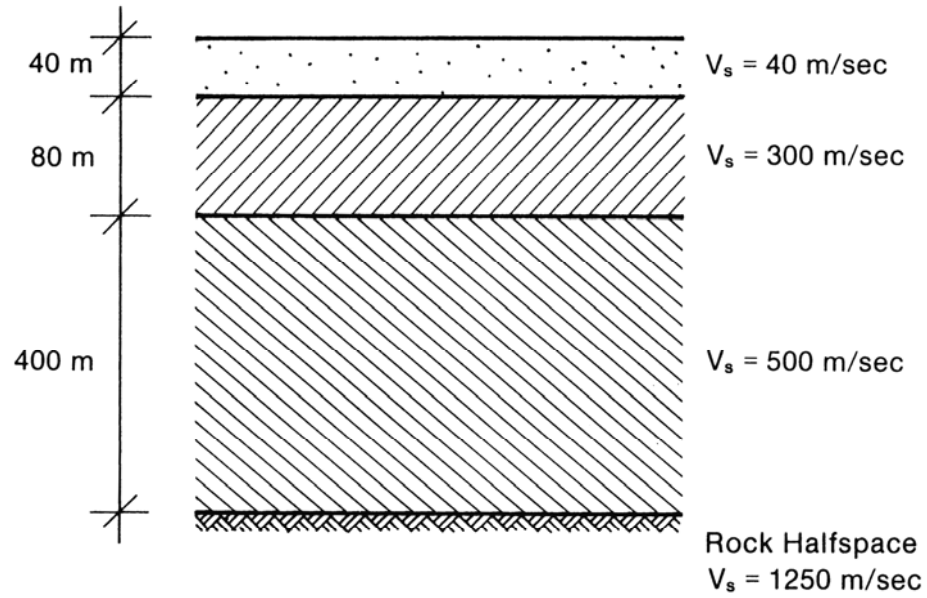
Figure 4.4 Soil Profile at Strong Motion Station, Central de Abastos-Oficinas, in

Mexico City (after Ayala and O'Rourke, 1989)
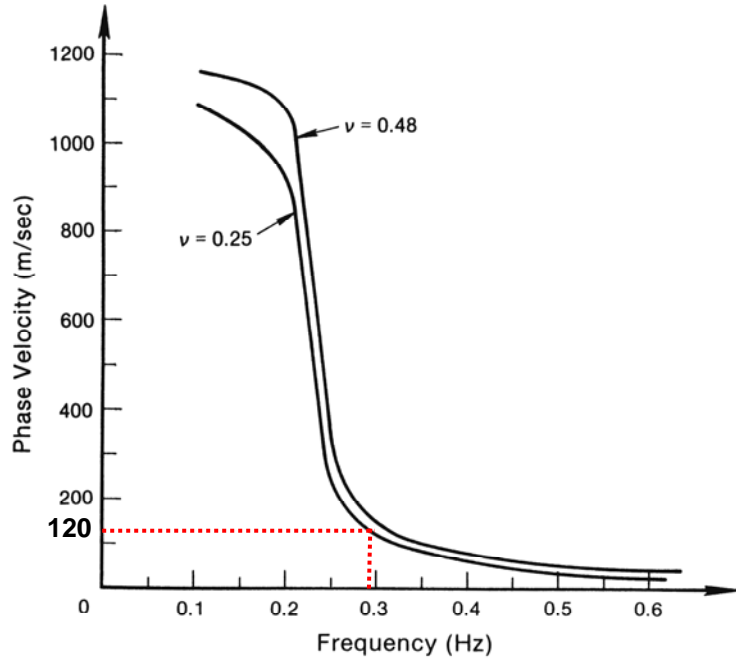
Figure 4.5 R-Wave Dispersion Curves for the Soil Profile Shown in Figure 4.4

(after Ayala and O'Rourke, 1989)

84

It should be emphasized that the lake bed sediments of Mexico City have unusual geometric and material properties, which are not generally encountered. Nevertheless, these conditions illustrate how certain naturally occurring soil formations, especially those associated with deep soft deposits of clay, can result in the generation of surface waves with low phase velocity, relatively high particle velocity, and long period motion.

4.3 ANALYTICAL MODEL FOR SURFACE WAVE INTERACTION WITH JCCPS

In this section, an analytical model is developed to analyze surface wave interaction with JCCPs. In this study the term JCCP is used to represent pipelines composed of reinforced concrete and steel cylinders that are coupled with mortared, rubber-gasket bell-and-spigot joints.

4.3.1 JCCPs

As discussed by O'Rourke et al. (2004c), there are different types of JCCPs, such as concrete cylinder pipes (CCPs), bar wrapped concrete cylinder pipes (BWCCPs), and prestressed concrete cylinder pipes (PCCPs). Governing standards for the current design of such pipelines include AWWA C301 (1999) and C303 (2002). Pipe segment lengths are generally 6 to 12 m.

Section 5.4 provides a detailed description of the material properties and joint characteristics for various types of pipelines, which are widely used in water supplies in North America. A representative cross-section of JCCP joints collected from the

design and as-built drawings of trunk lines investigated as part of this study is shown in Figure 5.12, and the characteristics of JCCP joints are described in Section 5.4.3.4. The performance of many JCCPs is influenced by the rubber-gasket bell-and-spigot joints. The rubber gasket is often 18 to 22 mm wide when compressed to form a water-tight seal. Cement mortar is poured in the separation between adjoining sections of pipe to further seal the joint. The pullout capacity of the joint, in terms of axial slip to cause leakage, depends on how much movement can occur before the rubber gasket loses its compressive seal. This capacity will vary according to pipe positioning during field installation and subsequent movement of the pipeline.

The pullout resistance of the joint is also affected by the tensile behavior of the cement mortar at the joints. The mortar cracking strain ranges from 0.5×10^{-4} to 1.5×10^{-4}, with a typical value of 1.0×10^{-4} (Avram et al., 1981). It is not uncommon for the mortar at the JCCP joints to be cracked and separated as a result of shrinkage during cure as well as subsequent operational loads and movement in the filed.

Investigations of the axial pullout capacity of the JCCP joints are described by Wang (2006), in which the as-built dimensions of actual JCCP joints are evaluated, and a probabilistic model is developed for estimating their as-built axial pullout capacity. His study shows that the initial position of the gasket during construction is well modeled by a uniform distribution of locations between maximum inward and outward penetration of the gasket inside the bell housing of the adjoining pipe. The 90% exceedance value is the distance of the gasket inside the joint that is exceeded by 9 out of 10 JCCP joints, and corresponds to 3-4 mm of axial slip before initial loss of compression. Subsequent operational loads and pipeline movement will subtract from this slip capacity. As a minimum, therefore, about 1 of every 10 joints cannot reliably

accommodate more than 3-4 mm of axial slip. Given this level of tolerance, JCCP joints are sensitive to seismic wave interaction, which has the potential to induce leakage and even complete disengagement of adjoining pipe sections under severe seismic motions.

4.3.2 Performance of JCCPs during Previous Earthquakes

The performance of JCCPs during previous earthquakes was varied, depending on pipeline characteristics and location and the TGD and PGD, respectively. Ayala and O'Rourke (1989) reported significant repairs in JCCPs after the 1979 Guerro and 1985 Michoacan earthquakes. Repairs were concentrated at the joints of trunk and transmission pipelines, and were especially severe for the 1985 Michoacan earthquake. For example, there were 60 repairs in Federal District JCCP transmission lines to yield a relatively high repair rate of 1.7 repairs/km. Ayala and O'Rourke (1989) further reported that most of the water supply damage was due to surface wave propagation effects. Damage to JCCP trunk lines after the Loma Prieta earthquake was low (Eidinger, 1998). In contrast, damage to JCCP trunk lines after the 1994 Northridge earthquake was high. Lund and Cooper (1995) reported that significant damage was sustained by 1370-mm- and 838-mm- diameter JCCP trunk lines in Santa Clarita Valley at welded compound bends and as pullout at rubber gasket joints on long horizontal reaches. They further reported that there were 15-20 major pulled joints on a 1980-mm-diameter JCCP trunk line in Simi Valley.

One method for estimating pipeline damage in future earthquakes is to develop regressions between observed repair rates during previous earthquakes and measured seismic parameters. O'Rourke et al. (2004b) developed a linear regression for JCCP

repairs collected in the Los Angeles area after the 1994 Northridge earthquake. The regression was developed for repair rate versus peak ground velocity, V_p, because this seismic parameter has been shown to be the most statistically significant one influencing TGD-related pipeline repairs (O'Rourke and Jeon, 2000).

It should be noted that this regression is developed based on repairs in JCCPs after the 1994 Northridge earthquake in the Los Angeles area. The JCCPs were affected predominantly by body waves during the Northridge earthquake. The regression, therefore, is not appropriate for estimating damage to JCCPs under surface wave effects. Because of the limited data regarding damage to JCCPs under the effects of surface waves, it is useful to develop analytical models that can provide insight about the mechanism of the soil-structure interaction under surface wave effects.

4.3.3 Surface Wave Interaction with JCCPs

Figure 4.6 shows an incremental section of continuous buried pipeline, dx, subjected to a surface wave, simplified as a sinusoidal wave with maximum amplitude of the ground strain, $\varepsilon_{mg} = V_p / C_{Ph}$, where V_p is peak ground particle velocity and C_{Ph} is the phase velocity along the pipe axial direction. The shear transfer between pipe and soil per unit pipe length is f, and the pipe axial stiffness is equal to the product of the pipe material modulus, E, and cross-sectional area, A. The rate of pipe strain, ε_p, accumulation is given by

$$\frac{d\varepsilon_p}{dx} = \frac{f}{EA} \tag{4.3}$$

88
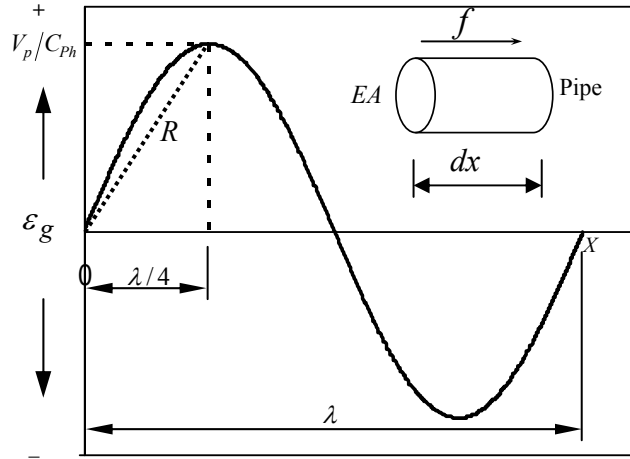
Figure 4.6 Sinusoidal Wave Interaction with Pipe Element

The rate of ground strain, ε_g , accumulation is

$$\frac{d\varepsilon_g}{dx} = \frac{d}{dx}(\frac{V}{C_{Ph}})$$

(4.4)

in which V is the particle velocity.

It is noted that the displacement of a continuous pipeline cannot exceed that of the adjacent ground soil. As such, if the strain accumulation rate of a continuous pipeline is larger than that of the ground at every point of the pipeline, the pipeline will deform in the same way that the ground deforms. In this case, the pipeline is called a fully flexible pipeline, for which the following equation is satisfied

$$\frac{d\varepsilon_p}{dx} > \frac{d}{dx}(\frac{V}{C_{Ph}})$$

(4.5)

89

For a sinusoidal wave, the maximum rate of ground strain, ε_g, accumulation is

$$\left[\frac{d}{dx}\left(\frac{V}{C_{Ph}}\right)\right]_{max} = \frac{2\pi V_p}{\lambda C_{Ph}} \tag{4.6}$$

in which λ is the wave length. Combining Equations 4.4, 4.5, and 4.6 results in

$$\frac{f}{EA} > \frac{2\pi V_p}{\lambda C_{Ph}} \tag{4.7}$$

which is the requirement that must be met for a fully flexible pipeline. If R equals the ratio of V_p/C_{Ph} to the rise distance, $\lambda/4$, which can be discerned from strong motion records, then

$$\frac{f}{EA} > \frac{\pi R}{2} \tag{4.8}$$

establishes the qualification for a fully flexible pipeline, provided that the wave form approximates a sinusoidal function.

When Equation 4.8 cannot be satisfied for a pipeline and seismic wave combination, the strain accumulation rate of the pipeline is lower than that of the ground along part of the pipeline, and therefore, the pipeline is relatively rigid and not able to deform in unison with the ground. Figure 4.7 shows the seismic response of a continuous, relatively rigid pipeline under the action of a surface wave. This figure shows that relative movement between soil and pipe transfers shear to the pipeline.

90

a) Strain Response

b) Displacement Response
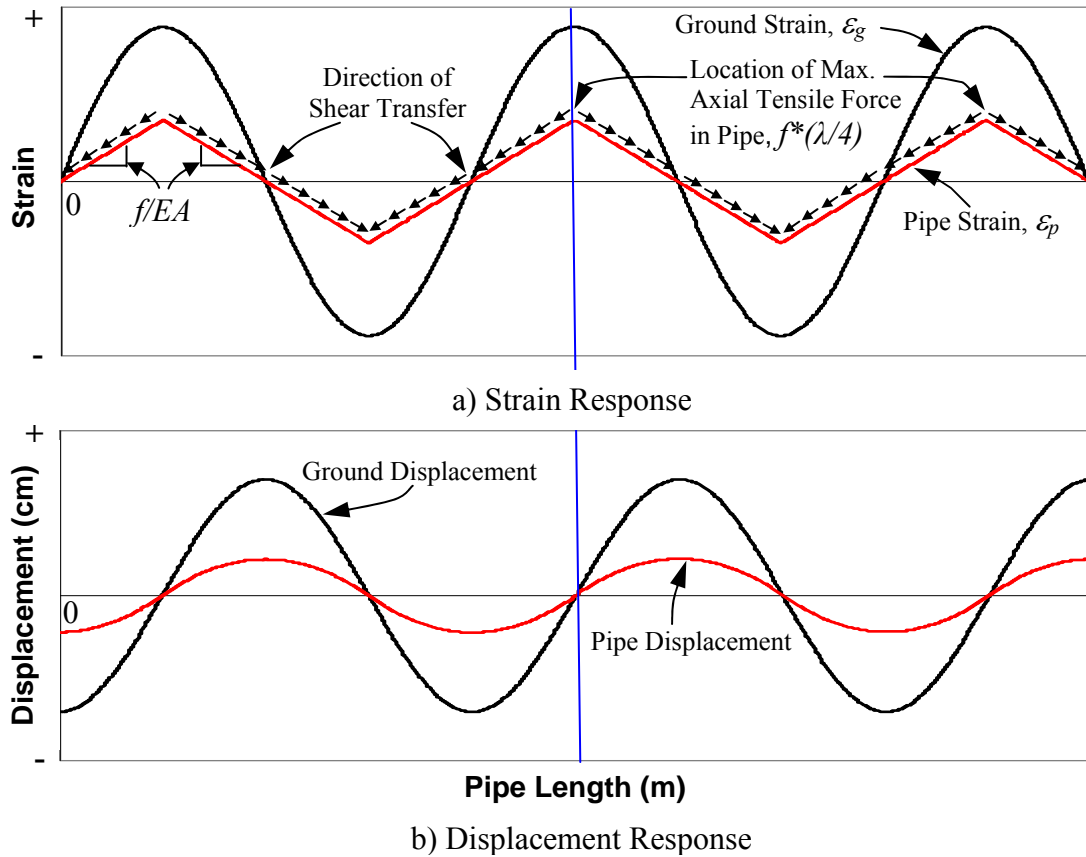
Figure 4.7 Sinusoidal Wave Interaction with a Continuous Relatively Rigid Pipeline

Because the axial stiffness of the pipeline is relatively large, the shear transfer is not sufficient to cause the same deformation in soil and pipe.

The shear transfer is shown in Figure 4.7a with small arrows indicating its direction. The shear transfer changes its direction in every half wavelength at the point where the ground displacement changes its direction. The axial force in the pipeline is the integration of the shear transfer along the pipe axis. The axial force increases from zero where the ground strain is zero to its maximum value $f^*(\lambda/4)$ after a quarter of wavelength of shear accumulation. In the case shown in Figure 4.7a, the maximum axial tensile force occurs at the point with peak positive ground strain, and

91

the maximum axial compressive force occurs at the point with peak negative ground strain.

When the maximum tensile force in the pipeline exceeds the tensile capacity of a locally weak joint, the joint will be cracked, and the axial tensile force at the pipe ends connected with the joint will drop to zero. It is assumed that the joints on either side of the cracked joint have full mortar connectivity to mobilize tensile capacity across the joints. Figure 4.8 shows the seismic response of a relatively rigid pipeline with a cracked joint under the action of a sinusoidal surface wave. It is noted that both the pipeline and sinusoidal wave are symmetric with respect to the cracked joint. To understand the mechanism of soil-structure interaction, the following explanation focuses on the left half of the pipeline and ground system.

Before cracking of the joint, the left half of the pipeline is in force equilibrium under the shear transfer and tensile force generated by the right half of the pipeline. After the crack forms, the force from the right half of the pipeline drops to zero, and therefore, the left half of the pipeline is not in force equilibrium and tends to shrink back to the left. The shear transfer needs to be redistributed to keep the pipeline in new force equilibrium. The ground at the cracked joint has zero displacement and moves from the cracked joint to the left. In the vicinity of the cracked joint, the pipe displacement is larger than the ground displacement and the shear transfer from the ground to pipeline resists the elastic rebound of the pipeline until the ground displacement equals the pipe displacement at point A. After that, the ground displacement is larger than the pipe displacement, and the shear transfer direction reverses. The integration of the differential strain between pipeline and ground from the cracked joint to the shear transfer reversal point, A, is represented by half of the

92

a) Strain Response

b) Displacement Response
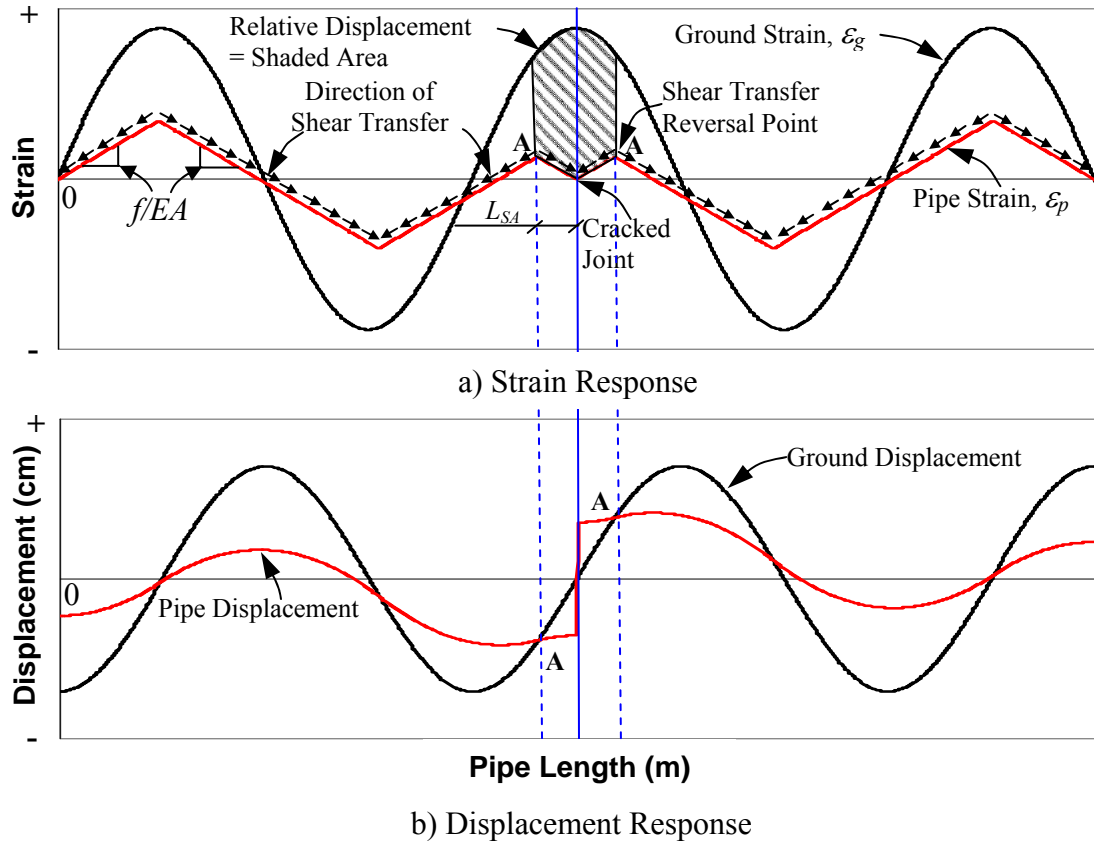
Figure 4.8 Sinusoidal Wave Interaction with a Relatively Rigid Pipeline with a Cracked Joint

shaded area in Figure 4.8a. It is the relative displacement between the pipeline and ground at the cracked joint, which equals one half of the relative joint displacement. The length, L_{SA}, in Figure 4.8a, is called the strain accumulation length in this study. It is the length from the cracked joint to point A, where the direction of relative displacement between pipeline and soil reverses. The strain accumulation length, L_{SA}, is determined by soil-structure interaction.

When affected by body waves, pipelines generally exhibit fully flexible behavior because the high apparent wave velocity drives the ground strain

accumulation rate to lower than the pipeline strain accumulation rate. When affected by surface waves, pipelines can be either fully flexible or relatively rigid.

The response of a fully flexible pipeline is briefly discussed. Reference should be made to Wang (2006) for further details. Figure 4.9 shows the sinusoidal seismic wave interaction with a fully flexible pipeline with a cracked joint. Because the pipeline is fully flexible, $\varepsilon_p = \varepsilon_g$ everywhere the pipeline is continuous. At the cracked joint, the pipeline cannot sustain strain, so $\varepsilon_p = 0$. As the wave passes across the cracked joint, strain in the continuous pipeline on each side of the joint accumulates linearly at a slope of f/EA until $\varepsilon_p = \varepsilon_g$, after which pipe and ground strains are indistinguishable. The shaded area in Figure 4.9a represents the integration of the differential strain between the pipeline and ground, which equals the relative joint displacement and occurs as axial slip.

For seismic wave interaction with a relatively rigid pipeline, the relative joint displacement is determined by soil-structure interaction. Finite element (FE) methods are used to model the surface wave interaction with JCCPs.

4.3.4   Finite Element Model

FE analyses of surface wave interaction with JCCPs were performed using the program BSTRUCT (Chang, 2006; Goh and O'Rourke, 2000). Figure 4.10 shows a schematic view of the FE model. The pipeline was modeled with beam column elements that were connected to the ground by spring-slider elements capable of representing shear transfer as an elasto-plastic process.

a) Strain Response

b) Displacement Response
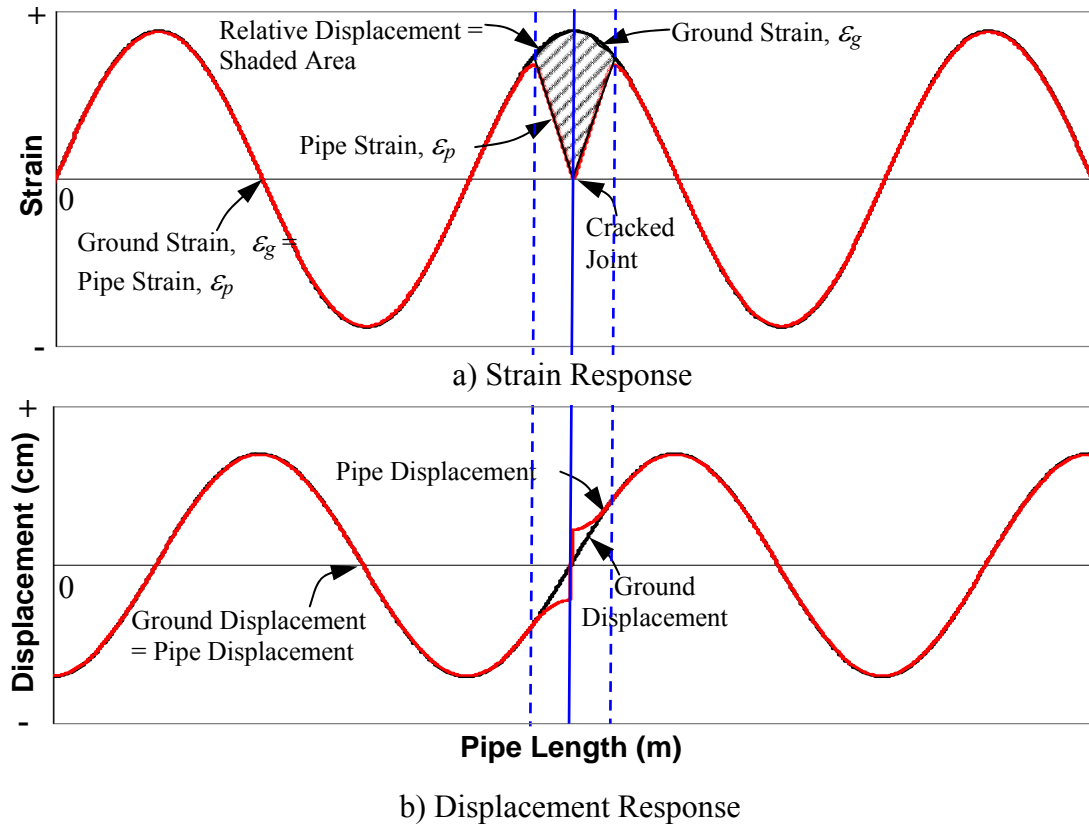
Figure 4.9 Sinusoidal Wave Interaction with a Relatively Flexible Pipeline with a Cracked Joint
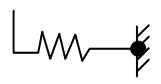
As recommended by the Committee on Gas and Liquid Fuel Lifelines (1984), the interrelation between unit shear transfer f and relative pipe-soil displacement was modeled as a bilinear relationship with linear rise to f at a relative displacement of 3 mm and constant f thereafter, as shown in Figure 4.11.
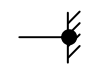
Values of f can be calculated according to the procedures summarized by O'Rourke (1998). For a pipeline buried in cohesionless soil, the maximum shear transfer per unit distance, f, is
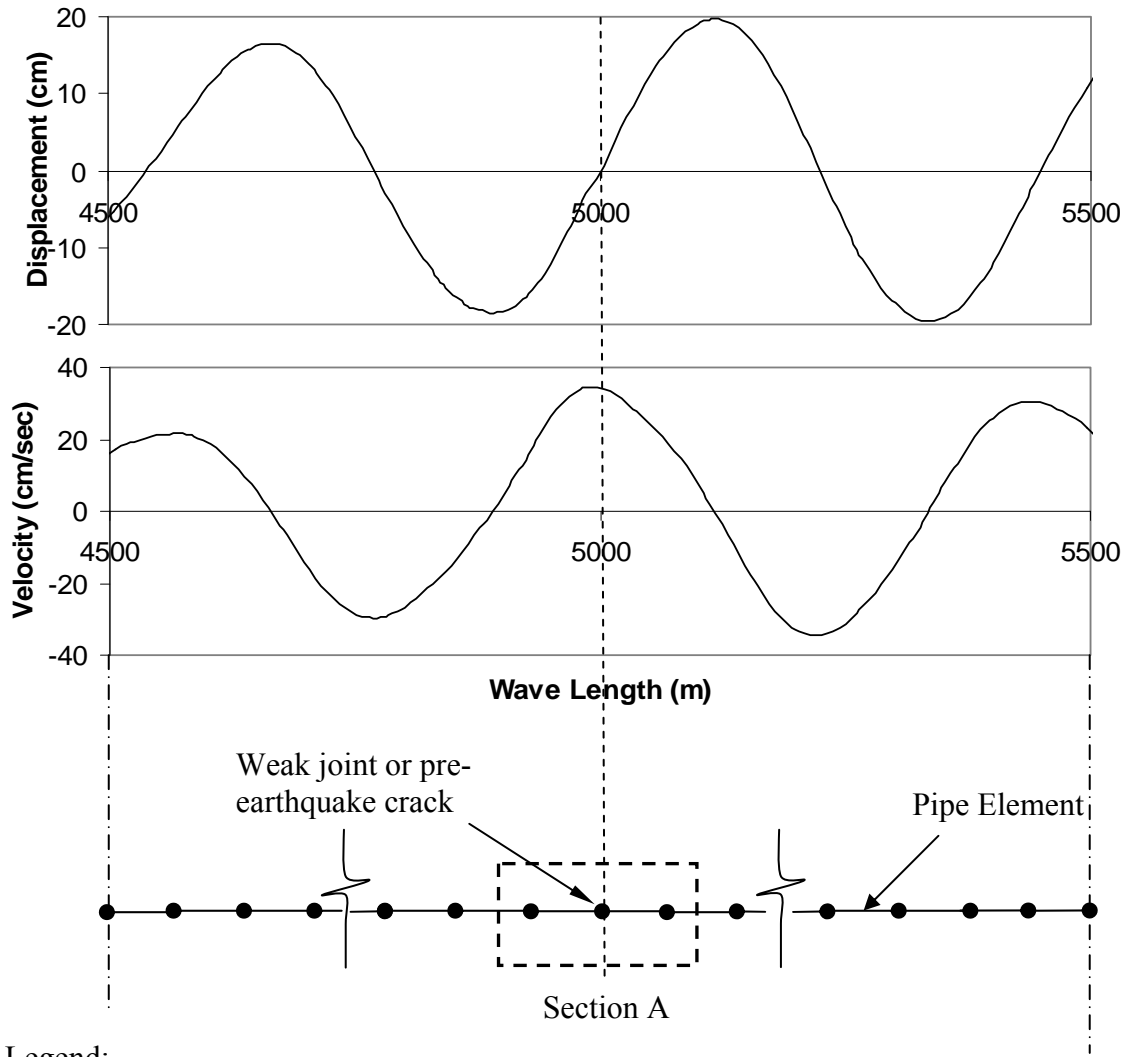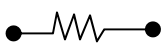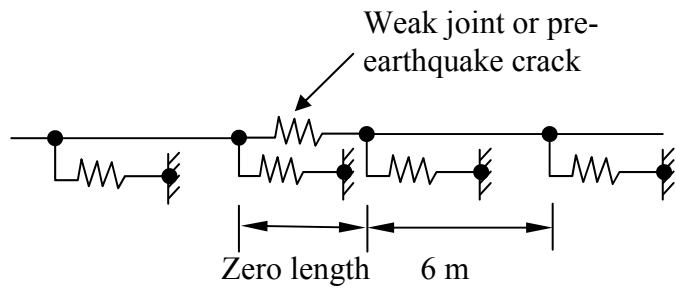
Figure 4.10 Finite Element Model for Seismic Wave Interaction with Pipeline
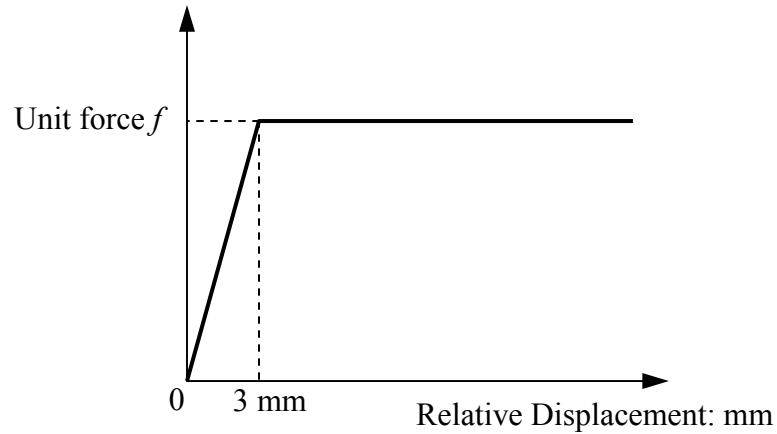
Figure 4.11 Elasto-Plastic Model for Unit Shear Transfer Between
Ground Soil and Pipeline

$$f = 1/2\pi D(1 + K_0)\gamma z_p \tan \delta \qquad (4.9)$$

in which z_p is the depth to pipe centerline, γ is soil unit weight, K_0 is the coefficient of at-rest horizontal soil stress (generally $0.5 \le K_0 \le 1.0$ for pipe in backfilled trenches), δ is the angle of interface frictional resistance, and D is the outside pipe diameter. If the pipeline is buried in cohesive soil, the maximum f is

$$f = \alpha s_u \pi D \qquad (4.10)$$

in which s_u is the undrained shear strength of the surrounding soil and α is an adhesion factor that accounts for the degree of shear transfer between the pipe and soil. The angle of interface friction for sands between pipe and soil was varied between $32°$ and $40°$, and the adhesion between pipe and soil, αs_u , for silts and clays was varied between 25 and 60 kN/m^2.

The locally weak joint in the JCCP was modeled as a spring-slider element with zero length. As discussed previously, joints in the field are occasionally cracked and separated due to installation and subsequent ground movement distress. Such joints, being cracked and separated, have very low axial pullout resistance that for modeling purposes can be taken as negligible.

The strong motion recording at Central de Adastos - Oficinas (Lake Zone) in the north-south direction during the 1985 Michoacan earthquake in Mexico City, as shown in Figure 4.3b, was used as ground motion input. As discussed in Section 4.2.2, there is clear evidence of surface waves in this record. Time records of strong motion were converted to displacement versus distance records by assuming that $x = C_{Ph}t$, in which x is distance, t is time from the strong motion recording, and C_{Ph} is the phase velocity. The phase velocity, C_{Ph}, is taken as 120 m/sec from the dispersion curves shown in Figure 4.5, based on a predominant period of 3.5 sec, determined from the strong motion velocity records shown in Figure 4.3b. The seismic displacement versus distance record was superimposed on the spring-slider elements, which then conveyed ground movement to the pipeline by means of the elasto-plastic properties used to characterize the spring-sliders. As illustrated in Figure 4.10, when the maximum slope of the displacement versus distance record (corresponding to maximum ground particle velocity in the velocity record) was superimposed on the weak pipeline joint, the maximum axial slip of the joint was calculated.

The FE analysis was used to evaluate seismic wave interaction with the 1829-mm-(72 in.)-diameter jointed concrete Federal District Aqueduct (FDA) in Mexico City, which was damaged during the 1985 Michoacan earthquake due to R-wave propagation effects (Ayala and O'Rourke, 1989). Because details of the FDA

construction are not available, its physical properties were taken from the as-built drawing of the Bay Division Pipeline No. 3, which is also an 1829-mm-(72 in.)-diameter JCCP (O'Rourke, et al., 2004a). The properties are shown in Table 4.1. Further parametric studies showed that joint movement is not sensitive to pipe physical properties. It was assumed that the pipeline is orientated parallel to the direction of wave propagation, which results in the maximum joint pullout movement. The FE model was composed of 1666 pipe elements and 1669 spring slider elements over a distance of roughly 10 km for an average element length of 6m.

Figure 4.12 shows the displacement of soil and pipeline after soil-structure interaction, Figure 4.13 shows the relative displacement between ground soil and pipeline, and Figure 4.14 shows the strain of ground soil and pipeline. In addition to an overview of soil-structure interaction, a close-up view in the vicinity of the joint, cross-section A, is also provided for Figures 4.12 to 4.14.

Figure 4.12 shows that the pipeline displacement is smaller than the ground displacement because the pipeline is relatively rigid and the shear transfer is not sufficient for the pipeline to deform in unison with the ground soil. Figure 4.13 shows that the maximum relative joint displacement is 16 cm. Figure 4.14 shows that the pipe strain starts to accumulate from both sides of the cracked joint at a slope of f/EA, until point A, at which the direction of the strain accumulation reverses. The area between the two strain reversal points in the vicinity of the weak joint represents the relative joint separation. The high relative joint displacement, 16 cm, indicates a strong potential for joint pullout and disengagement of JCCPs under surface wave effects.

Table 4.1 JCCP Physical Properties and Ground Conditions for FE Analysis

Inside Diameter: (mm)	1828.8
Thickness of Steel Cylinder: (mm)	1.5
Thickness of Concrete Wall: (mm)	177.8
Compressive Strength of Concrete: (MPa)	31.0
Young's Modulus of Concrete: (GPa)	26.4
Outside Radius of Concrete: (mm)	1092.2
Inside Radius of Concrete: (mm)	914.4
Concrete Area: (mm^2)	1120836.9
Steel Rod Diameter: (mm)	9.5
Steel Rod Area: (mm^2)	4.3
Young's Modulus of Steel: (GPa)	200
Inside Radius of Steel Cylinder: (mm)	963.7
Outside Radius of Steel Cylinder:(mm)	965.2
Steel Cylinder Area: (mm^2)	92.0
Total Steel Area: (mm^2)	96.3
Modulus Ratio Between Steel and Concrete	7.6
Equivalent Area for Steel: (mm^2)	73050.9
Total Area: (mm^2)	1193887.8
Unit Weight of Soil: (kN/m^3)	18.9
Friction Angle: (deg)	35.0
K_o	0.43
Buried Depth to Pipe Center: (m)	2.0
f:(kN/m)	39.5
f/EA: (1/m)	4.1E-06
EA/f: (m)	2.4E+05
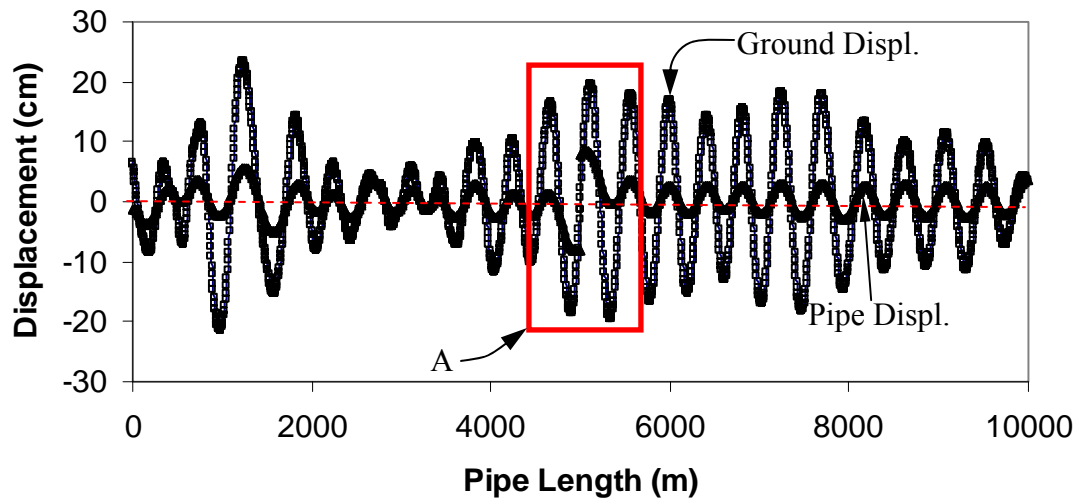
a) Overview
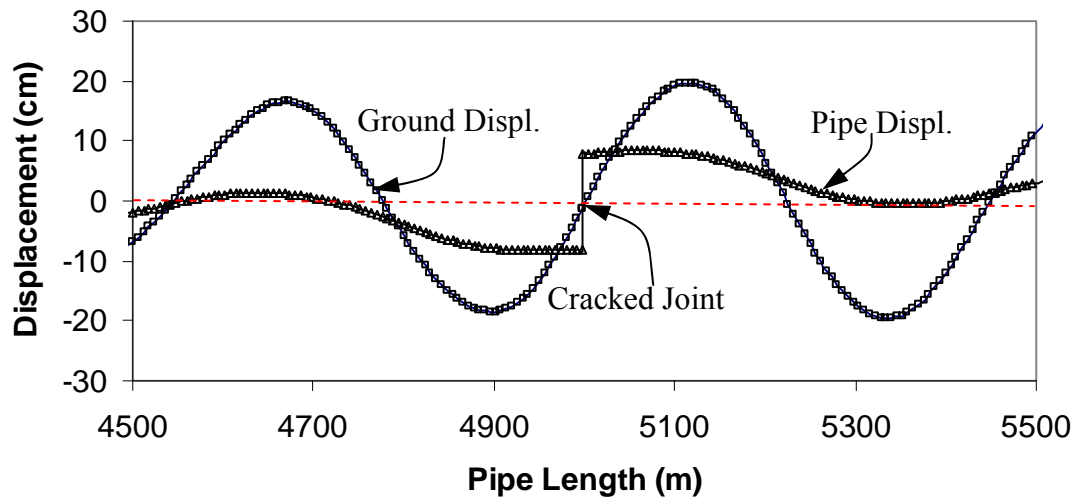
b) Detail A

Figure 4.12 FE Simulation of Ground and Pipeline Displacements for Surface Wave

Interaction with JCCP

101
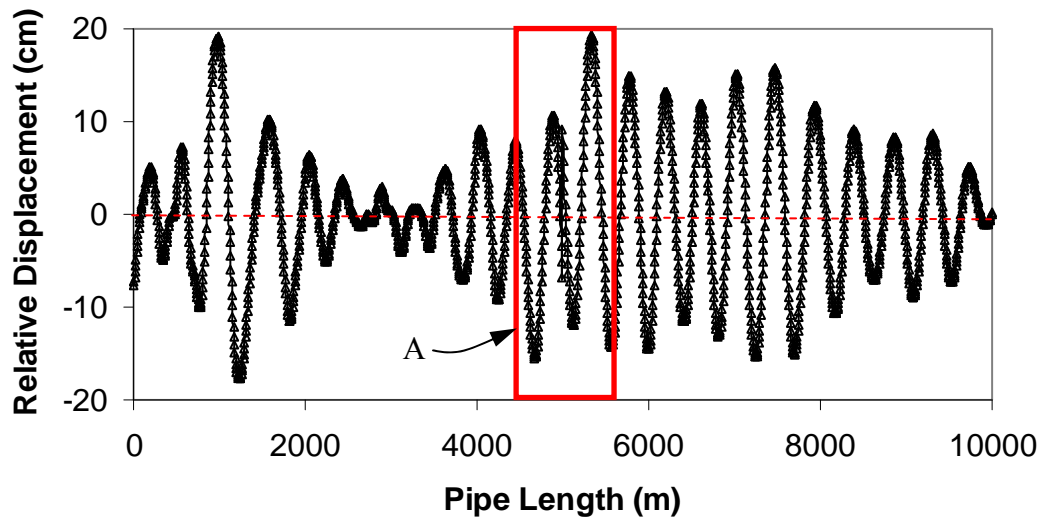
a) Overview

b) Detail A

Figure 4.13 FE Simulation of Pipeline-Ground Relative Displacement for Surface

Wave Interaction with JCCP
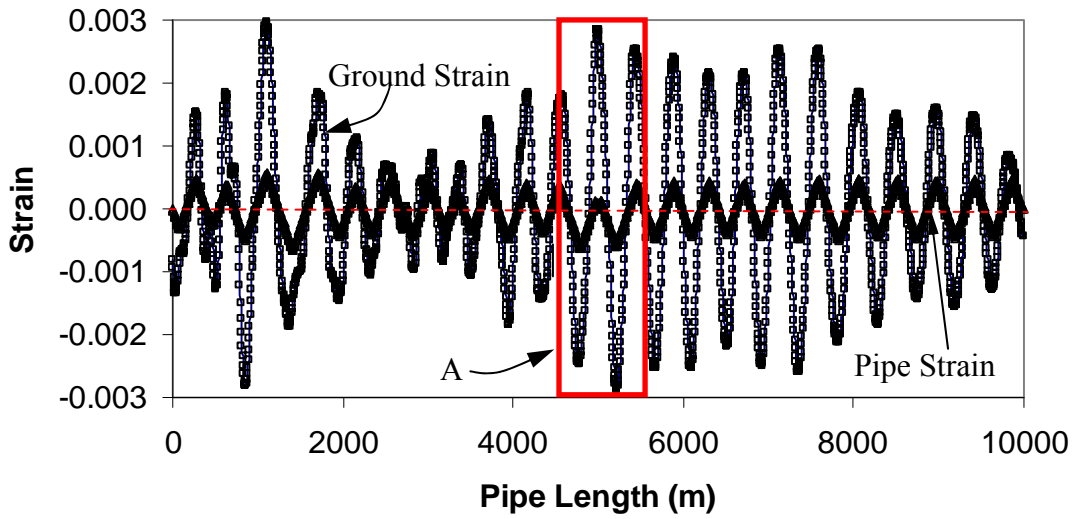
a) Overview
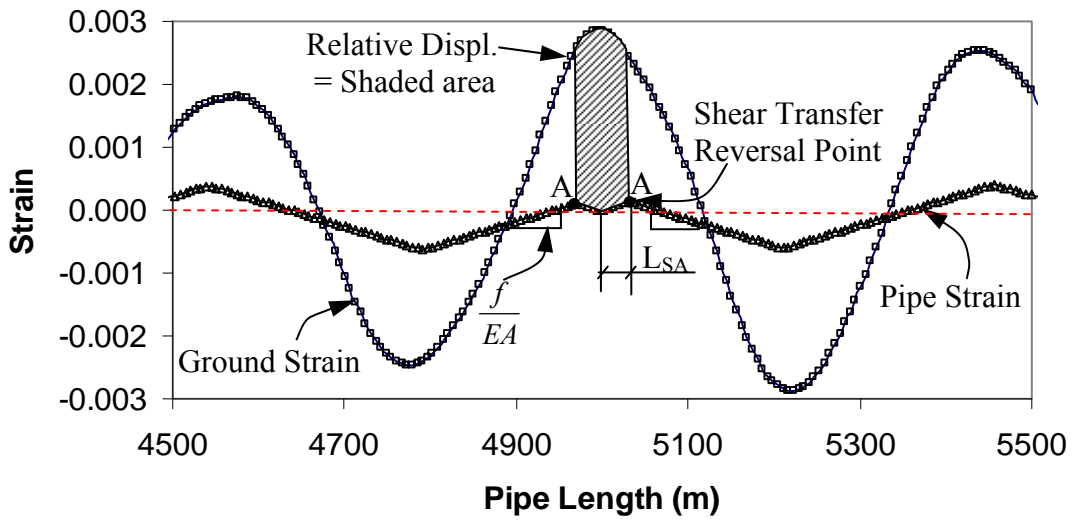
b) Detail A

Figure 4.14 FE Simulation of Ground and Pipeline Strains for Surface Wave

Interaction with JCCP

103

4.3.5 Universal Relationship

Parametric studies of the relative joint displacement were performed on 1829-mm-diameter and 2438-mm-diameter JCCPs using FE analyses for various ground conditions (by changing frictional angle of soil), pipeline properties (by changing EA combination), and seismic wave characteristics (by changing predominant period, ground velocity, and phase velocity). The finite element results, together with the results from Wang (2006) on the body wave interaction with JCCPs, are summarized in Figure 4.15 with two dimensionless parameters, δ/δ_0 and f/EAR. In total 320 finite element analyses were performed. The parameters used in the analyses for pipeline properties, ground conditions, and wave characteristics are summarized in Table 4.2. It is noted that δ_0 is defined as the area under the seismic sinusoidal ground strain pulse (Figure 4.6) and can be calculated by

$$\delta_0 = \int_0^{\lambda/2} \frac{V_p}{C_a} \sin(\frac{2\pi x}{\lambda}) dx \tag{4.11}$$

where C_a is the apparent wave propagation velocity of seismic waves and is equal to the phase velocity, C_{Ph}, for surface waves. When Equation 4.11 is combined with

$$\lambda = C_a T \tag{4.12}$$

in which T is the predominant period of the seismic wave, δ_0 can be expressed as
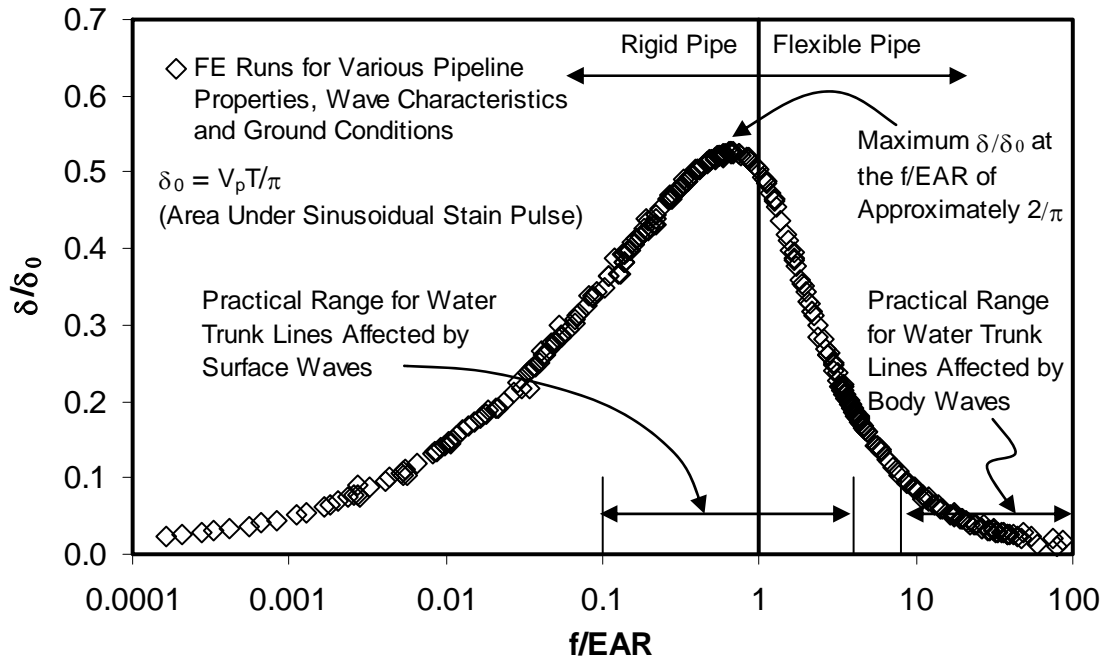
Figure 4.15 Universal Relationship Between δ/δ_0 and f/EAR

$$\delta_0 = \frac{V_p T}{\pi} \qquad (4.13)$$

The dimensionless parameter, δ/δ_0, indicates the relative joint displacement normalized with respect to a displacement index of the seismic wave characteristics. The dimensionless parameter, f/EAR, represents a combination of key ground conditions, pipeline properties, and seismic wave characteristics. The shear transfer between soil and pipeline, f, is a function of interface shear strength properties between soil and pipe, pipeline burial depth, and pipe diameter in the unit of force per length. The EA is the axial stiffness of the pipe. As shown in Figure 4.6, the seismic wave is characterized by R, which is the ratio of V_p/C_a to $\lambda/4$. As shown in Figure 4.15, δ/δ_0 increases from 0 to roughly 0.53 as f/EAR increases from 0 to $2/\pi$. Thereafter, δ/δ_0 decreases with f/EAR, and approaches zero when f/EAR tends to 100.

105

Table 4.2 Summary Table for FE Analysis Parameters

Ground Conditions	Clay with Undrained Strength S_u: 1~200 kPa * Dry Sand with Friction Angle of: 25°~43° Saturated Sand with Effective Friction Angle ϕ': 35° *
Pipeline Properties	1372-mm Diameter and 146-mm Wall Thickness Pipe with Axial Deformation Stiffness EA: 1.87×10^7 kN* 1829-mm Diameter and 178-mm Wall Thickness Pipe with Axial Deformation Stiffness EA: $1.97 \times 10^6 \sim 6.29 \times 10^9$ kN 1981-mm Diameter and 146-mm Wall Thickness Pipe with Axial Deformation Stiffness EA: $3.25 \times 10^5 \sim 3.25 \times 10^9$ kN* 2438-mm Diameter and 216-mm Wall Thickness Pipe With Axial Deformation Stiffness EA: $3.12 \times 10^6 \sim 4.99 \times 10^{10}$ kN
Seismic Body Wave Characteristics (Sinusoidal Wave) *	Peak Particle Velocity Along Pipe Axial Direction V_p: 150 cm/sec or 177 cm/sec Wave Propagation Velocity Along Pipe Axial Direction C_a: 2500 m/sec or 1000 m/sec Predominant Period T: 1 sec or 1.5 sec
Seismic Surface Wave Characteristics (Sinusoidal Wave)	Peak Particle Velocity V_p: 10~60 cm/sec Phase Velocity C_{Ph}: 50~2500 m/sec Predominant Period T: 1~20sec

*: Please refer to Wang (2006) for details

Wang (2006) proposed a criterion for determining if a pipeline is either relatively flexible or rigid. According to this criterion, a relatively flexible pipeline is defined as one for which

$$\frac{f}{EAR} > 1 \qquad (4.14)$$

In contrast, a pipeline is considered relatively rigid when

$$\frac{f}{EAR} \leq 1 \qquad (4.15)$$

The criterion defines a relatively flexible and rigid pipeline based on an f/EAR value of 1, which is easy to apply and close to $2/\pi$, at which δ/δ_0 reaches its maximum value. Practical ranges of f/EAR for water trunk lines affected by surface and body waves are also shown in Figure 4.15. Water trunk lines tend to behave as relatively flexible pipelines when affected by body waves, and act as either relatively rigid or flexible pipelines when affected by surface waves.

With known ground conditions, pipeline properties, and seismic wave characteristics, f/EAR and δ_0 can be calculated and joint displacement, δ, can be estimated directly using Figure 4.15. Consider, for example, a JCCP with 1575-mm diameter and 157-mm wall thickness subjected to a sinusoidal surface wave with $V_p = 30$ cm/sec, phase velocity $C_{Ph} = 200$ m/sec, and $T = 4$ sec. The pipeline is buried at a

depth of 1.70 m to the center of pipeline in soil with $\gamma = 18.8$ kN/m^3 and $\phi' = 35°$. The EA, R, f, and δ_0 are calculated as 2.8×10^7 kN, 7.5×10^{-6} m^{-1}, 103.9 kN/m, and 38.2 cm, respectively, resulting in $f/EAR = 0.49$. Using Figure 4.15, δ/δ_0 is estimated as 0.518, and the relative joint displacement, δ, is about 19.8 cm. Consider the same pipeline with the same ground conditions, subjected to a body wave with $V_p = 100$ cm/sec, $C_a = 2500$ m/sec, and $T = 1$ sec. R and δ_0 are calculated as 6.4×10^{-7} m^{-1} and 31.8 cm, respectively, resulting in $f/EAR = 5.8$. Therefore, δ/δ_0 from Figure 4.15 is about 0.135, and the relative joint displacement, δ, is only about 4.3 cm.

4.3.6   Concrete Cracking Effects

In previous sections, it is assumed that joints on either side of a locally weak joint have full mortar connectivity to mobilize tensile capacity across the joints. The concrete mortar, which is poured in the field to seal the joints, will be cracked when the strain in the joint exceeds it cracking strain limit. The cracking of the concrete mortar changes the geometry of the pipeline and reduces the strain accumulation length. Therefore, the joint displacement is closely related to the joint cracking strain. In this section, the effects of cracking strain are explored.

Figure 4.16 illustrates seismic displacement and ground strain interaction with a JCCP. Each part of Figure 4.16 shows the ground strain, ε_g, expressed as V/C_{Ph}, plotted on the vertical axis. The horizontal axis is the distance, x, along the longitudinal axis of the JCCP. The distance is expressed as the product of the phase velocity, C_{Ph}, and the predominant period, T, of seismic wave. The velocity pulse

a) Seismic wave interaction with pipeline (Overview)

b) Seismic wave interaction with pipeline (t= t_1)

c) Seismic wave interaction with pipeline (t= t_2)

d) Seismic wave interaction with pipeline (t= t_3)

e) Seismic wave interaction with pipeline (t= t_4)
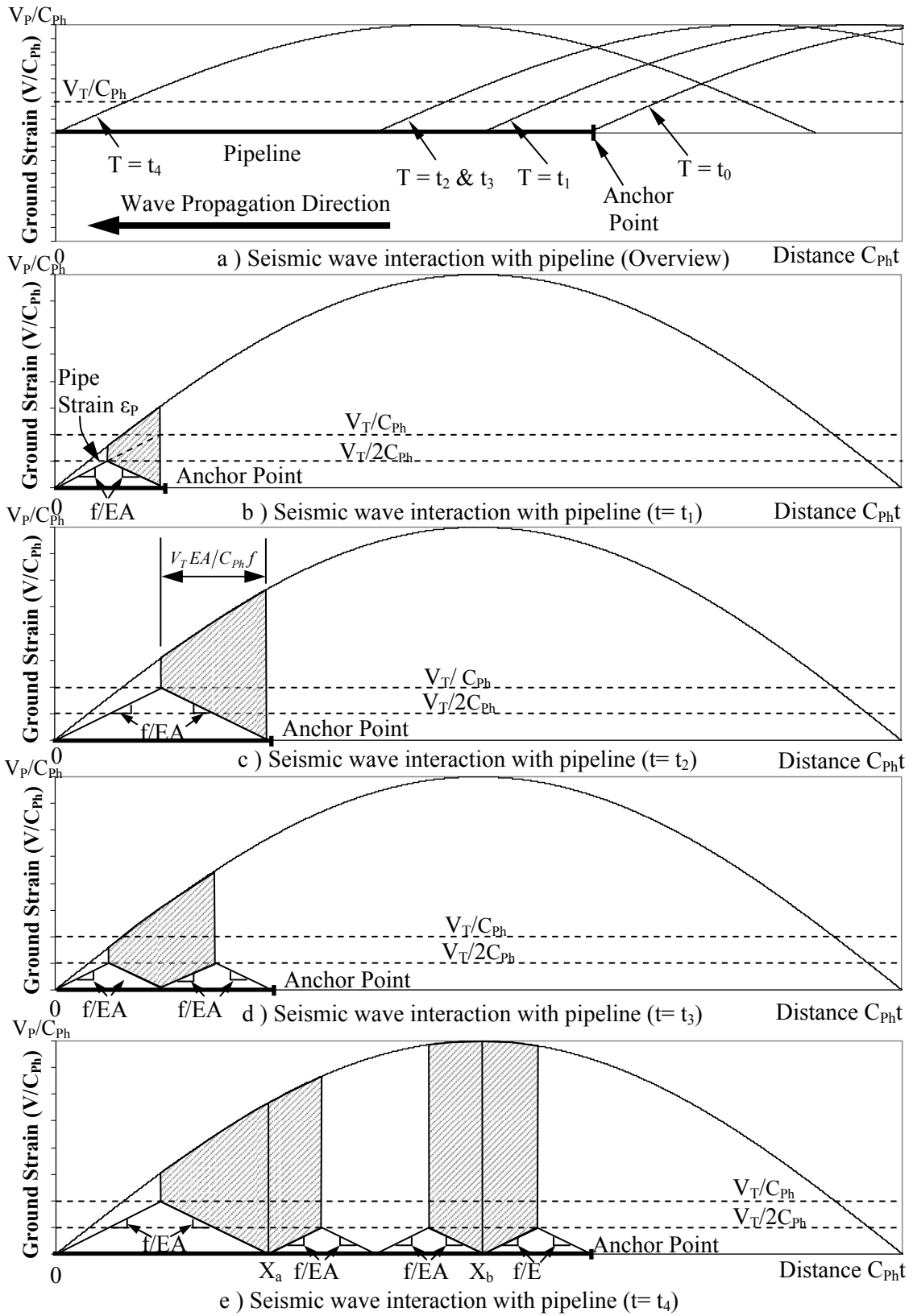
Figure 4.16 Process of Seismic Wave Interaction with Pipeline

109

shown in Figure 4.16 corresponds to half of a sinusoidal wave, and develops tensile strains in the ground.

Figure 4.16 shows the progression of a seismic wave at various times, t_0 through t_4, as it approaches and moves into the ground surrounding the JCCP that terminates at an anchor point. When the seismic wave intersects with the pipeline, the strain begins to accumulate at a slope f/EA from the intersection point, noted as point O in Figure 4.16. Because the pipeline is relatively rigid, the rate for pipe strain accumulation is slower than that of the ground strain accumulation, so $\varepsilon_p < \varepsilon_g$ everywhere along the pipeline until t_1, when the first joint next to the anchor point reaches its tensile strain capacity, $\varepsilon_T = V_T/C_{Ph}$, and cracks (Figure 4.16b). The threshold velocity, V_T, is the velocity that generates ground strain equal to the tensile strain capacity of the concrete mortar. A joint, which is cracked and separated, has very low axial pullout resistance that for modeling purpose can be taken as negligible. At the cracked joint, the pipeline cannot sustain strain, so $\varepsilon_p = 0$. To satisfy force equilibrium after cracking, the strain will accumulate from the intersection point, O, and the cracked joint, both of which have $\varepsilon_p = 0$, at the same slope of f/EA, but in opposite directions, until $\varepsilon_p = \varepsilon_T/2$, where ε_T is the cracking strain at the joint. Therefore, at the middle point of the pipeline between the cracked joint and the point where the seismic wave intersects the pipeline, O, the shear transfer is zero and the pipe displacement is equal to the ground displacement.

The shaded area in Figure 4.16b represents the integration of the differential strain between the pipeline and ground, which equals the relative joint displacement and occurs as axial slip. In a similar fashion, the shaded areas in the subsequent figures represent relative joint displacements and axial slips. As the seismic wave propagates, another joint left of the first cracked joint is also subjected to its tensile strain limit at t_2 (Figure 4.16c). The distance between these two joints, L, can be determined by

$$L = \frac{V_T/C_{Ph}}{f/EA} = \frac{V_T EA}{C_{Ph} f} \qquad (4.16)$$

The joint cracks when its tensile strain capacity is exceeded (Figure 4.16d) at t_3, which occurs immediately after t_2. On the right side of the newly cracked joint, the pipeline segment between the two cracked joints must have zero strain at each cracked end. To satisfy force equilibrium, the strain will accumulate linearly from both ends at the same slope of f/EA until $\varepsilon_p = \varepsilon_T/2$, where ε_T is the joint cracking strain. On the left side of the newly cracked joint, the strain will also accumulate linearly from both ends at the same slope of f/EA until $\varepsilon_p = \varepsilon_T/2$. With continued wave propagation, the next joint will crack at a distance, L, left of the previously cracked joint (Figure 4.16e). This process repeats itself as the wave moves forward along the pipeline.

The two most critical cases for the relative joint displacement are illustrated in Figure 4.16e. The relative joint displacement attains its first local maxima at X_a just before the next joint left of X_a cracks. The joint displacement, δ_a, can be calculated from the shaded area on the left side of Figure 4.16e. The shaded area on the right of Figure 4.16e at X_b illustrates the second possible maximum joint displacement, δ_b.

This movement occurs when the peak ground velocity, V_p, passes across the cracked pipeline. The maximum relative joint displacement is the larger of the two possible joint displacements.

Figure 4.17 illustrates a simplified procedure for calculating the shaded areas in Figure 4.16e. The relative joint displacement for the first potentially maximum case, δ_a, is calculated by subtracting the areas of the two triangles, 1 and 2, shown in Figure 4.17 from the integral of the ground strain from a distance $(V_T/C_{Ph})*(EA/f)$ to $(5/2)*(V_T/C_{Ph})*(EA/f)$. The integral of the ground strain is calculated as

$$A = \int_{\frac{V_T}{C_{Ph}}\frac{EA}{f}}^{\frac{5}{2}\frac{V_T}{C_{Ph}}\frac{EA}{f}} \frac{V_P}{C_{Ph}}\sin(2\pi\frac{x}{C_{Ph}T})dx = \frac{V_PT}{\pi}\sin(\frac{7\pi V_T}{2C_{Ph}^2T}\frac{EA}{f})\sin(\frac{3\pi V_T}{2C_{Ph}^2T}\frac{EA}{f}) \qquad (4.17)$$

The areas A_1 and A_2 are calculated as

$$A_1 = \frac{1}{2}\left(\frac{V_T}{C_{Ph}}\right)^2\frac{EA}{f} \qquad (4.18)$$

$$A_2 = \frac{1}{8}\left(\frac{V_T}{C_{Ph}}\right)^2\frac{EA}{f} \qquad (4.19)$$

Combining Equations 4.17 through 4.19 results in

$$\delta_a = A - A_1 - A_2 = \frac{V_PT}{\pi}\sin(\frac{7\pi V_T}{2C_{Ph}^2T}\frac{EA}{f})\sin(\frac{3\pi V_T}{2C_{Ph}^2T}\frac{EA}{f}) - \frac{5}{8}\left(\frac{V_T}{C_{Ph}}\right)^2\frac{EA}{f} \qquad (4.20)$$

112
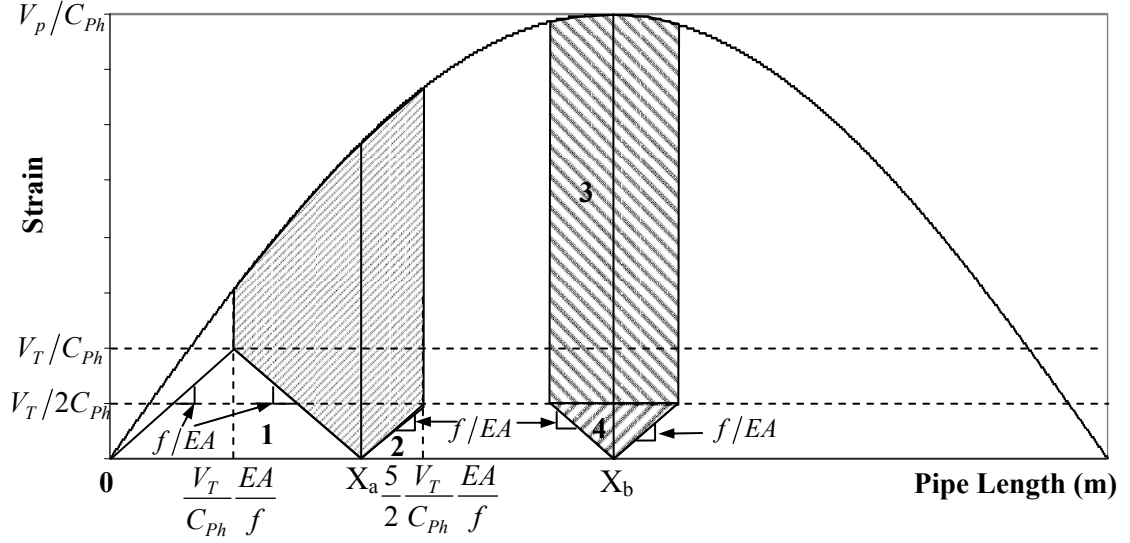
Figure 4.17 Simplified View of Sinusoidal Wave Interaction with JCCP Considering Concrete Cracking Effects

The value of V_T/C_{Ph} is equivalent to the tensile cracking capacity, ε_T, of the JCCP joints. Combining $\varepsilon_T = V_T/C_{Ph}$, $\lambda = C_{Ph}T$ and Equation 4.20, results in

$$\delta_a = A - A_1 - A_2 = \frac{V_P T}{\pi}\sin\left(\frac{7\pi}{2}\frac{\varepsilon_T}{\lambda}\frac{EA}{f}\right)\sin\left(\frac{3\pi}{2}\frac{\varepsilon_T}{\lambda}\frac{EA}{f}\right) - \frac{5}{8}\varepsilon_T{}^2\frac{EA}{f} \qquad (4.21)$$

Similarly, the relative joint displacement for the alternative maximum case, δ_b, can be decomposed into two area components,

$$\delta_b = A_3 + A_4 \qquad (4.22)$$

where A_3 and A_4 are calculated as

$$A_3 = \left(\frac{V_T}{C_{Ph}}\right)^2 \frac{EA}{f}\left(\frac{V_p}{V_T} - \frac{1}{2}\right) \qquad (4.23)$$

113

$$A_4 = \frac{1}{4}\left(\frac{V_T}{C_{Ph}}\right)^2 \frac{EA}{f} \tag{4.24}$$

Combining Equations 4.23 and 4.24 results in

$$\delta_b = A_3 + A_4 = \left(\frac{V_T}{C_{Ph}}\right)^2 \frac{EA}{f}\left(\frac{V_p}{V_T} - \frac{1}{4}\right) \tag{4.25}$$

Again, combining $\varepsilon_T = V_T / C_{Ph}$ and Equation 4.25, results in

$$\delta_b = \varepsilon_T^2 \frac{EA}{f}\left(\frac{V_p}{C_{Ph}\varepsilon_T} - \frac{1}{4}\right) \tag{4.26}$$

Based on above analysis, when the maximum strain in the relative rigid pipeline exceeds the limit of concrete cracking strain, the largest relative joint displacement is chosen from either Equation 4.21 or 4.26. The maximum strain in a relatively rigid pipeline can be calculated as

$$\varepsilon_{P\max} = \frac{\lambda}{4}\frac{f}{EA} \tag{4.27}$$

which is the strain accumulated in a quarter of wavelength, as shown in Figure 4.7.

When the maximum strain in the pipeline is smaller than the concrete cracking strain, the relative joint displacement can be estimated using the universal relationship provided in Figure 4.15.

The cracking strain for concrete mortar ranges from 0.00005 to 0.00015, with a typical value of 0.0001 (Avram et al., 1981). For the same pipeline and surface wave combination used in the FE model in Section 4.3.4, using Equation 4.27, the maximum strain in the pipeline can be calculated as 0.000432, which is larger than the cracking limit of the concrete mortar. By accounting for the cracking of concrete mortar and choosing the cracking strain as 0.0001, the joint displacement calculated by Equations 4.21 and 4.26 is 5.4 cm (2.10 in.) and 6.0 cm (2.36 in.), respectively. As such, the larger value, 6.0 cm, provides a reasonable estimate of the axial joint slip for a segmented JCCP in the field. This value is larger than the axial pullout capacity of a typical rubber gasket joint and might lead to the disengagement of adjoining JCCP sections.

The model presented in this section accounts for cracking where the tensile capacity of the pipeline joint is exceeded, and therefore is compatible with strain limits of the pipeline material. The cracking of joints transforms the pipeline from a continuous structure to a segmented one. The model, therefore, accounts for geometric nonlinearity. It is able to track changes in geometric properties, shear transfer, pipeline strain accumulation, and joint displacement during seismic wave passage along the pipeline.

4.4 ANALYTICAL MODEL FOR SURFACE WAVE INTERACTION WITH CI PIPELINES

In previous sections, an analytical model was developed for seismic wave response analyses of JCCPs. In this section, this model is expanded to analyze the seismic wave response of CI pipelines composed of lead-caulked joints.

4.4.1 CI Pipelines

A CI pipeline is one of the oldest and most commonly used pipelines for water and gas distribution in North America. Typically, CI pipe segments are connected by lead-caulked joints. The detailed description of the CI pipe material properties and joint characteristics is provided in Section 5.4 together with various other types of pipelines.

Figure 4.18 summarizes axial force versus. displacement data after Prior (1935) from a testing program of lead-caulked joints for water trunk and distribution pipelines. The test data correspond to pipe internal diameters of 450 and 610 mm. Because the plot contains data for pipes with different diameters, the axial force is expressed in terms of kN per circumferential length. Two force-displacement models are shown in the figure, corresponding to rigid and elasto-plastic behaviors. Both models show that a very small axial displacement, 0 for the rigid model and 2.5 mm for the elasto-plastic model, is needed to mobilize the full axial tensile capacity of the joints. The data suggest that the joint tensile capacity remains approximately constant with additional movement after it is mobilized.
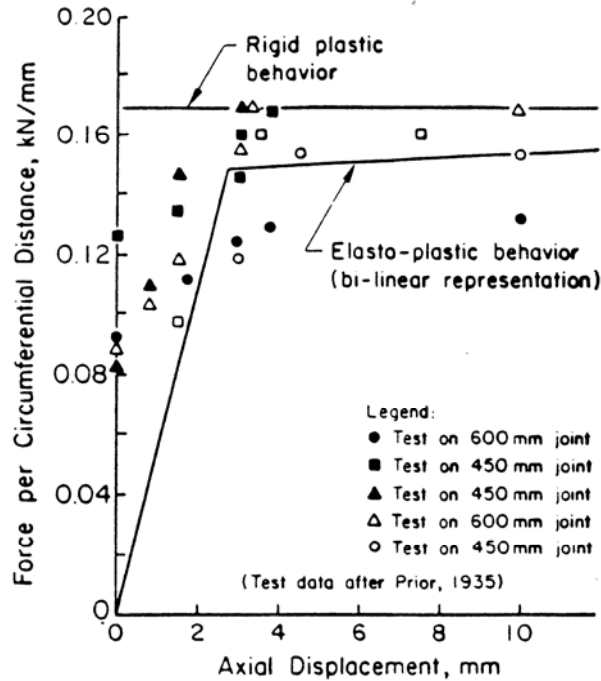
Figure 4.18 Axial Force vs. Displacement for Lead Caulked Joints

(after Prior, 1935)

The pullout capacity of the joint in terms of axial slip to cause leakage depends on how much movement can occur before the lead caulking loses its compressive seal. Based on the laboratory test data, Untrauer et al. (1970) reported that, after an initial period of very small leakage, the lead-caulked joints can sustain an axial slip from 25 to 50 mm (1 to 2 in.) without further loss of water. This laboratory behavior was corroborated by field observations from deformed CI water mains in areas of fault creep by O'Rourke and Trautmann (1980).

4.4.2   Seismic Wave Interaction with CI Pipelines

Figure 4.19 illustrates the seismic response of a CI pipeline with lead caulked joints. It is assumed that there is a locally weak joint in the pipeline and the pipeline
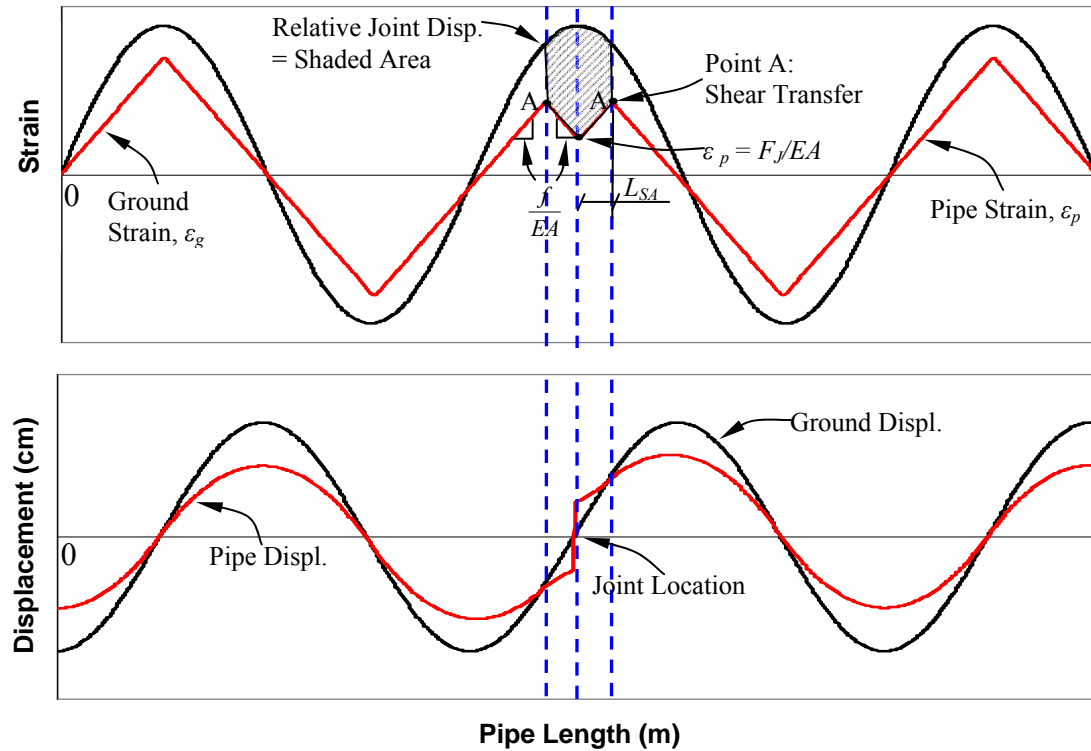
Figure 4.19 Sinusoidal Wave Interaction with CI Pipeline

on either side of the joint behaves as a continuous one. The ground strain, ε_g, is expressed as V/C_{Ph}, in which, V and C_{Ph} are the particle ground and phase velocities along the pipe axis, respectively.

The strain at the pipe ends connected with the lead-caulked joint is controlled by the tensile capacity of the joint and is equal to $\varepsilon_p = F_J/EA$, where F_J is the joint tensile capacity and EA is the axial stiffness of the pipeline. As a wave passes across the joint, strain in the continuous pipeline on both sides of the joint accumulates linearly from $\varepsilon_p = F_J/EA$ at a slope of f/EA until the reversal of the relative displacement (point A in Figure 4.19), after which pipe strain accumulates at the same slope but with opposite direction. There is no relative displacement between pipe and

118

ground at point *A* where the reversal of relative displacement occurs. The integration of the differential strain between the pipeline and ground from the joint to point *A*, as represented by half of the shaded area in Figure 4.19 is the relative displacement between the pipeline and ground at the joint, which equals one half of the relative joint displacement.

Comparing Figures 4.8 and 4.19 shows that the difference between the seismic response of the JCCP and CI pipeline is that the strain begins to accumulate from $\varepsilon_p = 0$ for the JCCP and from $\varepsilon_p = F_J / EA$ for the CI pipeline. The difference results from the different tensile behavior of rubber-gasket bell-and-spigot and lead caulked joints in the JCCP and CI pipeline, respectively. The JCCP joint has a brittle tensile failure behavior, which cannot provide tensile resistance after it cracks. The CI joint has a ductile tensile failure behavior, for which the tensile capacity remains approximately constant with additional movement after its pullout resistance is mobilized.

In this study, a brittle joint is used for a joint with brittle tensile behavior, and a ductile joint is used for a joint with ductile tensile behavior. A brittle joint can be treated as a special case of a ductile joint, which has zero joint capacity, $F_J = 0$. Factors affecting the relative displacement of a brittle joint are the strain accumulation length L_{SA}, seismic parameter, V_p / C, and the relative stiffness between pipeline and soil, EA/f. The pullout displacement of a ductile joint is also a function of the joint pullout capacity, F_J. The relative displacement of ductile joints under the effects of seismic waves can be analyzed using the FE method.

4.4.3   Finite Element Model

With the same finite element model as the one shown in Figure 4.10, the response of a 610-mm-(24-in.)-diameter CI pipeline was analyzed under the effects of surface waves. Pipe properties and ground conditions are summarized in Table 4.3. The joint was modeled in accordance with the elasto-plastic behavior shown in Figure 4.20. The interrelation between joint pullout capacity, F_J, and axial displacement was modeled as a bilinear relationship with linear rise to $F_J = 275$ kN at a relative displacement of 2.5 mm and constant F_J thereafter.   The values of joint pullout capacity and axial displacement are consistent with those provided by Prior (1935), as shown in Figure 4.18, for a 610-mm-(24-in.) diameter pipeline.   The sinusoidal seismic wave was assumed with $PGV = 30$ cm/sec, $C_{Ph} = 120$ m/sec, and $T = 3.5$ sec, which are consistent with the PGV, C_{Ph}, and T of the recorded surface waves during the 1985 Michoacan earthquake in Mexico City.

Figures 4.21 to 4.22 show the relative displacement between pipe and ground, as well as pipe and ground strains. From Figure 4.21, the relative joint displacement is 13.7 cm, which is distributed symmetrically either side of the joint to reflect the symmetric shape of a sinusoidal wave. Figure 4.22 shows that the strain at the pipe ends connected with the joint is roughly 9.14E-5, equal to F_J/EA. The strain starts to accumulate from the pipe ends at a slope of f/EA, and the direction of strain accumulation reverses at point A.   The integration of differential strain between ground soil and pipeline within the two strain reversal points in the vicinity of the joint is the relative joint displacement. The high predicted relative joint movement, 13.7 cm, indicates a strong potential for joint pullout and disengagement for the CI pipeline under surface wave effects.

Table 4.3 CI Pipeline Physical Properties and Ground Conditions for FE Analysis

CI Pipeline Properties	
Diameter (mm)	610.0
Wall Thickness (mm)	22.4
Buried Depth (m)	1.0
Center Depth (m)	1.2
Inside Radius of Pipe (mm)	282.6
Outside Radius of Pipe (mm)	305.0
Cross-sectional Area of Pipe (mm^2)	41350.4
Young's Modulus of CI(GPa)	70.0
Unit Weight of Soil (kN/m^3)	18.9
Interface Angle (deg)	35.0
K_o	0.43
f (kN/m)	22.0
f/EA (1/m)	7.6E-06
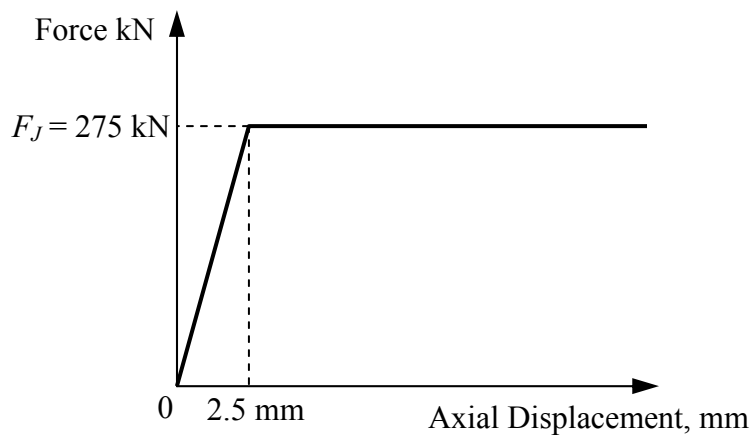
Figure 4.20 Elasto-Plastic Model for Axial Force vs. Displacement for Lead Caulked Joints
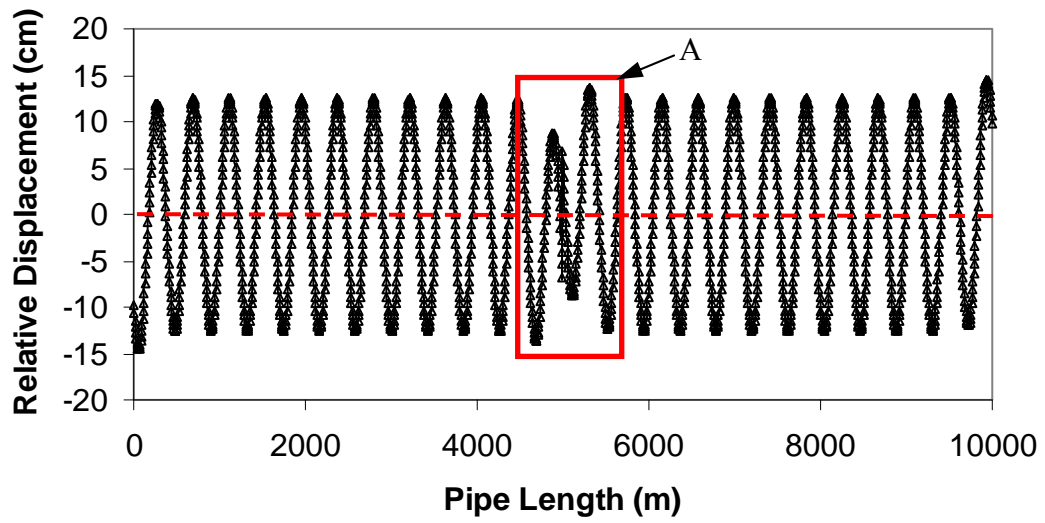
a) Overview
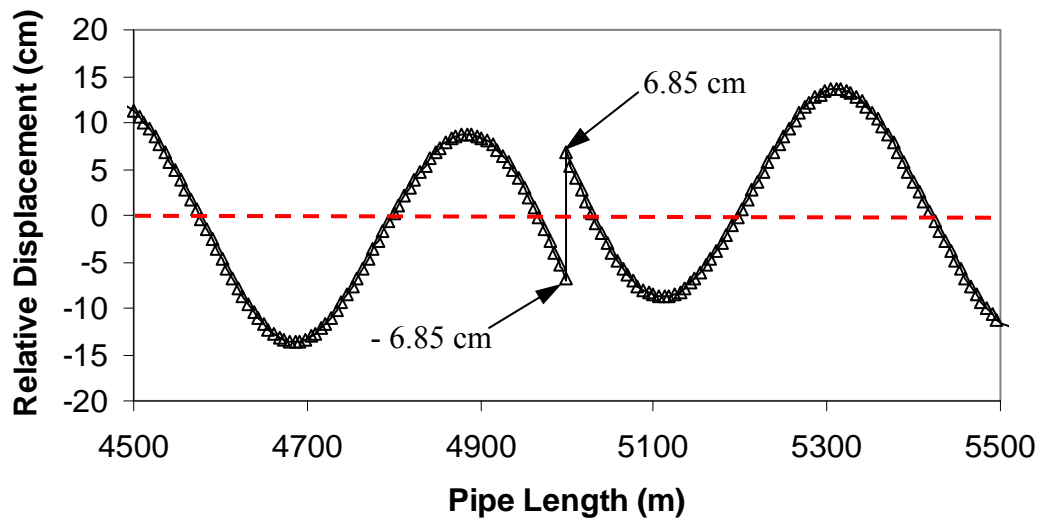
b) Detail A

Figure 4.21 Pipe-Ground Relative Displacement for Sinusoidal Wave Interaction with CI Pipeline
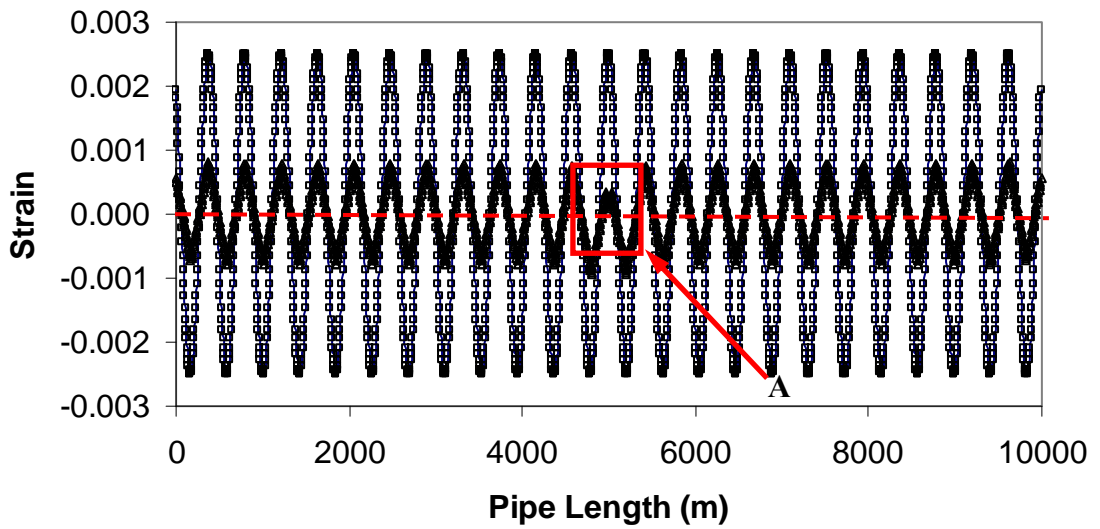
a) Overview
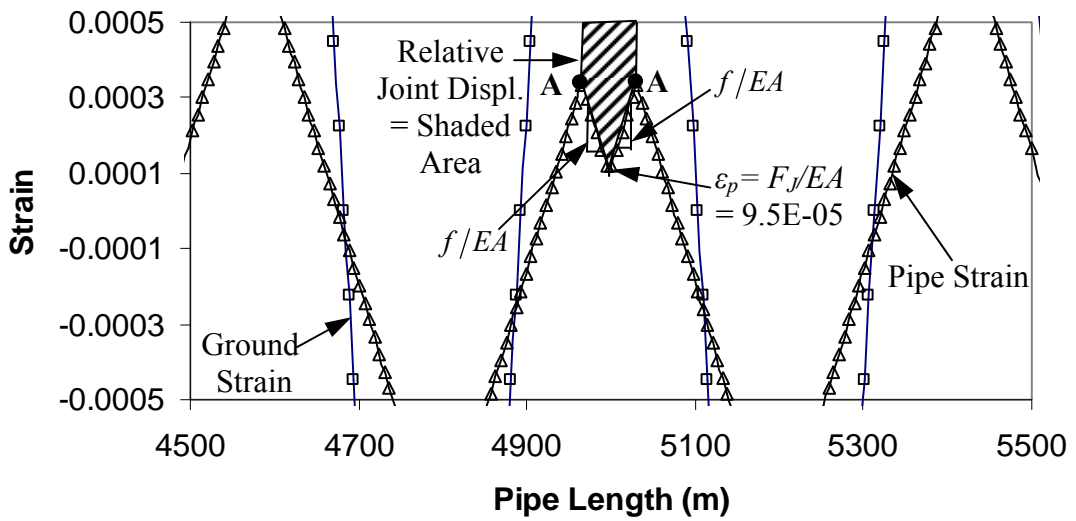
b) Detail A

Figure 4.22 Pipe and Ground Strain for Sinusoidal Wave Interaction with CI Pipeline

4.4.4 Relative Joint Displacement Reduction Curves

Figure 4.15 provides a dimensionless chart which can be used to estimate the relative joint displacement of virtually any JCCP under the effects of seismic waves. This section expands the application of the dimensionless chart to estimate the joint pullout displacement of CI pipelines by considering the ductility of the joint using dimensionless reduction curves.

4.4.4.1 Normalized Parameters

Based on above analyses, the relative displacement of a ductile joint is a function of the joint capacity. Figure 4.23 shows the strain response of a relatively rigid pipeline with a ductile joint possessing different capacities. In this figure, the joint capacity is expressed as a dimensionless parameter, $(F_J/EA)/\varepsilon_{Pmax}$, in which F_J is the joint tensile capacity, EA is the pipeline axial stiffness, F_J/EA is the strain at the pipe ends connected with the joint, and ε_{Pmax} is the maximum possible strain at the pipe ends with a value of $(f/EA)*\lambda/4$. The maximum pipe strain, ε_{Pmax}, occurs when the axial stiffness of the joint is equal to or higher than the pipeline. The parameter $(F_J/EA)/\varepsilon_{Pmax}$ represents the normalized strain at the pipe ends, connected with the joint, from which the strain begins to accumulate.

For a brittle joint, which has zero joint capacity after being cracked, strain at ends of the pipe begins to accumulate from zero, resulting in the longest strain accumulation length, L_{SA}, and the largest relative joint displacement. With increased joint capacity, $(F_J/EA)/\varepsilon_{Pmax}$ increases. At the same time, the strain accumulation length, L_{SA}, and the relative joint displacement decrease. When the $(F_J/EA)/\varepsilon_{Pmax}$ is
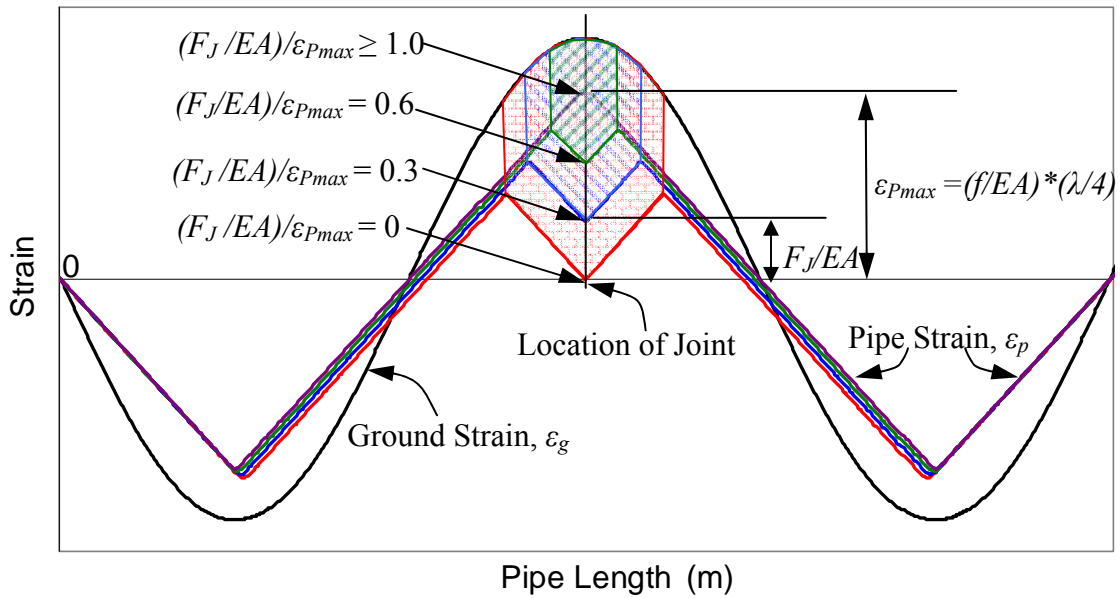
Figure 4.23 Strain Response Curve for a Relatively Rigid Pipeline with Different Values of $(F_J/EA)/\varepsilon_{Pmax}$

equal to or larger than 1, strain at ends of the pipe is equal to the maximum possible pipe strain. The strain accumulation length, L_{SA}, is zero, leading to a zero relative joint displacement if the elastic elongation of the pipeline is neglected. Because the relative joint displacement reaches its maximum value when the joint capacity is zero, i.e. brittle joint case, the displacement of a ductile joint, δ_J, can be normalized with respect to the displacement of a brittle joint, δ, and expressed as a dimensionless parameter, δ_J/δ.

4.4.4.2 Reduction Curves from FE Analyses

Figure 4.24 summarizes the relationship between the normalized joint displacement, δ_J/δ, and normalized pipe strain, $(F_J/EA)/\varepsilon_{Pmax}$, from 15 sets of FE analyses for three different pipeline and wave combinations. The simulations were performed for an 1980-mm-(78-in.)-diameter JCCP under the effects of a surface

125
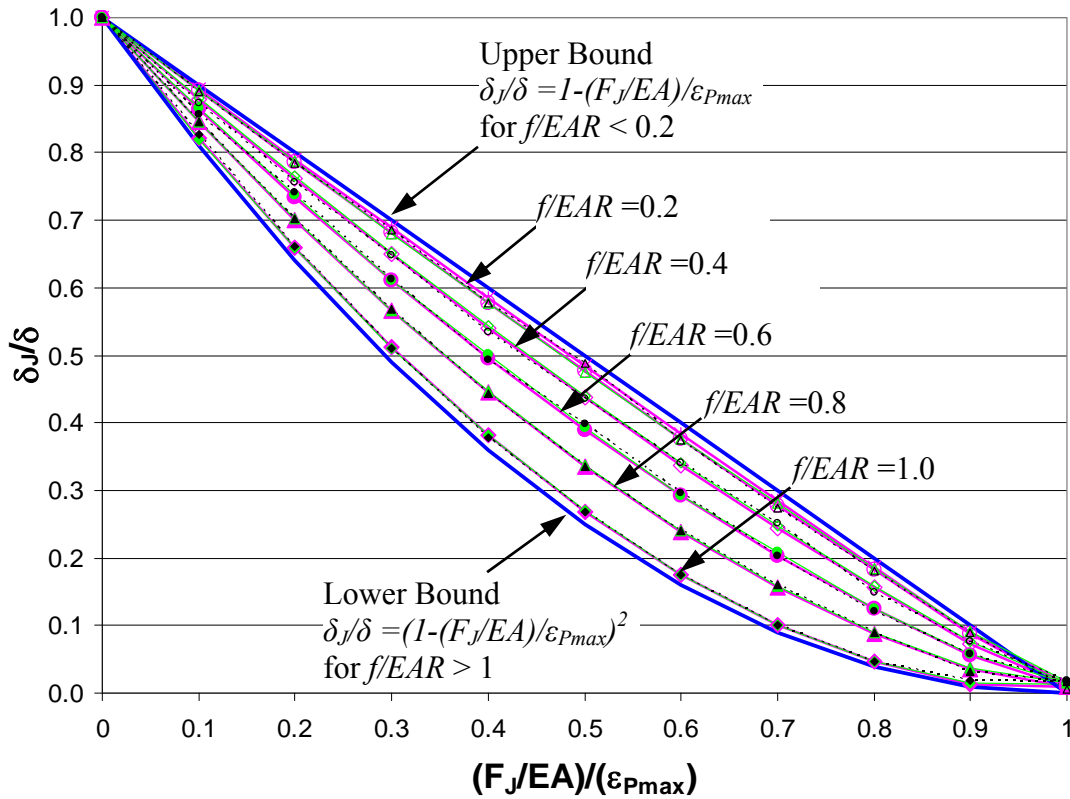
Figure 4.24 Reduction Curves from FE Analysis Results

wave with $PGV = 30$ cm/sec, phase velocity, $C_{Ph} = 200$ m/sec, and predominate period, $T = 3.5$ sec, a 610-mm-(24-in.)-diameter CI pipeline under the effects of a body wave with $PGV = 177$ cm/sec, apparent wave propagation velocity $C_a = 2500$ m/sec, and $T = 1$ sec, and an 1828-mm-(72-in.)-diameter JCCP under the effects of a surface wave with $PGV = 25$ cm/sec, $C_{Ph} = 100$ m/sec, and $T = 3.5$ sec. For each pipe and wave combination, the Young's modulus of pipe material was varied artificially and different f/EAR values were obtained. For each f/EAR value, ten runs of FE analyses were performed by varying the joint capacity with $(F_J/EA)/\varepsilon_{Pmax}$ values ranging from 0 to 1. In total, the results from 150 FE runs are summarized in Figure 4.24. Because these curves show the reduction of the relative displacement for ductile joints with respect to brittle joints, they are called relative joint displacement reduction curves in this study.

Figure 4.24 shows that δ_J/δ decreases from 1 to 0 with an increase of $(F_J/EA)/\varepsilon_{Pmax}$ from 0 to 1. All reduction curves are bounded by an upper bound, $\delta_J/\delta = 1- (F_J/EA)/\varepsilon_{Pmax}$, and a lower bound, $\delta_J/\delta = (1-(F_J/EA)/\varepsilon_{Pmax})^2$. When f/EAR is equal to or larger than one, all reduction curves converge to the lower bound. With decreasing *f/EAR*, the reduction curves shift from a lower bound to upper bound. When *f/EAR* is equal to or less than 0.2, all reduction curves converge to the upper bound. For different pipeline and seismic wave combinations, if their *f/EAR* values are same, they share the same reduction curve.

4.4.4.3   Lower Bound

The lower bound of the reduction curves are for pipeline-wave interactions with *f/EAR* equal to or larger than 1, which lies in the relatively flexible pipeline range as defined by Equations 4.14 and 4.15. Wang (2006) conducted a detailed study of the reduction curves for relatively flexible pipelines. Figure 4.25 shows the strain response of a relatively flexible pipeline with a joint having capacities equal to 0 and F_J. Half joint displacement, $0.5\delta_J$, corresponding to joint capacity of F_J, is shown as the blue shaded area. Half joint displacement, 0.5δ, corresponding to joint capacity of 0, is shown as the red shaded area. The ratio of the relative displacement between a ductile and brittle joint, δ_J/δ, is the ratio of the blue to red shaded areas. The red shaded area, δ, can be approximated as the triangle, *ABM*, and the blue shaded area, δ_J, can be approximated as the triangle, *ADC*. The error associated with this approximation is minimal, generally smaller than 10% based on the calculations for various sinusoidal wave and pipeline combinations. The area ratio, δ_J/δ, can be expressed as
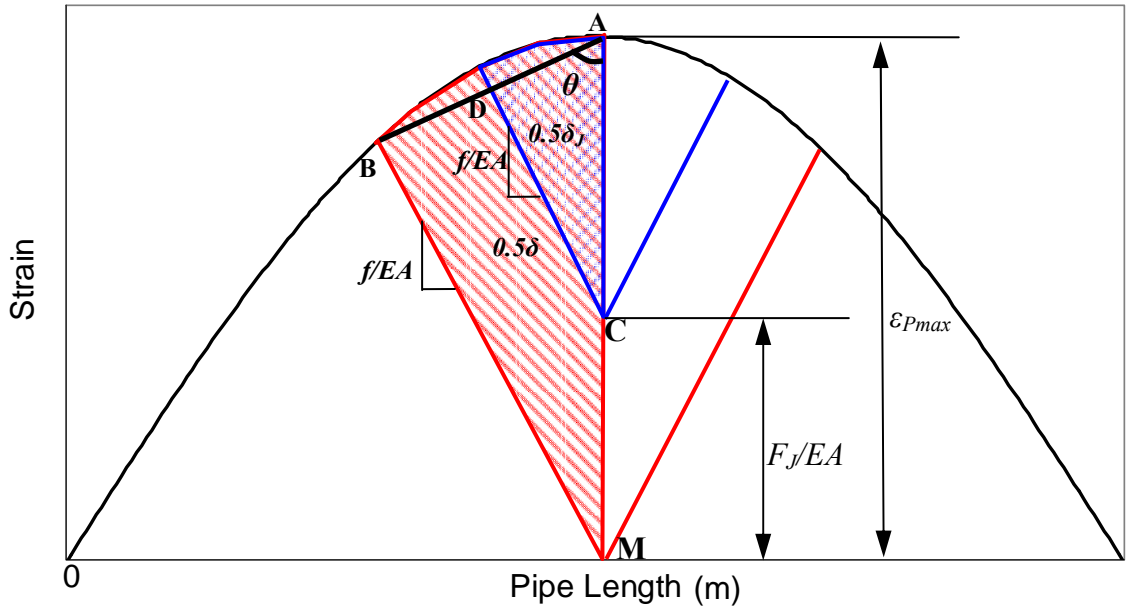
Figure 4.25 Strain Response Curves of a Relatively Flexible Pipeline

$$\frac{\delta_J}{\delta} = \frac{S_{\Delta ADC}}{S_{\Delta ABM}} = \frac{1/2 \times AD \times AC \times \sin\theta}{1/2 \times AB \times AM \times \sin\theta} = \frac{AD \times AC}{AB \times AM} \qquad (4.28)$$

where $S_{\Delta ADC}$ and $S_{\Delta ABM}$ are the areas of triangles ADC and ABM, respectively. It is noted that CD and MB are in parallel. Thus

$$\frac{AD}{AB} = \frac{AC}{AM} \qquad (4.29)$$

Substituting Equations 4.29 into 4.28 results in

$$\frac{\delta_J}{\delta} = \frac{AC^2}{AM^2} = \frac{\left(\varepsilon_{P\max} - (F_J / EA)\right)^2}{\varepsilon_{P\max}^2} = \left(1 - \frac{(F_J / EA)}{\varepsilon_{P\max}}\right)^2 \qquad (4.30)$$

which provides a lower bound for the reduction curves.

128

4.4.4.4   Upper Bound

Figure 4.26 shows three strain response curves of a relatively rigid pipeline with joints having brittle and ductile tensile behavior, as well as a joint with stiffness equal to or larger than the stiffness of the pipe material, respectively. By drawing a line, *DFG*, through the peak points of the three strain curves, the relative displacement of both the brittle and ductile joints can be divided into two parts.   One part is associated with the trapezoid, *ADFB*, for the ductile joint and *ADGC* for the brittle joint, as shown in Figure 4.26. The other part is a triangle, *DEF* for the ductile joint and *DMG* for the brittle joint, as shown in Figure 4.26. Although it is hard to prove that the three peak strain points are in the same line mathematically, this assumption appears to be valid when the pipeline is very stiff.   The limiting case is when the pipeline is perfectly rigid, for which the three strain response curves converge to the same flat line and the three peak strain points are all in this line.

When the pipeline is very stiff relative to the ground soil, i.e. the *f/EAR* value is very small, the strain response curves are very flat. Thus, the areas of triangles *DEF* and *DMG* are typically very small, and can be ignored.   The ratio of the relative displacement between the ductile and brittle joints can be approximated as the area ratio of *ADFB* to *ADGC,* such that

$$\frac{\delta_J}{\delta} \approx \frac{S_{ADFB}}{S_{ADGC}} \tag{4.31}$$

where S_{ADFB} and S_{ADGC} are the areas of *ADFB* and *ADGC*, respectively. By drawing a line, $AB'C'$, in parallel with line DFG, S_{ADFB} and S_{ADGC} can be approximated as
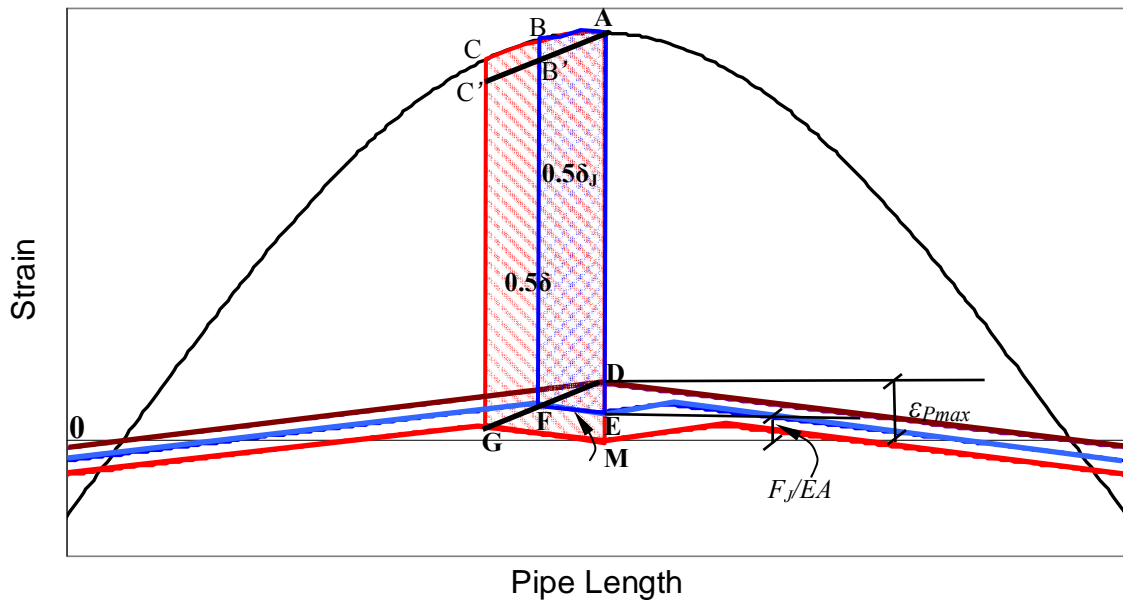
Figure 4.26 Strain Response Curves of a Relatively Rigid Pipeline

$$S_{ADFB} \approx S_{ADFB'} \qquad (4.32)$$

$$S_{ADGC} \approx S_{ADGC'} \qquad (4.33)$$

The errors associated with Equations 4.32 and 4.33 are small, and decrease with increasing relative stiffness of the pipeline. When the pipeline becomes stiffer, the slope of the lines DFG and $A'B'C'$ becomes smaller, and the errors associated with Equations 4.32 and 4.33 decrease. When the relative stiffness of the pipeline becomes infinite, the errors associated with Equations 4.32 and 4.33 approach zero.

Combing Equations 4.31 to 4.33 results in,

$$\frac{\delta_J}{\delta} \approx \frac{S_{ADFB'}}{S_{ADGC'}} \qquad (4.34)$$

Because AD, $B'F$, and $C'G$ are all in parallel,

$$\frac{\delta_J}{\delta} \approx \frac{S_{ADFB'}}{S_{ADGC'}} = \frac{DF}{DG} \tag{4.35}$$

Because *EF* and *OG* are also in parallel,

$$\frac{\delta_J}{\delta} = \frac{DF}{DG} = \frac{DE}{DM} = \frac{\varepsilon_{P\max} - (F_J/EA)}{\varepsilon_{P\max}} = 1 - \frac{(F_J/EA)}{\varepsilon_{P\max}} \tag{4.36}$$

which provides an upper bound for the reduction curves. Figure 4.24 shows that, when the *f/EAR* values are equal to or smaller than 0.2, the reduction curves are very close to the upper bound.

4.4.4.5   Reduction Curves for Engineering Usage

Based on the above analyses, the reduction curves are only a function of *f/EAR*. For different *f/EAR* values, δ_J/δ = *(1- (F$_J$/EA)/ε$_{Pmax}$)^2* provides a lower bound and δ_J/δ = *1- (F$_J$/EA)/ε$_{Pmax}$* provides an upper bound for the reduction curves. For engineering application, it is proposed that when *f/EAR* is greater than or equal to 1, the reduction curve δ_J/δ = *(1- (F$_J$/EA)/ε$_{Pmax}$)^2* can be used; when *f/EAR* is smaller than or equal to 0.2, the reduction curve δ_J/δ = *1- (F$_J$/EA)/ε$_{Pmax}$* can be used, and when *f/EAR* lies between 1 to 0.2, linear interpolation between the upper and lower bounds can be used. The error associated with the interpolation is minimum and without significance in engineering practice. Using the interpolation, every reduction curve corresponding to a specific *f/EAR* value has a closed form solution and can be easily calculated for design purposes. Figure 4.27 shows the reduction curves for engineering applications.
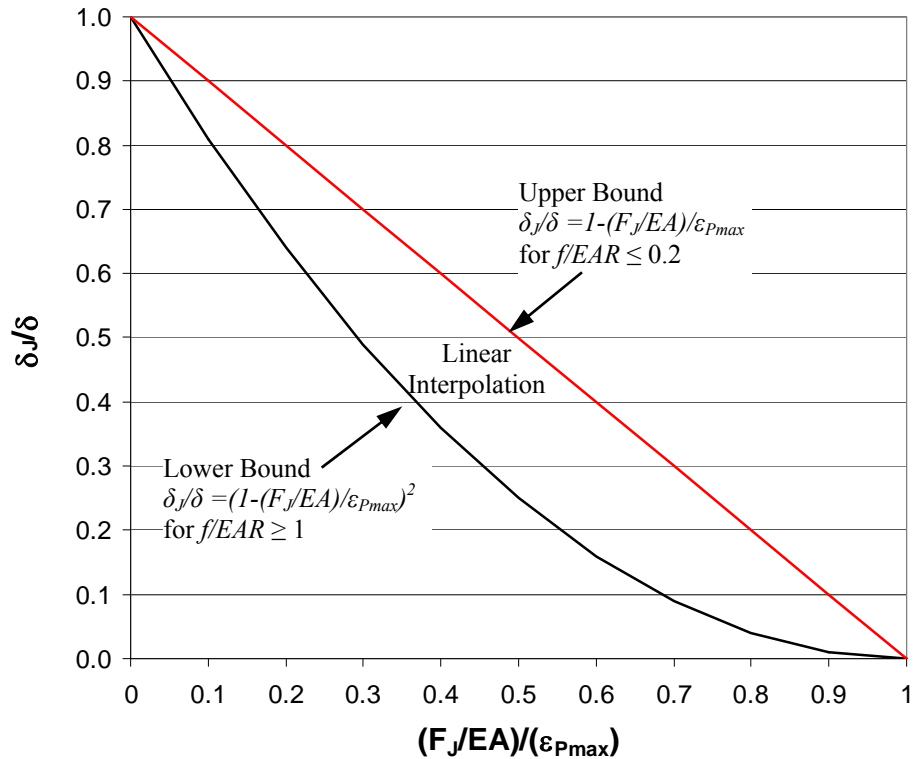
Figure 4.27 Reduction Curves for Engineering Usage

Combining the universal relationship provided in Figure 4.15 and the reduction curves in Figure 4.27, it is possible to estimate the joint displacement of virtually any pipeline with either brittle or ductile joints under the effects of seismic waves. When the CI pipeline in Section 4.4.2 is affected by a surface wave with $PGV = 30$ cm/sec, $C_{Ph} = 120$ m/sec, and $T = 3.5$ sec, the f/EAR value is 0.32. Using Figure 4.15, a δ/δ_0 of 0.48 can be obtained and δ_0 can be calculated as 33.42 cm based on the wave characteristics. For a brittle joint, the relative displacement can be calculated as 0.48*33.42 = 16 cm. For a ductile joint with capacity of $F_J = 275$ kN and pipeline axial stiffness, $EA = 2.89E+06$ kN, the maximum pipeline strain, ε_{Pmax}, can be calculated as 8.0E-04, and $(F_J/EA)/\varepsilon_{Pmax}$ can be calculated as 0.12, which leads to a reduction factor of 0.88 according to Figure 4.27. As such, the axial slip of the ductile

joint can be estimated as 0.88*16 = 14.1 cm, which is 3 percent larger than the finite element result, 13.7 cm.

Although the models developed above are intended for the analysis of seismic wave interactions with pipelines, they are also applicable to seismic wave interactions with other linear structures. For example, the models can be utilized to estimate the displacement at connections between subaqueous tunnels and shore facilities when subjected to near source strong motion. Recent work to retrofit the Bay Area Rapid Transit System has focused on the potential slip San Francisco Bay (Wu, et al., 2003). Concerns about relative joint displacement during seismic wave interaction, similar to those for pipelines, have a strong influence on the retrofitting requirements for this transportation lifeline.

CHAPTER 5

PIPE DAMAGE MODELING

5.1   INTRODUCTION

The flow and pressure conditions in a water supply system after earthquakes can be predicted using hydraulic network analysis with special treatment of negative pressures. To predict the flow and pressure conditions, pipeline damage, including leaks and breaks, needs to be added into the network, followed by the hydraulic simulation of the damaged system. Commercial hydraulic network analysis software packages are designed for undamaged systems. Currently, pipe breaks and leaks are not accounted for in these software packages. Previous researchers (e.g., Ballantyne, et al., 1990; Markov, et al., 1994; Hwang, et al., 1998) developed their own methods for simulating pipe damage in hydraulic network analysis.

This chapter presents methods for pipe damage simulation in hydraulic network analysis. It begins with a brief review of previous research on this subject, followed by the definition of pipe leaks and breaks. The hydraulic simulation of leaks and breaks are discussed thereafter, with special attention to leak simulation. The methodology of leak simulation and the verification of the methodology are discussed. A brief review of material properties, joint characteristics, and seismic damage mechanisms, is provided for various types of pipelines. A classification for leak scenarios is proposed and mathematical formulations are developed to determine the opening area of each leak scenario. Finally, the implementation of the pipeline break and leak models in association with Monte Carlo simulation is described.

135

5.2   PREVIOUS RESEARCH

In this section, previous work on modeling pipe leaks and breaks is briefly described under the first three subheadings that follow. The practical implication of the different models proposed for damaged pipelines is provided under the fourth subheading.

5.2.1   Ballantyne et al. Model

Ballantyne et al. (1990) classified pipe damage into leaks and breaks. They considered damage modes, such as joint looseness, circumferential cracks, and corrosion-related damage (pinholes and small blow-outs) as leaks. Longitudinal cracks, joint splits, and pipe ruptures were considered to be breaks. Based on their review of field data collected after previous earthquakes, Ballantyne et al. assumed that 85% of the damage to cast iron pipelines occurs as leaks and 15% occurs as breaks under transient ground deformation (TGD) effects. They also assumed that half the damage to cast iron pipes occurs as leaks and half occurs as breaks under permanent ground deformation (PGD) effects. Pipe damage was then divided into leaks and breaks according to these relative percentages.

In hydraulic network analyses performed by Ballantyne, et al. (1990), leaks and breaks were simulated with a fictitious pipeline connected with the damaged pipe on one end and with a fixed-grade node (an empty reservoir) on the other, representing free discharge to the surrounding soil. The length and roughness coefficient of the fictitious pipeline were fixed as 30 m (100 feet) and 120, respectively. The diameter of the fictitious pipeline was varied from 25 mm (1 in.) to 200 mm (8 in.) to simulate

breaks and various levels of leakage. The number of locations of pipeline damage was estimated using pipe fragility curves, relating repair rate (repairs per unit pipe length) to Modified Mercalli Intensity (MMI).

5.2.2   Hwang et al. Model

Hwang et al. (1998) modeled pipe damage as leaks and breaks following the same classification criteria proposed by Ballantyne et al. (1990). A damaged pipeline was modeled by adding a node (orifice node) at the middle of the pipeline, and the orifice area was determined as the summation of the break and leak areas in the pipeline. The opening area for a leak was taken as 3% of the pipe cross-sectional area, and the opening area for a break was taken as the entire pipe cross-sectional area. If the summation of the opening area was larger than the pipe cross-sectional area, the summation of opening area was taken as the pipe cross-sectional area. The discharge through the orifice created by the total opening area was determined by

$$Q = CA\sqrt{2gH} \tag{5.1}$$

where Q is the discharge from the orifice, C is an experimental coefficient with a value of 0.64, H is the water head at the orifice node, A is the total opening area, and g is the acceleration of gravity.

To implement this model in hydraulic network analyses, the number of leaks and breaks in each pipeline was estimated using Monte Carlo simulations with the assumption that pipe damage follows a Poisson process. The mean damage arrival rate was estimated on the basis of correlations with seismic hazard parameters, such as

peak ground velocity and permanent ground deformation. Hwang et al. assumed that, under TGD effects, 85% of the damage to cast iron pipes occurs as leaks and 15% occurs as breaks; and 96% of the damage to ductile iron pipes occurs as leaks and 4% occurs as breaks. For pipe damage induced by PGD, 50% occurs as breaks and 50% occurs as leaks for all types of pipelines. Damage was then classified as either leaks or breaks according to their relative percentages using Monte Carlo simulation.

5.2.3   Markov et al. Model

Researchers at Cornell University (Markov et al. 1994; Khater and Grigoriu, 1989) assumed that all pipeline damage occurred as breaks. To model a break, the original pipeline was disconnected completely and the two disconnected ends were open to the atmosphere. To implement this model in hydraulic network analyses, the damage states, broken or intact, of each pipeline was determined using Monte Carlo simulation by assuming that pipe breaks follow a Poisson process with a mean arrival rate, correlated with seismic hazard parameters.   One break was then added at the middle point of each damaged pipeline.

5.2.4   Discussions of the Three Models

Ballantyne et al. (1990) and Hwang et al. (1998) used similar models and assigned the same relative percentages to pipe breaks and leaks for cast iron pipelines. They modeled pipe breaks and leaks as an orifice in the pipe wall. A pipe break or leak is differentiated by the different size of the opening area. To consider the energy loss of water flow from the orifice to the surrounding soil, Ballantyne et al. used a fictitious pipeline with a certain length, roughness, and diameter, and attributed the

energy loss to the frictional loss along the fictitious pipeline. Hwang et al. used an orifice node and assumed that the energy loss is accounted for by minor loss. In real situations, the energy loss of water flow from an orifice in the pipe wall is due to flow turbulence created by the sudden expansion of water passing through the flow area of the orifice to an infinite area external to the pipe. This energy is one of the minor losses in hydraulic network analysis (Armando, 1987). From this point of view, the model provided by Hwang et al. is more consistent with reality. However, Hwang et al. did not justify the usage of the minor loss coefficient with a value of 0.64.

Ballantyne et al. and Hwang et al. simulated pipeline leaks and breaks, using the same model with different opening areas. The worst damage scenario was simulated by an orifice in the pipe wall with the same area as the pipe cross-sectional area. It is likely that complete separation or rupture of a trunk line will erode the surrounding soil, thus exposing the pipe opening to the atmosphere. Although the flow associated with some breaks in smaller diameter distribution pipelines (e.g. 100 to 150 mm in diameter) may be constrained by the surrounding soil, it is reasonable and only slightly conservative to assume that breaks under these conditions will be open to the atmosphere.

Ballantyne et al. and Hwang et al. summed all leak and break areas in the same pipeline and modeled the combined damage at one location in the pipeline. Water losses from both leaks and breaks are therefore affected by the location. For a long pipeline, the assumption that all breaks or leaks occur at one location may lead to significant errors. Such errors could be especially large for long trunk lines that do not connect to other pipelines for a long distance. The longest trunk line in the LADWP hydraulic network model is roughly 15 km.

Markov et al. modeled a pipe break by completely disconnecting the original pipeline and opening the broken ends to the atmosphere. This model provides a reasonable simulation for pipe breaks, but tends to overpredict slightly the water loss from the broken ends by ignoring energy loss from flow turbulence created by the sudden expansion of water passing through the flow area of the broken pipe end to an infinite area external to the pipe. Markov et al. did not provide models for pipeline leaks.

5.3 DEFINITIONS

To model a pipe leak and break properly, it is important to provide clear definitions for them. Following the seismic guidelines for water pipelines by the American Lifelines Alliance (2005), "a break is defined as the complete separation of a pipeline, such that no flow will pass between the two adjacent sections of the broken pipe; and a leak is defined as a small leak in a pipeline, such that water will continue to flow through the pipeline, albeit at some loss of pressure and flow rate being delivered, with some flow being lost through the leak". Leaks can include pin holes in pipe barrels, very minor joint separations on segmented pipelines, and very small splits in large diameter steel transmission pipelines. A pipe with a break loses its water transportation function totally, and a pipe with a leak loses its function partially.

5.4 PIPE LEAK SIMULATION

Previous earthquake damage data show that a majority of pipe damage occurs as leaks (Ballantyne et al., 1990). A leak is essentially an opening in the pipe wall or at a pipe joint, from which water is discharged into the surrounding soil with some

energy loss. Two key issues associated with pipe leak simulation are how to model the energy loss and how to decide the opening area.

5.4.1 Methodology

This section provides a description of the methodology for leak simulation used in hydraulic network analysis. The leak simulation model is developed from energy loss equations and validated using sprinkler data from the National Fire Protection Association (Puchovsky, 1999).

5.4.1.1 Theoretical Derivation

Figure 5.1 shows a longitudinal section of a pipeline which contains a leak with an orifice area A_1 in the pipe wall. Water flows from the left to right in the pipe with an internal pressure of p_1 and leaks into the surrounding soil through the orifice. The pressure, p_2, can be approximated as zero compared with the pipe internal pressure, p_1, which is typically from 0.14 Mpa to 1.4 Mpa (20 to 200 psi) above atmospheric levels. By ignoring the minor elevation difference between the pipe and the surrounding soil, the hydraulic head loss, Δh, from the leak can be calculated as

$$\Delta h = \frac{p_1 - p_2}{\gamma_w} = \frac{p_1}{\gamma_w} \tag{5.2}$$

where γ_w is the unit weight of water. The Δh from the leak is mainly attributed to the minor loss resulted from the sudden expansion of the flow cross-sectional area, which increases from A_1 of the orifice in the pipe wall to a substantially larger area, A_2,
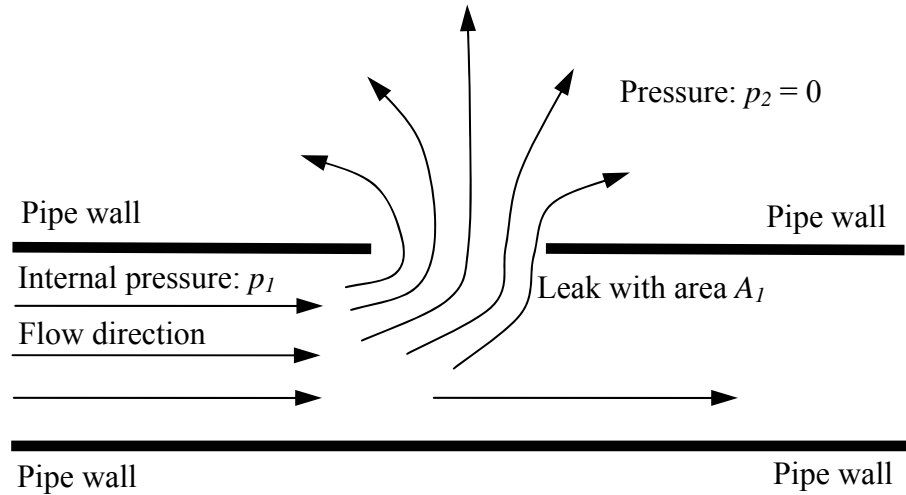
Figure 5.1 Longitudinal Section of a Leaking Pipe

external to the pipe, where water flow radiates three-dimensionally. The minor loss, Δh_m, in hydraulic network analysis is usually expressed as

$$\Delta h_m = \frac{K}{2gA_1^2}Q^2 \tag{5.3}$$

where K is the minor loss coefficient and g is the gravitational acceleration. The K value for the sudden expansion of the flow cross-sectional area is defined by the well-known Borda's formula in hydraulic engineering (Jeppson, 1976) as

$$K = (1 - \frac{A_1}{A_2})^2 \tag{5.4}$$

Because A_2 is substantially larger than A_1, A_1/A_2 approximates to zero, and hence, K approximates to 1.

Since Δh_m approximates to Δh, combining Equations 5.2 & 5.3 leads to

$$\frac{p_1}{\gamma_w} \approx \frac{K}{2gA_1^2}Q^2 = \frac{1}{2gA_1^2}Q^2 \tag{5.5}$$

Equation 5.5 can be rewritten as

$$Q = \left(\frac{2g}{K\gamma_w}\right)^{0.5} A_1 p_1^{0.5} = \left(\frac{2g}{\gamma_w}\right)^{0.5} A_1 p_1^{0.5} \tag{5.6}$$

Equation 5.6 is the governing equation for water loss from leaks. It shows that water loss from a leak is linearly proportional to the orifice area, A_1, and the square root of pipe internal pressure, p_1.

5.4.1.2 Validation Using Sprinkler Data

A pipe leak can be considered as analogous to a sprinkler used for fire protection, from which water discharge is governed by the following hydraulic equation (Puchovsky, 1999)

$$Q = C_D p^{0.5} \tag{5.7}$$

where Q is the flow rate through the sprinkler, C_D is the discharge coefficient, and p is the sprinkler operational pressure. The derivation procedure used in the leak model can be applied to the sprinkler, resulting in the same set of equations, i.e., Equations

5.2 to 5.6, where A_1 is the area of the sprinkler orifice and $p_1 = p$. Combining Equations 5.6 and 5.7 leads to

$$C_D = \left(\frac{2g}{K\gamma_w} \right)^{0.5} A_1 \tag{5.8}$$

To validate the model, a set of sprinkler data, which contains both the orifice size, A_1, and the corresponding discharge coefficient, C_D, are adopted to derive the relationship between C_D and A_1 and to compare the derived relationship with the theoretical relationship shown in Equation 5.8. Table 5.1 summarizes the data, which cover the typical range of sprinkler orifice areas used for fire protection purposes (Puchovsky, 1999). Figure 5.2 shows the comparison between the sprinkler data and model prediction. This figure shows that the theoretical predictions and real data follow closely spaced, parallel trends. The C_D of the real sprinklers is roughly 10% lower than the theoretical C_D. The lower C_D values of the real sprinklers are due to the inevitable frictional losses from the sprinklers since they have a short length; while the theoretical prediction ignores all frictional losses.

The consistency between the model predictions and sprinkler data provides confidence in applying the model to simulate pipe leaks, which might occur to a relatively larger orifice area than that of sprinklers used in fire protection. Figure 5.3 shows the relationship between the C_D and A_1 with A_1 values ranging from 0 to 12,500 mm^2 (20 in^2). When modeling pipe leaks after earthquakes, the orifice area is determined in accordance with leak characteristics. The estimates of leaking areas will be discussed in detail in Section 5.4.4.

Table 5.1 Relationship Between Sprinkler Discharge Coefficient and Orifice Size

(after Puchovsky, 1999)

Discharge Coefficient, C_D	Discharge Coefficient, C_D	Orifice Diameter		Orifice Area, A_I	
$[(L/s)/(kPa)^{0.5}]$	$[gpm/(psi)^{0.5}]$	mm	in.	mm^2	$in.^2$
0.03	1.4	6.40	0.25	32.17	0.05
0.05	1.9	8.00	0.31	50.27	0.08
0.07	2.8	9.50	0.37	70.88	0.11
0.10	4.2	11.00	0.43	95.03	0.15
0.14	5.6	12.70	0.50	126.68	0.20
0.19	8.0	13.50	0.53	143.14	0.22
0.27	11.2	15.90	0.63	198.56	0.31
0.34	14.0	19.00	0.75	283.53	0.44
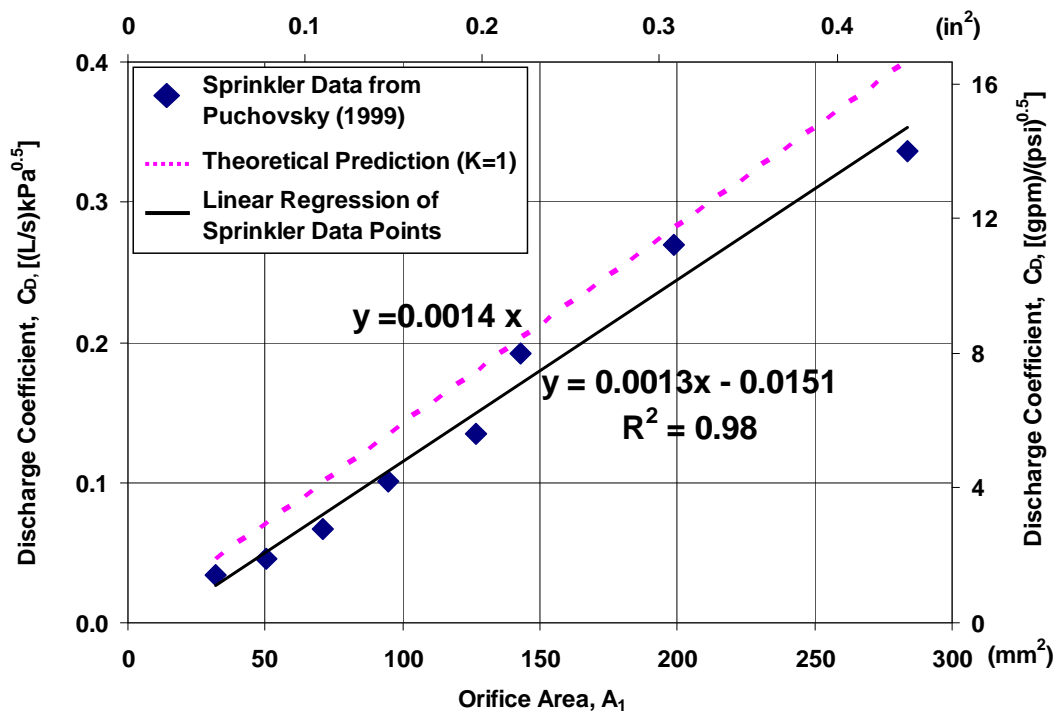
Figure 5.2 Comparison Between Model Predictions and Sprinkler Data

145
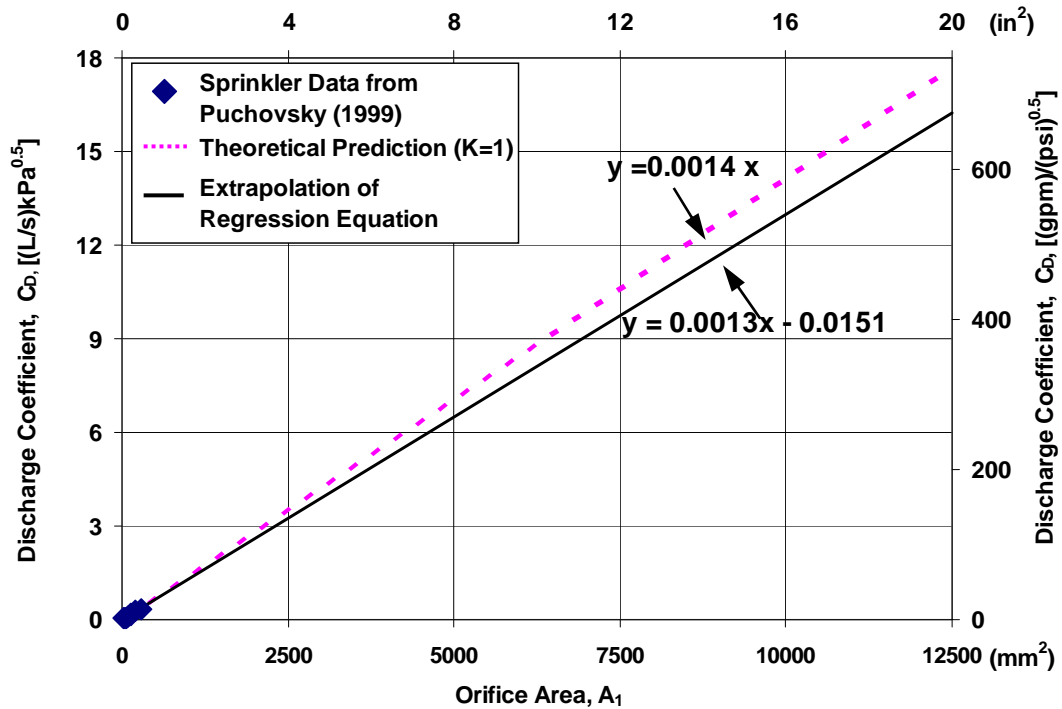
Figure 5.3 Relationship Between C_D and A_1 for Leakage

5.4.2 Hydraulic Model

In hydraulic simulations, a sprinkler is typically implemented as a fictitious pipe connected with a fixed grade node (an empty reservoir), which has the same elevation as the immediate upstream of the sprinkler. Following the model of the sprinkler, Figure 5.4 shows the pipe leak model in hydraulic network simulations, in which a fictitious pipe is added with one end connected to the leaking pipe and the other end open to the atmosphere, simulated as an empty reservoir with the same elevation as the leak location. A check valve is built into the fictitious pipe, allowing water to flow only from the leaking pipe to the reservoir but not the reverse. The roughness and minor loss coefficients of the fictitious pipe are taken as infinite and 1, respectively, such that all energy loss from the leak is related to the minor loss. The diameter of the fictitious pipe is determined by the leak orifice area.

146

Pipe Leaking
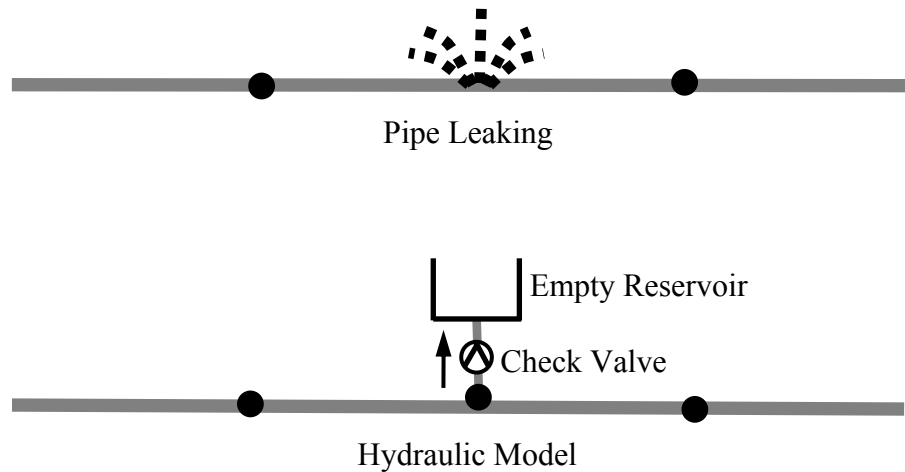
Hydraulic Model

Figure 5.4 Hydraulic Model for Pipe Leak

5.4.3   Pipe Property and Damage Mechanism Review

Using the leak model developed in the last section, a key input parameter is the leaking area. The leaking area depends on pipe material properties, joint characteristics, and earthquake damage mechanisms. A brief review of material properties, joint characteristics, and damage mechanisms is provided for five classes of pipelines, which are widely used in water supplies in North America.

5.4.3.1   Cast Iron Pipes

Cast iron pipelines have been used in the U.S. since 1817. A large portion of pipelines, especially distribution mains with relatively small diameters, in modern water supply systems are composed of cast iron. O'Rourke and Toprak (1997) reported that 72% of distribution mains, based on length in the LADWP system, are cast iron pipelines. A typical cast iron pipe segment is 3 (10) to 6 m (20 ft) long. Cast iron pipe segments are generally jointed together with bell-and-spigot lead caulked

147

joints. Figure 5.5 shows a section of cast iron pipe with a bell-and-spigot lead caulked joint, and Figure 5.6 provides a schematic drawing of the joint, which is typically constructed by: 1) packing oakum, which is a hemp yarn, into the joint; 2) pouring lead into the joint; and 3) ramming and tamping the lead into the joint with a caulking tool (O'Rourke and Trautmann, 1980).

The pullout capacity of a lead caulked joint is decided by two factors, the adhesive strength at the pipe/lead interface, C_a, and the depth of caulking lead, d_L. O'Rourke and Trautmann (1980) reported that the pullout capacity of the joint is much lower than the tensile capacity of the pipe material. The pullout capacity of the joint in terms of axial slip to cause leakage depends on how much movement can occur before the lead caulking loses its compressive seal. Based on the laboratory test data reported by Untrauer et al. (1970), between 25 to 50 mm (1 to 2 in.) of axial slip is a range that will result in significant leakage. After the slip capacity is exceeded, leaking may occur from the annular space between the bell and spigot.

Circumferential flexural failure in areas of ground curvature is another cause of damage to cast iron pipes due to the lack of ductility of pipe material and joints. Cast iron is considered to be a brittle material with a tensile strain capacity generally lower than 0.5 percent. For relatively small diameter pipelines, the pipe barrel is vulnerable to circumferential cracking due to flexure. O'Rourke and Pease (1992) reported that more than 80 % of damages to cast iron pipes with diameters ranging from 100 to 200 mm (4 to 8 in.) in the Marina District after the 1989 Loma Prieta earthquake was round cracks occurring in pipe barrels.

Figure 5.5 Cast Iron Pipe with Bell-and-Spigot Lead Caulked Joint

(after American Lifelines Alliance, 2005)
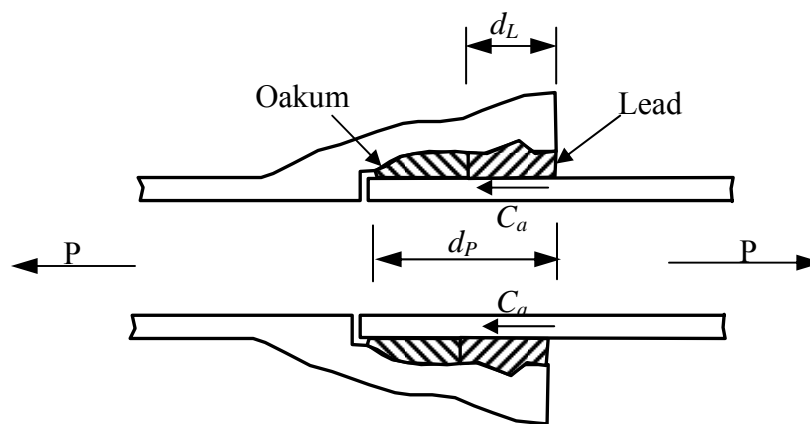
Figure 5.6 Schematic Drawing of Bell-and-Spigot Lead Caulked Joint Cross-Section

Corrosion is an important hazard for metal pipelines. The process of corrosion is complicated, and detailed descriptions can be found in the literature (e.g., AWWA, 1964; Thielsch, 1965). Typically, there are four types of corrosion that affect buried metal pipes, including galvanic, electrolytic, stress, and biochemical. Galvanic corrosion occurs when dissimilar metals are joined in an electric circuit in the presence of an electrolyte. Electrolytic corrosion occurs when a buried metal pipe serves as a return path for DC circuits used in transportation or other industries. It is a common practice with DC circuits to make use of the ground as a return path for current. A metal pipe buried underground has smaller resistance than the ground and may serve as the return path for the current, which results in corrosion to the metal pipe end where the current leaves it. Stress corrosion occurs in areas with points of concentrated stress adjacent to the areas of uniform stress, such as the area around rivets in riveted steel pipes, under conditions where an electrolyte is present. Biochemical corrosion results from chemical changes, which can be induced by microorganisms in soils surrounding the pipe or water inside the pipe.

Corrosion can occur either inside or outside a pipe and leave pinhole or local defects in the pipe wall. These defects are areas of reduced strength and ductility, and are potential locations of damage under seismic loading. One economic way to control corrosion is to provide protective coatings either internally or externally, or both, and to provide catholic protection.

Another damage mechanism for cast iron water supply pipelines is a longitudinal split of the pipe wall under the combined effects of seismic loading and high internal pressure. A longitudinal split may be initiated by deterioration or defects in the pipe wall created during metal fabrication or resulting from corrosion.

5.4.3.2 Ductile Iron Pipes

Ductile iron differs from cast iron in that its graphite is spheroidal or nodular instead of flakes. This results in greater strength, ductility and toughness. Figure 5.7 shows photos of the ductile iron pipe segments with bell-and-spigot push-on joints, which are the most commonly used joints for ductile iron pipelines. Figure 5.8 shows a schematic drawing of a push-on joint. Typically a rubber ring gasket is compressed during the insertion of the ring end into the bell end to form a water-tight seal at the joint. The insertion distance using manufacturer's common recommendations is roughly 25 mm (1 in.) for a pipe segment with a typical length of 5.3 m (16 ft).

The pullout resistance of a push-on joint is provided by the rubber gasket ring, and is very small. Furthermore, the rubber gasket ring tends to deteriorate with age. After more than 25 mm (1 in.) of axial pullout, the rubber gasket begins to lose its compressive seal and leaking starts to occur from the annular space between the bell and spigot ends. Therefore, ductile iron pipelines are vulnerable to pullout. In contrast to cast iron pipelines, which are vulnerable to circumferential flexural failure in areas of ground curvature, ductile iron pipelines can accommodate the ground deformation much better due to the ductility of its pipe material. Local loss of pipe wall and longitudinal crack can also occur in ductile iron pipelines for the same reasons as those for the cast iron pipelines.

5.4.3.3 Riveted Steel Pipes

Riveted steel pipelines are a class of pipeline in older sections of water supplies. They are no longer produced in the U.S. Figure 5.9 shows a photo of a

Figure 5.7 Ductile Iron Pipes with Bell-and-Spigot Push-On Joints

(after American Lifelines Alliance, 2005)
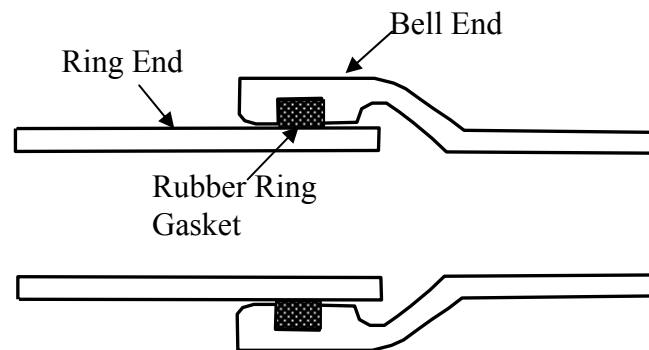
Figure 5.8 Schematic Drawing of Bell-and-Spigot Push-on Joint Cross-Section

riveted steel pipeline installed in 1925. Typically, riveted steel pipelines are made with the pipe section edges overlapped to form lap joints both longitudinally and circumferentially (Crocker, 1945). It is customary to use rivets of about the same material as the plate and to caulk the overlapping edges to obtain a water-tight joint. A common riveted steel pipeline has two rows of rivets for the longitudinal seam joint, but just one line of rivets for the circumferential joints (American Lifelines Alliance, 2005). Figures 5.10a and b show schematic drawings of the rivet connections along the pipe circumferential and longitudinal directions.

Repairs of riveted steel pipelines by the LADWP after the 1994 Northridge earthquake showed that seismic damage was often in the form of sheared rivets at circumferential and longitudinal seams. Rivets may be preferential locations for corrosion due to the stress concentration. Corrosion products are often visible around rivets at the external surfaces of old riveted steel pipelines. The shear failure of rivet connections may lead to leaking from the space between the inner and outer pipe plates. Similar to cast iron and ductile iron pipes, the local loss of pipe wall and longitudinal splits can also occur in riveted steel pipelines.

5.4.3.4 Jointed Concrete Cylinder Pipes

Jointed concrete cylinder pipes (JCCPs) are a particular class of pipelines used for water trunk and transmission facilities in North America. In this study the term JCCP is used to represent pipelines composed of reinforced concrete and steel cylinders that are coupled with mortared, rubber-gasket bell-and-spigot joints. As discussed by O'Rourke et al. (2004c), there are a variety of JCCPs, such as concrete cylinder pipe (CCP), bar wrapped concrete cylinder pipe (BWCCP), and prestressed

153

Figure 5.9 Riveted Steel Pipeline (after American Lifelines Alliance, 2005)
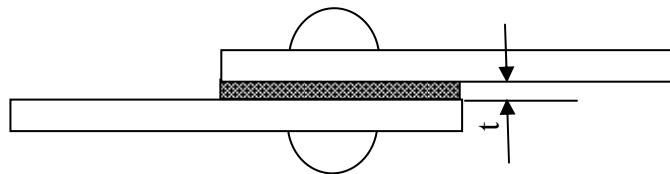
(a) Circumferential Rivet Connection
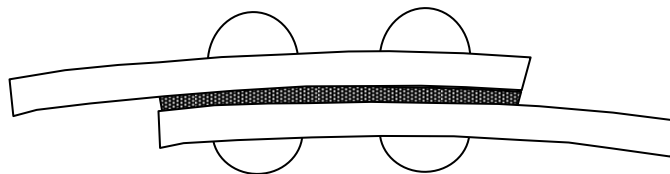
(b) Longitudinal Rivet Connection

Figure 5.10 Schematic Drawings of Rivet Connections

concrete cylinder pipe (PCCP). Figure 5.11 shows a JCCP damaged during the 1994 Northridge earthquake. Figure 5.12 shows a representative cross-section of a JCCP joint collected from the design and as-built drawings of JCCPs investigated as part of this study. More examples of JCCP joints can be found in the American Lifelines Alliance (2005).

All designs and methods of construction of JCCPs rely on a rubber-gasket bell-and-spigot connection. The rubber gasket is often 18 to 22 mm wide when compressed to form a water-tight seal. Cement mortar is poured in the field to seal the joint. The axial tensile capacity of the joint depends on the tensile strength of the poured mortar connection and pullout resistance of the gasket, both of which are relatively low. It is not uncommon for the mortar at JCCP joints to be cracked and separated as a result of forces induced during installation or in response to subsequent operational loads and movements in the field. O'Rourke et al. (2004a) summarized inspection results of the field joint conditions of the Bay Division Pipelines in San Francisco. They reported that roughly 2% of the JCCP joints were cracked and separated to varying extents, with a maximum separation of 20 mm (0.75 in.).

The pullout capacity of the joint in terms of axial slip to cause leakage depends on how much movement can occur before the rubber gasket loses its compressive seal. As discussed in Section 4.3.1, the axial pullout capacity of the joint can be evaluated using a probabilistic model. As a minimum, about 1 of every 10 joints cannot reliably accommodate more than 3-4 mm of axial slip. Given this level of tolerance, JCCP joints are sensitive to seismic loadings, which have the potential to induce leakage from the annular space between the bell ring and spigot. Field observations of damage to the JCCPs found that the majority of locations of damage occurred as joint annular
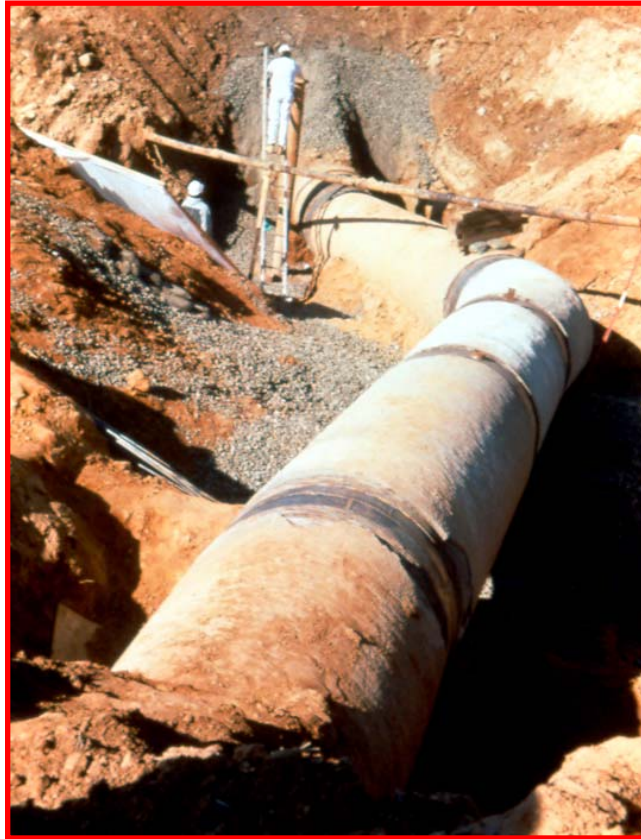
Figure 5.11 Photo of JCCP and Joints (Photo by Ballantyne)
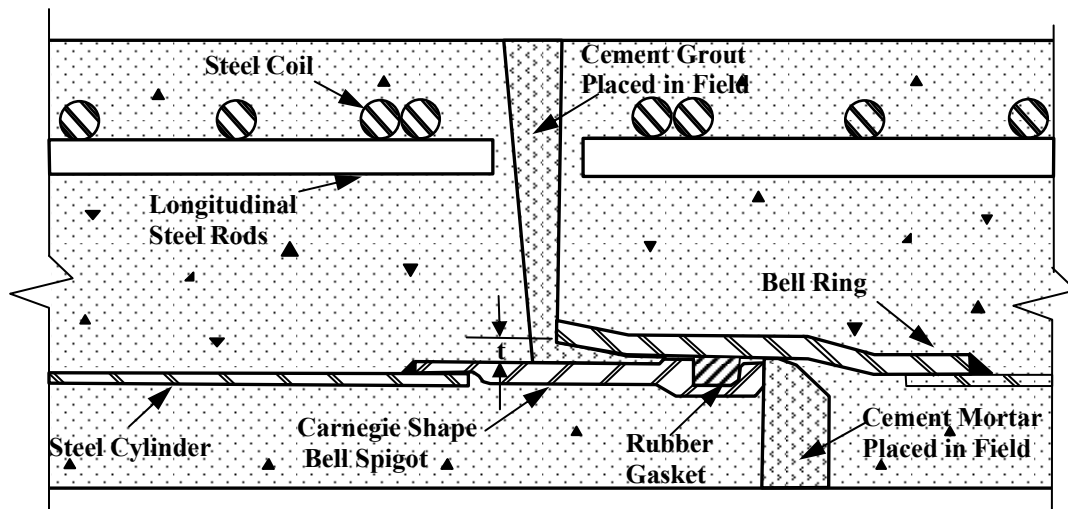
Figure 5.12 Schematic Drawing of JCCP Joint Cross-Section

disengagement (Ayala and O'Rourke, 1989). Since JCCPs are composites of reinforced concrete and steel pipe or thin steel cylinders, longitudinal and circumferential cracks in the pipe barrel will be infrequent.

5.4.3.5 Welded Steel Pipes

Steel pipes are used in many high-pressure water distribution systems in regions of high seismicity due to the favorable mechanical properties of steel, such as high strength, ability to yield or deflect under load, ability to bend without breaking, and resistance to shock. A common method of joining steel pipe segments is the welded slip joint, which is fabricated by inserting the straight end of one steel pipe section into the bell end of another, and joining the two sections with one or two circumferential fillet welds. Figure 5.13 shows a section of steel pipeline with a welded slip joint used for lab testing. Figure 5.14 provides a schematic drawing of a single circumferential fillet weld. A welded steel pipeline is typically ductile and capable of mobilizing large strain associated with significant tensile yielding before rupture.

The principle failure mode of a welded steel pipeline is local buckling under compressive forces (Jones, et al., 2004). As illustrated in Figure 5.14 b, local buckling typically occurs at the location of maximum curvature in the bell casing of a welded slip joint in the form of wrinkling and outward deformation. The compressive force to buckle the bell casing can be substantially lower than that required to buckle and fail a straight pipe section (Eidinger, 1999). Excessive buckling will tear the pipe barrel and cause leakage. As reported by Lund and Cooper (1995), a local tear occurred in a 3050-mm(120-in.)-diameter welded steel pipeline during the 1994 Northridge

Figure 5.13 Steel Pipe with Welded Slip Joint
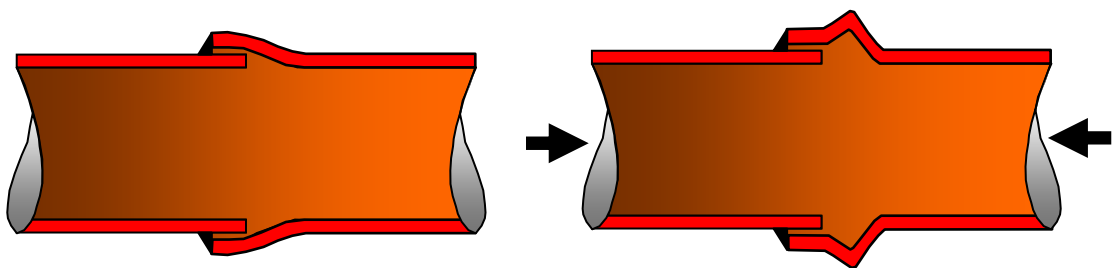
a) Before Buckling   b) After Buckling

Figure 5.14 Schematic Drawing of Welded Slip Joint Cross-Sections

earthquake, and resulted in a 1.5-m (60-in) circumferential split in the curved portion of the bell casing of the welded slip joint. The damaged welded steel pipeline and the removed part of the pipe wall are shown in Figures 5.15 and 5.16, respectively.

Modern steel pipelines are generally well protected by coatings so that corrosion is unlikely to occur. Due to the ductility and high strength of steel and the welded joints, longitudinal cracks and joint looseness are unlikely to occur.

5.4.4   Leak Classification

As discussed in the last section, pipelines can have various damage states under earthquake loading effects. To develop a rational basis for leakage simulation, this study classifies leaks into five scenarios, based on different damage states, and recommends simulating leakage as a function of pipe diameter.

5.4.4.1   Annular Disengagement

The first leak scenario is annular disengagement, which refers to joint looseness of segmented pipelines resulting from joint axial pullout movement during seismic loading. A schematic drawing of annular disengagement occurring at a bell-and-spigot joint is shown in Figure 5.17. This leak scenario may occur in cast iron, ductile iron, jointed concrete cylinder, and riveted steel pipelines. For cast iron, ductile iron, and jointed concrete pipelines, annular disengagement results from the relative pullout movement of the joint bell and spigot ends, and the subsequent loss of gasket compressive seal. For riveted steel pipelines, annular disengagement occurs due to the relative pullout movement of the inner and outer pipe section edges and the

159
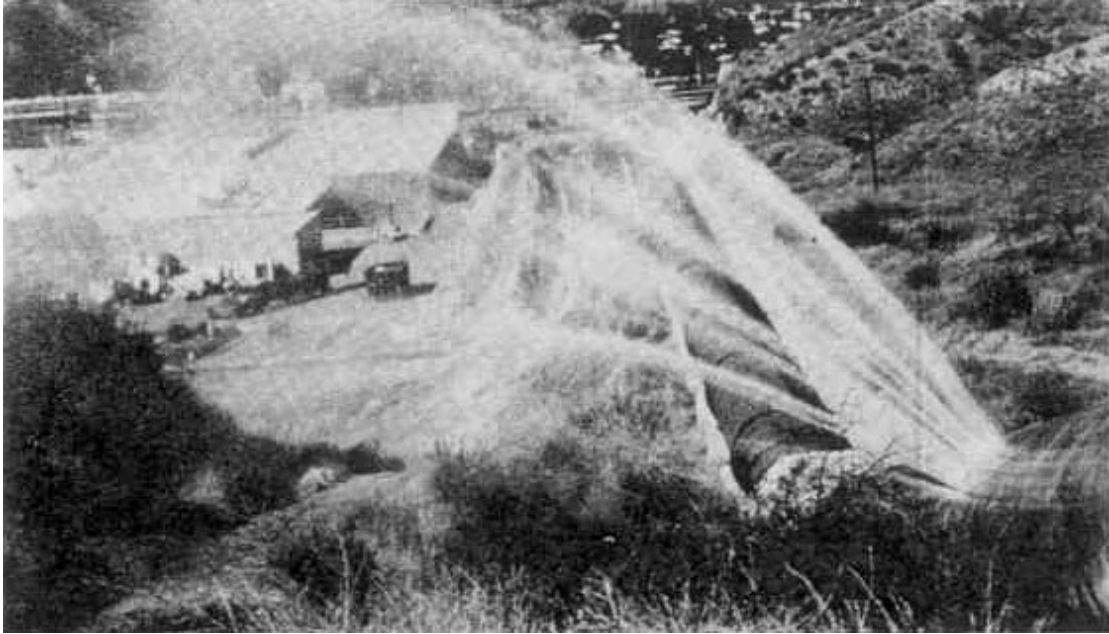
Figure 5.15 Photo Showing Pipe Leak in a 3050-mm-Diameter Welded Steel Pipe

(after Lund and Cooper, 1995)
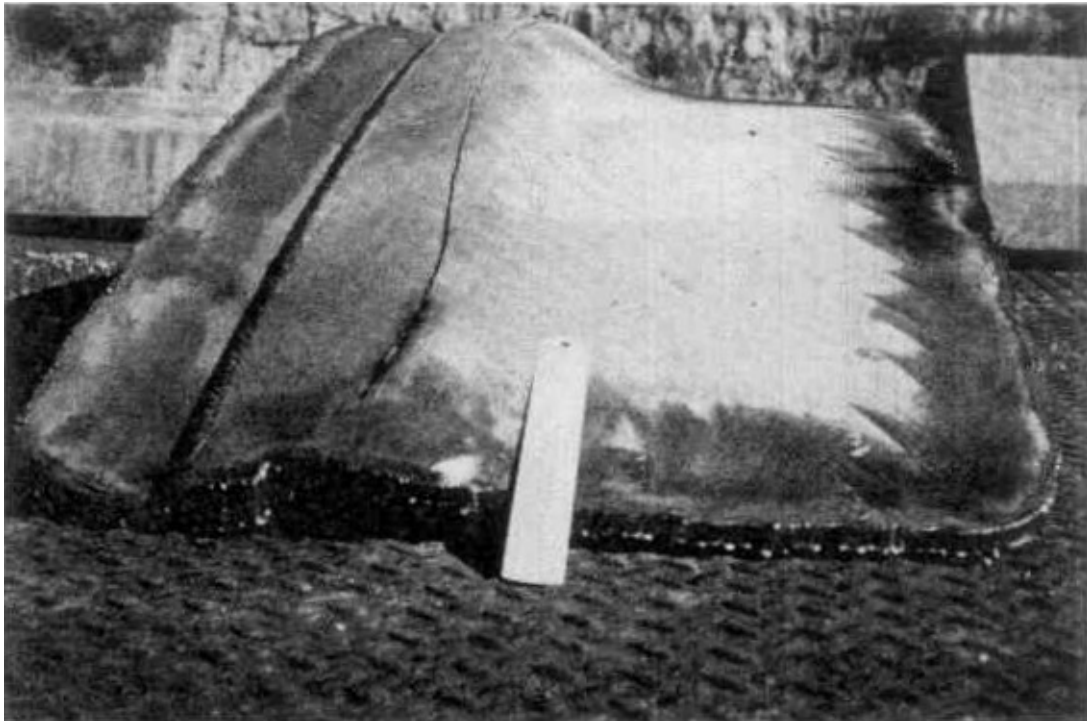
Figure 5.16 Photo Showing Removed Section of Pipe Wall with a 1.5-m-Split at

Welded Slip Joint (after Lund and Cooper, 1995)
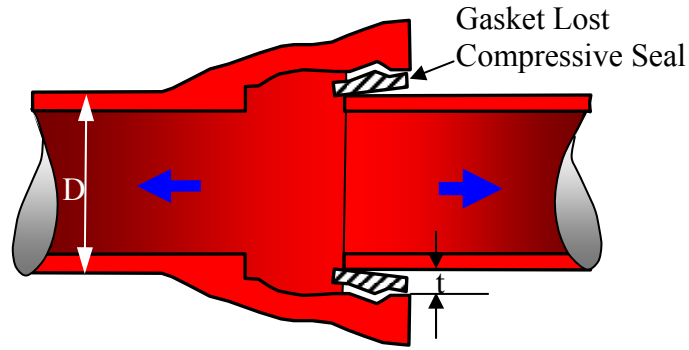
Figure 5.17 Schematic Drawing of Annular Disengagement at Bell-and-Spigot Joint

subsequent loss of the compressive seal of caulking material. The opening from annular disengagement occurs in the circumferential direction, and its area is determined by the joint configuration, relative pullout movement, and condition of the gasket seal or caulking material. To estimate the opening area of an annular disengagement, the opening area, called equivalent orifice area (EOA) in this study, is correlated to an area index, the maximum possible annular area, and calculated as

$$A = k \times A_{max} \qquad (5.9)$$

where A is the EOA, A_{max} is the maximum annular area, and k is a constant. The A_{max} is decided by the configuration of the joint and can be estimated as

$$A_{max} \approx tD\pi \qquad (5.10)$$

where D is the pipeline diameter and t is the thickness of maximum possible annular space.

161

Substituting Equation 5.10 into 5.9 results in

$$A = k \times A_{max} = tkD\pi \qquad (5.11)$$

Since a leak is modeled as a fictitious pipeline in hydraulic network analysis, the orifice needs to be converted into a pipe with a cross-sectional area equal to the EOA. The diameter of the fictitious pipe, called equivalent orifice diameter (EOD) in this study, can be calculated as

$$d = \sqrt{4A/\pi} = 2\sqrt{tkD} \qquad (5.12)$$

The maximum possible annular space of the bell-and-spigot gasket joints used in cast iron and ductile iron pipelines can be approximated as the thickness of the gasket, which ranges roughly from 10 (0.4) to 16 mm (0.65 in.) (Crocker, 1945). For the bell-and-spigot joints used in JCCPs, the maximum possible space for leaking can be taken as the maximum space between the flared end of the bell and spigot, indicated as t in Figure 5.12. This space is roughly 8 (0.3) to 10 mm (0.4 in.) according to the as-built and design drawings used in this study (O'Rourke, et al., 2004a). The maximum annular space of a riveted joint connection can be taken as the thickness of caulking material, indicated as t in Figure 5.10. Due to the lack of data on the caulking material thickness, it is assumed that the caulking material is similar in thickness to that of the pipe wall. By reviewing the characteristics of riveted steel pipelines with diameters ranging from 100 (4) to 1829 mm (72 in.) in the LADWP system, it was found that their wall thickness varies from 3.5 (0.14) to 14 mm (0.56 in.) with an average value of 7 mm (0.25 in.).

Because the range of the *t* values for the four types of pipelines, to which annular disengagement may occur, is relatively small, to simplify simulations, a default value of 10 mm (0.4 in.), is proposed for the *t* value. The 10 mm represents a rough average of the annular space, *t*, of the four types of pipelines. As for the ratio of the real leak area to the maximum possible leak area, a default value of 0.3 is proposed on the basis of field observations (O'Rourke, 2005) from previous earthquakes.

5.4.4.2 Round Crack

The second leak scenario is a round crack, which refers to the circumferential cracking of pipe barrel or joint under the effects of bending or the combination of bending and tensile forces. A schematic drawing of a round crack is shown in Figure 5.18. Round cracks occur in pipes composed of brittle material and joints, such as cast iron pipes with lead caulked joints. The EOA is decided by the opening angle of the crack and pipe diameter, and can be calculated as

$$A = 0.5\pi D \times (\theta D) = 0.5\pi\theta D^2 \tag{5.13}$$

where θ is the open angle of the crack and D is the pipe diameter.

The EOD of a round crack can be calculated as

$$d = \sqrt{4A/\pi} = \sqrt{4(0.5\pi\theta D^2)/\pi} = \sqrt{2\theta}D \tag{5.14}$$

Based on field observations (O'Rourke, 2005), a default value of 0.5° is proposed for the opening angle in this study.
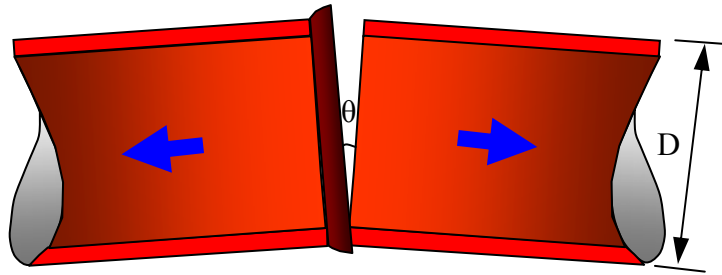
Figure 5.18 Schematic Drawing of Round Crack

5.4.4.3   Longitudinal Crack

The third leak scenario is a longitudinal crack, which refers to the cracking of the pipe barrel or seam along the pipe longitudinal direction caused by the external loading and/or high internal pressures during earthquakes. A schematic drawing of a longitudinal crack is shown in Figure 5.19. The longitudinal cracking may be initiated by some micro cracks or local defects in the pipe wall. Metal pipes, including cast iron, ductile iron, and riveted steel are vulnerable to longitudinal cracking. JCCPs are unlikely to be cracked longitudinally due to reinforcing steel and the presence of steel pipe or thin steel casings. Longitudinal cracking occurs infrequently in steel water pipes because of the high tensile strength and ductility of the steel.

The EOA of a longitudinal crack can be calculated as

$$A = L \times W \tag{5.15}$$

where L and W are the length and width of the crack, respectively. The length, L, is in the pipe axial direction and can be taken as the length of a pipe section. The width, W, is in the pipe circumferential direction and can be estimated as a function of the
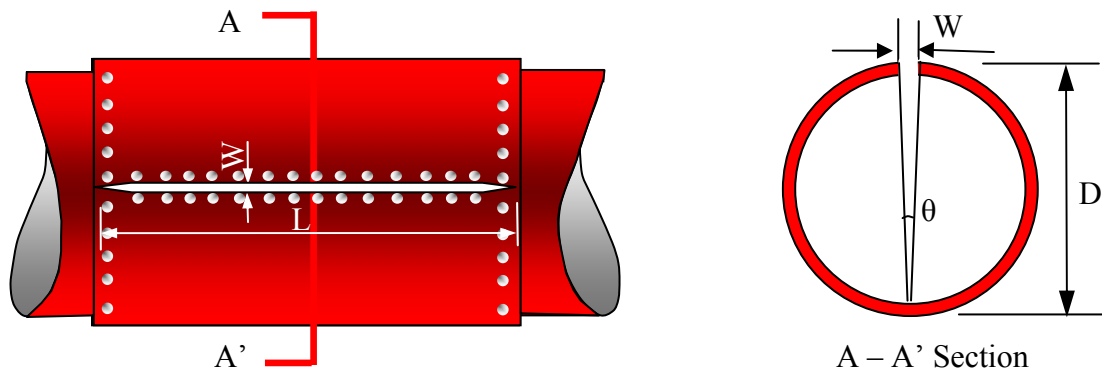
Figure 5.19 Schematic Drawing of Longitudinal Crack

opening angle, θ, of the crack and pipe diameter, D. The width, W, can be calculated as

$$W = D\theta \tag{5.16}$$

Substituting Equation 5.16 into Equation 5.15 results in

$$A = W \times L = LD\theta \tag{5.17}$$

The EOD of a longitudinal crack can be calculated as

$$d = \sqrt{4A/\pi} = 2\sqrt{LD\theta/\pi} \tag{5.18}$$

The length of a pipe section varies from pipe to pipe, depending mainly on pipe materials. Thirteen meters (40 ft) provides a reasonable, but conservative estimate of the length of metal pipes. The opening angle of the longitudinal crack is estimated as 0.1° from field observations (O'Rourke, 2005).

165

5.4.4.4 Local Loss of Pipe Wall

The fourth leak scenario is the local loss of pipe wall. This leak scenario is caused by the loss of a small portion of pipe wall, which deteriorates by corrosion, under the earthquake loading effects. A schematic drawing of a local loss of pipe wall is shown in Figure 5.20. The EOA of a local loss of pipe wall can be calculated as

$$A = L \times W \tag{5.19}$$

where L and W are the length and width of the orifice. The length, L, is along the pipe longitudinal direction and can be estimated as a ratio, k_1, of pipe diameter as

$$L = k_1 \times D \tag{5.20}$$

The width, W, is along the pipe circumferential direction and can be estimated as a ratio, k_2, of the pipe circumferential length to yield

$$W = k_2 \pi D \tag{5.21}$$

Substituting Equations 5.20 and 5.21 into 5.19 results in

$$A = \pi k_1 k_2 D^2 \tag{5.22}$$

The EOD of a local loss of pipe wall can be calculated as
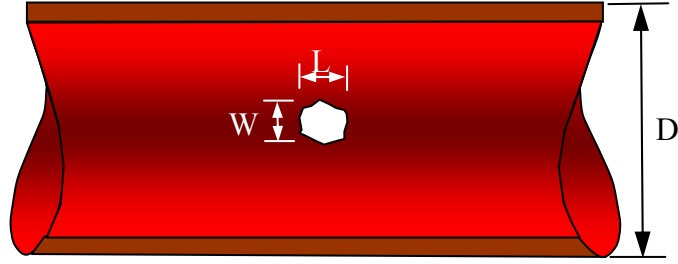
Figure 5.20 Schematic Drawing of Local Loss of Pipe Wall

$$d = \sqrt{4A/\pi} = \sqrt{4(\pi k_1 k_2 D^2)/\pi} = 2\sqrt{k_1 k_2}\,D \qquad (5.23)$$

The loss of pipe wall due to corrosion is usually small. Five percent is proposed as a rough estimate of each of the parameters, k_1 and k_2, in this study.

5.4.4.5   Local Tear of Pipe Wall

The fifth leak scenario is a local tear of a pipe wall, which typically occurs as a rupture in the bell casing of wrinkled welded slip joints induced by compressive forces. A schematic drawing of a local tear of a steel pipeline with welded slip joint is shown in Figure 5.21.

The EOA of a local tear of pipe wall can be calculated as

$$A = L \times W \qquad (5.24)$$

in which, L and W are the length and width of the split, respectively. The length, L, is along the pipe circumferential direction and can be estimated with a ratio, k, of the pipe circumferential length,
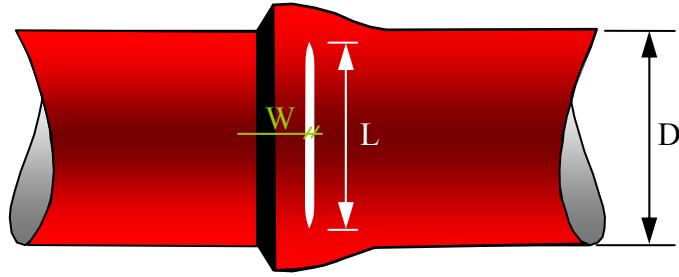
Figure 5.21 Schematic Drawing of Local Tear of Pipe Wall

$$L = k\pi D \tag{5.25}$$

Substituting Equation 5.25 into Equation 5.24 results in

$$A = W \times L = k\pi DW \tag{5.26}$$

The EOD of a local tear of pipe wall can be calculated as

$$d = \sqrt{4A/\pi} = \sqrt{4(k\pi D * W)/\pi} = 2\sqrt{kWD} \tag{5.27}$$

Damage to the 3050-mm(120-in.)-diameter welded steel pipeline during the 1994 Northridge earthquake, shown in Figures 5.15 and 5.16, is a local tear of pipe wall, which has a length of roughly 20% of the pipe circumferential length and a width of 12 mm (0.5 in.). The value for length of a local tear is proposed as 30% of the pipe circumferential length, and the width is assumed to be 12 mm (0.5 in.) in this study.

It is noted that the EOA is a function of pipe diameter for each leak scenario. As discussed in Section 5.4.1, water loss from a leak is a linear function of the orifice area. As such, the water loss is also a function of the pipe diameter. Figure 5.22
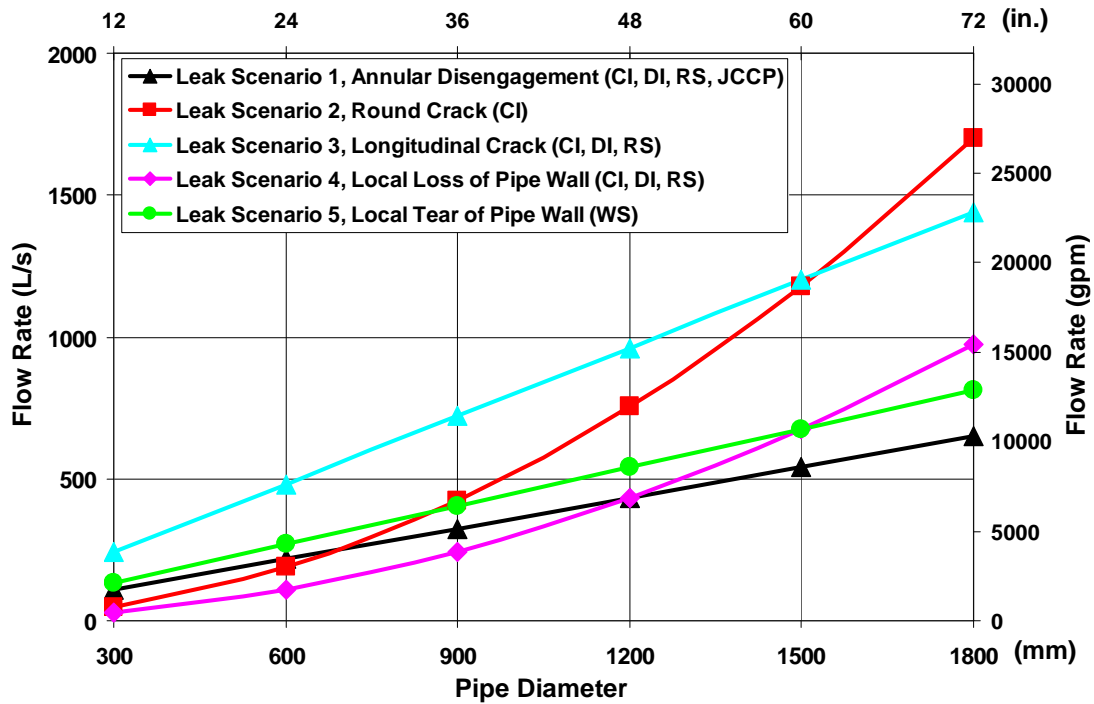
Figure 5.22 Water Loss for Five Leak Scenarios as a Function of Pipe Diameter

shows the relationship between water loss and pipe diameter for the five leak scenarios with an assumed pipe internal pressure of 0.69 MPa (100 psi), a typical value of pipe internal pressure in water supplies. From this figure, water losses increase in proportion to pipe size for each leak scenario, and significant differences exist among the leak scenarios. For large diameter pipelines, the round and longitudinal cracks are two potentially large leaks, which result in most water losses, and leakage associated with the other three scenarios is smaller.

5.4.5 Probability of Leak Scenarios

Since each type of pipeline can have multiple types of leaks, the relative likelihood of each leak scenario has to be estimated for each type of pipeline to model

pipe leaks using Monte Carlo simulation. Based on pipeline material and joint properties, as well as limited field data, a probability table shown in Table 5.2 is proposed for the five leak scenarios associated with various types of pipelines.

Table 5.2 shows that for segmented pipelines, such as cast iron, ductile iron, riveted steel, and jointed concrete pipes, more weight is placed on the leak scenarios associated with joint looseness or separation, and less weight is placed on longitudinal cracks, local tear of pipe wall, and corrosion-related leaks. This is consistent with field observation after earthquakes that joints are the most vulnerable parts of segmented pipelines. For CI pipelines, a round crack has slightly more weight than annular disengagement. The riveted steel pipelines are more vulnerable to annular disengagement than longitudinal cracking because there is only one line of rivets along the pipe circumferential seam; in contrast, there are two rows of rivets along the longitudinal seam.

It should be noted that the only leak scenario for welded steel pipelines is the local tear of pipe wall resulting from compressive buckling. The majority of locations of local buckling, although they need to be repaired after earthquakes, are not severe enough to tear the pipe wall and cause leakage. A conservative estimate adopted in this work is that 80% of repairs from local buckling would not cause leakage, and 20% of repairs would cause leakage. It is necessary, therefore, to discount the repair rate to 20% when using the repair rate to estimate the number of leaks for steel pipeline performance simulation after earthquakes. As more field data become available, the probabilities shown in Table 5.2 can be refined.

170

Table 5.2 Probability of Leak Scenarios for Different Types of Pipelines

Pipe Material	Scenario 1 Annular Disengagement	Scenario 2 Round Crack	Scenario 3 Longitudinal Crack	Scenario 4 Local Loss of Pipe Wall	Scenario 5 Local Tear of Pipe Wall
Cast Iron	0.3	0.5	0.1	0.1	N/A[1]
Ductile Iron	0.8	N/A[1]	0.1	0.1	N/A[1]
Riveted Steel	0.6	N/A[1]	0.3	0.1	N/A[1]
Welded Steel	N/A[1]	N/A[1]	N/A[1]	N/A[1]	1.0
Jointed Concrete	1.0	N/A[1]	N/A[1]	N/A[1]	N/A[1]

1: Not Applicable

5.5   PIPE BREAK SIMULATION

Following the definition of pipe breaks used in this study, a break is a complete disconnection of the original pipeline. Water can flow from the two broken ends into the surrounding soil. Figure 5.23 shows the hydraulic model of a pipe break, in which the original pipeline is disconnected at the location of the break, and each of the broken ends is open to the atmosphere, which is simulated by an empty reservoir. Similar to the simulation technique for a pipe leak, a minor loss coefficient of 1 and a check valve are added to each broken end to represent the energy loss and to prevent water from flowing back into the broken pipeline.

5.6   IMPLEMENTATION OF PIPE DAMAGE MODELS

To simulate the earthquake performance of a water supply system, pipe damage, including breaks and leaks, needs to be added in the network. Hydraulic
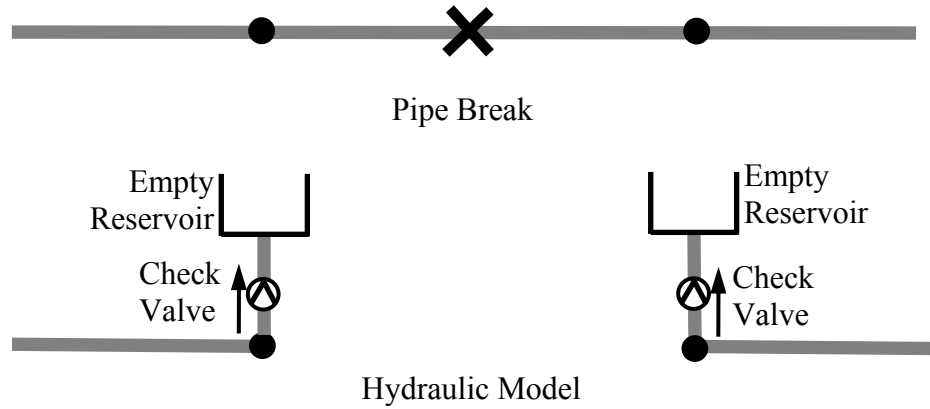
Figure 5.23 Hydraulic Model for Pipe Break

simulation is then performed on the damaged network to predict the flow and pressure distributions. The pipeline break and leak models can be implemented into a hydraulic network both deterministically and probabilistically.

5.6.1 Deterministic Implementation

The deterministic implementation specifies the number and location of leaks and breaks, and the orifice area of each leak, occurring in a pipeline network. Pipe leaks and breaks are then added in the network using the models shown in Figures 5.4 and 5.23, respectively. The deterministic implementation can be used to simulate the performance of a water supply system under a specific damage scenario.

5.6.2 Probabilistic Implementation

The probabilistic implementation generates randomly distributed pipeline breaks and leaks in the system according to pipeline repair rate, RR, length, L, and the conditional probability of pipe break, P_{bk}, given that damage occurs. In addition, the

probabilistic implementation determines the type of each leak probabilistically. The probabilistic implementation includes three steps: generating pipe damage, deciding on damage states (leak or break), and determining leak type.

5.6.2.1 Generating Pipe Damage

To generate the locations of pipe damage probabilistically, it is assumed that pipe damage follows a Poisson process with a mean arrival rate equal to repair rate, *RR*. The repair rate is correlated with the seismic hazard parameters, such as peak ground velocity (PGV) and permanent ground deformation (PGD).

For a Poisson process with a mean arrival rate *RR*, let L_1 be the first location of damage, which is measured from the upstream node of the pipeline along its longitudinal direction. Let L_k be the distance between the $(k-1)^{th}$ and k^{th} locations of damage. The $\{L_1, L_2, \cdots, L_k, \cdots\}$ is called the sequence of interarrival distances in Poisson processes (Sheldon, 2000). The actual distance of the kth location of damage measured from the pipe upstream node is the cumulative distance from L_1 to L_k. For instance, if $L_1 = 0.1L$ and $L_2 = 0.5L$, where *L* is the length of the original pipeline, then the first location of damage occurs at 0.1 time of pipe length measured from the pipe upstream node, and the second location of damage occurs at $0.1 + 0.5 = 0.6$ time of pipe length.

The L_1, L_2, $\cdots$, L_k can be simulated as independent exponential random variables with a mean equal to $1/RR$ (Sheldon, 2000) and generated using the Monte Carlo simulation algorithm

$$L_k = -\frac{1}{RR}\ln(1 - u_1) \tag{5.28}$$

where u_1 is a random variable which is uniformly distributed between 0 and 1. By generating the interarrival distance L_k repeatedly until the cumulative length exceeds the pipe length, L, it is able to determine the locations of damage in the pipeline. Figure 5.24 provides an illustration of the pipe damage generation. In this example, three locations of damage are generated at A, B and C, respectively, in the pipeline, because the cumulative length of the fourth location of damage exceeds the pipe length.

5.6.2.2   Deciding on Damage State

After generating pipe damage for each location of damage, a uniformly distributed random number μ_2 over (0, 1) is generated and compared with the conditional probability of pipe break, P_{bk}, given that damage occurs. The damage is treated as a break if μ_2 exceeds P_{bk}, and a leak otherwise.

5.6.2.3   Determining Leak Type

The third step determines the type of each leak probabilistically and calculates the orifice area of each leak using the equations developed in Section 5.4.4. The probabilities of each type of leak, corresponding to various types of pipeline, are listed in Table 5.2. To determine the type of each leak, a uniformly distributed random number, μ_3, over (0, 1) is generated and compared with the cumulative probability of the leak types associated with the pipeline. For example, the probability that a leak in

L_1, L_2, L_3, and L_4 are Interarrival Lengths
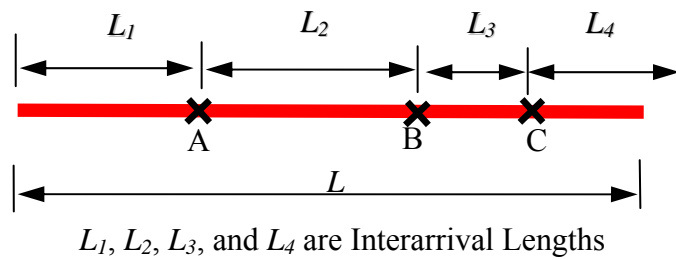
Figure 5.24 Poisson Process for Pipe Damage Generation

a cast iron pipeline is an annular disengagement is 0.3, round crack is 0.5, longitudinal crack is 0.1, and local loss of pipe wall is 0.1. The leak is classified as an annular disengagement if the uniformly distributed random number is within the range between 0 and 0.3; round crack if within the range between 0.3 and 0.8, longitudinal crack if within the range between 0.8 and 0.9, and local loss of pipe wall if within the range between 0.9 and 1.0. After deciding on the leak scenario, the EOA and EOD can be calculated for each leak.

`

CHAPTER 6

MULTI-SCALE TECHNIQUE FOR WATER SUPPLY SYSTEM MODELING

6.1   INTRODUCTION

As described in Chapter 3, most previous simulations of the earthquake performance of water supply systems have either focused on small systems, such as the San Francisco Auxiliary Water Supply System (Khater and Grigoriu, 1989; Markov et al., 1994), or modeled larger systems by representing only the largest diameter pipelines (Ballantyne et al., 1990).

Khater and Waisman (1999) proposed an approach for simulating a large water supply system. In their approach, the system response is simulated using a simplified hydraulic network model that only includes large diameter pipelines and replaces small diameter pipelines with demand nodes. They also performed hydraulic analyses that reflected the earthquake-induced breaks in small diameter pipelines using Monte Carlo simulation procedures. The hydraulic analysis results were then applied to assess system serviceability with the simplified hydraulic network model and associated demands.

This chapter describes a multi-scale technique for modeling large water supply systems through application to the LADWP water supply system. The technique uses a system-wide trunk line model, which includes large diameter trunk lines, and

replaces small diameter distribution lines with demand nodes. The earthquake demands at nodes in the trunk system are simulated by means of fragility curves relating demand to repair rate in local distribution networks. The repair rate is correlated with seismic hazard parameters, such as peak ground velocity and permanent ground deformation. The fragility curves are developed on the basis of distribution network simulations.

Following the introduction, the multi-scale modeling technique is explained with a simple example in Section 6.2. Section 6.3 provides a description of the LADWP water supply system, including the trunk and distribution network models used in this study. Section 6.4 describes the LADWP distribution network simulations, which provide fragility curves for assessing earthquake demands at nodes in the trunk system. Monte Carlo simulation procedures and results are presented. Fragility curves are developed based on the Monte Carlo simulation results. The fragility curves are then tested by an independent distribution network. Two appendices, Appendices A and B, showing the details of the LADWP distribution network models and the Monte Carlo simulation results, are presented at the end of this report.

6.2 MULTI-SCALE MODELING TECHNIQUE

Water supply systems are characterized by broad coverage and a high level of detail. The broad coverage is associated with large service area. The high level of detail is related to the large amount of different pipelines and facilities in the system. A hydraulic network model, which models both broad coverage and component details, will be difficult to manage and troubleshoot. One technique for simulating a complex system is to decouple various parts of the system, apply models with appropriate

levels of complexity to each part, and integrate the decoupled analyses to show system performance.

This decoupling technique is illustrated using the simple water supply system shown in Figure 6.1, in which water flows from the reservoir R through large diameter pipelines RO, OA, and AB, and is distributed in local communities a and b through small diameter pipelines. All demand nodes in the system are shown as small black dots. The large diameter pipelines in the water supply system are trunk lines that serve as the backbone of the system by transporting water from sources to local areas. In contrast, small diameter pipelines are distribution lines, which receive water from trunk lines and distribute it to customers.

Figure 6.2 shows the multi-scale models for the system, which is decoupled into a trunk line system and two distribution systems. In the trunk line system, distribution networks a and b are replaced with demand nodes RA and RB. The demands at nodes RA and RB are aggregated demands from local distribution networks a and b, respectively. The trunk line model has broad coverage but with reduced level of detail. In the distribution networks a and b, water sources from the trunk lines are modeled as virtual reservoirs VRA and VRB, which have the same hydraulic grades as those at locations A and B in the original system, respectively. These distribution models have a high level of detail. Using multi-scale modeling, such as shown in Figure 6.2, a complex water supply system can be decoupled into several systems, which have manageable complexity.

In general, a trunk line model can provide an overview of system response, but with reduced local resolution. A trunk line model is potentially well suited for

179
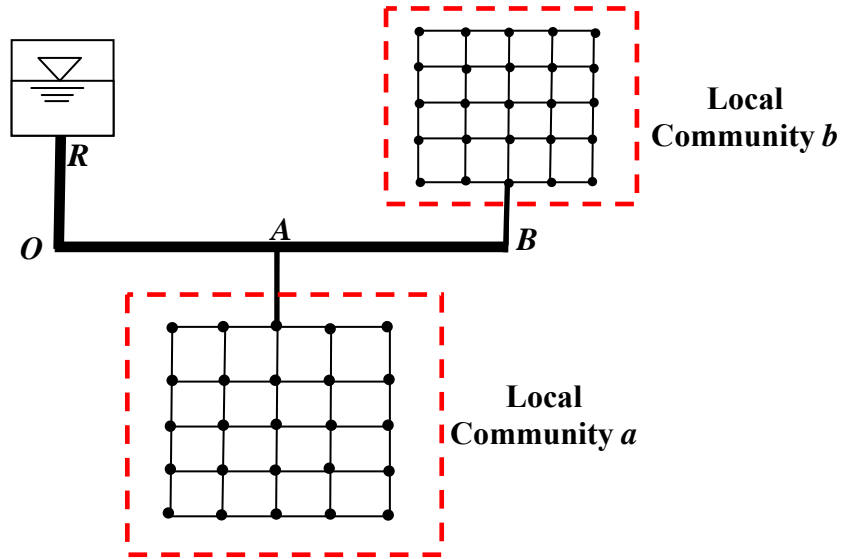
Figure 6.1 Example of a Simple Water Supply System
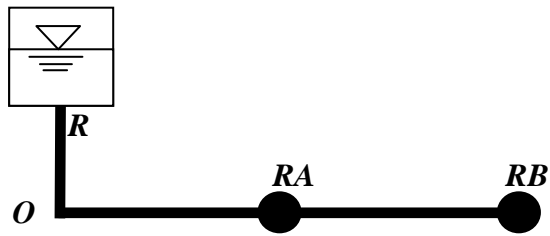
a) Trunk Model
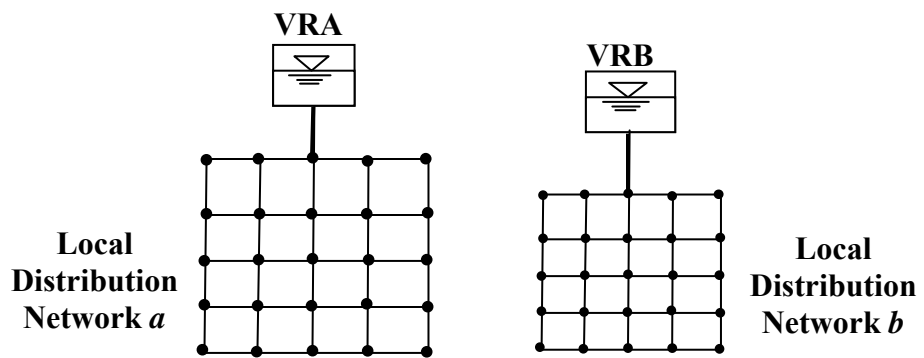
b) Distribution Models

Figure 6.2 Multi-Scale Models for a Simple Water Supply System

planning and operational assessments that help to identify the effects of major component disruption and prioritize limited resources for emergency response and system restoration. Earthquake simulation results from this model are also suited for economic impact evaluation that focuses on the business disruption consequences of water loss to distribution areas. In contrast, distribution models provide high resolution locally. These models are suitable for impact assessments related to specific communities and fire flow simulation.

A trunk line model can give an accurate prediction of flows and pressures in the trunk system if the nodal demands can be simulated accurately. These demands represent the aggregated demands from the downstream distribution systems. In normal operations, the demands from the distribution network are known values that are relatively easy to simulate. The demands are much more difficult to simulate during earthquakes.

The earthquake demands are related to distribution network damage. A generic parameter to quantify distribution network damage is repair rate, expressed as repairs per unit length of pipeline. The repair rate is, in turn, correlated with seismic hazards, such as peak ground velocity or permanent ground deformation. A rational approach is to correlate earthquake demand to repair rate in the distribution network. Seismic hazards are probabilistic in nature. To consider the uncertainties associated with seismic damage to distribution networks, Monte Carlo simulations are performed, and earthquake demands are simulated by fragility curves relating demand to repair rate.

6.3   LADWP SYSTEM AND MODEL DESCRIPTIONS

The multi-scale modeling technique is applied to the earthquake simulation of the LADWP water supply system. This section provides a brief description of the LADWP system, including the trunk and distribution network models.

6.3.1   LADWP Water Supply System

The LADWP water supply system serves the highly-populated Los Angeles area. The LADWP system, as shown in Figure 6.3, consists of more than 12,000 km of pipelines, serving 660,000 customers who compromise 3.8 million people in a service area of approximately 1,200 km^2 (LADWP, 2003). The water consumption of the LADWP system in a typical summer and winter day is about 2.50 and 1.21 million m^3 (660 and 320 million gallons), respectively. The system has three sources to meet its water demands: local groundwater basins, the First and Second Los Angeles Aqueducts (FLAA and SLAA, respectively), and transmission pipelines and tunnels of the Metropolitan Water District (MWD). Water from MWD is provided mainly by the State Water Project - West Branch, and delivered through the Foothill Feeder to Los Angeles. Normally, FLAA, SLAA and MWD sources account for roughly 85% of the total water supply, and the local groundwater wells make up the other 15%. Raw water from FLAA, SLAA and the Foothill Feeder is treated in the Van Norman Complex, located in the northern part of San Fernando Valley. The treated water then flows from north to south, primarily driven by gravity.

The LADWP system can be divided into 13 subsystems: Granada Hills (GH), Foothills (FH), Sunland/Tujunga (ST), Valley Floor (VF), Encino Hills (EH), Santa

Figure 6.4 LADWP Trunk Line Model

Figure 6.3 LADWP Water Supply System

Monica Mountains (SM), Hollywood Hills (HH), Westside (WS), Santa Ynez (SY), Mountain Washington (MW), Highland Park (HP), Central City (CC), and Harbor (H). Among the 13 subsystems, the VF and CC are the two largest, serving the heavily populated San Fernando Valley and Los Angeles central city. The other 11 subsystems are distributed around these two large subsystems. To accommodate elevation variations and keep water pressure at acceptable levels, each subsystem is further divided into several pressure zones. In total, the LADWP system includes 106 pressure zones. The pressure zone is named after the highest hydraulic grade, the sum of elevation and pressure heads, in the zone. For example, pressure zone 1000 means the highest hydraulic grade in this zone is 1000 ft (330 m). Wang (2006) provides a detailed description of the LADWP water supply system.

6.3.2 LADWP Trunk System Model

To simulate system response under different operational scenarios, LADWP developed a system-wide hydraulic network model. This model is used for planning and operational purposes by LADWP and works with the software H2ONET (LADWP, 2002), which is a member of the EPANET family. The major features of H2ONET are discussed in Section 2.6.2. The H2ONET hydraulic network model is shown in Figure 6.4. It includes 2186 km of pipelines with diameters generally larger than or equal to 300 mm (12 in.). Some smaller diameter distribution lines are also included in the model. The remaining 9800 km of distribution lines are modeled as demand nodes shown as yellow dots in Figure 6.4. The network also includes 230 regulator stations, 110 tanks and reservoirs, 151 local groundwater wells, and 73 pump stations. There are 591 valves set to control water flow and pressure in the 230 regulator stations, including 498 pressure reducing valves, 45 flow control valves, 50

throttle control valves, and 8 user defined valves. In general, multiple valves are set in one regulator station to either control water flows in different pipes or serve as standby valves to increase the reliability of the regulator station. There are 284 pumps at the 73 pump stations. Each local groundwater well is equipped with a pump for extracting water.

Six different sets of demand are defined in the database, which are demands for a typical winter day, a typical summer day, an ultimate summer day, the 1998 maximum day, a historical maximum day, and an ultimate maximum day. These demand sets are defined by LADWP for planning and operational purposes.

This trunk system model is able to simulate performance throughout the LADWP system or parts of the system, such as the 6 subsystems (subsystem VF, GH, FH, EH, ST, and SM) in the San Fernando Valley. When modeling part of the system, some virtual components are added to model other parts of the network that are outside the model in terms of input-output relationships. For example, if the part of system being modeled supplies water to other parts of the system, then a virtual demand is added at the boundary of the model to represent water outflow.

6.3.3   LADWP Distribution System Models

In addition to the trunk system model, LADWP developed roughly 30 distribution system models. These local distribution models are pressure zone based. For relatively large pressure zones, they are modeled as one distribution network model. For relatively small pressure zones, they are combined into one distribution network model. The smallest diameters of pipelines in these distribution network

models are 100 (4) and 150 mm (6 in.). The majority of pipelines in the distribution networks has diameters smaller than or equal to 300 mm (12 in.). Appendix A provides a pie chart showing the pipe diameter distribution of each distribution network.

Six representative distribution network models were obtained from LADWP. Five of them, systems 1449, 1000, 579, 448 & 462, and 426 were used to develop fragility curves for earthquake demand simulations. Fragility curves developed from Monte Carlo simulations from the five distribution networks were used to predict performance in the sixth distribution network, and the prediction was compared with the results of simulations performed explicitly with the hydraulic model for the sixth network.

A map showing the locations of the six distribution systems is provided in Figure 6.5. The distribution systems 1449, 1000, 579, and 205 cover the pressure zones 1449, 1000, 579, and 205, respectively. System 448 & 462 combines the two pressure zones, 448 and 462, because they are located close to each other. System 426 includes pressure zone 426 and the two small zones, 405 and 420. Appendix A provides an expanded view of each distribution network.

The five distribution systems used to develop the fragility curves were carefully selected from the 30 distribution system models developed by LADWP according to the following criteria: 1) widely distributed throughout the LADWP area, 2) representative of different network topologies, 3) representative of different pressure levels, and 4) reasonable size. System 1449 is located in the hillside area in the northeast of San Fernando Valley with a very high mean pressure of 820 kPa (119
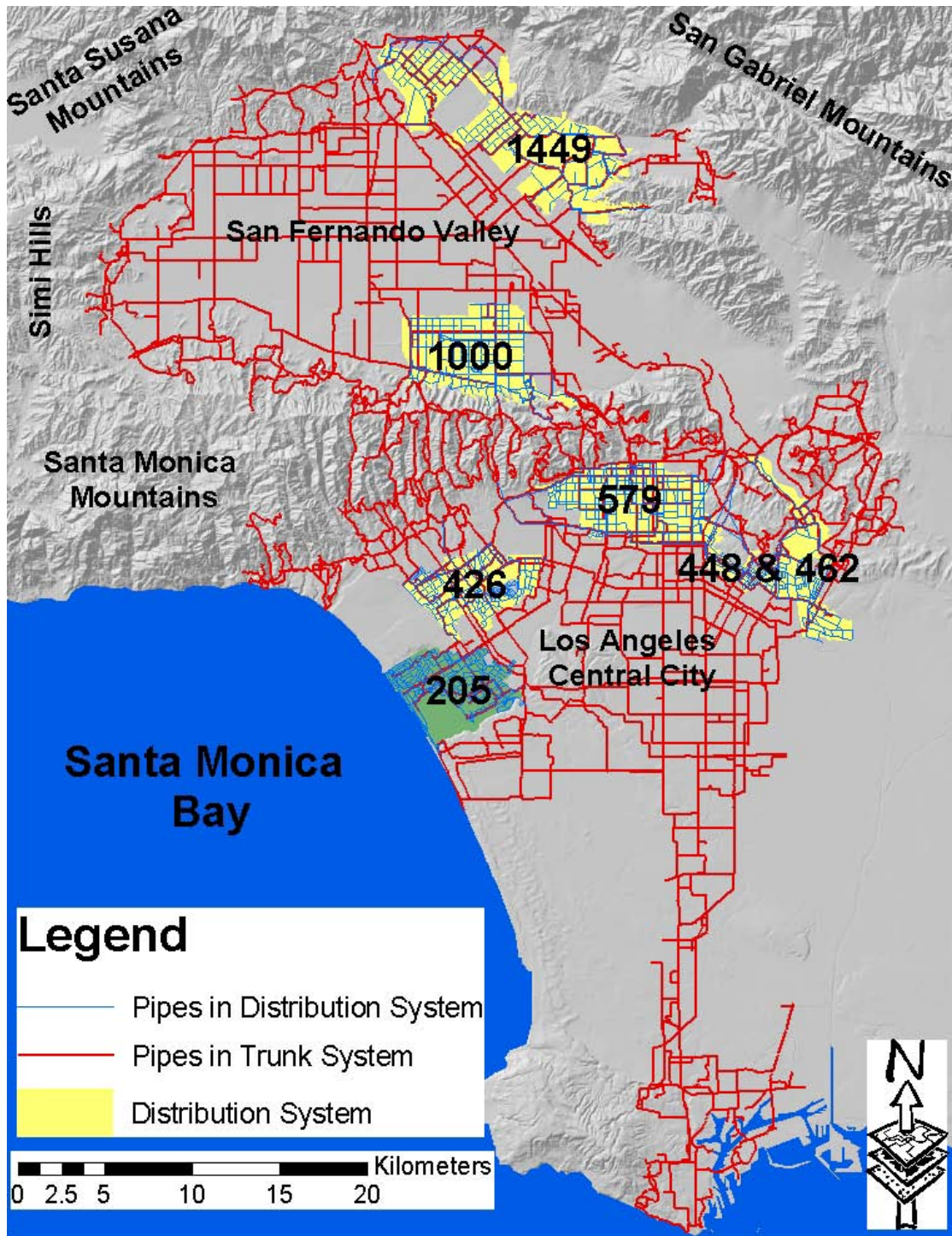
Figure 6.5 Locations of the Six LADWP Distribution Systems

psi). System 1000 is located in a flat area in the southern San Fernando Valley with a mean pressure of 786 kPa (114 psi). Systems 579 and 448 & 462 are located in the northeast portion of the Los Angeles central city with half hillside and flat areas and a mean pressure of 655 (95) and 572 kPa (83 psi), respectively. System 426 is located in the flat area in the northwest portion of the Los Angeles central city with a 427 kPa (62 psi) mean pressure. The mean pressures of the five distribution networks range from 427 (62) to 820 kPa (119 psi), which approximately covers the range of the mean pressures in the entire LADWP system. In general, there are 130 to 200 km of pipelines in each distribution network model.

6.4 DISTRIBUTION NETWORK SIMULATIONS

This section focuses on distribution network simulations and the development of fragility curves for the assessment of earthquake demands in the trunk line model.

6.4.1 Simulation Procedures

The distribution network models include a limited number of large diameter trunk lines as well as many small diameter distribution lines. In distribution system simulations, pipe damage is evaluated only in the distribution lines since the trunk line damage is accounted for explicitly in the trunk system model. This simulation technique decouples damage to trunk and distribution systems. This decoupling technique slightly overestimates water loss due to simultaneous damage in both the trunk and distribution systems because water losses from distribution pipeline damage are not diminished by trunk line losses. This modeling approach therefore provides a conservative assessment of system serviceability. The conservatism is limited because

188

damage in the trunk system is relatively infrequent due to the comparatively small number of trunk lines in the distribution network models.

The distribution network simulations are performed by GIRAFFE, standing for Graphical Iterative Response Analysis for Flow Following Earthquakes. GIRAFFE is a hydraulic network analysis software package, equipped with the algorithms for negative pressure treatment and pipeline damage simulation, described in Chapters 3 and 5. The general procedure for simulations using GIRAFFE is to represent system damage first, then solve for flow and pressure conditions in the damaged system, followed by the iterative negative pressure elimination process. The salient features of GIRAFFE are described in Chapter 7.

To simulate the distribution system damage, all distribution lines are assumed to have an identical mean repair rate because the distribution model covers a relatively small area in which the spatial variability of seismic hazard parameters is limited. The locations of damage are generated using Monte Carlo simulations, as described in Section 5.6.2.

Pipeline damage is classified as breaks or leaks using the assumption adopted in HAZUS (NIBS, 1997) that 80% of earthquake damage occurs as leaks and 20% occurs as breaks under the transient ground deformation effects. These percentages are close to those applied by Ballantyne et al. (1990) and Hwang et al. (1998), who assumed 15% is breaks and 85% is leaks for PGV-related damage to cast iron pipelines.

To decide on the leak orifice area for leakage simulation, pipe material information is needed. The LADWP distribution system database developed at Cornell University was used for this information. The Cornell database was developed by digitizing analogue maps of the LADWP system, which includes roughly 11,000 km of distribution lines. Toprak (1999) and Jeon (2002) provide a detailed description of the database. The statistics on pipeline composition show that the majority of distribution lines are composed of cast iron. The percentage of cast iron pipelines for distribution networks 1449, 1000, 579, 448 & 462, and 426, is 82%, 91%, 88%, 85%, and 83%, respectively. To simplify the simulation, it is assumed all distribution pipelines are composed of cast iron. Linear regressions between earthquake-induced pipeline repair rates and various seismic hazards including PGV (O'Rourke and Toprak, 1997; Jeon and O'Rourke, 2005) for different types of pipelines, show that the regressions for cast iron pipelines provide, in general, a relationship that is consistent and slightly conservative with respect to those of other distribution lines.

For cast iron pipelines, four leak scenarios are possible, which are annular disengagement, round crack, longitudinal crack, and local loss of pipe wall. The relative percentages of the four leak scenarios are 30%, 50%, 10%, and 10%, respectively, as described in Chapter 5. For each leak, a uniformly distributed random number between 0 and 1 is generated. If the random variable is within 0 to 0.3, the leak is assigned as an annular disengagement; 0.3 to 0.8, round crack; 0.8 to 0.9, longitudinal crack; and 0.9 to 1, local loss of pipe wall. The equivalent leak orifice area is calculated using the equations developed in Section 5.4.4 and the damage to each pipe is then added into the network.

Hydraulic network analysis was performed for the damaged system using GIRAFFE, which uses the EPANET engine to solve flow equations with the iterative approach, described in Chapter 3, to eliminate negative pressures. Flows in representative trunk lines before and after damage to distribution lines were monitored, and the flows after damage were normalized with respect to those before damage. Because hydraulic network analysis solves the continuity equation with nodal demands as input parameters, it is unable to track directly the variation of nodal demands during the simulation. Flows in trunk lines were therefore used as a proxy for the demands because water in the trunk lines is directly related to the nodal demands. The monitored flows in each distribution network are shown in Appendix A.

6.4.2   Simulation Results

Monte Carlo simulations were performed for repair rates (RRs) ranging from 0.02 to 100. It is of no practical significance to model pipeline damage with an RR lower than 0.02, which means, on average, one location of damage in 50 km of pipelines. Previous research (Jeon, 2002) shows that RR equal to 1 repair/km provides an approximate upper bound for the PGV-related damage to buried pipelines. RR of 1 to 100 repairs/km represents a level of damage that exceeds most levels of earthquake related pipeline damage, except for those in areas of very large, highly localized permanent ground deformation.

Figures 6.6 and 6.7 show simulation results of normalized demand (ND) vs RR corresponding to different RR ranges for Pipes 9 and 5 in distribution network 1449. Normalized demand is defined as the ratio of demand from a distribution network after damage to demand before damage. These figures show that the relationships between
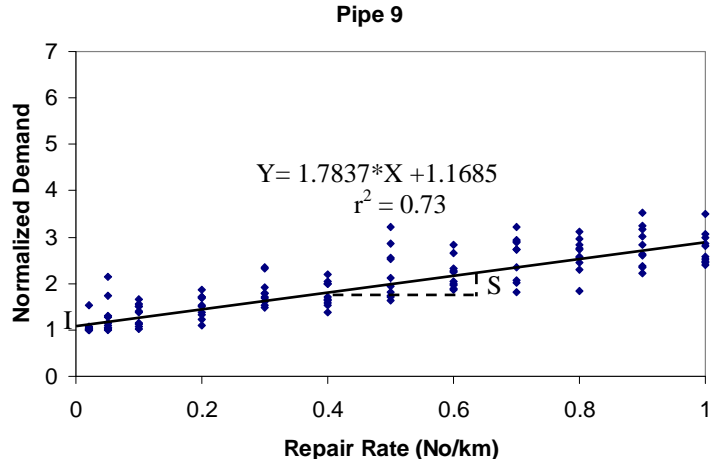
Pipe 9

Y= 1.7837*X +1.1685
$r^2 = 0.73$

a) RR Ranging from 0 to 1 Repairs/km

Pipe 9

Linear trend for RR smaller than 2 repairs/km

Separation of ND for Heavily Damage States

b) RR Ranging from 0 to 10 Repairs/km

Pipe 9

Separation of ND for Very Heavily Damage States
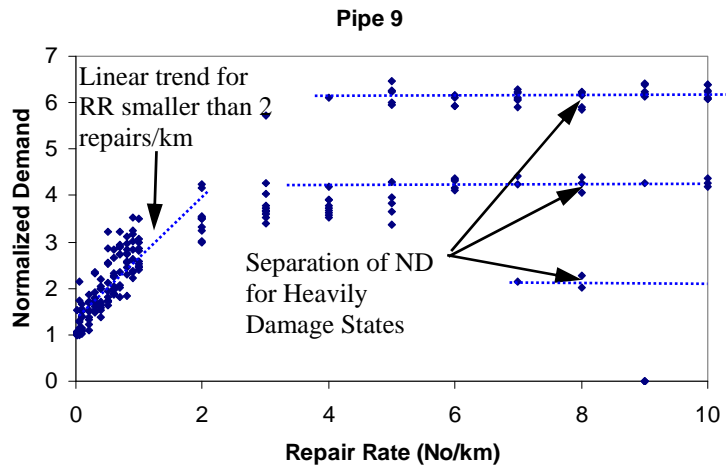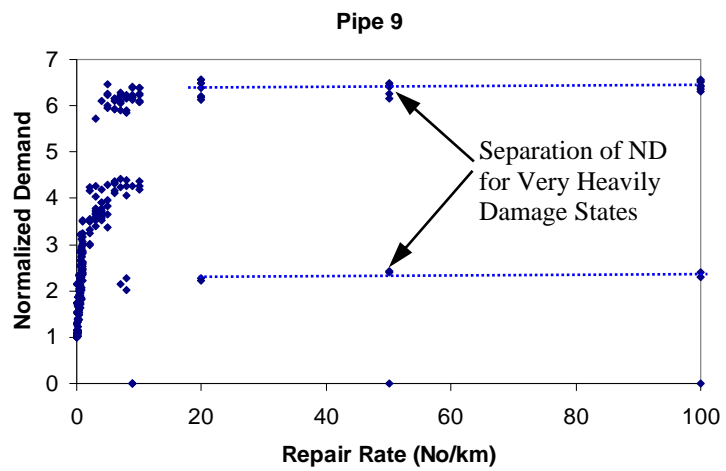
c) RR Ranging from 0 to 100 Repairs/km

Figure 6.6 ND vs. RR Relationship for Various Damage States for Pipe 9
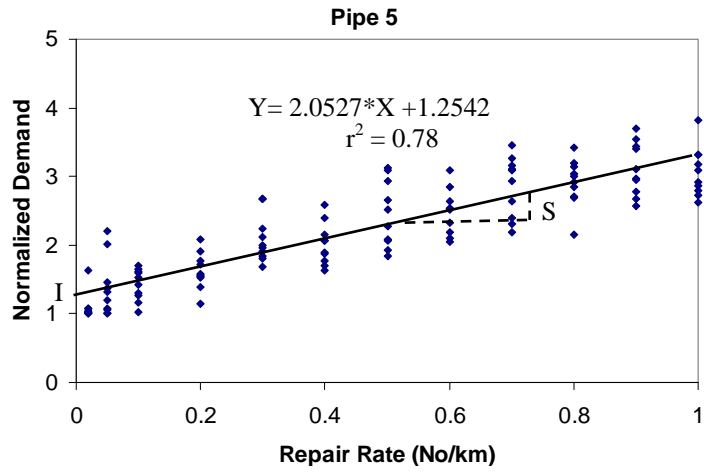
Pipe 5

a) RR Ranging from 0 to 1 Repairs/km
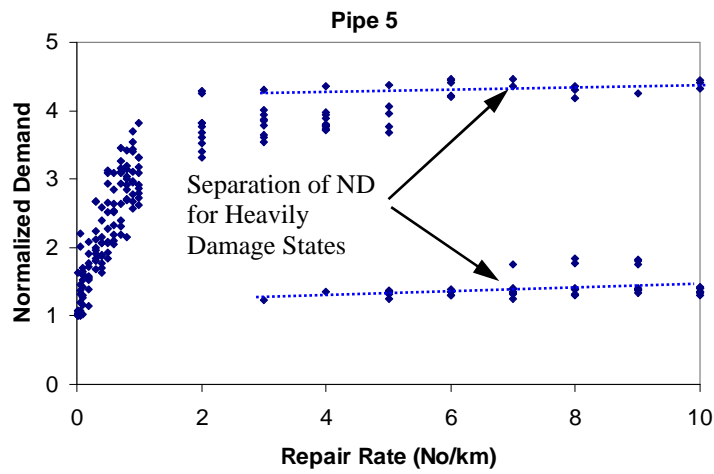
Pipe 5

b) RR Ranging from 0 to 10 Repairs/km
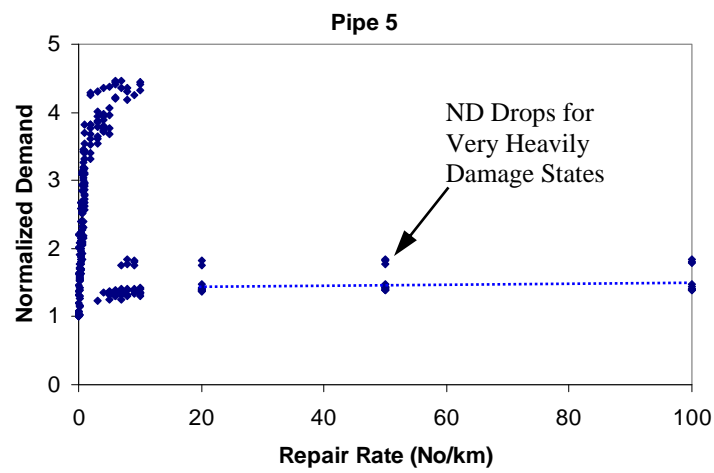
Pipe 5

c) RR Ranging from 0 to 100 Repairs/km

Figure 6.7 ND vs. RR Relationship for Various Damage States for Pipe 5

ND and RR follow increasing trends to RR of roughly 2 repairs/km, above which a change in performance can be discerned. When RR values are 2 to 10 repairs/km, ND begins to separate into different trends. At RR from 10 to 100 repairs/km, the system response follows a limited number of discrete trends, and in some cases ND drops to very low levels, which indicate that the system is severely damaged and not able to supply water in a reliable and stable way.

Since RR equal to 1 repair/km provides an approximate upper bound for the PGV-related damage to buried pipelines, statistics were developed for simulation results with RR ranging from 0.02 to 1 repairs/km. The number of Monte Carlo simulations was automatically determined by the GIRAFFE self-termination algorithm. GIRAFFE monitors the mean and coefficient of variation (COV) of ND, as the number of Monte Carlo simulations increases. If the mean and COV of ND with additional simulations are within 2% difference when compared with those without additional simulations, GIRAFFE terminates the Monte Carlo simulations.

Various types of regression functions were used to correlate ND and RR. Linear regressions were found to provide correlations with highest statistical significance between ND and RR. The linear regressions between ND and RR for the 26 monitored pipes for damage states with RR ranging from 0.02 to 1 repairs/km are presented in Appendix B.

Figure 6.8 summarizes the linear regressions for the 26 locations in the five distribution networks where flows were monitored before and after the simulation of damage states. Table 6.1 provides a summary for the pipelines that served as monitoring stations, including the ID (identification number) of the monitored pipeline
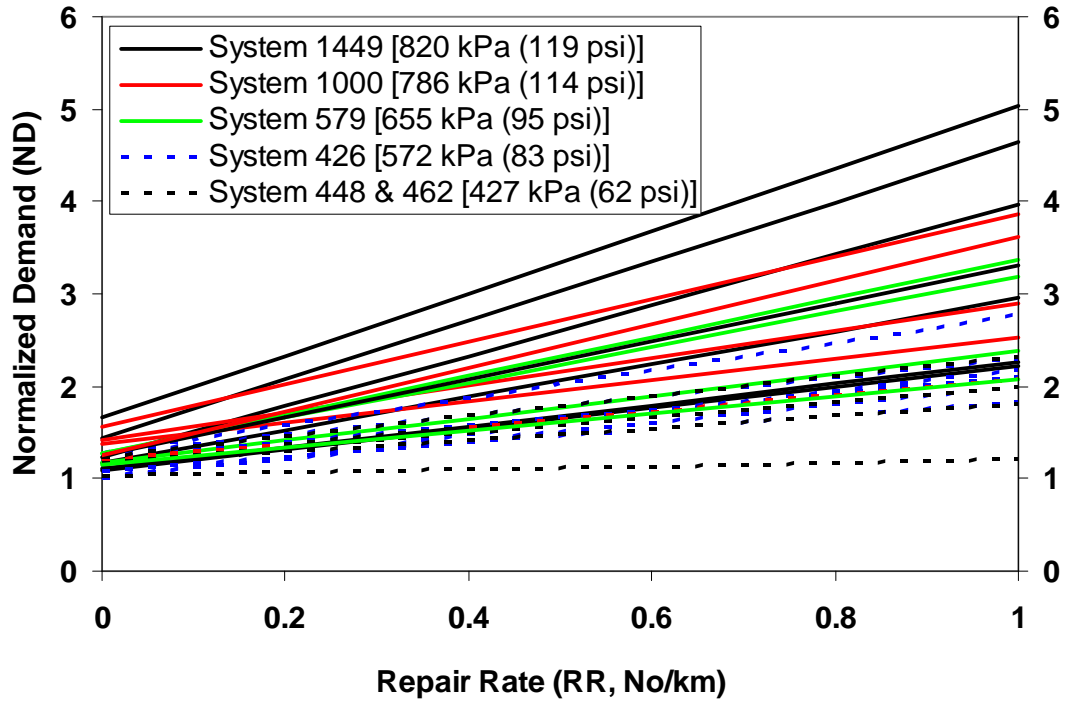
Figure 6.8 Relationship Between Normalized Demand and Repair Rate

in the hydraulic network database, pipe diameter, original flow rate, as well as slope and intercept of the linear regression pertaining to each monitoring location. The mean and standard deviation of the slopes and intercepts for the regressions associated with each distribution network, together with the mean pressure (MP) of that distribution network, are listed in Table 6.1. The MP is the average of nodal pressures in the distribution network. Water loss caused by pipe damage, including both leaks and breaks, is a function of pipe internal pressure. The MP, therefore, is an important parameter for characterizing water loss in damaged pipeline networks.

6.4.3 Fragility Curve Construction

Since linear regressions provide the most statistically significant correlation between ND and RR, a linear function is proposed to relate *ND* to *RR* as

Table 6.1 Simulation Results for Five Representative Distribution Networks in LADWP System

Zone No.	Mean Pressure		Pipe ID	Pipe Diameter		Initial Flow		Slope	Mean Slope	Slope STD*	Intercept	Mean Intercept	Intercept STD*
	kPa	psi		mm	(in.)	(L/s)	(gpm)						
1449	820	119	4	914	36	810	12845	3.37	2.20	0.92	1.66	1.28	0.20
			161	406	16	82	1299	3.19			1.44		
			40	762	30	194	3072	2.73			1.24		
			5	1067	42	581	9214	2.05			1.25		
			9	1524	60	840	13322	1.78			1.17		
			2	914	36	610	9673	1.15			1.11		
			21	914	36	954	15116	1.13			1.10		
1000	786	114	88	305	12	63	1002	2.34	1.82	0.60	1.26	1.41	0.12
			87	356	14	144	2288	2.31			1.56		
			178	305	12	82	1298	1.47			1.43		
			153	305	12	147	2324	1.15			1.38		
579	655	95	366	305	12	97	1534	2.10	1.54	0.56	1.27	1.21	0.06
			38	914	36	395	6260	1.92			1.27		
			483	2540	100	1902	30152	1.21			1.17		
			227	610	24	407	6455	0.92			1.15		
426	572	83	64	406	16	276	4368	1.49	1.05	0.26	1.28	1.15	0.12
			3	305	12	77	1226	1.19			1.00		
			176	305	12	144	2287	1.05			1.26		
			5	610	24	525	8326	0.97			1.02		
			124	406	16	218	3461	0.87			1.22		
			1	762	30	737	11682	0.74			1.09		
448 & 462	427	62	41	1067	42	588	9316	1.09	0.72	0.34	1.24	1.16	0.08
			140	1016	40	801	12694	0.87			1.21		
			42	610	24	168	2667	0.82			1.17		
			37	610	24	164	2594	0.65			1.15		
			1	1067	42	806	12777	0.19			1.02		

* STD: Standard Deviation

$$ND = I + S * RR \qquad (6.1)$$

in which *ND* is the normalized demand, *I* and *S* are the intercept and slope of the regression, respectively, and *RR* is the repair rate. The *RR*, in turn, is correlated with peak ground velocity. Equation 6.1 relates the distribution network damage states to seismic hazard intensity, and provides the basis for generating fragility curves for distribution system performance.

6.4.3.1 Observations

Figure 6.8 and Table 6.1 show that there are significant differences among the different regressions. In general, the regression lines from distribution systems with a relatively high MP are higher than those from distribution systems with a relatively low MP. The highest regression lines are from System 1449, which has the highest MP of 820 kPa (119 psi). The lowest regression lines are from System 448 & 462, which has the lowest MP = 427 kPa (62 psi). The regression lines from other distribution systems lie between those with the highest and lowest MPs and increase with increasing MP.

To show how ND varies as MP, the slope and intercept of the linear regression of ND vs RR for each monitoring location in each distribution network is plotted vs MP in Figures 6.9 and 6.10, respectively. The intention of monitoring flows at specific locations throughout a distribution network is to estimate the expected demand of that distribution network on the trunk line system. The expected nodal demand is estimated by determining the mean slope and intercept associated with the linear regressions of ND vs RR for the multiple sampling locations in each distribution
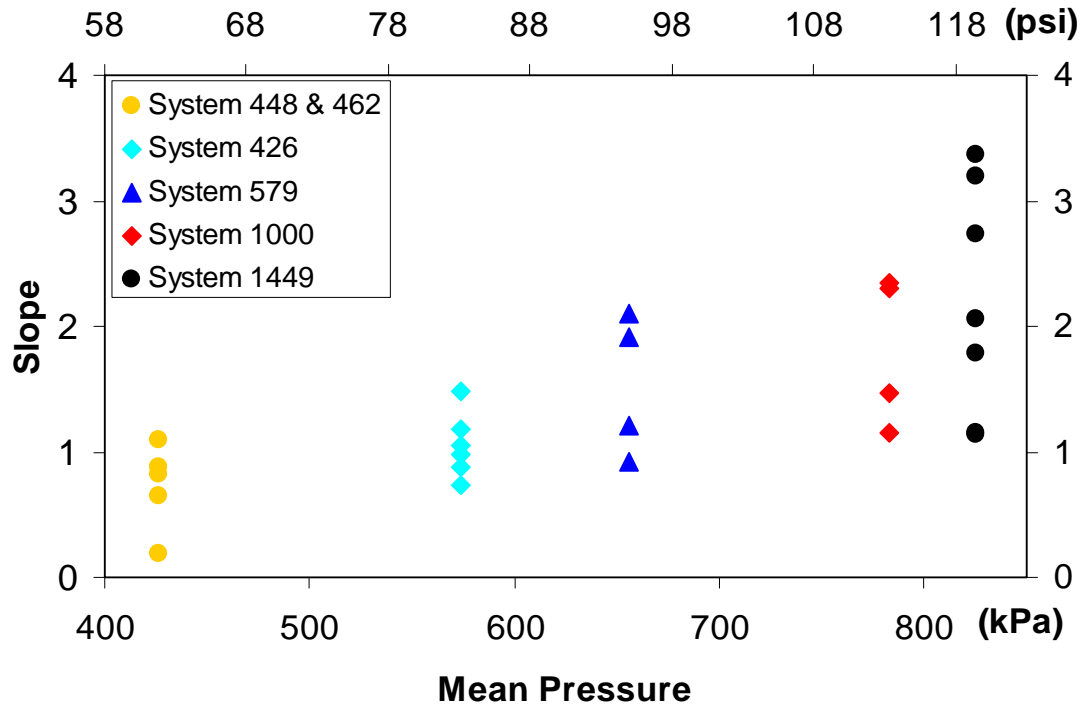
Figure 6.9 Regression Relationship Between Mean Pressure and Slope
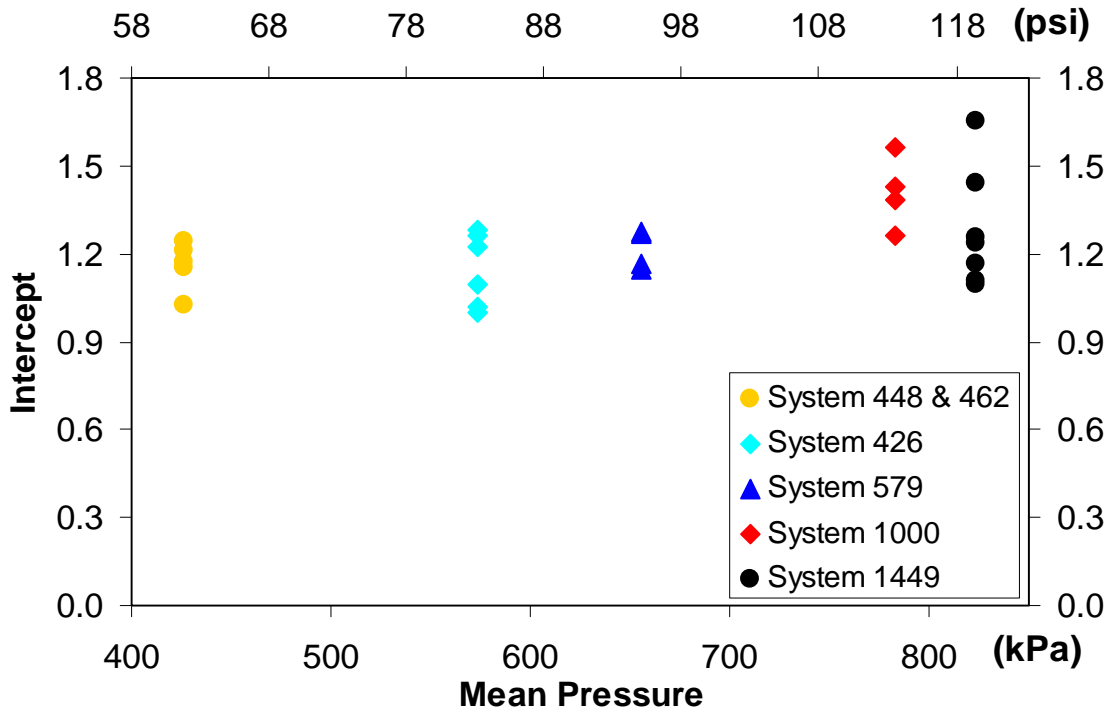
Figure 6.10 Regression Relationship Between Mean Pressure and Intercept

198

network. The mean slopes and intercepts are plotted vs MP in Figures 6.11 and 6.12, respectively. The high r^2 values associated with these plots show that the variation of the mean values, and hence estimate of nodal demands, is well explained by the regression equations.

The variability of flows sampled at different locations should also be correlated with MP because higher pressures will tend to drive higher water losses in a damaged network. To estimate the variability of the estimated NDs with respect to MP, the standard deviations of the slopes and intercepts associated with the ND vs RR regressions are plotted in Figures 6.13 and 6.14.

6.4.3.2 Mean Regression with Noise Term

In this section, a linear regression with a noise term is proposed to estimate the slope and intercept of ND vs RR relationship. The mean slope and intercept are linearly correlated with MP, while a noise term is used to express the variability of the slope and intercept. The noise term is modeled as a Gaussian random variable with zero mean and variance, which is correlated with MP.

Using the mean regression with noise term, the slope, S, of the correlation between ND and RR, is estimated as

$$S = SI + SS \times MP + N(0, \sigma_S) = -0.877 + 0.0248 MP + N(0, \sigma_S) \qquad (6.2)$$

where SI and SS are the intercept and slope of the slope term, S, and $N(0, \sigma_S)$ is a Gaussian random variable with zero mean and standard deviation σ_S. The values of
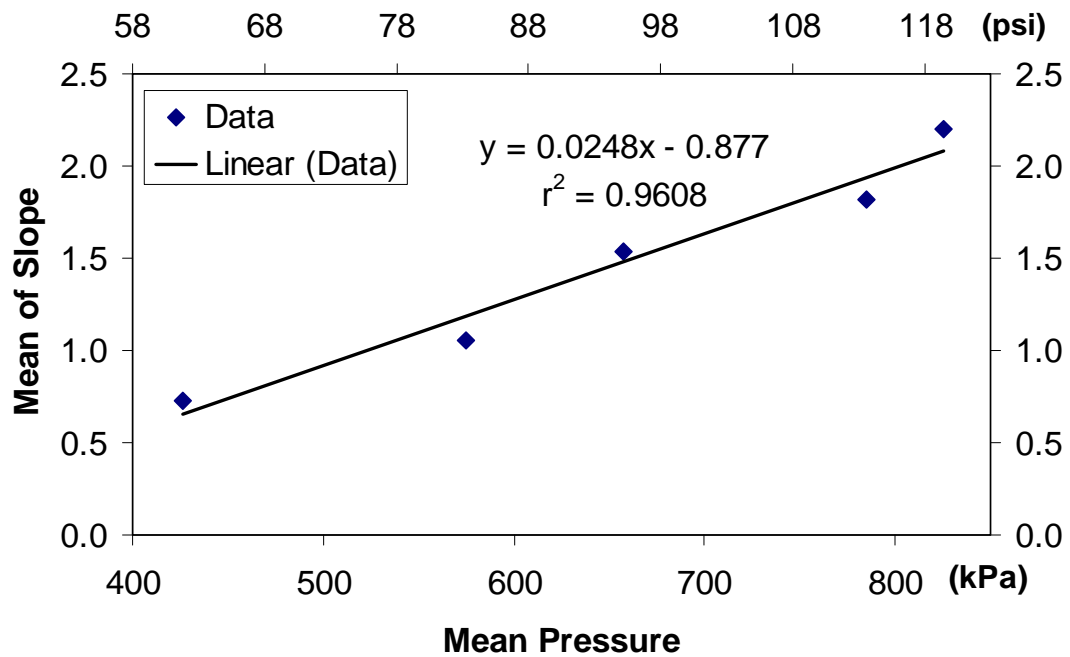
Figure 6.11 Regression Relationship Between Mean Pressure and Mean Slope
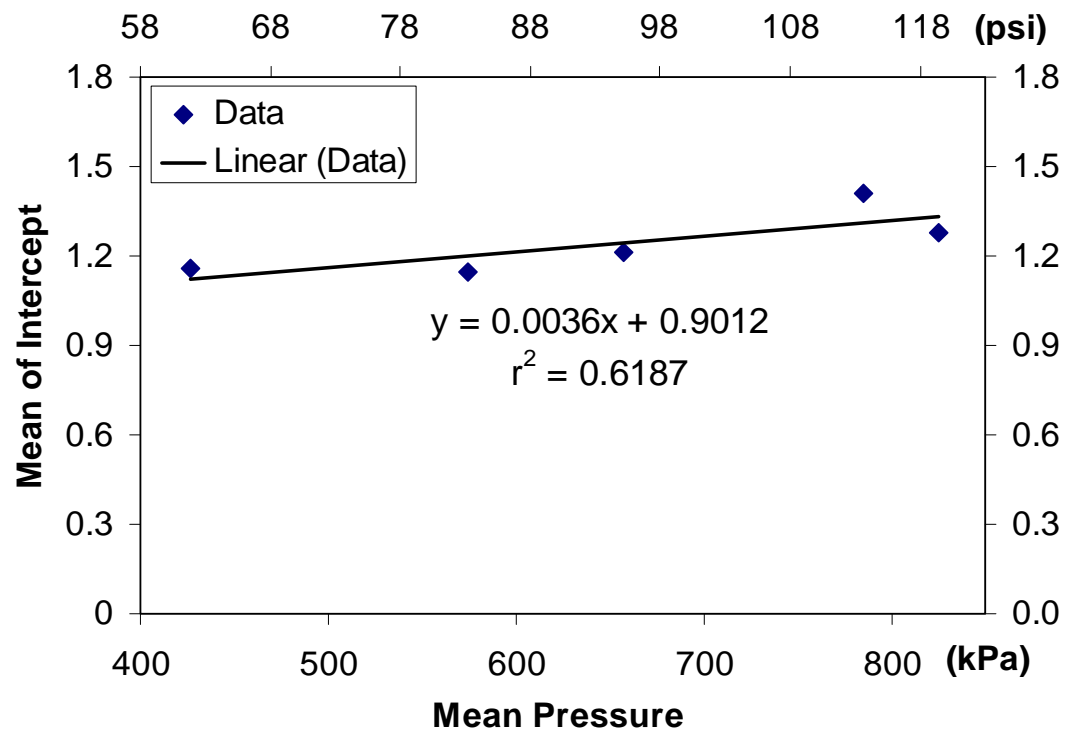
Figure 6.12 Regression Relationship Between Mean Pressure and Mean Intercept
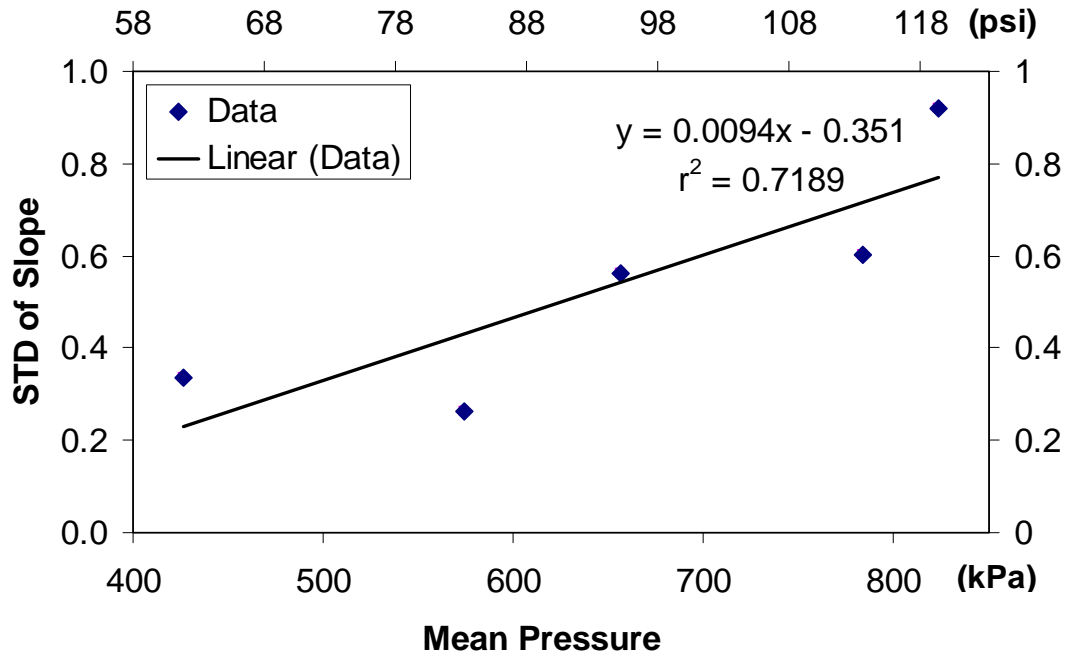
Figure 6.13 Regression Relationship Between Mean Pressure and Standard Deviation

of Slopes
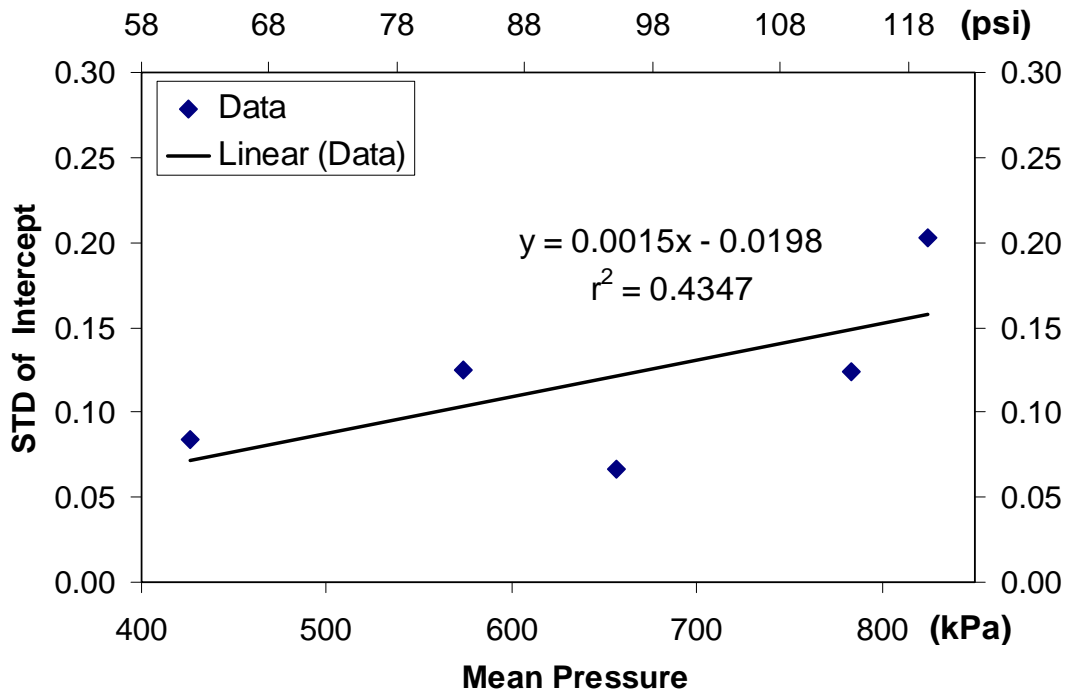
Figure 6.14 Regression Relationship Between Mean Pressure and Standard Deviation

of Intercepts

SI and *SS* are determined from the regression equation shown in Figure 6.11. The value of σ_s is evaluated using the regression equation shown in Figure 6.13.

$$\sigma_S = ISD + SSD \times MP = 0.0094MP - 0.3510 \tag{6.3}$$

where the *ISD* and *SSD* are the intercept and slope of the linear regression between the standard deviation of the slope term, *S*, and *MP*.

Similarly, the intercept, *I*, of the correlation between ND and RR is estimated as

$$I = II + IS \times MP + N(0, \sigma_I) = 0.9012 + 0.0036MP + N(0, \sigma_I) \tag{6.4}$$

in which, *II* and *IS* are the intercept and slope of the intercept term, *I*, and $N(0, \sigma_I)$ is a Gaussian random variable with zero mean and standard deviation of σ_I. The values of *II* and *IS* are determined from the regression equation shown in Figure 6.12. The value of σ_I is evaluated using the regression equation shown in Figure 6.14 as

$$\sigma_I = IID + ISD \times MP = 0.0015MP - 0.0198 \tag{6.5}$$

where the *IID* and *ISD* are the intercept and slope of the linear regression between the standard deviation of the intercept term, *I*, and *MP*.

Substituting Equations 6.2 to 6.5 into 6.1, *ND* can be estimated as a function of *RR* and *MP* with the following equation

$$\begin{aligned}
ND &= I + S \times RR \\
&= \left[II + IS \times MP + N(0, \sigma_I) \right] + \left[SI + SS \times MP + N(0, \sigma_S) \right] \times RR \\
&= \left\{ 0.9012 + 0.0036MP + N\left[0, (-0.0198 + 0.0015MP) \right] \right\} \\
&\quad + \left\{ -0.877 + 0.0248MP + N\left[0, (-0.351 + 0.0094MP) \right] \right\} RR
\end{aligned}$$
(6.6)

Please note that all the above regressions are performed with *MP* in the units of psi. When applying Equation 6.6 to predict *NDs*, the *MP* needs to be converted into the units of psi. The *MP* is influenced by the physical and operational properties of the water supply network, and the *RR* is related to seismic hazard parameters. Equation 6.6 correlates the mean slope and intercept of *ND* vs *RR* regressions with *MP*, and characterizes the variability of slope and intercept.

Statistically Equation 6.6 can provide an accurate prediction of mean NDs over a large area, and therefore may be more suitable for regional economic impact assessments. With Equation 6.6, however, it is possible to underestimate ND, and therefore overestimate the serviceability, with 50% chance for each individual demand node. This is because the variation of the slope and intercept, associated with the linear regression of ND vs RR, with respect to the mean value is simulated as a Gaussian random variable with 0 mean. For each individual demand node, the predicted slope and intercept, and therefore ND, may be lower than their expected values with a probability of 0.5. With the increase of the number of demand nodes, the average of slopes and intercepts, and therefore NDs, for all the nodes will converge to their expected values.

It is useful to provide a conservative estimate of the NDs for emergency situation simulations, such as fire emergency response. An appropriately conservative estimate may be taken at the 90% confidence level, as explained in the next subsection.

6.4.3.3 90% Confidence Level Regression

In Equation 6.6, the parameters, *II*, *IS*, *SI*, *SS*, are mean estimates. Using the 26 locations, the confidence intervals of these parameters can be estimated. The methodology for estimating the confidence intervals of the parameters of a linear regression from experimental data can be found in traditional text books on statistics (e.g., Ronald, et al., 1998) and the confidence intervals can be estimated using the Regression Function under the Data Analysis menu in Microsoft EXCEL.

Selecting the Mean Pressure column in Table 6.1 as X and the Slope column in Table 6.1 as Y, the 90% confidence intervals of the regression parameters, *SI* and *SS*, for the slope term, *S*, are calculated as

$$0.01640 \leq SS \leq 0.0347 \tag{6.7}$$
$$-1.8433 \leq SI \leq -0.0514 \tag{6.8}$$

Similarly, the 90% confidence intervals of *II* and *IS* are calculated as

$$0.0010 \leq IS \leq 0.0055 \tag{6.9}$$
$$0.7017 \leq II \leq 1.1412 \tag{6.10}$$

Because the purpose of using the confidence estimates is to provide a conservative estimate, the lower confidence estimates do not have practical significance. Only the upper 90% confidence estimates are used. The 90% confidence limit of the slope, *S*, can be estimated as

$$S = SI + SS \times MP = -0.0514 + 0.0347 \times MP \qquad (6.11)$$

and the 90% confidence limit of the intercept, *I*, can be estimated as

$$I = II + IS \times MP = 1.1412 + 0.0055 \times MP \qquad (6.12)$$

Therefore, the 90% confidence level of *ND* as a function of *RR* and *MP* can be expressed as

$$
\begin{aligned}
ND &= I + S \times RR \\
&= \left[II + IS \times MP\right] + \left[SI + SS \times MP\right] \times RR \\
&= \left(1.1412 + 0.0055MP\right) + \left(-0.0514 + 0.0347MP\right)RR
\end{aligned}
\qquad (6.13)
$$

6.4.4   Test of Fragility Curves

To test the predictive capabilities of the fragility curves, they were used to predict performance of a sixth distribution network, and the predictions were compared with the results of simulations performed explicitly with the hydraulic model for the sixth network. The sixth distribution network covers pressure zone 205 in the LADWP system. A map of this local distribution network superimposed on the trunk line network is shown in Appendix A. The same Monte Carlo procedures as described in Section 6.4.1 were applied during the System 205 simulation. The detailed simulation results are shown in Appendix B.

The mean pressure of System 205 is 490 kPa (71 psi), as determined by averaging its nodal pressures in an undamaged state. The mean and 90% confidence levels of the ND vs RR are plotted in Figure 6.15 by substituting the MP = 71 psi

205
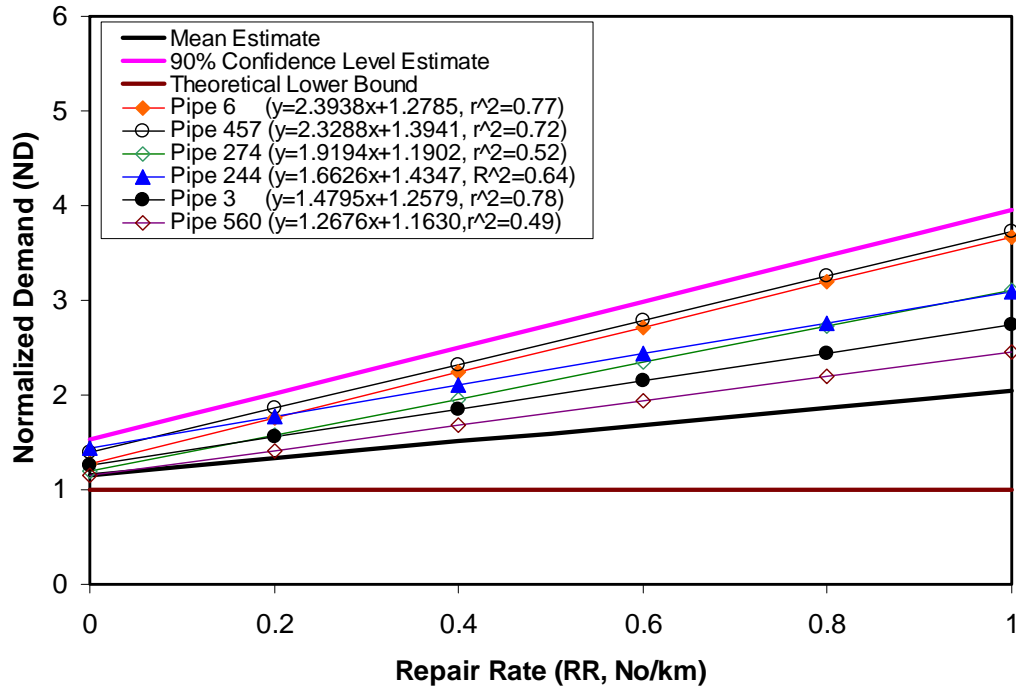
Figure 6.15 Comparison Between Simulated and Predicted Results for Distribution

System 205

(490 kPa) into Equations 6.6 and 6.13, respectively. Furthermore, the lower bound of

ND =1 is also shown in Figure 6.15 for reference. The linear regressions of ND vs RR

from simulation results at 6 monitoring locations are also plotted in Figure 6.15.

Figure 6.15 shows that the simulation results lie between the mean and 90%

confidence level predictions. Although the simulation results plot above the mean

regression, they all fall well within the 90% confidence level, suggesting that a 90%

confidence margin is appropriate for predicting local distribution network performance.

The characteristics of System 205 deserve some commentary. As shown in

Figure 6.5, System 205 is at the end of the trunk line flow paths, and is the only

network so located that was evaluated in this work. Water flow cannot by-pass

damage in the System 205 pipelines that are downstream of all trunk line sources. As a result, the flows and losses in System 205 tend to be relatively larger than those in distribution networks with both upstream and downstream trunk line interconnections. In addition, the percentage of distribution pipelines is larger in System 205 than in other local distribution networks studied because it has fewer trunk lines integrated within it. This bias tends to generate additional break and leak locations in the local network, which affects a smaller aggregate length of trunk lines. The ND, which is evaluated from monitoring points in the smaller length of trunk lines, will be weighted to reflect greater losses per level of repair rate.

CHAPTER 7

EVALUATION OF NORTHRIDGE EARTHQUAKE PERFORMANCE

7.1 INTRODUCTION

To implement the modeling methodology, as described in Chapters 3, 5, and 6, a software package, GIRAFFE, was developed for hydraulic network analyses of heavily damaged water supply systems. GIRAFFE, standing for Graphical Iterative Response Analysis for Flow Following Earthquakes, has special features to treat negative pressures, simulate various levels of leakage, assess earthquake demand associated with distribution networks, and perform Monte Carlo simulations.

To assess the capabilities of GIRAFFE, the response of the LADWP water supply to the Northridge earthquake is used to compare the actual measured flows in a heavily damaged system with earthquake simulation results. To monitor network performance, the LADWP operates a Supervisory Control and Data Acquisition (SCADA) system. The records of flow meters at key locations in the LADWP system before and after the Northridge earthquake were collected and compared with the GIRAFFE simulation results.

This chapter starts with a description of the software package GIRAFFE. It then proceeds to the observed performance of the LADWP system during the 1994 Northridge earthquake, followed by the GIRAFFE simulation of the LADWP system

response to the Northridge earthquake, and comparisons between simulated and observed performance.

7.2 GIRAFFE

A software package, GIRAFFE, was developed to help implement the modeling approaches proposed in this study. GIRAFFE embodies an iterative procedure for negative pressure elimination as described in Chapter 3, methods for simulating pipeline breaks and leaks as described in Chapter 5, and the simulation of earthquake demands associated with distribution networks as explained in Chapter 6. GIRAFFE involves over 7000 lines of C++ code and works iteratively with the EPANET hydraulic network analysis engine. GIRAFFE can perform both deterministic and probabilistic simulations, and provides results which can be directly linked to GIS to conduct spatial analysis and map presentations.

A complete GIRAFFE package consists of an EPANET graphical user interface, an EPANET hydraulic analysis engine, and a GIRAFFE core code. The GIRAFFE package includes six major modules, which are system definition, system modification, seismic damage, earthquake demand simulation, hydraulic network analysis, and compilation of results. A flow chat of GIRAFFE simulation is shown in Figure 7.1. The major functions of each module are introduced in the following sections.
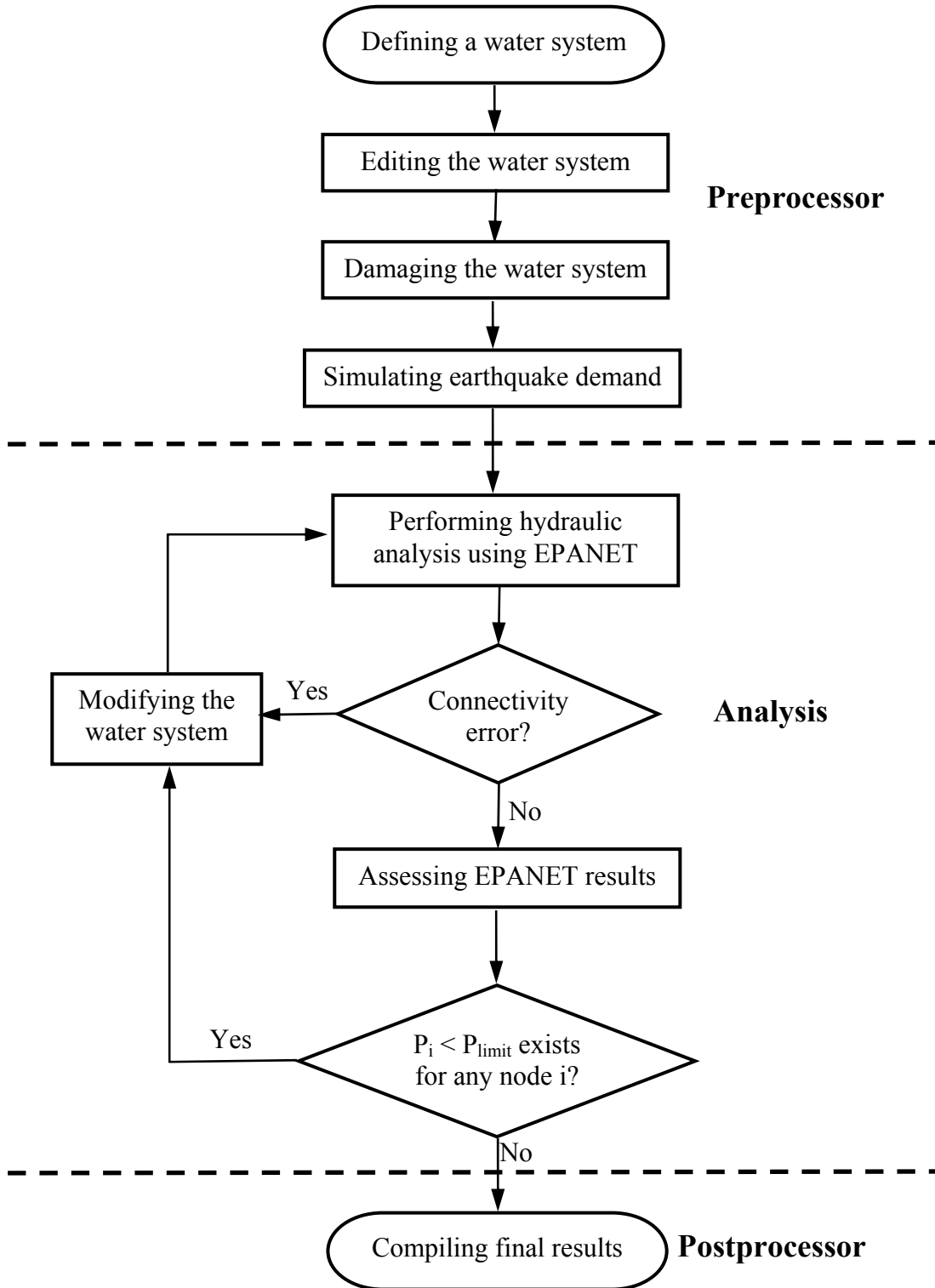
Figure 7.1 GIRAFFE Simulation Flow Chart

211

7.2.1 System Definition

The system definition module defines the hydraulic network being analyzed. It provides information on the physical and operational properties, topology, and demands of a system. The detailed information needed for defining a hydraulic network is described in Chapter 2. GIRAFFE utilizes the graphical user interface of EPANET for network definition and visualization. Users can refer to the EPANET manual (Rossman, 2000) for the details on how to define a hydraulic network. The system definition information from the graphical user interface is stored in a data file with the format which can be read by EPANET engine. Users can also work with other software packages, such as H2ONET, to define a hydraulic network and then export the system definition file into the EPANET format. Because of the wide usage of EPANET engine, most of the commercial software packages for hydraulic network analysis can export their system definition files into the EPANET format. The EPANET format serves as a common platform for data exchanges among different hydraulic network analysis software packages.

7.2.2 System Modification

The system modification module is used to modify a hydraulic network to perform a specific simulation scenario. Users can add or remove components and change the physical and operational properties of components in the hydraulic network model. Users can modify the system graphically using the EPANET graphical user interface or modify the system definition data file directly.

7.2.3   System Damage

The damage module adds damage to pipelines. Algorithms for damage to other components, such as tanks, pumps, and valves, can be incorporated in GIRAFFE because the architecture of the code allows for the addition of parallel damage characterization modules.

The detailed modeling methodology for pipe damage is described in Chapter 5. In general, a break or leak can be modeled. For a pipe leak, there can be five different scenarios, which are annular disengagement, round crack, longitudinal crack, local loss of pipe wall, and local tear of pipe wall. One pipe can have multiple breaks and leaks. Two simulation options, deterministic and probabilistic, are provided for pipe damage.

7.2.3.1   Deterministic Simulation

The deterministic option allows users to specify the location of each break, and the location and orifice area of each leak. The location of each break and leak is characterized by a unique pipe ID and a length ratio. A length ratio is the relative length, between the pipe upstream node and the damage location, with respect to the pipe length. Each pipe is connected to upstream and downstream nodes that have geo-coordinates. By knowing the pipe ID in which the damage occurs and the length ratio, one can locate damage precisely. Multiple breaks or leaks in the same pipeline are distinguished by different length ratios. All damage information is stored in an input text file. The basic input parameters for a pipe break are the pipe ID and length ratio.

The basic input parameters for a pipe leak include the pipe ID, length ratio, and the equivalent orifice diameter.

To model a pipe break, GIRAFFE modifies the system definition file by deleting the original pipe according to its unique pipe ID and adding two new pipes and two empty reservoirs following the method described in Section 5.5.

To model a pipe leak, GIRAFFE modifies the system definition file by: 1) adding a new junction at the leak location to divide the original pipe into two new pipes; 2) adding an empty reservoir which has the same elevation as the leak location; 3) and adding a new pipe with a length of 1 foot, roughness coefficient of 1,000,000, and minor loss coefficient of 1 to connect the newly added junction and reservoir. The leak simulation method is described in Section 5.4.

7.2.3.2 Probabilistic Simulation

The probabilistic option generates randomly distributed pipe breaks and leaks according to repair rate, RR, pipe length, L, and conditional pipe break probability, P_{bk}, given that damage occurs. For each leak, the probabilistic simulation option randomly generates the scenario of each leak and calculates the orifice area. The probabilistic simulation of pipe damage includes three steps: generating pipe damage, deciding the damage state as a leak or break, and deciding the scenario and orifice area of each leak.

The basic input parameters for generating pipe damage are the mean repair rate, RR, and length, L, of each pipeline. The repair rate, RR, is correlated with seismic

hazard parameters and is an input parameter for each pipe. The length, L, of each pipe can be obtained from the hydraulic network database. The pipe damage is assumed to follow a Poisson process with a mean arrival rate equal to mean repair rate, RR. For a Poisson process, the arrival length between two locations of damage follows an exponential distribution. By continually generating the damage arrival length using Monte Carlo simulation until the cumulative length of the damage exceeds the pipeline length, the locations of damage can be determined. The detailed Monte Carlo simulation algorithm is described in Section 5.6.2.

After generating the locations of damage for each pipeline, another uniformly distributed random number between 0 and 1 is generated for each location of damage. This random number is compared with the conditional pipe break probability, P_{bk}. If the uniformly distributed random number is greater than the pipe break probability, then the damage is classified as a leak, otherwise, it is a break. The pipe break probability is an input parameter which is estimated from pipe damage data collected from previous earthquakes.

To decide the leak orifice area, a uniformly distributed random number between 0 and 1 is generated for each leak. This random number is compared with the cumulative probability of each leak scenario for a pipeline with specific material composition. The probabilities of each leak scenario for various types of pipelines widely used in North American are listed in Table 5.2. The equivalent orifice area for each leak is then calculated using equations developed in Section 5.4.4.

7.2.4 Earthquake Demand Simulation

The earthquake demand simulation module implicitly considers the effects of damage to small diameter distribution pipelines, which are not included in the hydraulic network model, by increasing nodal demands. The detailed modeling methodology for earthquake demand simulation is provided in Chapter 6.

The earthquake demand simulation is pressure zone based. The basic input parameters are mean pressure (MP) and repair rate (RR) associated with each demand node. For a demand node, MP is the average nodal pressure in the pressure zone in which the demand node is located before system damage. The MP can be obtained by performing hydraulic network analysis on the undamaged system and then conducting statistical analysis on the nodal pressures with respect to pressure zones. The RR represents the repair rate of the distribution lines around the demand node. For PGV-related pipe damage, the RR is calculated using regression relationships between PGV and RR developed from previous investigations (e.g., Jeon, 2002; Jeon and O'Rourke, 2005). The determination of RR for a given earthquake scenario involves spatial manipulation and is performed using GIS, which gives the RR related to each demand node as input to GIRAFFE. The GIS procedures for determining the RR is explained in Section 7.3.3.2 for the Northridge earthquake case history simulation.

Two implementation options are provided in GIRAFFE, mean prediction with noise terms and 90% confidence level prediction. With the input MP and RR for each demand node, GIRAFFE calculates the normalized demand using Equations 6.6 and 6.13 for mean and 90% confidence level predictions, respectively. The standard normal random variables in Equation 6.6 are generated by the computer. GIRAFFE

then calculates the demands after the earthquake by multiplying the normalized demands with the original demands, and modifies the system definition file by replacing the original demands with the earthquake demands.

7.2.5   Hydraulic Network Analysis

This module uses the EPANET hydraulic network engine iteratively to solve the damaged hydraulic network and eliminate negative pressures. Only steady state simulation is performed. As shown in Figure 7.1, the damaged system is sent to EPANET engine for hydraulic network analysis. It is possible that the damaged system cannot be solved because some elements may not have connectivity with the main system due to earthquake damage. In this case, the EPANET engine gives error messages, which tell the user the ID of each element disconnected from the main system. GIRAFFE reads the error messages and fixes the errors by eliminating the disconnected elements from the database. GIRAFFE then checks the nodal pressures, and identifies the lowest nodal pressure in the system. If the lowest pressure is higher than the preset pressure limit, which is zero for negative pressure elimination, the hydraulic analysis stops. If the lowest pressure is lower than the pressure limit, the program eliminates the node, the links connected to this node, and other operational parameters associated with the node and links. After each step of elimination, GIRAFFE performs hydraulic network analysis again and this process continues until there is no pressure lower than the pressure limit in the system. The reason to use a pressure limit instead of zero is to increase the flexibility of the program. For example, it can be used to identify the areas with inadequate pressures for fire fighting by setting a pressure limit specified for fire fighting purposes.

217

7.2.6 Compilation of Results

This module compiles the hydraulic analysis results into the format compatible with GIS. It also provides a performance index to measure the system serviceability.

7.2.6.1 Hydraulic Network Analysis Results

The final hydraulic analysis results are compiled such that they can be linked to GIS. Because in GIS, junctions, pipes, pumps, valves, and tanks are different layers which can be exported from the H2ONET LADWP model database, the hydraulic analysis results are compiled for these five types of elements. Please note, reservoirs are treated as a special type of tanks which have fixed grade. The major outputs for pipes, valves, and pumps are the flow rate through them. The major outputs for junctions and tanks are the pressure and grade at them. For the components that are eliminated from the main system due to either negative pressure or connectivity problems, their results are set to zero to represent the isolation of these components. For deterministic simulation, the outputs for the five types of components are reported. For probabilistic simulation, the outputs for the five types of components are reported for the last run of the Monte Carlo simulation. The flow rates in pipes and pressures at junctions, which are the key outputs, are reported for each Monte Carlo simulation run. The mean, standard deviation, and coefficient of variation of the flow rate in each pipe and pressure at each node for all Monte Carlo simulation runs are also calculated and reported.

7.2.6.2   Performance Index

This module provides an index for measuring the seismic serviceability of a damaged water supply system.   The serviceability is defined as the ratio of the available demand to required demand corresponding to a seismic damage scenario,

$$S_s = \frac{Q_T}{Q_T^*} \tag{7.1}$$

where S_s is the serviceability, Q_T is the available demand, and Q_T^* is the required demand. The serviceability can be calculated for each demand node and for the entire system. For deterministic simulation, the serviceability for each demand node is either 0, if this demand node is isolated due to the negative pressure or connectivity problems, or 1, if this demand can be satisfied.   The serviceability for the entire system is the sum of the demands that can be satisfied over the sum of the total required demands. For probabilistic simulation, the system serviceability is reported in a matrix format. For each Monte Carlo simulation run, the serviceability is reported for each demand node and for the entire system. The mean, standard deviation, and coefficient of variation of the nodal and system serviceability for all Monte Carlo simulation runs are also calculated and reported.

7.3   GIRAFFE SIMULATION OF NORTHRIDGE EARTHQUAKE PERFORMANCE

To assess the capabilities of GIRAFFE, it was used to simulate the earthquake response of the LADWP system to the Northridge earthquake. The water outages and

flows at key locations, simulated by GIRAFFE, were compared with the documented water outages and flows measured by LADWP before and after the earthquake.

7.3.1　LADWP System Performance during Northridge Earthquake

The Northridge earthquake (M_w=6.7) struck Los Angeles at 4:30 a.m. local time on January 17, 1994. The damage to water supply systems during the Northridge earthquake is among the most extensive experienced in U.S. history, and is comparable to the damage sustained during the 1906 San Francisco and 1971 San Fernando earthquakes. The Northridge earthquake damaged 82 locations (Davis, 2003) in trunk lines (pipe diameter $\geq$ 610 mm, 24 in.) and 1013 locations (Jeon, 2002) in distribution lines (pipe diameter < 610 mm, 24 in.) in the LADWP system. Among the 82 trunk line repairs, 70 occurred in the LADWP trunk lines and 12 occurred in the trunk lines operated by Metropolitan Water District (MWD). The MWD trunk lines are embedded in the LADWP system and do not supply water to the LADWP system normally. Five water tanks in the LADWP system were also damaged. Approximately 15% of the population in Los Angeles was subjected to water outages, ranging from 1 to 7 days. Figure 7.2 shows the spatial distribution of the trunk line repairs, distribution repairs (Jeon and O'Rourke, 2005), damaged tanks (Brown, et al., 1995), and water outage areas (Lund et al., 2005) after the earthquake. Most locations of the component damage and subsequent water outage areas were in San Fernando Valley. The cost to repair the LADWP water supply system was about $44 million (Eguchi and Chung, 1995; Tierney, 1997). The detailed performance of the LADWP system during the Northridge earthquake is documented by Lund and Cooper (1995).
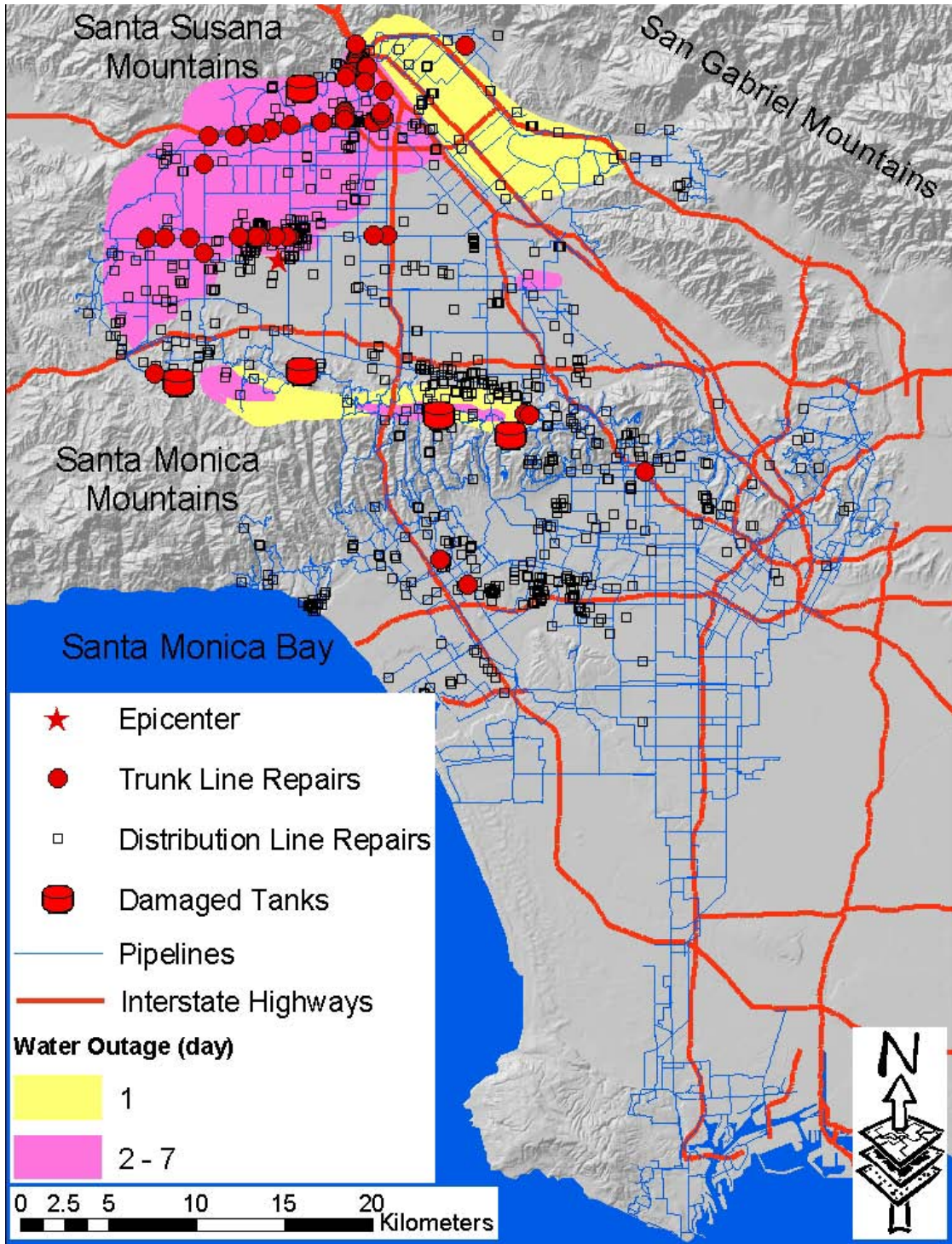
Figure 7.2 LADWP Damaged Tanks, Trunk and Distribution Line Repairs, and Water

Outage Areas after the Northridge Earthquake

221

7.3.2   LADWP Hydraulic Model for Northridge Earthquake

The multi-scale modeling technique developed in Chapter 6 is applied to simulate the LADWP water supply response to the Northridge earthquake. This technique simulates the trunk system response explicitly and simulates the distribution system response implicitly by increasing nodal demands in the trunk system. The LADWP system and the system-wide trunk system hydraulic model are described in Sections 6.3.1 and 6.3.2, respectively. Figure 7.2 shows that more than 95% of trunk line repairs, 80% of distribution repairs, all damaged tanks, and all water outages occurred in San Fernando Valley. To simplify the simulation, only the response of the LADWP system in San Fernando Valley, or northern half of the system, is simulated explicitly. This southern half of the system is simulated as boundary conditions.

The northern half of the system consists of six subsystems: Granada Hills (GH), Foothills (FH), Sunland/Tujunga (ST), Valley Floor (VF), Encino Hills (EH), and Santa Monica Mountains (SM). The hydraulic model for these six subsystems is called the Valley-Six submodel shown in Figure 7.3. The Valley-Six submodel consists of 4674 links and 3878 nodes to model the 967 km of pipelines, 76 regulator stations, 51 pump stations, 72 tanks and reservoirs, and 140 local groundwater wells. There are 188 valves in the 76 regulator stations and 167 pumps in the 51 pump stations. Each local groundwater well is equipped with a pump for extracting water.

There are 441 demand nodes distributed around the northern half of the system. The majority of nodal demands are smaller than 63 liters per second (1000 gpm), which are mostly consumed by local residents. A few nodal demands are higher than 63 liters per second (1000 gpm), and they are mainly related to industry usage. Three
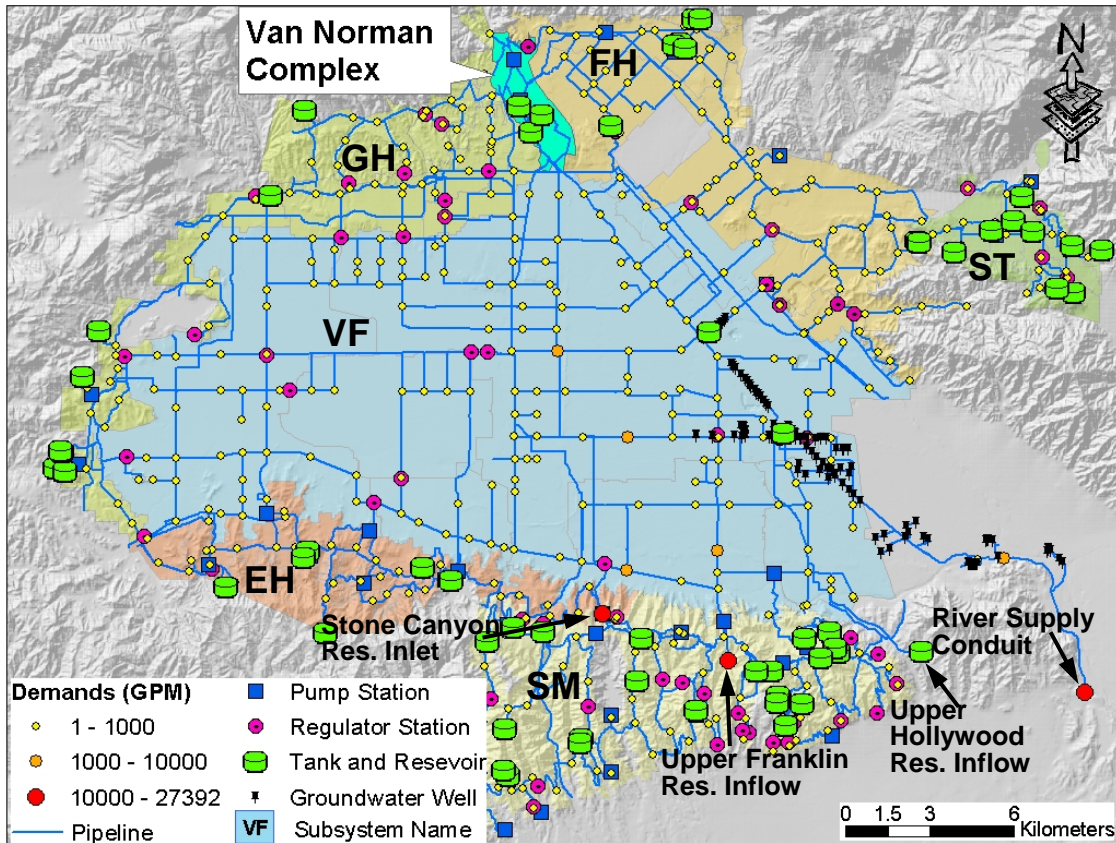
Figure 7.3 LADWP Hydraulic Model for Northridge Earthquake Simulation

(1000 gpm = 63 L/s)

nodes, indicated as big red dots at Stone Canyon Reservoir Inlet, Upper Franklin Reservoir Inflow, and River Supply Conduit in Figure 7.3, have a demand larger than 630 liters per second (10,000 gpm), which are virtual demands representing water flow to the southern half of the system. Another connection between the Valley-Six submodel and the southern half of the system is the Upper Hollywood Reservoir Inflow, which is modeled as a virtual tank, representing water transportation to and from the Upper Hollywood Reservoir. These virtual elements serve as the boundary conditions for the Valley-Six submodel. The response of the Valley-Six subsystem can be simulated after setting boundary conditions.

7.3.3 Damage Simulation

To simulate the response of the Valley-Six subsystem, the damage to components needs to be added into the model, followed by hydraulic network analysis using GIRAFFE. The damage simulation is discussed in the following sections.

7.3.3.1 Trunk Line Damage

Because the MWD trunk lines did not supply water to the LADWP customers during the Northridge earthquake, the 12 locations of damage in the MWD trunk lines were not simulated. Among the 70 locations of LADWP trunk line damage, 67 are in the trunk lines in the Valley-Six hydraulic model. One location is in the southern half of the LADWP system. The other two locations are in the trunk lines, which are not included in the hydraulic network model. These three locations were not simulated.

The detailed simulations of the 66 locations of LADWP trunk line damage are described in Appendix C. In total, three breaks, in the Granada Trunk Line (GTL), Rinaldi Trunk Line (RTL), and LA City Trunk Line, respectively, and 26 leaks were simulated. The leaks were classified into five scenarios based on the damage descriptions in Tables C1 to C5. The opening area of each leak was calculated using the equations developed in Section 5.4.4. Multiple leaks, which are located close to each other in the same pipeline, were simulated as one leak with an appropriately increased orifice area. Leaks and breaks, which are located close to each other in the same pipeline, were simulated as one break by disconnecting the pipeline completely.

7.3.3.2 Distribution Line Damage

Distribution lines account for the highest proportion of components in the LADWP system, and suffered the most extensive damage during the 1994 Northridge earthquake. A comprehensive GIS database, including information on distribution pipeline length, composition, size, and repairs after the Northridge earthquake, was developed by O'Rourke and Toprak (1997), O'Rourke et al. (1996), and Toprak (1999). The total length of the LADWP distribution lines is about 10,750 km with 72% composed of cast iron. Most pipelines have a diameter of 150 mm (46%) or 200 mm (27%). There were 1,405 original repair records provided by LADWP. After a careful evaluation of them, it was determined that 1,013 records were valid for damage to distribution mains. It was further found that only 944 out of 1,013 repairs have pipe composition and geodetic coordinates. The 944 repairs were used to develop the regression relationships between RR and PGV for pipelines composed of different materials. The procedures for developing the regressions are provided by Jeon (2002). These regressions can be used to estimate the damage to distribution lines in future earthquakes.

Since distribution lines are not modeled explicitly in the LADWP trunk model, it is not able to model damage to distribution lines directly. To include the effects of damage to distribution lines, the method developed in Chapter 6 is applied, in which the distribution damage was implicitly modeled as increased demands at nodes in the trunk system. To apply this method, the PGV contours, developed by Jeon (2002) using the PGV recordings collected at 148 strong motion stations after the Northridge earthquake, were used to obtain the PGV associated with each demand node. The detailed procedures for generating the PGV contours are described by Jeon (2002).

225

When the PGV contour GIS and demand node GIS combined, the PGV in association with each demand was determined. This PGV represents the PGV for the distribution network around the demand node. The distribution network RR was then calculated based on the linear regression relationship for cast iron pipelines developed by Jeon (2002)

$$Ln(RR) = 1.21Ln(PGV) - 6.81 \qquad (7.2)$$

Hydraulic network analysis was performed on the trunk model prior to earthquake damage. The pressure was summarized for nodes in each pressure zone and the mean pressure, MP, was calculated. The MP was assigned to each demand node within the pressure zone. With the known mean pressure, MP, and repair rate, RR, the normalized demand was calculated by

$$
\begin{aligned}
ND &= I + S \times RR \\
&= (II + IS \times MP) + (SI + SS \times MP) \times RR \qquad (7.3) \\
&= (0.9012 + 0.0036 \times MP) + (-0.877 + 0.0248 \times MP) \times RR
\end{aligned}
$$

where all the symbols have the same meaning as those used in Equation 6.6 in Section 6.4.3.2. In contrast to Equation 6.6, which includes a noise term for slope, S, and intercept, I, respectively, to model the uncertainties associated with normalized demands, Equation 7.3 is deterministic for the Northridge earthquake scenario.

The distribution of normalized demands is shown in Figure 7.4. This figure shows that the demands increase by 1 to 2.8 times the customer demand due to damage to distribution lines during the Northridge earthquake. The nodes with the highest normalized demand are located in the Van Norman Complex area, where the

226
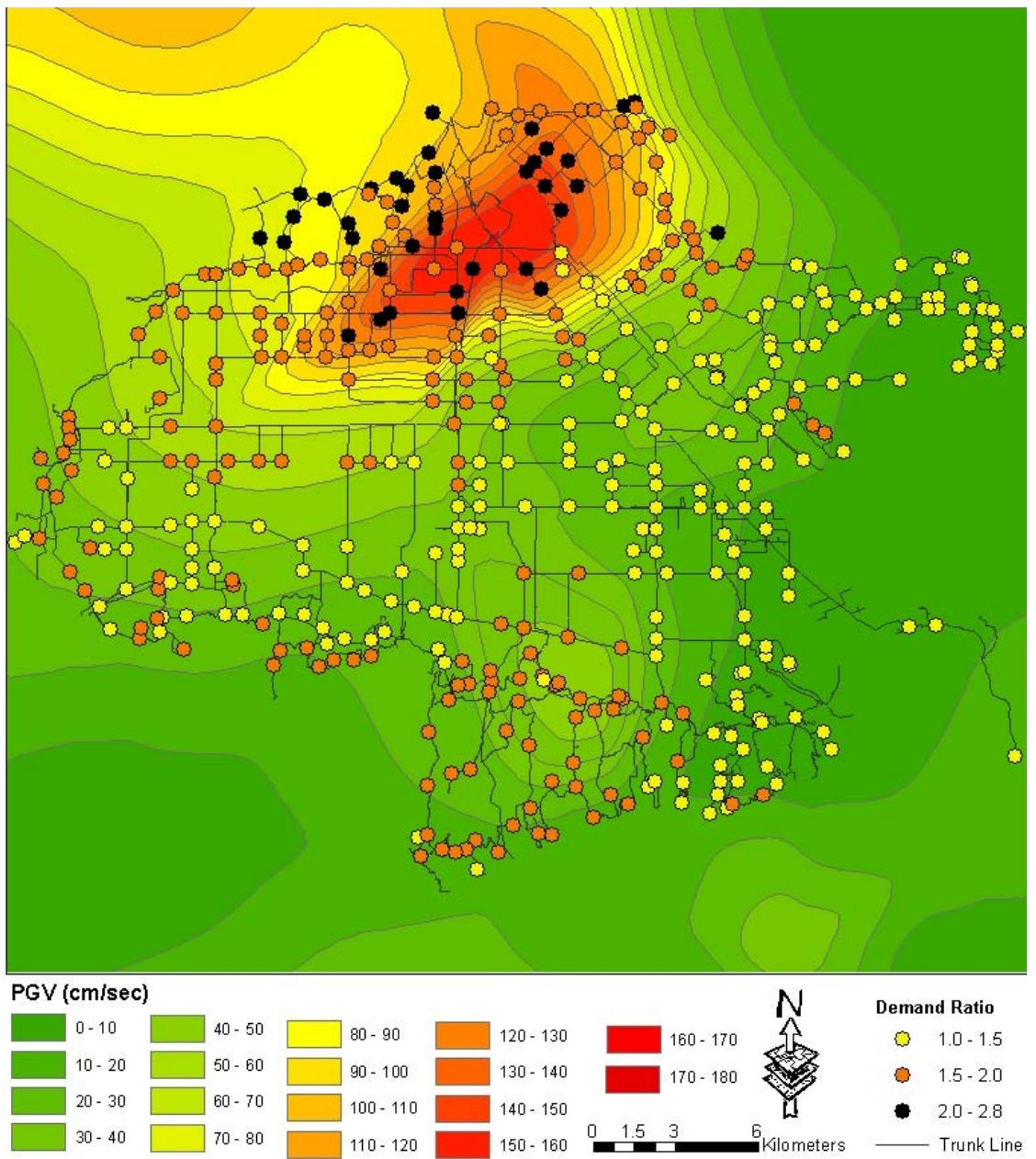
Figure 7.4 Normalized Demands of Valley-Six Subsystem after Northridge Earthquake

PGVs are the highest. In general, the normalized demands in mountainous areas are higher than those in flat areas because the pipe internal pressure in mountainous areas is higher than that in flat areas. The high variation of elevations in the mountainous areas requires a high overall pressure to supply customers at multiple locations.

7.3.3.3   Tank Damage

In general, reservoirs and water tanks performed well during the Northridge earthquake. Brown et al. (1995) summarized the performance of 65 LADWP tanks in service at the time of earthquake (48 welded or riveted steel tanks and 17 reinforced concrete or prestressed concrete tanks). Only 5 tanks were damaged. The damaged tanks are indicated as pink symbols in Figure 7.5. Roof collapse and inlet/outlet pipe damage occurred in the Coldwater Canyon, Beverly Glen, and Zelzah Tanks. The Granada High Tank collapsed completely and was removed permanently from service after the earthquake. Inlet/outlet pipe damage occurred to the Topanga Tank. Since damage to all these tanks occurred to the inlet/outlet pipes, the inlet/outlet pipes were disconnected in the hydraulic network simulation of post-earthquake performance. The current LADWP trunk line model, which was used in this research, does not include the Granada High Tank, and therefore, it was not simulated.

It was known through personal communications with LADWP engineers (Vargas, 2005; Adams, 2005) that the Kittridge Tanks (including the Kittridge Tank No 1 and 2) and De Soto Reservoir were depleted shortly after the earthquake. The Kittridge Tanks are located along the western margin of San Fernando Valley and supplied by the GTL. The broken section of the GTL cut off the water source to the

228
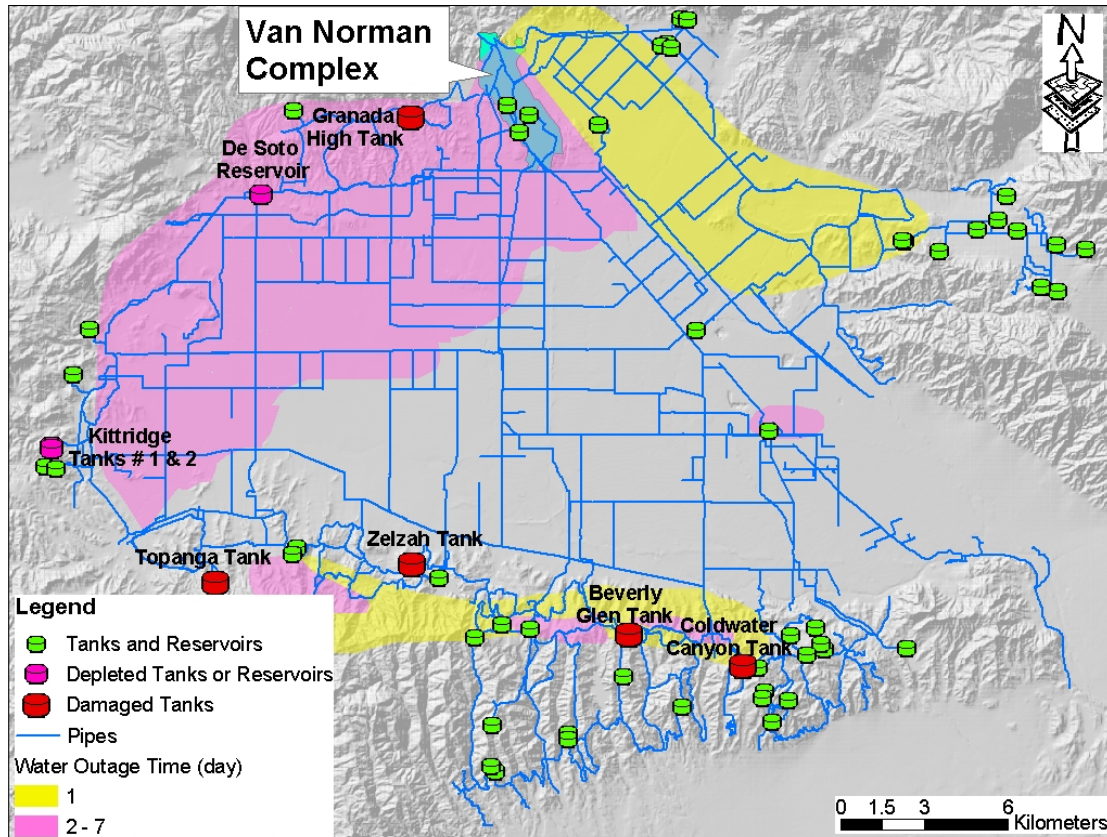
Figure 7.5 LADWP Tanks and Reservoirs, and Damaged Tanks

after Northridge Earthquake

Kittridge Tanks and was not able to refill them for over one week after their depletion.

The De Soto Reservoir is located along the northern margin of San Fernando Valley

and supplied by the RTL. The broken section of the RTL cut off the water source to

the De Soto Reservoir. The RTL was not able to refill the reservoir for over one week

after its depletion. Numerical simulation results showed that the Kittridge Tanks and

De Soto Reservoir would be depleted in about 2 and 1 hours after the earthquake,

respectively, if not refilled. To include the effects of the depletion of the Kittridge

Tanks and De Soto Reservoir, they were closed after the earthquake in the simulations.

7.3.3.4 Water-Electric Power Interaction

The interaction between water and electric power was accounted for in the simulation. The Northridge earthquake caused a system-wide blackout of the LADWP electric power system immediately after the earthquake, and it took from 1 to 27 hours to restore power (LADWP, 1994). The electric power outage affected the operation of pump stations directly. The spatial distributions of pump stations and electricity outage time are shown in Figure 7.6. A large portion of pump stations are located around the Santa Monica Mountains, where the electricity outage time was less than 8 hours. A small portion of pump stations are located in San Fernando Valley, Granada Hills, Foothills, and Sunland/Tujunga, where the electricity outage lasted for 15-27 hours. Generally, pump stations have diesel generators as backup power. The performance of pump stations during previous natural disasters showed that the diesel generators were able to generate enough power for the operation of small pump stations, but not enough for large ones. The largest pump station, Van Norman Pump Station No. 2, is located in the Van Norman Complex, where the electricity outage lasted for the longest time. Accordingly, the Van Norman Pump Station No. 2 was turned off in the hydraulic network simulation of post-earthquake performance.

7.3.4 SCADA Data

To monitor network performance, the LADWP operates a Supervisory Control and Data Acquisition (SCADA) system. The records of flow meters before and after the earthquake in the northern half of the system were collected and reviewed. Due to the earthquake damage and electricity outage, some of the SCADA data are not
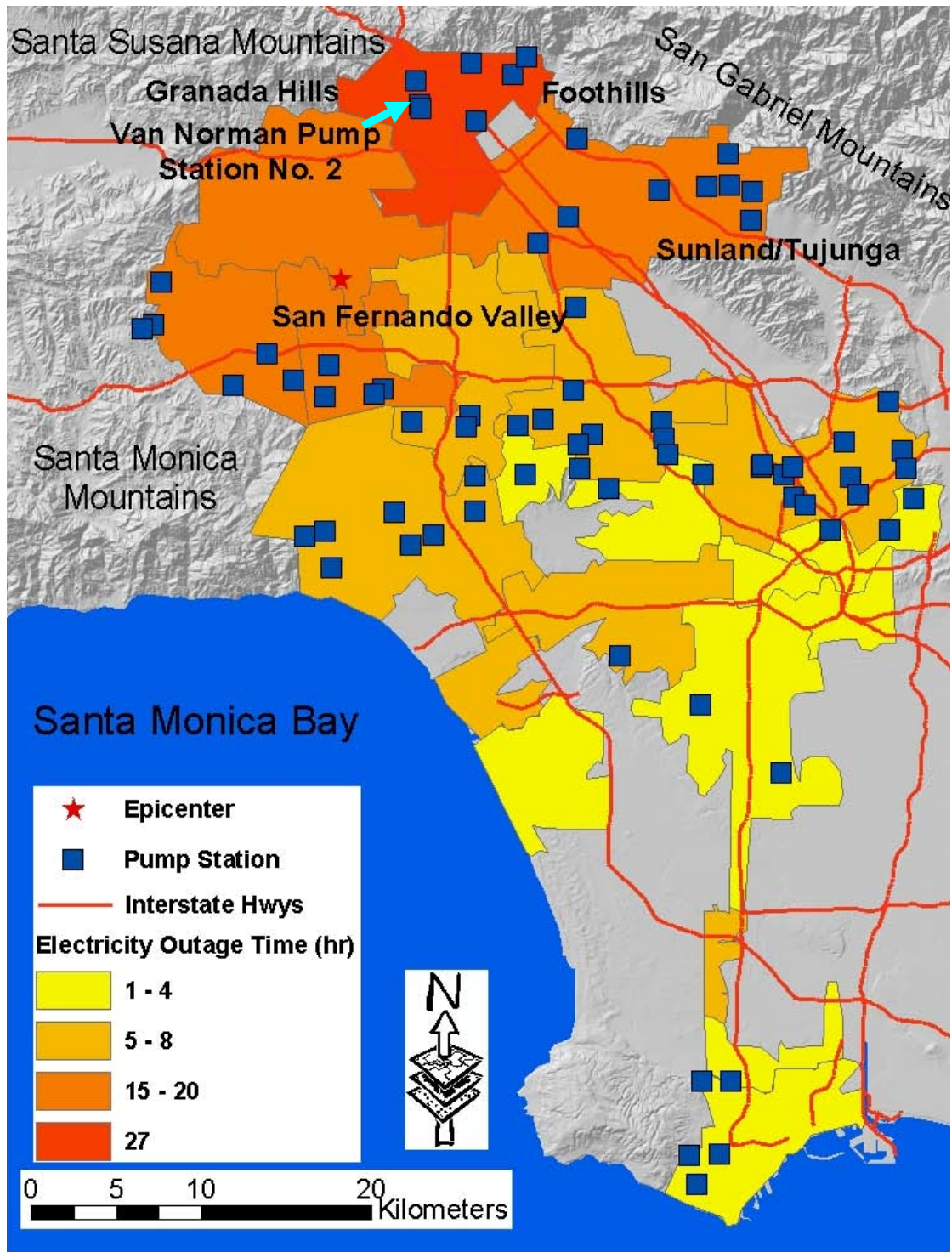
Figure 7.6 Superposition of Spatial Distribution of Electricity Outage Time and Pump

Stations

reliable. A screening process was, therefore, conducted before utilizing the SCADA data. Two screening criteria were adopted to assure the quality of the data: 1) the meters indicating zero flow before and after the earthquake were considered to have malfunctioned or have been out of service; and 2) the meters with a maximum recorded flow smaller than 63 liters per second (1000 gpm) were not used because the flows in such lines are too small and too sensitive to local variations in predicted damage. Records at 13 locations were selected and utilized for three major purposes: 1) setting boundary conditions, 2) providing clues on system reconfiguration shortly after the earthquake; and 3) comparing monitored and simulated flows.

7.3.4.1   Boundary Conditions

The four flow meter records at the River Supply Conduit, Upper Hollywood Reservoir Inflow, Upper Franklin Reservoir Inflow, and Stone Canyon Reservoir Inlet, which are indicated as red circles in Figure 7.7, were used to set boundary conditions. The virtual demands at nodes for the River Supply Conduit, Upper Franklin Reservoir Inflow, and Stone Canyon Reservoir Inlet, representing flows to the southern half of the system, were recalibrated in accordance with the actual flow records at the three locations before and after the earthquake, respectively. The virtual tank, Upper Hollywood Reservoir, was changed to a virtual demand node and its demand was calibrated in accordance with the actual flow records.

7.3.4.2   System Reconfiguration

Three flow meter records, at the LA City, Haskell, and Hayvenhurst Trunk Lines in the lower Van Norman Complex, respectively, as illustrated by green squares
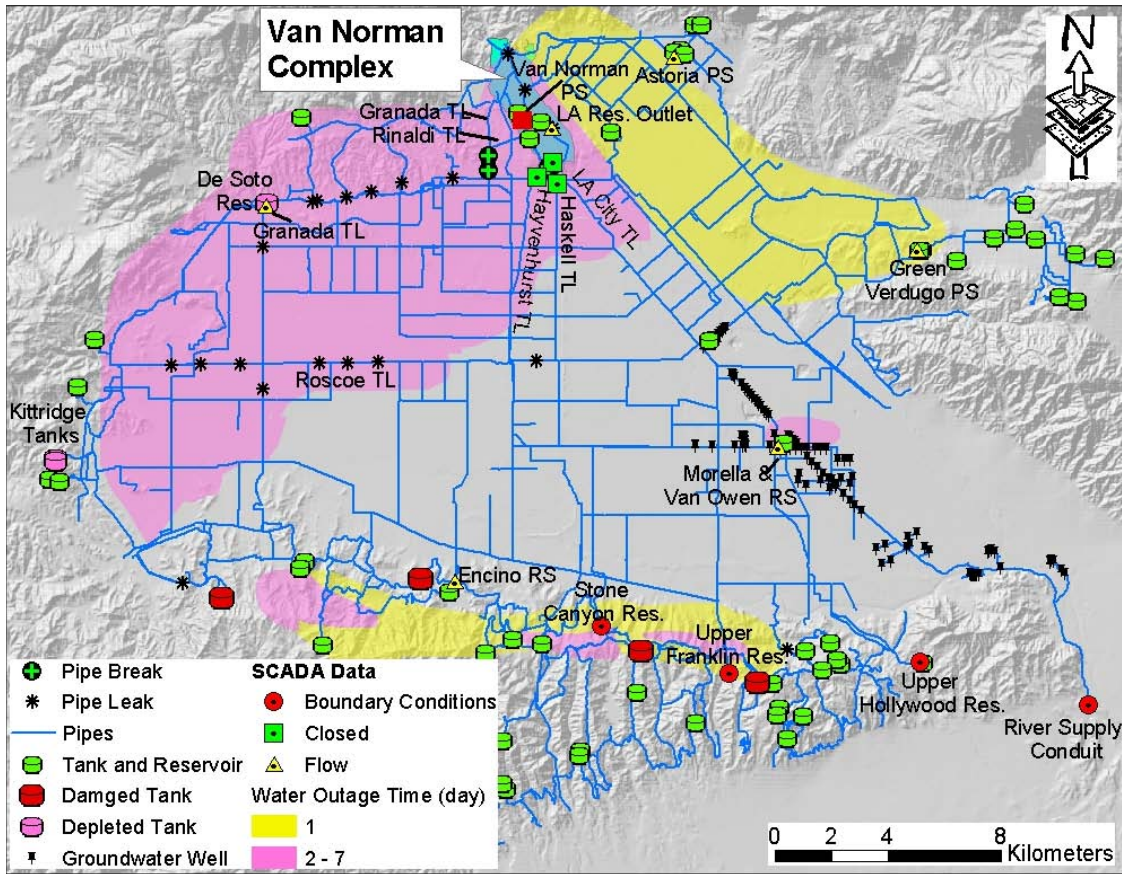
Figure 7.7 System Damage and SCADA Flow Meters

in Figure 7.7, were utilized to provide guidance on how the system was reconfigured shortly after the earthquake.   The three flow meter records showed that flows decreased to zero shortly after the earthquake, indicating that local damage had been isolated to curtail water losses.   The isolated section of the LA City Trunk Line is located upstream of its connection with the LA Reservoir Outlet, the main water source to the LA City Trunk Line. Therefore, the isolation had little impact on the water flow southward through the LA City Trunk Line.

233

7.3.4.3　Flow Comparison

Six SCADA flow meters records at the LA Reservoir Outlet, Encino Reservoir outflow, Granada Trunk Line, Morella & Van Owen Regulator Station, Astoria Pump Station, and Green Verdugo Pump Station, respectively, were used to compare the measured flows and simulation results. The flow meters are shown as yellow triangles in Figure 7.7.

7.3.5　Simulation Results

Since the Northridge earthquake occurred in January, a typical winter demand was applied in the simulation. The Valley-Six hydraulic model was exported from H2ONET software and imported into GIRAFFE. Component damage was then added into the network model and hydraulic network analysis was performed. Figure 7.8 shows the GIRAFFE simulation results, superimposed by the observed water outages (Lund et al., 2005). The original no-flow pipes in the intact system and the damage-induced no-flow pipes are color coded by pink and red, respectively. The unsatisfied demands, from which the customers should not receive water, are illustrated by yellow dots. Most damage-induced no-flow pipes and unsatisfied demands are consistent with the areas of observed water outage for 2 days or more. The water outages of less than a day are related to temporary isolations that were restored after inspections revealed no serious damage to local trunk lines.

Figure 7.9 shows detailed comparisons between GIRAFFE simulations and the recorded flows. In general, the simulated flows compare favorably with the monitored flows at each location.
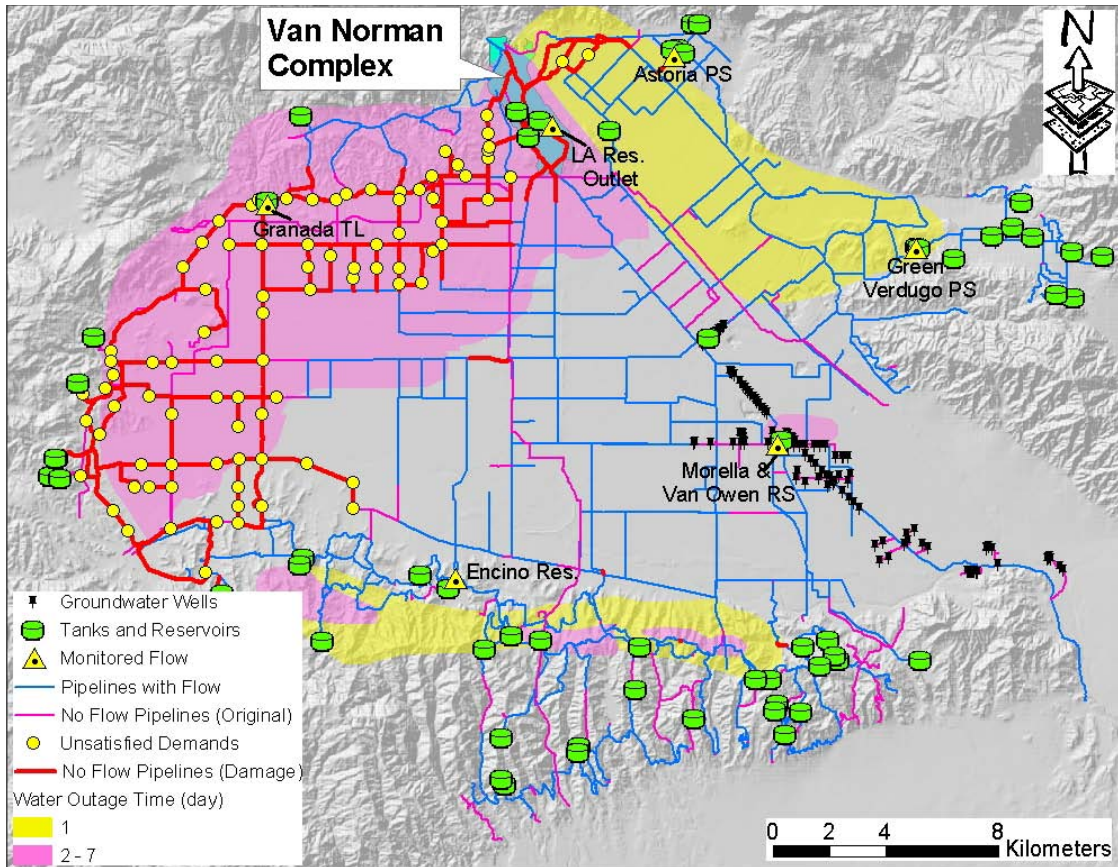
Figure 7.8 GIRAFFE Simulation Results

Figure 7.9a shows that the monitored flows in the LA Reservoir Outlet varied from 11,500 to 14,000 L/s depending on fluctuations in demand at different times of the day. The flow reached its lowest value roughly at midnight and highest at 8 to 9 o'clock in the morning, reflecting the lowest and highest water consumptions at these times. The steady state simulation shows that the flow rate in the LA Reservoir Outlet prior to the earthquake was 12,100 L/s, which represents a rough average of the monitored daily flows. The flow from the LA Reservoir increased to roughly 20,000 L/s shortly after the earthquake because of water losses from damage to major trunk lines downstream of it. As discussed in Section 7.3.3.2, the LA City, Haskell, and Hayvenhurst Trunk Lines, which are supplied by the LA Reservoir Outlet, sustained
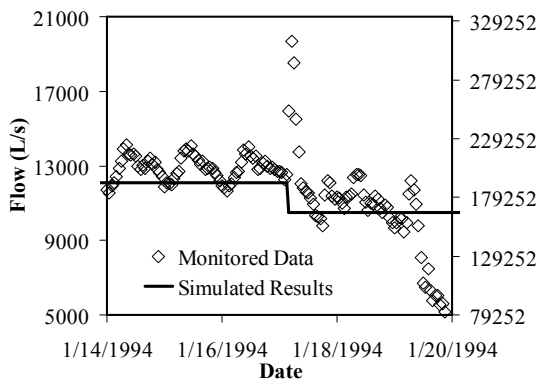
(a) LA Reservoir Outlet
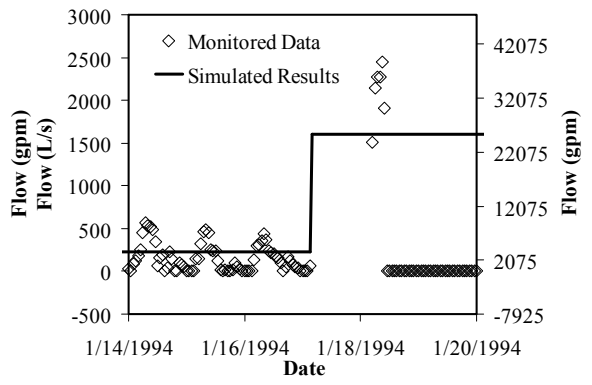
(b) Encino Reservoir Outflow
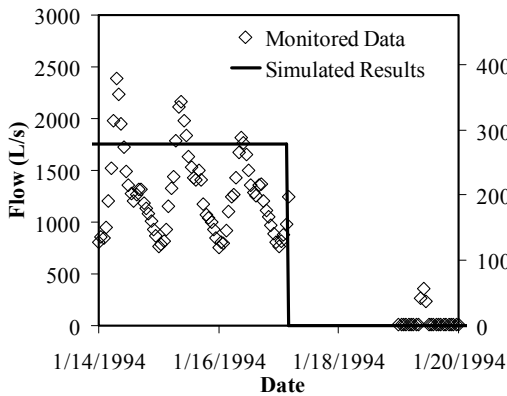
(c) Granada Trunk Line Flow
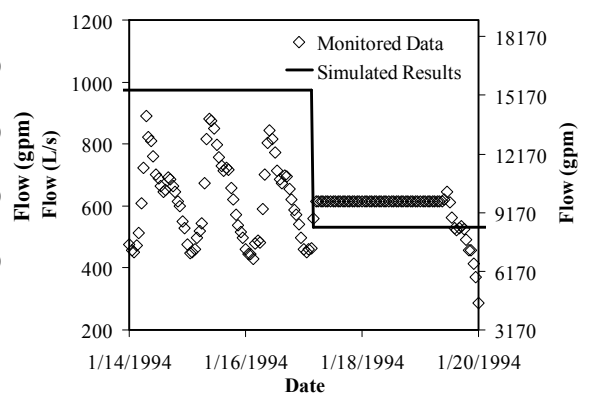
(d) Morella & Van Owen Regulator Station
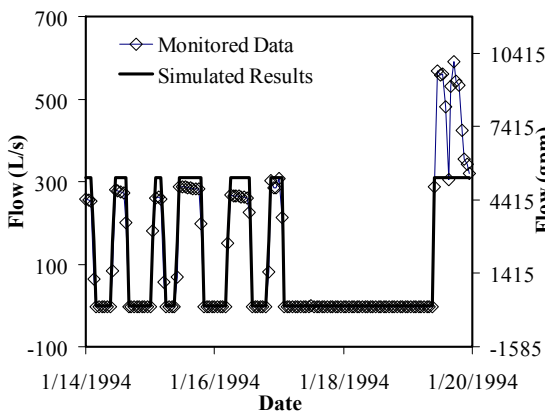
(e) Astoria Pump Station
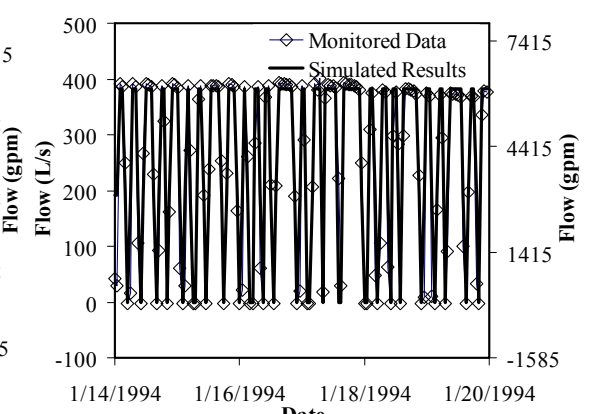
(f) Green Verdugo Pump Station

Figure 7.9 Comparisons Between GIRAFFE Results and Monitored Data

236

severe damage during the earthquake and were promptly isolated in the lower Van Norman Complex after the earthquake to curtail water losses. After isolation, the flow in the LA Reservoir Outlet dropped to between 10,000 and 12,500 L/s. The post-earthquake simulation was performed after the isolation of the three pipe sections and showed that the flow rate in the LA Reservoir Outlet is 10,500 L/s, which falls in the range of monitored flows after the earthquake. Five days after the earthquake, flow in the LA Reservoir Outlet decreased as repairs were undertaken in the LA aqueducts and Van Norman Complex. Decreased flow related to system repairs was not simulated.

Figure 7.9b shows that the monitored flows at the Encino Reservoir Outflow station vary from 0 to 550 L/s depending on fluctuations in demand. The simulated flow prior to earthquake is roughly 250 L/s, which lies in the range of the monitored flows. The earthquake increased flows at the Encino Reservoir Outflow station significantly. This is because the Encino Reservoir had to provide more water to the southern part of San Fernando Valley after the earthquake to compensate the loss of water sources, which are normally from the northern part of San Fernando Valley. The post-earthquake simulated flow is 1600 L/s, which is within the range of monitored flows, varying from 1500 to 2500 L/s.

Figure 7.9c shows that the Granada Trunk Line (GTL) supplies roughly 750 to 2500 L/s water to customers in normal situations. The simulated flow rate, 1750 L/s, represents a rough average of the real flow rates. The earthquake ruptured the GTL completely and resulted in zero simulated flow, which is consistent with the monitored zero flow rate.

Figure 7.9d shows that roughly 400 to 900 L/s of water flows through the Morella & Van Owen Regulator Station prior to earthquake. The simulated flow rate, 970 L/s, is approximately 10 % higher than the highest monitored flow. The water source of the Morella & Van Owen Regulator Station is from local groundwater wells. It is possible that LADWP uses more water from local groundwater wells in recent years, which results in a higher flow through the Morella & Van Owen Regulator Station than the monitored flows before the Northridge earthquake. After the earthquake, the simulated flow drops to 550 L/s, which is roughly 10 % lower than the monitored flow.

Figure 7.9e shows that the simulated flows vary from 0 to 300 L/s at Astoria Pump Station, which matches the monitored flows very well. After the earthquake, both the simulated and monitored flows at the Astoria Pump Station drop to zero. The fluctuations of flow rates after January 19 might be associated with system repairs and testing of the pump station. These fluctuations were not simulated in this study.

Figure 7.9f shows that the simulated and monitored water flows through the Green Verdugo Pump Station are very consistent. The earthquake did not affect water flows through the Green Verdugo Pump Station because it is located far away from the system damage that occurred in the San Fernando Valley.

It should be noted that there are some differences between the 1994 system in operation during the Northridge earthquake and the 2002 system represented by the hydraulic network model. One example is the Granada High Tank, which collapsed during the 1994 Northridge earthquake and was removed from the system. Also, the

demand used in the simulation is based on the typical winter demand used in the 2002 system model, which may slightly be different from the demand in January 1994.

In general, the GIRAFFE simulation compares favorably with the major features of the observed response of the LADWP system during the 1994 Northridge earthquake. The validated GIRAFFE was applied as a major tool for the seismic performance evaluation of the LADWP system in conjunction with the state-of-the-art seismic hazard characterization in the California area. The evaluation was conducted by Wang (2006). In his study, the LADWP system response simulation was performed for 59 earthquake scenarios and system serviceability risk curves were constructed based on the simulation results. The simulation results and risk curves are logic and being used for community restoration, emergency planning, and regional economic impact assessments.

CHAPTER 8

SUMMARY AND CONCLUSIONS

8.1 INTRODUCTION

This report describes a comprehensive model for simulating the earthquake performance of water supply systems. The model is developed in conjunction with the water supply system operated by the Los Angeles Department of Water and Power (LADWP). It includes an algorithm for the hydraulic network simulations of heavily damaged water supply systems, an analytical model for analyzing seismic wave interaction with underground water supply pipelines, methods for simulating pipeline breaks and leaks in hydraulic network analysis, and a multi-scale technique for modeling complex water supply systems. The model is implemented in a computer code, GIRAFFE, which is validated by a favorable comparison of simulation results with observations and flow measurements for the heavily damaged LADWP water supply after the 1994 Northridge earthquake. The validated model is used as a major tool by Wang (2006) for the system performance evaluation of the LADWP water supply system in conjunction with state-of-the-art seismic hazard characterizations.

This chapter provides a summary of major research findings associated with the report. The sections that follow are organized to present a summary and research findings that correspond to the five objectives of the research, pertaining to: 1) hydraulic network analysis for damaged systems; 2) seismic response of buried pipelines to surface wave effects; 3) pipe damage modeling; 4) multi-scale technique for water supply system modeling; and 5) evaluation of Northridge earthquake

performance. The final section provides a discussion of research needs and future research directions.

8.2   HYDRAULIC NETWORK ANALYSIS FOR DAMAGED SYSTEMS

In this study, hydraulic simulation procedures for heavily damaged water supply systems are developed on the basis of an iterative approach to isolate the network nodes with negative pressures. They are implemented in a computer code, referred to as Graphical Iterative Response Analysis for Flow Following Earthquakes (GIRAFFE).

After conventional hydraulic network analysis of the damaged system, nodes with negative pressures are identified in GIRAFFE and isolated step by step, starting with the one of highest negative pressure. The isolation is simulated by eliminating the node and all the connected links. After each elimination, the flow and pressure conditions are updated.

The isolation approach, in effect, expresses a damage state as an operational state by converting the damaged network into one that meets the requirements of positive pressure and flow in all pipes. By eliminating pipelines with unreliable flow, it has the practical advantage of showing the system operator what parts of the network are no longer functional, and thus provides information about the most vulnerable distribution sectors and potential strategies for mitigation. The model does not account explicitly for water delivery and pressure losses associated with unsteady flow because accurate network analyses for this condition are not available. Instead,

the model removes the unreliable portions of the system to display the remaining part of the network that meets threshold serviceability requirements for positive pressure.

The computer code, GIRAFFE, builds on an open source hydraulic engine EPANET and employs the iterative approach for the treatment of negative pressures in the damaged water supply system. GIRAFFE incorporates algorithms for simulating various levels of leakage and assessing earthquake demand associated with distribution networks using fragility curves. GIRAFFE provides both deterministic and probabilistic simulation options with simulation results can be directly linked to GIS for visualization and map presentations.

8.3   SEISMIC RESPONSE OF BURIED PIPELINES TO SURFACE WAVE EFFECTS

Surface waves are generated by the reflection and refraction of body waves at the ground surface. Under the appropriate conditions, surface waves can be more potentially hazardous to buried pipelines than body waves by driving higher ground strains due to their relatively low phase velocity. When surface waves propagate along underground pipelines, the ground deformation transfers shear force to the pipeline. Because of the relatively low phase velocity of surface waves, the strain accumulation rate of ground soil is generally higher than that of the pipeline so that the pipeline is not able to deform in unison with the ground soil. The pipeline therefore exhibits a relatively rigid behavior under the surface wave effects.

Jointed concrete cylinder pipelines (JCCPs) are typically coupled with mortared, rubber-gasket bell-and-spigot joints. The JCCP joints are vulnerable to

axial pullout failure because of their relatively low tensile capacity with respect to both axial tensile force and displacement. Finite element analyses predicted a relative joint displacement of 16 cm for a-1829-mm-diameter JCCP under the action of the surface waves recorded during the 1985 Michoacan earthquake in Mexico City. The high predicted relative joint displacement indicates a strong potential of joint pullout and disengagement when the JCCP is affected by surface waves.

In conjunction with Wang's work (2006) on body wave effects, a dimensionless chart that incorporates the key parameters on pipeline properties, ground conditions, and wave characteristics is developed based on 320 runs of finite element simulations. This chart can be used to facilitate the computation of the joint pullout movement of virtually any conventional JCCPs affected by seismic waves. By accounting for the cracking of joint concrete mortar, the relative joint pullout movement of JCCPs is reduced significantly, because the joint cracking prevents strain accumulation across the cracked joints and reduces strain accumulation length along the pipeline. Roughly 6 cm of relative joint pullout movement was predicted for the-1829-mm-diameter JCCP under the action of a sinusoidal wave with peak ground velocity (PGV), phase velocity, and predominant period consistent with the PGV, phase velocity, and predominant period of the surface waves recorded during the 1985 Michoacan earthquake in Mexico City.

The analytical model is applied to other types of pipelines, such as cast iron (CI) trunk and distribution mains with lead-caulked joints. The lead-caulked joints have ductile pullout characteristics. The joint pullout resistance remains approximately constant after external tensile force reaches the maximum tensile capacity of the joint. The ductility of joint reduces the joint pullout displacement

244

compared with joints with brittle pullout characteristics, such as the JCCP joint. The reduction of the relative joint displacement can be estimated using dimensionless reduction curves developed on the basis of 150 runs of finite element simulations. By using the dimensionless chart and reduction curves together, it is able to estimate the joint pullout displacement of CI pipelines under the effects of virtually any seismic waves.

8.4   PIPE DAMAGE MODELING

Pipeline damage may result in substantial reduction of water and pressure, and change the flow patterns in a water supply system. A rational model for pipe damage simulation is needed for an accurate prediction of flow and pressure conditions in the water supply systems after earthquakes.

Pipe damage is classified into breaks and leaks. A break is modeled by completely disconnecting the original pipeline and opening the disconnected ends into the atmosphere.

A pipe leak is modeled as a fictitious pipe with one end connected to the leaking pipe and the other end open to the atmosphere. The roughness and minor loss coefficients of the fictitious pipe are taken as infinite and 1, respectively, such that all energy loss from the leak is related to the minor loss. The diameter of the fictitious pipe is determined by the leak orifice area. The validation of the leak simulation model using sprinkler data from the Nation Fire Protection Association shows that the water loss from the leak simulation is consistent with the water discharge from real sprinklers.

245

A review of pipe material properties, joint characteristics, and damage mechanisms, showed that pipe leaks can be classified into five types, which are annular disengagement, round crack, longitudinal crack, local loss of pipe wall, and local tear of pipe wall. This classification provides a rational basis for estimating leak orifice areas associated with various types of pipelines. Field observations from previous earthquakes found that leak orifice areas are, in general, related to pipe size. As such the orifice areas are simulated as a function of pipe diameter. Mathematical formulations relating orifice area to pipe diameter are developed for each leak type. Default values for the parameters used in these formulations are proposed. Probabilities for each leak type in association with various types of pipelines are estimated for Monte Carlo simulations.

The pipe leak and break models are implemented into hydraulic networks both deterministically and probabilistically. The deterministic implementation specifies the number and location of leaks and breaks, and the orifice area of each leak in the network. The probabilistic implementation generates randomly distributed pipe breaks and leaks in the network by assuming pipe damage follows a Poisson process with a mean arrival rate equal to repair rate. The repair rate is related to seismic hazard parameters, such as peak ground velocity and permanent ground deformation.

8.5 MULTI-SCALE TECHNIQUE FOR WATER SUPPLY SYSTEM MODELING

The LADWP water supply system response is simulated with a multi-scale technique that uses a hydraulic network model to represent the trunk line system with demand nodes connected to local distribution pipeline networks. The trunk line

system model includes 2200 km of pipelines, with diameters ranging from 300 (12) to 3850 mm (152 in.). The remaining 9800 km of pipelines, which are typically small diameter distribution lines, are replaced with demand nodes. Using this trunk line model for earthquake simulations, seismic damage to trunk lines are simulated explicitly by adding breaks and leaks, and damage to distribution lines are simulated implicitly by increasing demands at nodes in the trunk system. The increased demands are simulated by means of fragility curves relating demand to repair rate in the local distribution networks. The fragility curves are developed on the basis of Monte Carlo simulation results from five representative LADWP distribution networks.

Distribution network simulation results show that normalized demand (ND), defined as the ratio of demand after damage to a distribution network to that before damage, can be linearly correlated with repair rate, RR. The intercept and slope of the linear regressions of ND vs RR can be further correlated with a physical parameter, the mean pressure, MP, of the distribution network. The intercept and slope are statistically estimated from the Monte Carlo simulation data in the five representative distribution networks. Two methods, linear regressions with noise terms and 90% confidence level estimates, are proposed to estimate the slope and intercept of the linear regressions of ND vs RR.

8.6 EVALUATION OF NORTHRIDGE EARTHQUAKE PERFORMANCE

GIRAFFE is validated using the case history of the LADWP system response to the 1994 Northridge earthquake. Damage data from previous studies shows that more than 95% of LADWP trunk line repairs, 80% of distribution repairs, all damaged

tanks, and all water outages after the Northridge earthquake occurred in the San Fernando Valley. The LADWP system response to the Northridge earthquake was, therefore, simulated with the hydraulic network model, which covers the San Fernando Valley, or northern half of the system. The southern half of the system was simulated as boundary conditions, which were calibrated using the flow meter records from the SCADA data in the pre- and post-earthquake simulations.

The LADWP trunk line damage was simulated explicitly by adding breaks and leaks in the network. In total, 3 breaks and 26 leaks were simulated. The distribution line damage was simulated by increasing the demands at nodes in the trunk system using fragility curves. The damaged tanks were simulated by disconnecting the inlet/outlet pipes. The large pumps, which were not able to operate after the earthquake because of the electric power outage and lack of enough backup power, were closed in the post-earthquake simulation.

The GIRAFFE simulation results are shown to produce water outages consistent with the documented damage-induced water outages after the earthquake. The GIRAFFE simulated flows at key locations compare favorably with monitored flows by LADWP before and after the earthquake. The difference between the monitored and simulated flows is generally less than 10%.

8.7   FUTURE RESEARCH DIRECTIONS

The algorithm for the hydraulic network simulations of heavily damaged water supply systems developed in this study discounts unreliable flows through partial flow nodes because of the complicated flow conditions, which are not able to be solved

248

using current hydraulic network modeling techniques. It would be valuable to develop an algorithm, which is able to analyze the flow conditions around partial flow nodes. This algorithm can be implemented into hydraulic network analysis software packages to provide a more accurate prediction of flow and pressure conditions in heavily damaged systems.

The majority of pipe damage occurs as leaks. A key parameter for leakage simulation in hydraulic network analysis is the leak orifice area, which is determined by pipe material properties, joint characteristics, and earthquake damage mechanisms. The classification of leak types proposed in this study provides a rational basis for leakage simulation. The modeling procedures would be improved by a more detailed study of field data and experimental verification.

The current simulation model accounts for damage to pipelines, which are the most vulnerable components in water supply systems. The performance of tanks is incorporated in the model by accounting for water losses with time from damaged pipelines, as described by Wang (2006). Damaged tanks are modeled by disconnecting the inlet/outlet pipelines. Also loss of electric power is accounted for by the disruption of pump operations. Improvements of the simulations can be realized by developing more comprehensive models for components such as tanks, pumps, and regulator valves. Such models should be based on fragility curves that account for uncertainty in performance and are consistent with the probabilistic approach adopted in this work.

CHAPTER 9
REFERENCES

Adams, M. (2005). Personal Communications.

American Lifelines Alliance (2005). *Seismic Guidelines for Water Pipelines*. http://www.americanlifelinesalliance.org.

American Water Works Association (AWWA, 1964). "Steel Pipe Design and Installation." *AWWA Manual M11*. AWWA, Denver, CO.

American Water Works Association (AWWA, 1999). "Prestressed Concrete Pipe, Steel-Cylinder Type." *AWWA Standard C301-99*. AWWA, Denver, CO, 33p.

American Water Works Association (AWWA, 2002). "Concrete Pressure Pipe, Bar-Wrapped, Steel-Cylinder Type." *AWWA Standard C303-02*. AWWA, Denver, CO, 44p.

Armando, L. (1987). *Handbook of Hydraulic Engineering*. John Wiley & Sons, NY.

Applied Technology Council (ATC, 1991). "Seismic Vulnerability and Impact of Disruption of Lifelines in the Conterminous Untied States". *Applied Technology Council*. Redwood City, CA.

Avram, C., Facaoaru, I., Filimon, I., Mirsu, O., and Tertea, I. (1981). *Concrete Strength and Strains*. Elsevier Scientific Publishing Company, North-Holland, 557p.

Ayala, A.G. and O'Rourke, M.J. (1989). "Effects of the 1985 Michoacan Earthquake on Water System and Other Buried Lifelines in Mexico City." *Technical Report NCEER-89-0009*. National Center for Earthquake Engineering Research, Buffalo, NY.

Ballantyne, D.B., Berg, E., Kennedy, J., Reneau, R., and Wu, D. (1990). "Earthquake Loss Estimation Modeling of the Seattle Water System." *Technical Report*. Kennedy/Jenks/Chilton, Federal Way, Wash, WA.

Brown, K.J., Rugar, P.J., Davis, C.A., and Rulla, T.A. (1995). "Seismic Performance of Los Angeles Water Tanks." *Proceedings of the 4th U.S. Conference on Lifeline Earthquake Engineering*. ASCE, San Francisco, CA, 668-675.

Bruneau, M., Chang, S.E., Eguchi, R.T., Lee, G.C., O'Rourke, T.D., Reinhorn, A.M., Shinozuka, M., Tierney, K., Wallace, W.A., and Winterfeldt, D. (2003). "A Framework to Quantitatively Assess and Enhance the Seismic Resilience of Communities." *Earthquake Spectra*, Vol. 19, No. 4, 733-752.

Chang, J.-F. (2006). "P-Y Modeling of Soil-Pile Interaction." *Ph.D. Dissertation*. School of Civil & Environmental Engineering, Cornell University, Ithaca, NY.

Chang, S.E., Rose, A., Shinozuka, M., Svekla, W.D., and Tierney, K.J. (2000). "Modeling Earthquake Impact on Urban Lifeline Systems: Advances and Integration." *Research Progress and Accomplishments: 1999-2000*. Multidisciplinary Center for Earthquake Engineering Research, Buffalo, NY.

Chang, S.E., Seligson, H.A., and Eguchi, R.T. (1996). "Estimation of the Economic Impact of Multiple Lifeline Disruption: Memphis Light, Gas and Water Division Case Study." *Technical Report NCEER-96-0011*. National Center for Earthquake Engineering Research, Buffalo, NY.

Chang, S.E., Svekla, W.D., and Shinozuka, M. (2002). "Linking Infrastructure and Urban Economy: Simulation of Water Disruption Impacts in Earthquakes." *Environment and Planning B*, Vol. 29, No. 2, 281-301.

Collins, M.A., Cooper, L., Helgason, R., Kennington, J., and Le Blanc, C. (1978). "Solving the Pipe Networks using Optimization Technique." *Management Science*, Vol. 24, 747-760.

Committee on Gas and Liquid Fuel Lifelines (1984). *Guidelines for the Seismic Design of Oil and Gas Pipeline Systems*. ASCE, New York, NY, 471p.

Crane Company (1972). *Flow of Fluid through Valves and Fittings*. Crane Company, New York, NY.

Crocker, S. (1945). *Piping Handbook*. McGraw-Hill Book Company, Inc., USA.

Cross, H. (1936). "Analysis of Flow in Networks of Conduits or Conductors." *University of Illinois Experiment Station Bulletin No. 286*. Department of Civil Engineering, University of Illinois, Urbana Champaign, IL.

Davis, C.A. (1999). "Case Study of the Granada Trunk Line During Two Near-Field Earthquakes." *Proceedings of the 7th US-Japan Workshop on Earthquake Resistant Design of Lifeline Facilities. and Countermeasures for Soil Liquefaction.* Seattle, WA, O'Rourke, T.D., Bardet, J.P., and Hamada, M., eds., Technical Report MCEER-99-0019, 415-430.

Davis, C.A. (2003). Personal Communications.

Douglas, J.F., Gasiorek, J.M., and Swaffield, J.A. (1985). *Fluid Mechanics*. 2nd Edition, Great Britain at the Bath Press, Avon, UK.

Eguchi, R.T. (1982). "Earthquake Performance of Water Supply Components during the 1971 San Fernando Earthquake." *Technical Report 82-1396-2a*. J.H. Wiggins Company, Redondo Beach, CA.

Eguchi, R.T. and Chung, R.M. (1995). "Performance of Lifelines during the January 17, 1994 Northridge Earthquake." *Lifeline Earthquake Engineering, TCLEE Monograph No. 6*. O'Rourke, M.J. ed., ASCE, Reston, VA, 120-127.

Eguchi, R.T., Taylor, C.E., and Hasselman, T.K. (1983). "Earthquake Vulnerability Models for Water Supply Components." *Technical Report No. 83-1396-2c*. Prepared for the National Science Foundation, J.H. Wiggins Company, Redondo Beach, CA.

Eidinger, J.M. (1998). "Water Distribution System." *The Loma Prieta, California, Earthquake of October 17, 1989-Lifelines*. Schiff, A.J. ed., U.S. Geological Survey Professional Paper 1552-A, U.S. State Government Printing Office, Washington, D.C., A63-A86.

Eidinger, J.M. (1999). "Girth Joints in Steel Pipelines Subjected to Wrinkling and Ovalling." *Proceedings of the 5th U.S. Conference on Lifeline Earthquake Engineering*. Seattle, WA, 100-109.

Frankel, A., Mueller, C., Barnhard, T., Perkins, D., Leyendecker, E.V., Dickman, N., Hanson, S., and Hopper, M. (1996). "Documentation for June 1996 National Seismic Hazard Maps." *Open-File Report 96-532*. U.S. Geological Survey, Denver, CO.

Gilbert, G.K., Humphrey, R.L., Sewell, J.S., and Soule, F. (1907). "The San Francisco Earthquake and Fire of April 18, 1906 and Their Effects on Structures and Structural Materials." *Bulletin 324*. U.S. Geological Survey, U.S. Government Printing Office, Washington, D.C.

Goh, S.H. and O'Rourke T.D. (2000). "Geotechnical Engineering Analysis and Design for Pile Response to Liquefaction-Induced Ground Deformation." *Proceedings of the 12th World Conference on Earthquake Engineering*. Auckland, New Zealand.

Hall, J.F. (1995). "Northridge Earthquake of January 17, 1994, Reconnaissance Report." *Earthquake Spectra*, EERI, Oakland, CA, April.

Hall, W. and Newmark, N. (1977). "Seismic Design Criteria for Pipelines and Facilities." *Current State of Knowledge of Lifeline Earthquake Engineering*. ASCE, New York, NY, 18-34.

Haskell, N.A. (1953). "The Dispersion of Surface Waves in Multilayered Media." *Bulletin of the Seismological Society of America*, Vol. 43, No. 1, 17-34.

Hunter, P.R. (1997). *Waterborne Disease: Epidemiology and Ecology.* Chichester, UK: Wiley.

Hwang, H.H.M., Lin, H., and Shinozuka, M. (1998). "Seismic Performance Assessment of Water Delivery Systems." *Journal of Infrastructure Systems*, ASCE, Vol. 4, No. 3, 118-125.

Hwang, R.N. and Lysmer, J. (1981). "Response of Buried Structures to Traveling Waves." *Journal of the Geotechnical Engineering Division*, ASCE, Vol. 107, No. GT2, 183-200.

Idelchik, I.E. (1999). *Handbook of Hydraulic Resistance*. 3rd Edition, Begell House, New York, NY.

Japan Water Works Association (1996). *Report on Damage to Water Distribution Pipes Caused by the 1995 Hyogoken-Nanbu Earthquake*. in Japanese.

Jeon, S.-S. (2002). "Earthquake Performance of Pipelines and Residential Buildings and Rehabilitation with Cast-in-Place Pipe Lining Systems." *Ph.D. Dissertation,* School of Civil & Environmental Engineering, Cornell University, Ithaca, NY.

Jeon, S.-S. and O'Rourke, T.D. (2005). "Northridge Earthquake Effects on Pipelines and Residential Buildings." *Bulletin of the Seismological Society of America*, Vol. 95, No.1, 294-318.

Jeppson, R.W. (1976). *Analysis of Flow in Pipe Network*. Ann Arbor Science Publisher, Ann Arbor, MI.

Jones, S.L., O'Rourke, T.D., and Mason, J.A. (2004). "Design of Welded Slip Joints in Pipelines for Compressive Loading." *Proceedings of the 13th World Conference on Earthquake Engineering*. Vancouver, B.C., Canada, August 1-6, Paper No. 1625.

Kershaw D. (1978). "The Incomplete Choleski-Conjugate Gradient Method for the Iterative Solution of Systems of Linear Equations." *Journal of Computation Physics*, Vol. 26, 43-65.

Khater, M.M. and Waisman, F. (1999). "Small Diameter Pipelines Sensitivity Analysis." *Internal Report from National Institute of Building Sciences*. Washington, D.C.

Khater, M.M. and Grigoriu, M.D. (1989). "Graphical Demonstration of Serviceability Analysis." *Proceedings of the 5th International Conference on Structural Safety and Reliability*. San Francisco, CA, August, 525-532.

Kitaura, M., and Miyajima, M. (1996). "Damage to Water Supply Pipelines." *Special Issue of Soils and Foundations, Japanese Geotechnical Society*, 325-333.

KYPipe Company (2005). http://www.kypipe.com.

Lawson, A. C. (1908). "The California Earthquake of April 18, 1906." *Report of the State Earthquake Investigation Commission*. Carnegie Institute of Washington, No. 87, Vol. I, 451p.

Los Angeles Department of Water and Power (LADWP) (1994). *January 17, 1994 Northridge Earthquake Major Emergency Report.* Power Operating and Maintenance Division, Operating Engineering Section, Los Angeles, CA.

Los Angeles Department of Water and Power (LADWP) (1996). *Geotechnical Report on Earthquake Damage to the Granada Trunk Line at the Van Norman Complex*. Water Supply Division, Report No. AX500, Los Angeles, CA.

Los Angeles Department of Water and Power (LADWP) (2002). *H2ONET Hydraulic Model of the LADWP Water Supply System.* Los Angeles, CA.

Los Angeles Department of Water and Power (LADWP) (2003). *City of Los Angeles Water Services: Water Supply Fact Sheet.* http://www.ladwp.com/water/supply/facts/index.htm.

Lund, L. and Cooper, T. (1995). "Water System." *Northridge Earthquake: Lifeline Performance and Post-Earthquake Response, Technical Council on Lifeline Earthquake Engineering Monograph No. 8*, Schiff, A.J., ed., ASCE, New York, NY, 96-131.

Lund, L., Davis, C.A., and Adams, M.L. (2005). "Water System Seismic Performance 1994 Northridge-1995 Kobe Earthquakes." *Proceedings of 4th Japan-US Workshop on Seismic Measures for Water Supply*. AWWARF/FWWA, Kobe, Japan, Jan. 26-28.

Manson, M. (1908). *Reports on an Auxiliary Water Supply System for Fire Protection for San Francisco, California.* Board of Public Works, San Francisco, CA.

Markov, I., Grigoriu, M.D., and O'Rourke, T.D. (1994). "An Evaluation of Seismic Serviceability Water Supply Networks with Application to the San Francisco Auxiliary Water Supply System." *Technical Report NCEER-94-0001*, National Center for Earthquake Engineering Research, Buffalo, NY.

Miller, D.S. (1978). *Internal Flow System*. BHRA Fluid Engineering, Bedford, UK.

MIKENET (2005), http://www.dhisoftware.com/mikenet/

Moody, L.E. (1944). "Friction Factors of Pipe Flow." *Transactions of the American Society of Mechanical Engineers*, ASME, Vol. 16, New York, NY

MWH Soft, Inc. (1999). *H2ONET Users Guide*. Pasadena, CA.

National Institute of Building Sciences (NIBS, 1997). *Earthquake Loss Estimation Methodology HAZUS 97: Technical Manual.* Prepared for Federal Emergency Management Agency, Washington, D.C.

Okumura, T. and Shinozuka, M. (1991). "Serviceability Analysis of Memphis Water Delivery Systems." *Proceedings of the 3rd U.S. conference on Lifeline Earthquake Engineering*. Los Angeles, CA.

O'Rourke, M.J. and Liu, X. (1999). "Response of Buried Pipelines Subject to Earthquake Effects." *Research Monographic Series No. 3*. Multidisciplinary Center for Earthquake Engineering Research, Buffalo, NY.

O'Rourke, M.J., Castro, G., and Hossain, I. (1984). "Horizontal Soil Strain Due to Seismic Waves." *Journal of Geotechnical Engineering*, ASCE, Vol. 110, No. 9, 1173-1187.

O'Rourke, T.D. (1998). "An Overview of Geotechnical and Lifeline Earthquake Engineering." *Geotechnical Special Publication No. 75,* ASCE, Reston, VA. *Proceedings of Geotechnical Earthquake Engineering and Soil Dynamics Conference*. Seattle, WA, Vol. 2, 1392-1426.

O'Rourke, T.D. (2005). Personal Communications.

O'Rourke, T.D., Bonneau, A.L., Pease, J.W., Shi, P., and Wang, Y. (2006). "Liquefaction and Ground Failure in San Francisco." *Earthquake Spectra,* Vol. 22, the 1906 San Francisco Commemorative Issue.

O'Rourke, T.D. and Jeon S.-S. (1999). "Factors Affecting the Earthquake Damage of Water Distribution Systems." *Proceedings of 5th U.S. Conference on Lifeline Earthquake Engineering, Seattle*. ASCE, Reston, VA, 379-388.

O'Rourke, T.D. and Jeon S-S. (2000). "Seismic Zonation for Lifeline and Utilities." *Invited Keynote Paper on Lifelines in Proceedings of the 6th International Conference on Seismic Zonation*. Palm Springs, CA, 35p.

O'Rourke, T.D. and Jeon S.-S. (2002). "GIS Loss Estimation and Post-Earthquake Assessment of Residential Building Damage." *Proceedings of the 7th National Conference on Earthquake Engineering*. Boston, MA, EERI, Oakland, CA.

O'Rourke, T.D., Khater, M.M., and Grigoriu, M.D. (1985). "Earthquake Performance of the San Francisco Water Supply." *Technical Report*. National Center for Earthquake Engineering Research, Buffalo, NY.

O'Rourke, T.D. and Toprak, S. (1997). "GIS Assessment of Water Supply Damage from the Northridge Earthquake." *Spatial Analysis in Soil Dynamics and Earthquake Engineering*, *Geotechnical Special Publication No. 67*, Frost, J.D. ed., ASCE, Reston, VA, 117-131.

O'Rourke, T.D. and Trautmann C.H. (1980). *Analytical Modeling of Buried Pipeline Response to Permanent Earthquake Displacements.* School of Civil and Environmental Engineering, Cornell University, Ithaca, NY.

O'Rourke, T.D., Stewart, H.E., and Jeon, S-S. (2001). "Geotechnical Aspect of Lifeline Engineering." *Geotechnical Engineering*, ICE, Vol. 149, No. 1, 13-26.

O'Rourke, T.D., Wang, Y., and Shi, P. (2004a). "Seismic Wave Effects on Bay Division Pipelines." *Internal Report for San Francisco Public Utility Commission*, San Francisco, CA.

O'Rourke, T.D., Wang, Y., and Shi, P. (2004b). "Advances in Lifeline Earthquake Engineering." *Keynote Lecture of the 13th World Conference on Earthquake Engineering*, Vancouver, B.C., Canada, Paper No. 5003.

O'Rourke, T.D., Wang, Y., Shi, P., and Jones, S. (2004c). "Seismic Wave Effects on Water Trunk and Transmission Lines." *Proceedings of the 11th International Conference on Soil Dynamics & Earthquake Engineering, and 3rd International Conference on Earthquake Geotechnical Engineering*. Berkeley, CA, Vol. 2, 420-428.

O'Rourke, T.D. and Pease, J.W. (1992). "Large Ground Deformations and Their Effects on Lifelines: 1989 Loma Prieta Earthquake." *United States Case Studies of Liquefaction and Lifeline Performance during Past Earthquakes, Technical Report NCEER-92-0002*. O'Rourke, T.D. and Hamada, M., ed., National Center for Earthquake Engineering Research, Buffalo, NY.

Papageorgiou, A.S. and Kim J. (1993). "Propagation and Amplification of Seismic Waves in 2-D Valleys Excited by Obliquely Incident P- and SV-Waves." *Earthquake Engineering and Structural Dynamics*, Vol. 22, No. 2, 167-182.

Pei, D. and Papageorgiou, A.S. (1996). "Locally Generated Surface Waves in Santa Clara Valley: Analysis of Observations and Numerical Simulation." *Earthquake Engineering and Structural Dynamics*, Vol 25, No. 1, 47-63.

Philip, M.G., Richard, J.G. and John, I.H. (1992). *Fundamentals of Fluid Mechanics*. 2nd Edition, Addison-Wesley Publishing Company, USA.

Prior, J.C. (1935). "Investigation of Bell and Spigot Joints in Cast Iron Water Pipes." *Bulletin 87.* Ohio State University Experiment Station.

Puchovsky, M.T. (1999). *Automatic Sprinkler Systems Handbooks*, National Fire Protection Association (NFPA).

Ronald, E.W., Raymond, H.M., and Sharon, L.M. (1998). *Probability and Statistics for Engineering and Scientists*. 6th Edition, Prentice Hall/Upper Saddle River, NJ.

Rose, A., Benavides, J., Chang, S., Szczesniak, P., and Lim, D. (1997). "The Regional Economic Impact of an Earthquake: Direct and Indirect Effects of Elects of Electricity Lifeline Disruptions." *Journal of Regional Science*, Vol. 37, Issue 3, 437-458.

Rose, A. and Liao, S.-Y. (2003). "Understanding Sources of Economic Resiliency to Hazards: Modeling the Behavior of Lifeline Service Customers." *Research Progress and Accomplishments 2001-2003*. Multidisciplinary Center for Earthquake Engineering Research, Buffalo, NY, 149-160.

Rossman, L.A. (2000). *EPANET 2 Users Manual*. National Risk Management Research Laboratory, Office of Research and Development, U.S. Environmental Protection Agency, Cincinnati, OH.

Sano, Y., O'Rourke, T.D., and Hamada, M. (1999). "Geographic Information Systems (GIS) Evaluation of Northridge Earthquake Ground Deformation and Water Supply Damage." *Proceedings of the 5th U.S. Conference on Lifeline Earthquake Engineering*. Seattle, WA, Reston, VA, 832-839.

Scawthorn, C., O'Rourke, T.D., and Blackburn F.T. (2006). "The San Francisco Earthquake and Fire of 1906 - Enduring Lessons for Fire Protection and Water Supply." *Earthquake Spectra,* Vol. 22, the 1906 San Francisco Commemorative Issue.

Schussler, H. (1906). *The Water Supply of San Francisco, California*. Martin B. Brown Press, New York, NY.

Schwab, F. and Knoff, L. (1977). "Fast Surface Waves and Free Mode Computations." *Seismology: Surface Waves and Earth Oscillation Methods in Computation, Physics 11*, Academic Press, NY, 87-180.

Sheldon, M.R., (2000), *Introduction to Probability and Statistics for Engineers and Scientists*. 2nd Edition, Harcourt and Technology Company, San Diego, CA.

Shinozuka, M., Rose, A., and Eguchi, R.T., Eds. (1998). "Engineering and Socioeconomic Impacts of Earthquakes." *Monograph Series 2*. Multidisciplinary Center for Earthquake Engineering Research, Buffalo, NY.

Shinozuka, M., Hwang, H.H.M., and Murata, M. (1992). "Impacts on Water Supply of a Seismically Damaged Water Delivery System." Lifeline Earthquake Engineering in the Central and Eastern U.S., Ballantyne, D.B. ed., *TCLEE Monograph No. 5*, ASCE, Reston, VA, 43-57.

Shinozuka, M., Tan, R.Y., and Toike, T. (1981). "Serviceability of Water Transmission Systems under Seismic Risk." *Lifeline Earthquake Engineering, the Current State of Knowledge, 1981*, ASCE, New York, NY.

St. John, C.M., Zahrah, T.F. (1987), "Aseismic Design of Underground Structures." *Tunneling Underground Space Technology*, Vol. 2, No. 2, 165-197.

Streeter, V.L., Wylie, B.E., and Bedford, K.W. (1998). *Fluid Mechanics*. 9th Edition, WCB/McGraw-Hill, Boston, MA.

Steinbrugge, K.V., Schader, E.E., Bigglestone, H.C., and Weers, C.A. (1971). *San Fernando Earthquake, February, 9, 1971*. Pacific Fire Rating Bureau.

Subcommittee on Water and Sewerage Systems (1973). "Earthquake Damage to Water and Sewerage Facilities, San Fernando, California Earthquake of February 9, 1971." *U.S. Department of Commerce, N.O.A.A.*, Washington, D.C., Vol. 2, 75-193.

Swamee, P.K. and Jian, A.K. (1976). "Explicit Equations for Pipe Flow Problems." *Journal of Hydraulic Engineering*, ASCE, Vol. 102, No. 5, 657p.

Tanaka, S. (1996). "Lifeline Seismic Performance Analysis for Water and Electric Power Systems." *Ph.D. Dissertation*, Waseda University, Tokyo, Japan.

Thielsch, H. (1965). *Defects and Failures in Pressure Vessels and Piping*. Reinhold Publishing Corporation, New York, NY.

Thomas, M. (1984). *Analysis of Water Distribution Systems*. Reinhold Publishing Corporation, New York, NY.

Todini, E. and Pilati, S. (1987). "A Gradient Method for the Analysis of Pipe Networks." *Proceedings of the International Conference on Computer Application for Water Supply and Distribution*. Leicester, UK.

Toprak, S. (1999). "Earthquake Effects on Buried Lifeline Systems." *Ph.D. Dissertation*, School of Civil & Environmental Engineering, Cornell University, Ithaca, NY.

Trautmann, C.H., O'Rourke, T.D., Grigoriu, M.D., and Khater, M.M. (1986). "System Model for Water Supply Following Earthquakes." *Lifeline Seismic Risk Analysis - Case Studies*, ASCE, Reston, VA, 30-50.

Trifunac, M.D., Todorovska, M.I., and Lee, V.M. (1998). "The Rinaldi Strong Motion Accelerogram of the Northridge, California, Earthquake of January, 1994." *Earthquake Spectra*, Vol. 14, No.1, 225-239.

Tierney, K. (1997). "Business Impacts of the Northridge Earthquake." *Journal of Contingencies and Crisis Management*, Oxford, UK; Cambridge, MA: Blackwell Publisher, Vol. 5, No. 2, 87-97.

Untrauer, R.E., Lee, T.T., Sanders W.W., and Jawad, M.H. (1970), "Design Requirements for Cast iron Soil Pipe." *Bulletin 199*, Iowa State University, Engineering Research Institute, 60-109.

U.S. Environmental Protection Agency, USA (EPA, 2005). http://www.epa.gov/ORD/NRMRL/wswrd/epanet.html.

Vargas, V. (2005). Personal Communications.

Wald, D., Heaton, T.H., and Hudnut, K.W. (1996). "The Slip History of the 1994 Northridge, California, Earthquake Determined from Strong-motion, Teleseismic, GPS, and Leveling Data." *Bulletin of the Seismological Society of America*, 1996, 86 No. 1B, S49-S70.

Walski, T.M., Chase, D.V., and Savic, D.A. (2001). *Water Distribution Modeling*. Hastad Press, CT, USA.

Wang, Y. (2006). "Seismic Performance Evaluation of Water Supply Systems." *Ph.D. Dissertation*, School of Civil & Environmental Engineering, Cornell University, Ithaca, NY.

WaterCAD (2005), http://www.hasetad.com/software/watercad/

Wright, J.P. and Takada, S. (1980). "Earthquake Response Characteristics of Jointed and Continuous Buried Lifelines." *Grant Report No. 15, Prepared for National Science Foundation by Weidlinger Associates*, Grant No. PFR 78-15049.

Wood, D.J. and Carl, A.C. (1972). "Hydraulic Network Analysis Using Linear Theory." *Journal of the Hydraulics Division*, ASCE, 98 (HY7), 1157-1170.

Wu, C., Fok, E., Fotinos, G., Tseng, W., and Oberholtzer, G. (2003). "Seismic Assessment and Retrofit Concepts of the BART Transbay Tube." Advancing Mitigation Technologies and Disaster Response for Lifeline Systems, *Proceedings of the 6th US Conference and Workshop on Lifeline Earthquake Engineering.* Long Beach, CA, 203-212.

APPENDIX A

LADWP DISTRIBUTION NETWORK MODEL DESCRIPTIONS

This appendix provides a description of the six distribution network models used for LADWP distribution network simulations and the monitored pipes for characterizing water losses due to distribution network damage.

As discussed in the main text of Chapter 6, six representative distribution network models, covering distribution systems 1449, 1000, 579, 448 & 462, 426, and 205, were obtained from LADWP. Each distribution network model includes distribution pipelines and a portion of the trunk line system in the vicinity of the local distribution network. Figures A.1, A.3, A.5, A.7, A.9, and A.11 show the combined distribution and trunk pipelines that comprise the six distribution systems, respectively. To illustrate better the locations of trunk and distribution pipelines, the relevant portion of the LADWP trunk line system model is superimposed on each distribution network. In the figures, the thin green lines represent pipelines in the distribution networks, and the small green dots represent demand nodes in the distribution networks. The thick red lines represent trunk lines, and the big red dots represent demand nodes in the trunk system. For each thick red line, representing a trunk line, there is a corresponding thin green line, representing the trunk line as modeled in the distribution network. The big red demand nodes in the trunk system represent the locations of demands modeled in the LADWP trunk line model. The superposition of the distribution and trunk line models shows that these two data sets are consistent. Every trunk line in the trunk line system can be found in the distribution line network.

The pipe diameter distribution in the six distribution network models is shown in Figures A.2, A.4, A.6, A.8, A.10, and A.12. These figures show that the smallest diameter pipelines in the distribution network models are those with diameters of 100 (4) and 150 mm (6 in.) The majority of pipelines are those with diameters smaller or equal to 300 mm (12 in.) in contrast to the trunk line model, which mainly includes pipelines with diameters larger than or equal to 400 mm (16 in.)

Monte Carlo simulations were performed to the distribution networks with the procedures described in main text of Chapter 6. In distribution network simulations, pipe damage was evaluated only in the distribution lines since the trunk line damage is accounted for explicitly in the trunk system model. In each distribution network, multiple locations of flows were monitored in the trunk lines before and after earthquake damage to the distribution network. The locations of the monitored flows are shown in Figures A1, A3, A5, A7, A9, and A11 as yellow triangles. Since flows in trunk lines are distributed by means of demands in the distribution networks, the increase of flows in the trunk lines after earthquake damage represents the earthquake demands from the distribution network damage. To provide statistically significant sample flows, the multiple monitored flows are widely distributed in each distribution network.
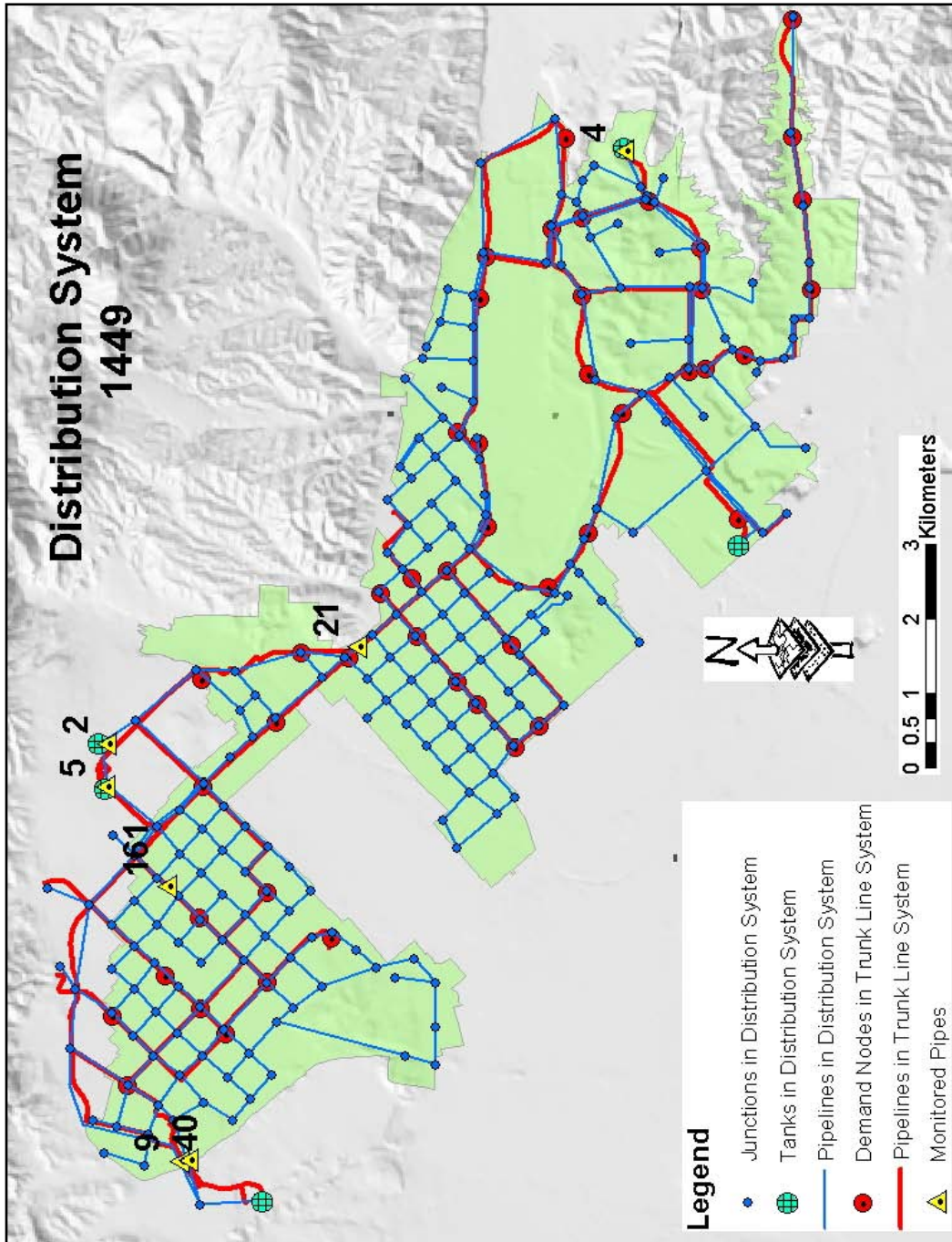
Figure A.1 Map Showing the Distribution System 1449 Hydraulic Network Model
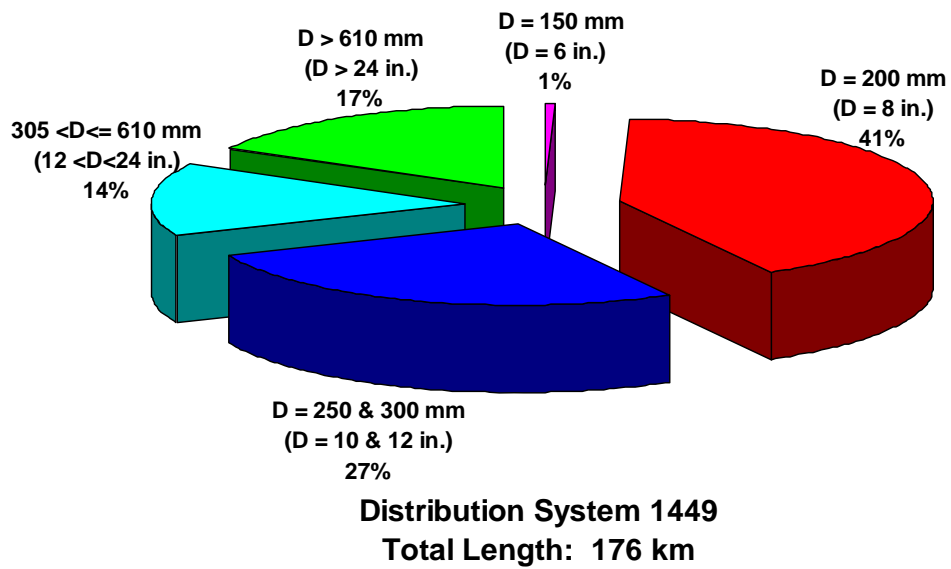
Figure A.2 Pie Chart Showing Distribution of Pipelines of Various Diameters

in System 1449
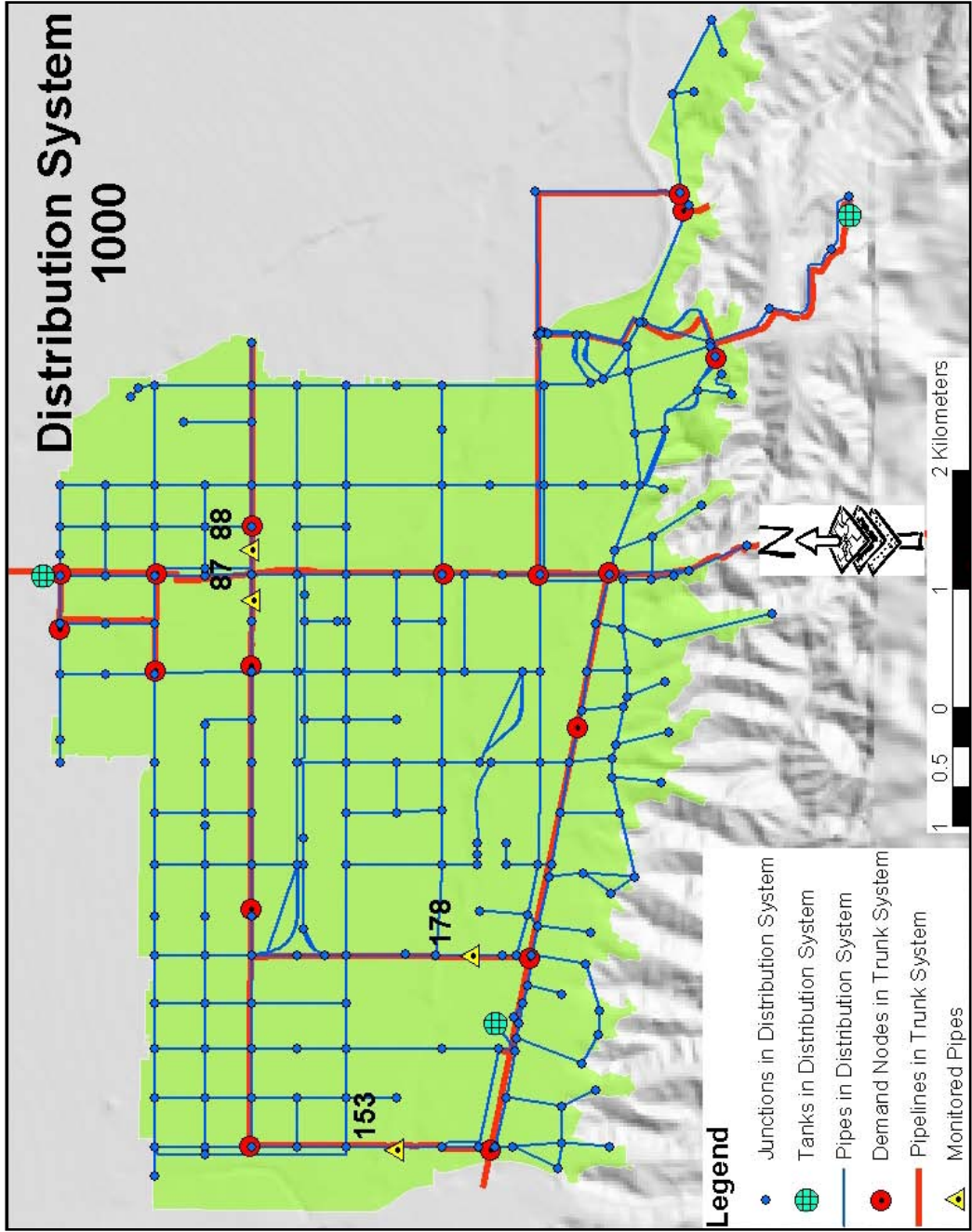
Figure A.3 Map Showing the Distribution System 1000 Hydraulic Network Model

**D > 610 mm
(D > 24 in.)
11%**

**D = 150 mm
(D = 6 in.)
5%**

**305 <D<= 610 mm
(12 <D<24 in.)
7%**

**D = 250 & 300 mm
(D = 10 & 12 in.)
22%**

**D = 200 mm
(D = 8 in.)
55%**

**Distribution System 1000
Total Length: 138 km**
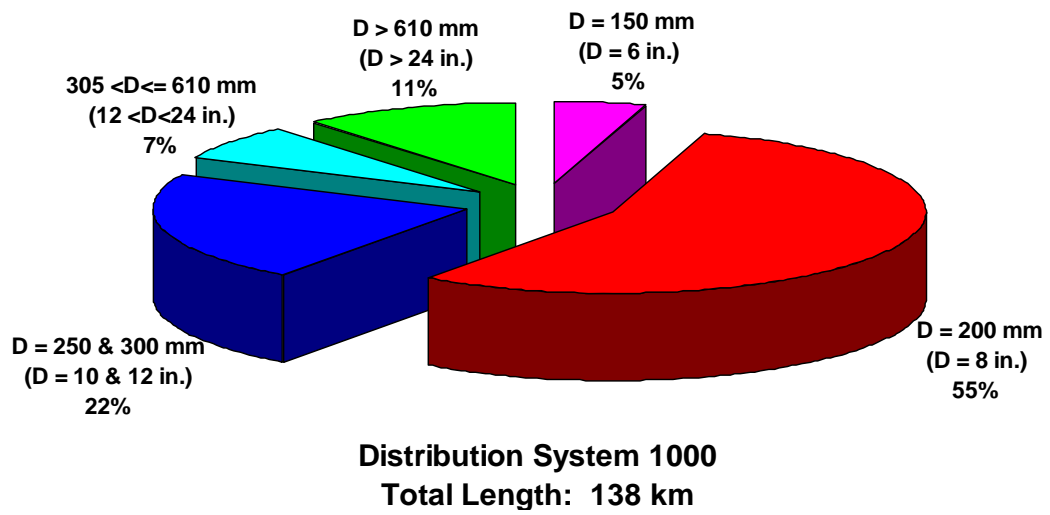
Figure A.4 Pie Chart Showing Distribution of Pipelines of Various Diameters

in System 1000
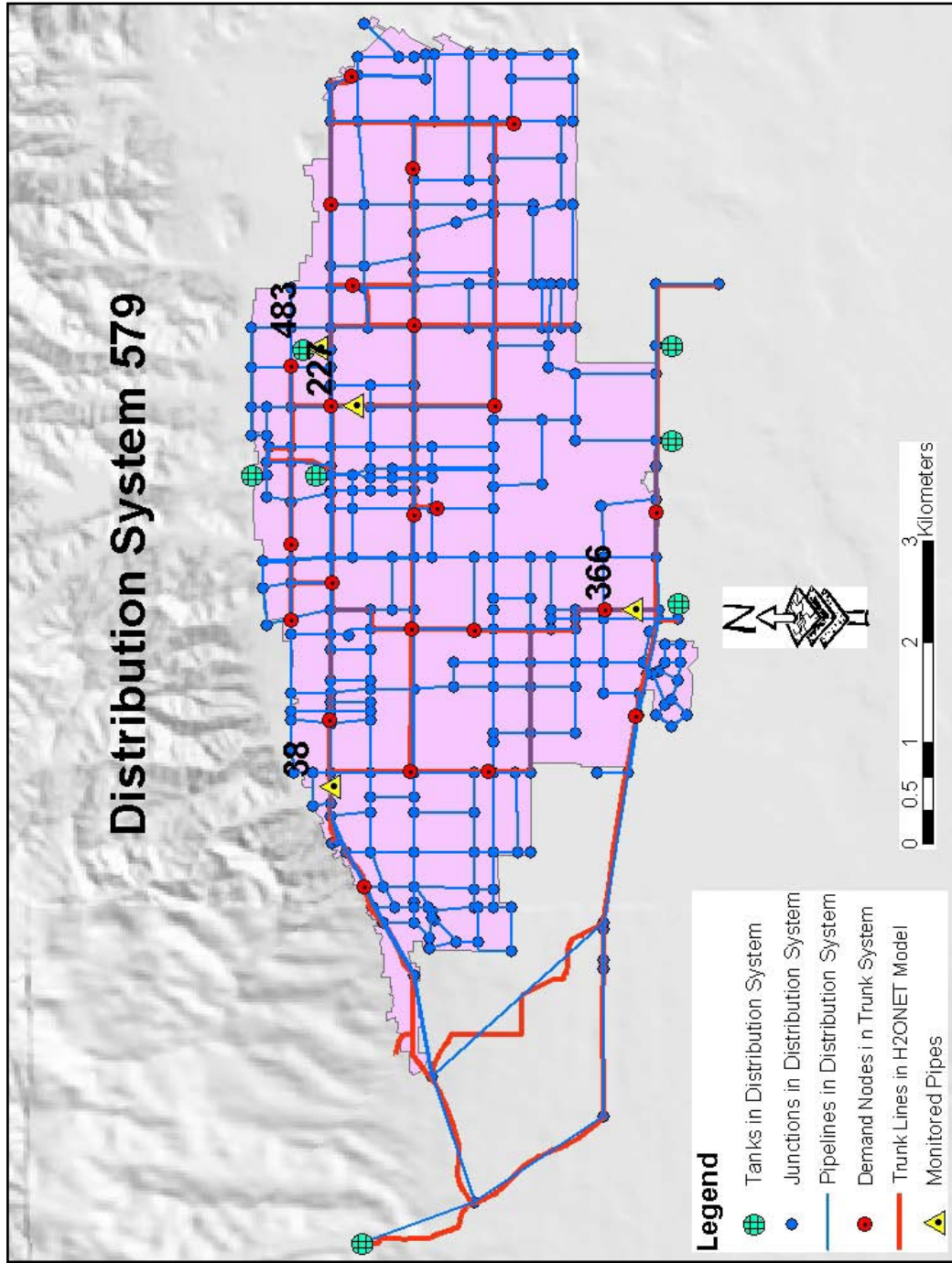
Figure A.5 Map Showing the Distribution System 579 Hydraulic Network Model

D > 610 mm
(D > 24 in.)
15%

305 <D<= 610 mm
(12 <D<24 in.)
9 %

D = 100 & 150 mm
(D = 4 & 6 in.)
8 %

D = 250 & 300 mm
(D = 10 & 12 in.)
18%

D = 200 mm
(D = 8 in.)
51 %

Distribution System 579
Total Length: 165 km
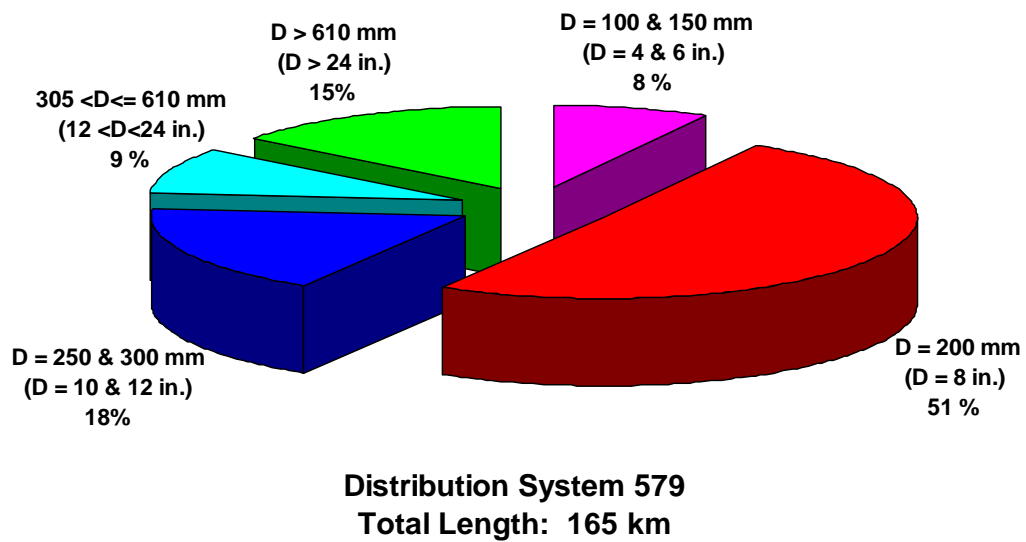
Figure A.6 Pie Chart Showing Distribution of Pipelines of Various Diameters

in System 579
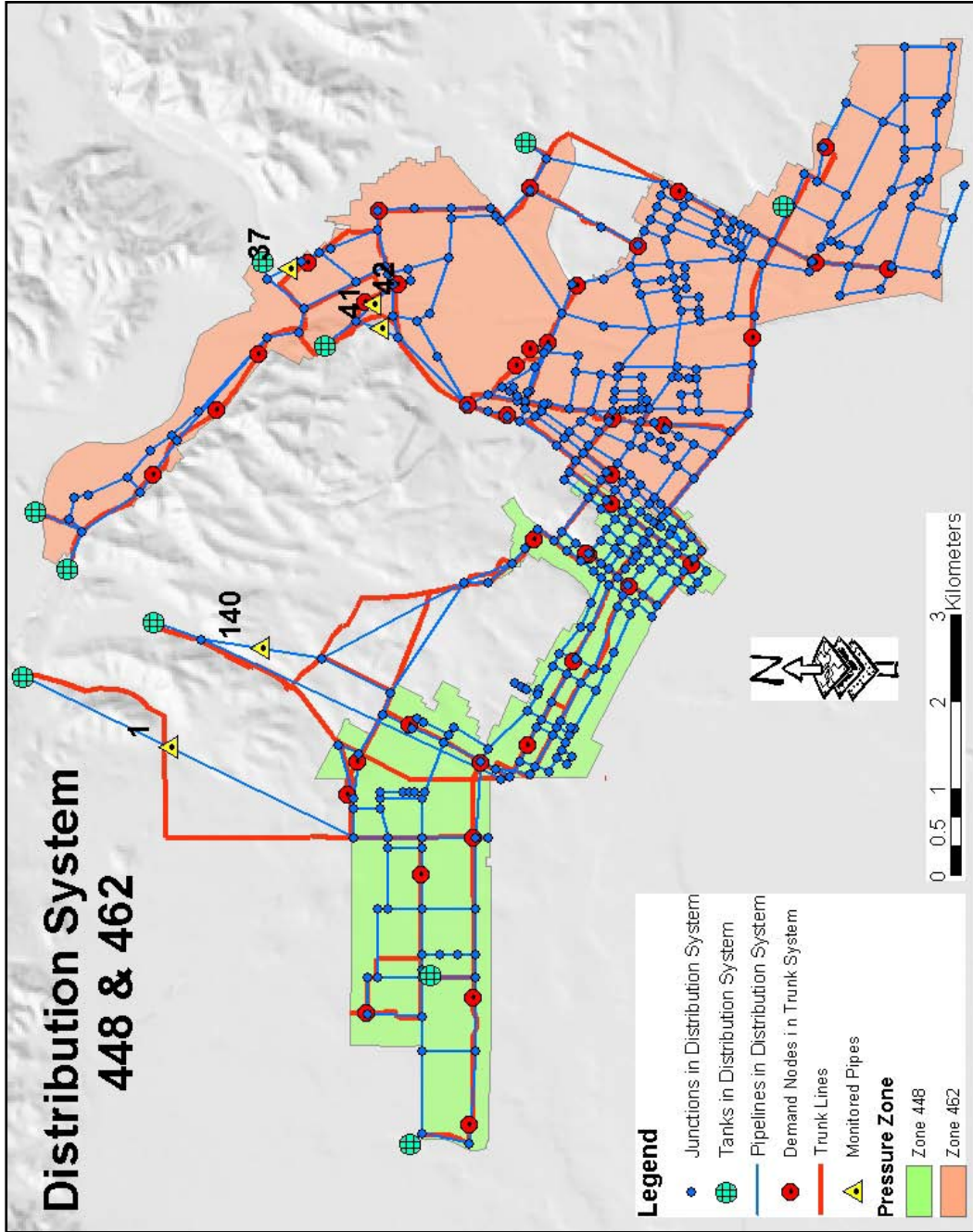
Figure A.7 Map Showing the Distribution System 448 & 4462 Hydraulic Network Model
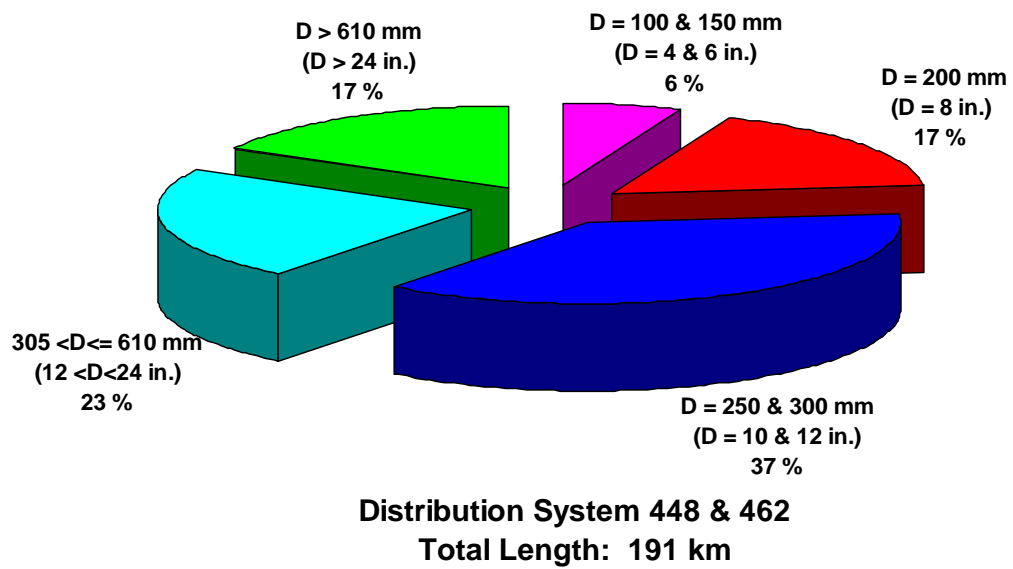
Figure A.8 Pie Chart Showing Distribution of Pipelines of Various Diameters

in System 448 & 462
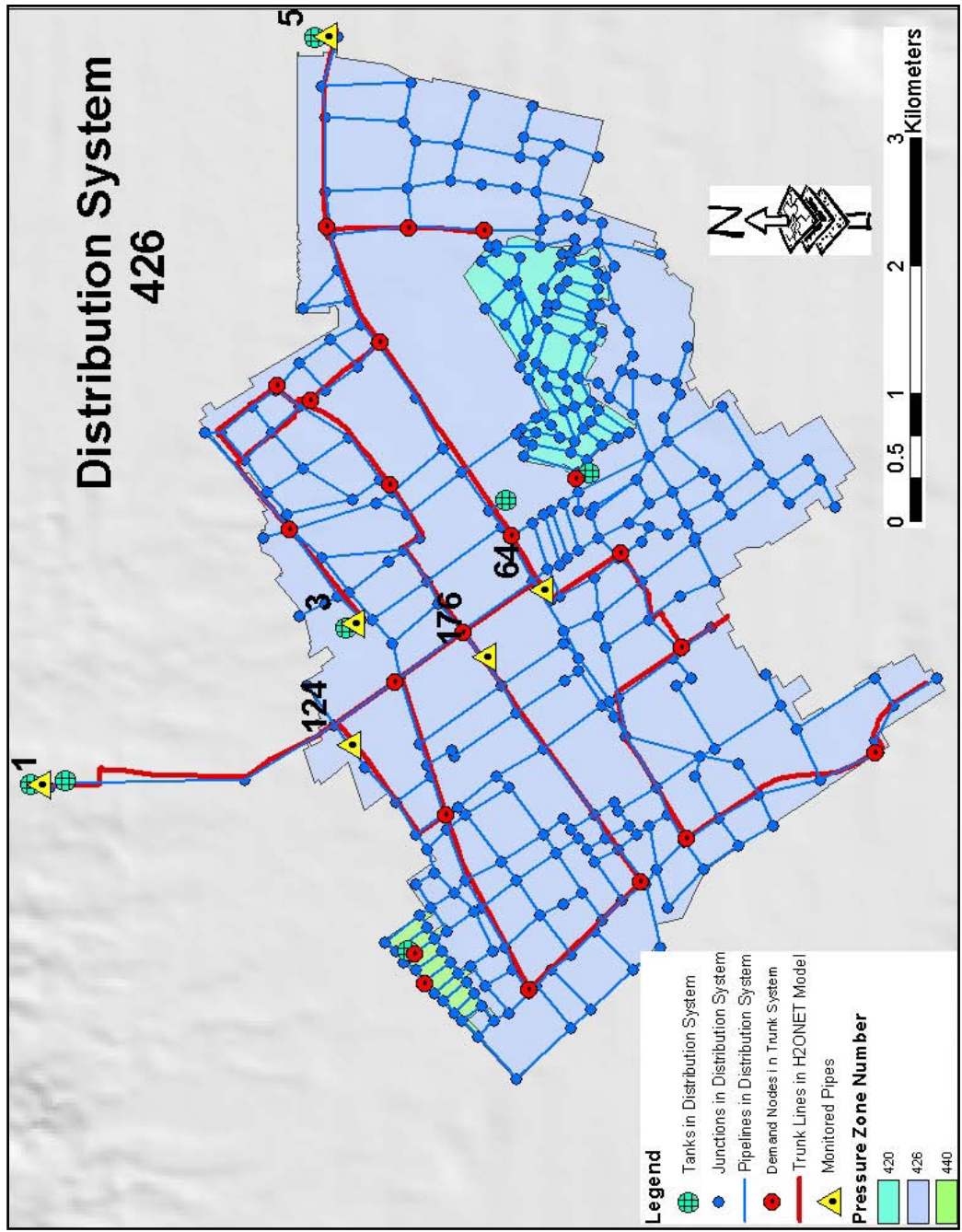
Figure A.9 Map Showing the Distribution System 426 Hydraulic Network Model

273

D > 610 mm (D > 24 in.) 6 %

305 <D<= 610 mm (12 <D<24 in.) 5 %

D = 250 & 300 mm (D = 10 & 12 in.) 21 %

D = 100 & 150 mm (D = 4 & 6 in.) 27 %

D = 200 mm (D = 8 in.) 41 %

Distribution System 426
Total Length: 130 km
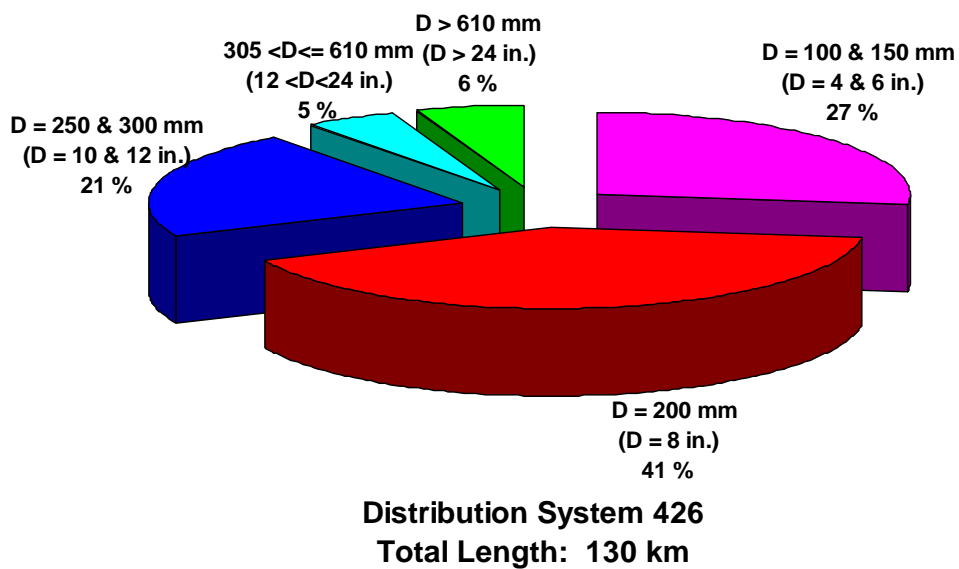
Figure A.10 Pie Chart Showing Distribution of Pipelines of Various Diameters

in System 426
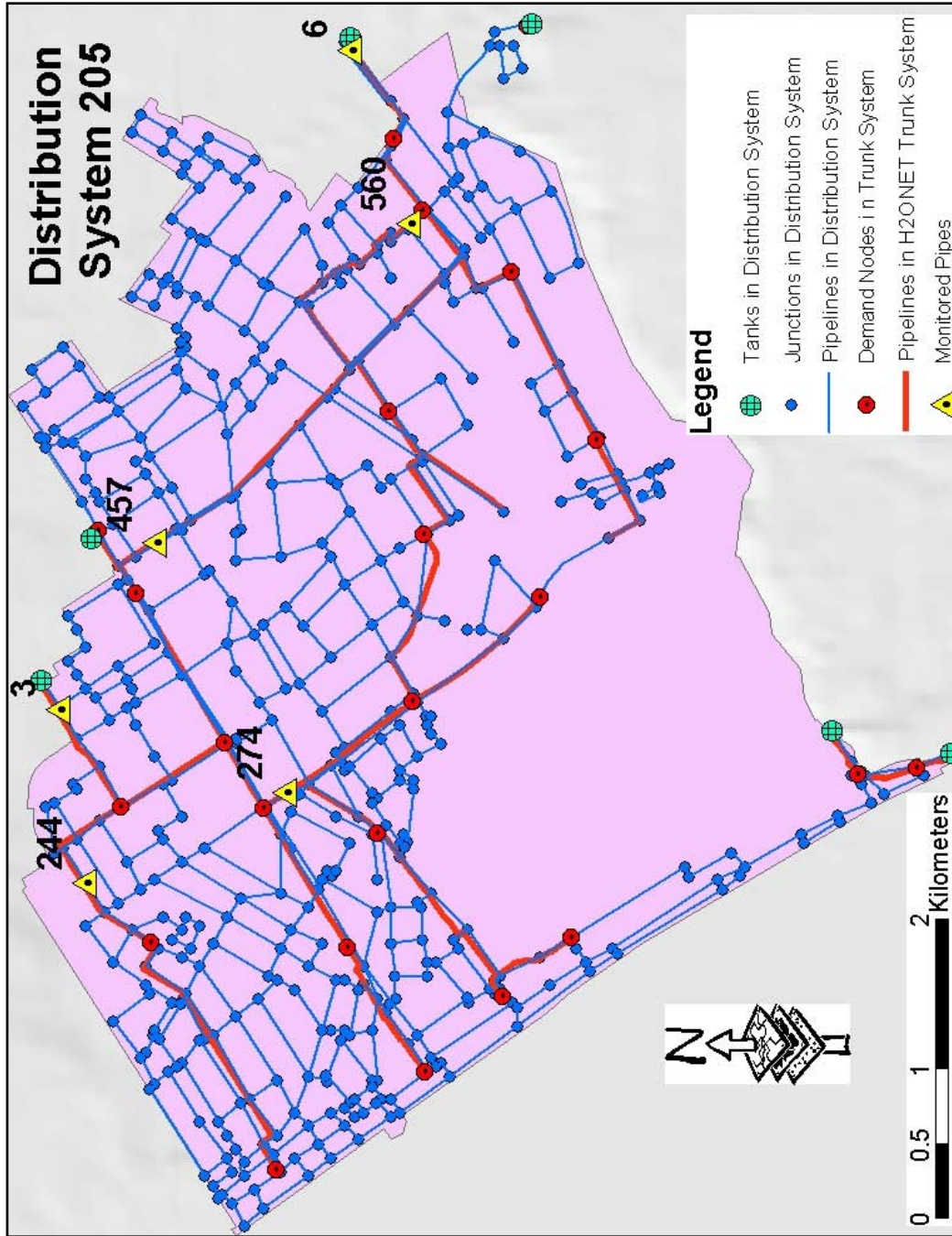
Figure A.11 Map Showing the Distribution System 205 Hydraulic Network Model
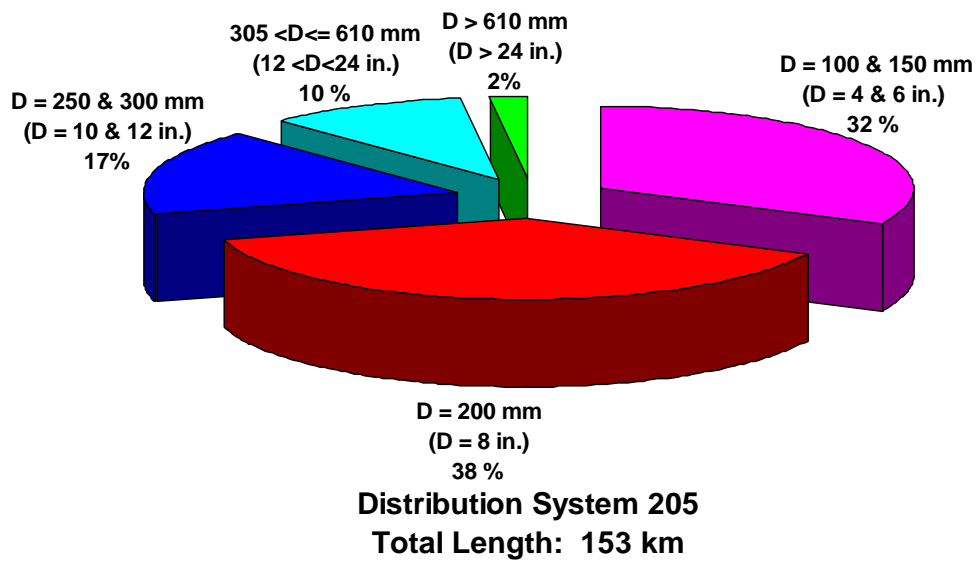
Figure A.12 Pie Chart Showing Distribution of Pipelines of Various Diameters

in System 205

APPENDIX B

LADWP DISTRIBUTION NETWORK SIMULATION RESULTS

This appendix presents the Monte Carlo simulation results of the monitored flows in the six LADWP distribution networks. In total, 26 locations of flows were monitored in Systems 1449, 1000, 579, 448 & 462, and 426, for the development of fragility curves, and 6 locations of flows were monitored in System 205 for the test of fragility curves.

As explained in the main text of Chapter 6, flows were monitored in representative trunk lines before and after earthquake damage to distribution networks. The flows after damage were normalized with respect to those before damage. The normalized flows provide a proxy for normalized demand (ND). Monte Carlo simulations were performed for a wide range of repair rates (RRs) varying from 0.02 to 100 repairs/km. Figures 6.6 and 6.7 show that the relationships between ND and RR follow consistent increasing trends to RR of roughly 2 repairs/km, above which certain patterns of performance can be discerned. When RR values range from 2 to 10 repairs/km, ND begins to separate into different trends. At RR from 10 to 100 repairs/km, the system response follows a limited number of discrete trends, and in some cases ND drops to very low levels, which indicate that the system is severely damaged and not able to supply water in a reliable and stable way. Previous research (Jeon, 2002) shows that RR equal to 1 repair/km provides an approximate upper bound for the PGV-related damage to buried pipelines. Statistics were developed for simulation results with RR ranging from 0.02 to 1 repairs/km.

The Monte Carlo simulation results for RR ranging from 0.02 to 1 repairs/km in the six distribution systems are shown in Figures B.1 to B.6. In each figure, one plot represents simulation results from one monitored pipe. In each plot, one dot represents one Monte Carlo simulation run for a given RR. The linear regression function and the coefficient of determination, r^2, are also shown in each plot. The pipe ID in each plot is consistent with the ID of the monitored pipes, shown in Figures A.1, A.3, A.5, A.7, A.9, and A.11.
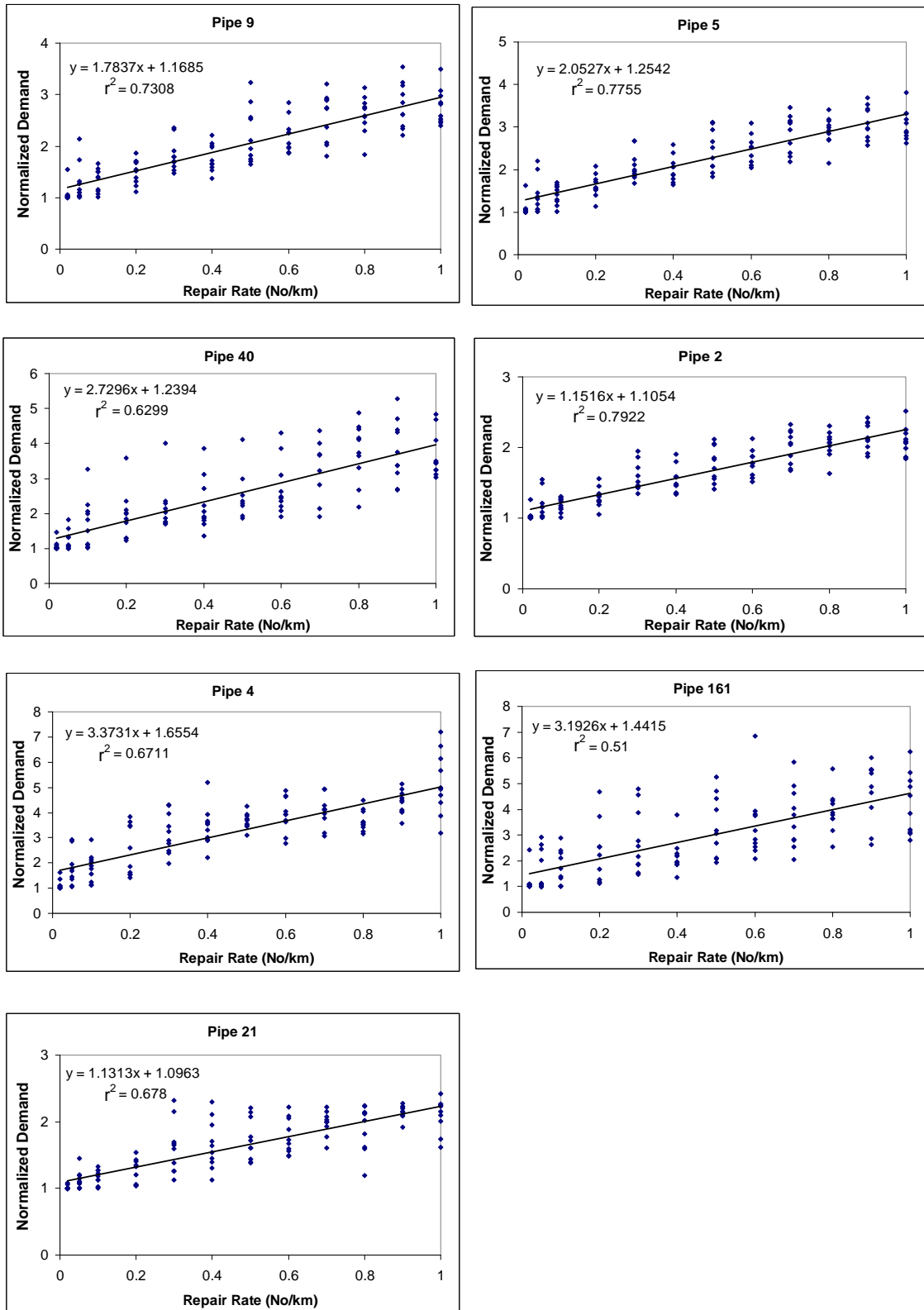
Figure B.1 Simulation Results for Monitored Pipes in Distribution System 1449

Pipe 88

$y = 2.3442x + 1.2622$
$r^2 = 0.5754$

Pipe 178

$y = 1.4705x + 1.4268$
$r^2 = 0.6129$

Pipe 153

$y = 1.1466x + 1.3815$
$r^2 = 0.5516$

Pipe 87

$y = 2.3085x + 1.5627$
$r^2 = 0.6316$
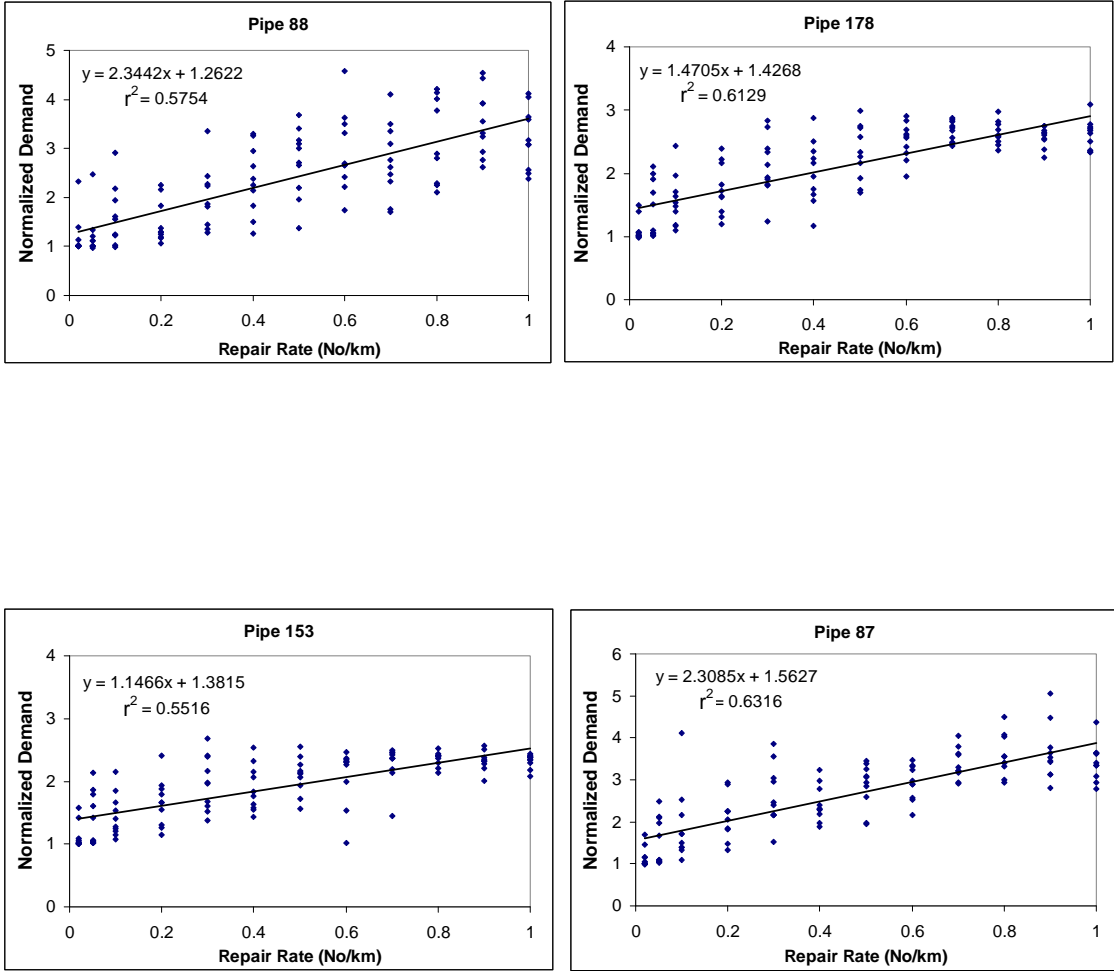
Figure B.2 Simulation Results for Monitored Pipes in Distribution System 1000
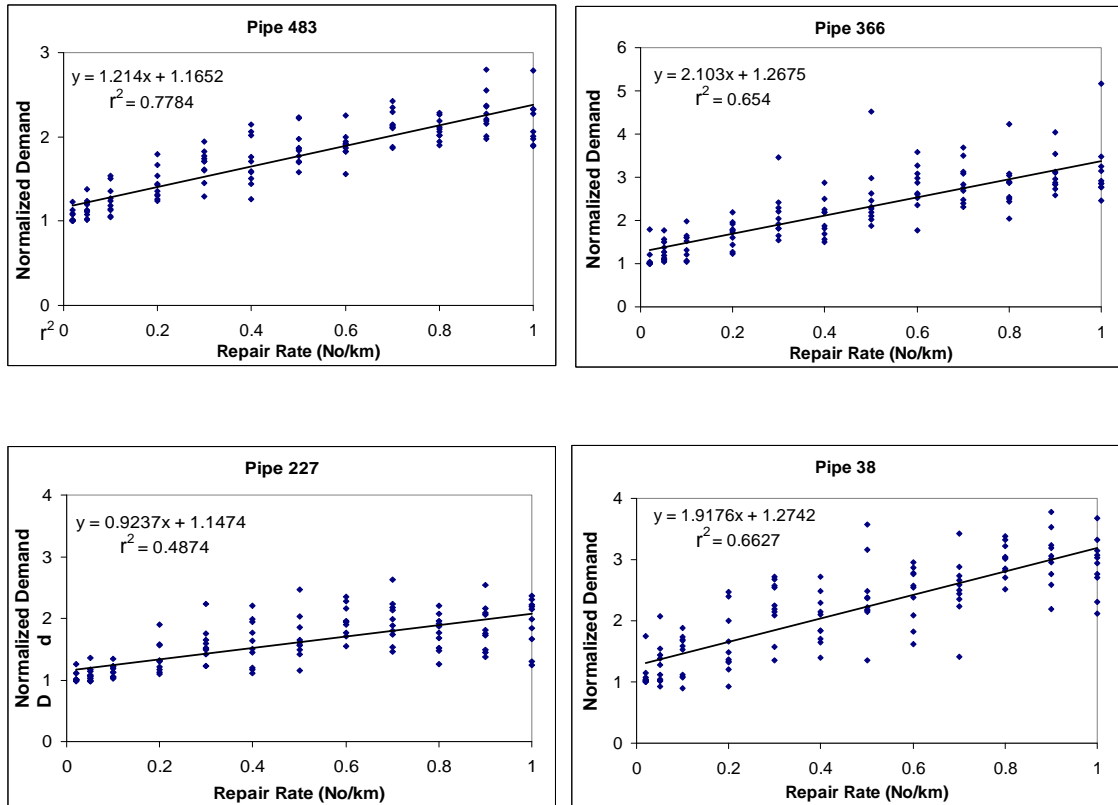
Figure B.3 Simulation Results for Monitored Pipes in Distribution System 579
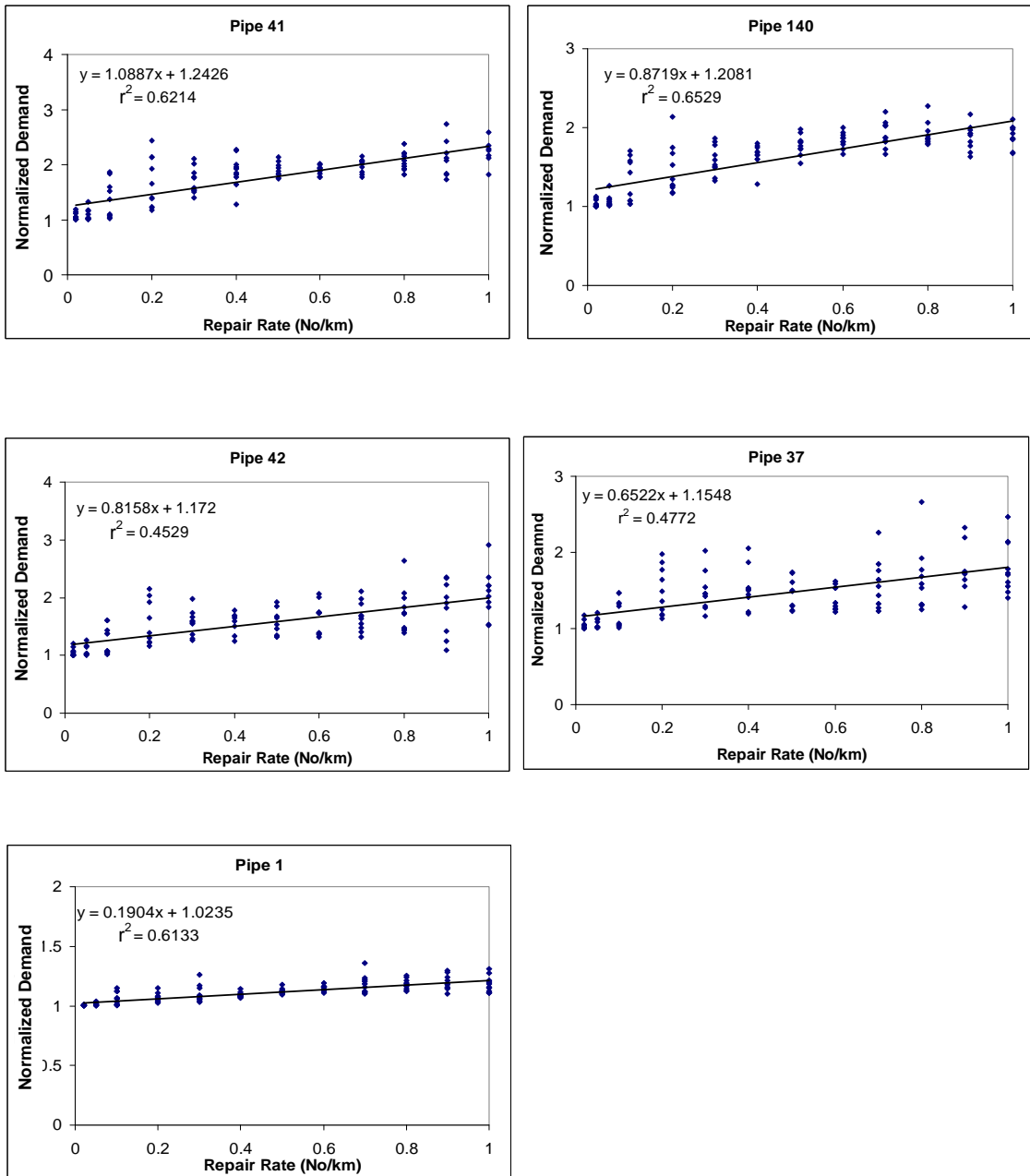
Figure B.4 Simulation Results for Monitored Pipes in Distribution System 448 & 462
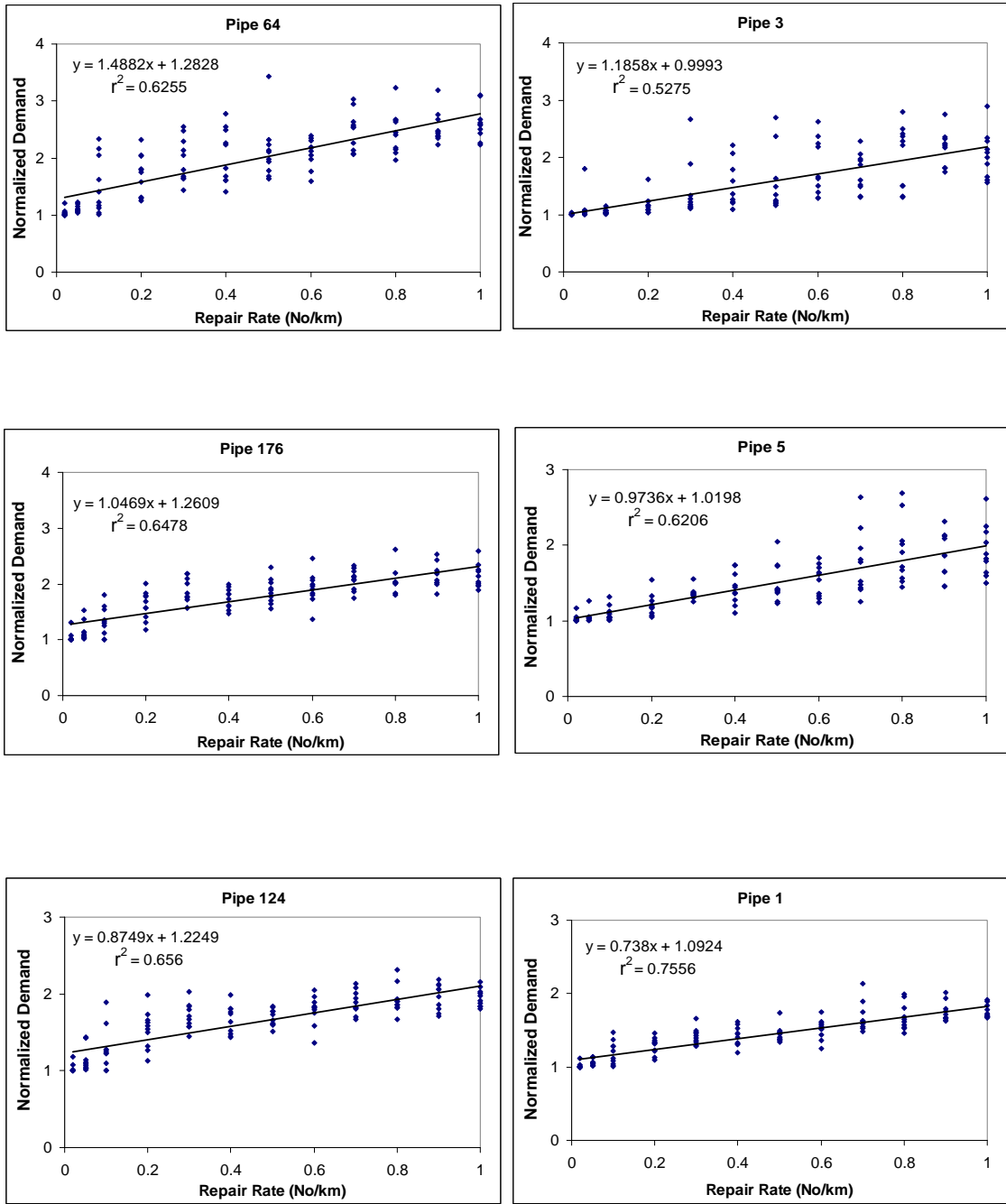
Figure B.5 Simulation Results for Monitored Pipes in Distribution System 426

Pipe 3

y = 1.4795x + 1.2579
r^2 = 0.7837

Normalized Demand

RR (Repairs/km)

Pipe 457

y = 2.3288x + 1.3941
r^2 = 0.7219

Normalized Demand

RR (Repairs/km)

Pipe 274

y = 1.9194x + 1.1902
r^2 = 0.5181

Normalized Demand

RR (Repairs/km)

Pipe 244

y = 1.6626x + 1.4347
r^2 = 0.6441

Normalized Demand

RR (Repairs/km)

Pipe 6

y = 2.3938x + 1.2785
r^2 = 0.7676

Normalized Demand

RR (Repairs/km)

Pipe 560

y = 1.2676x + 1.163
r^2 = 0.4889

Normalized Demand

RR (Repairs/km)
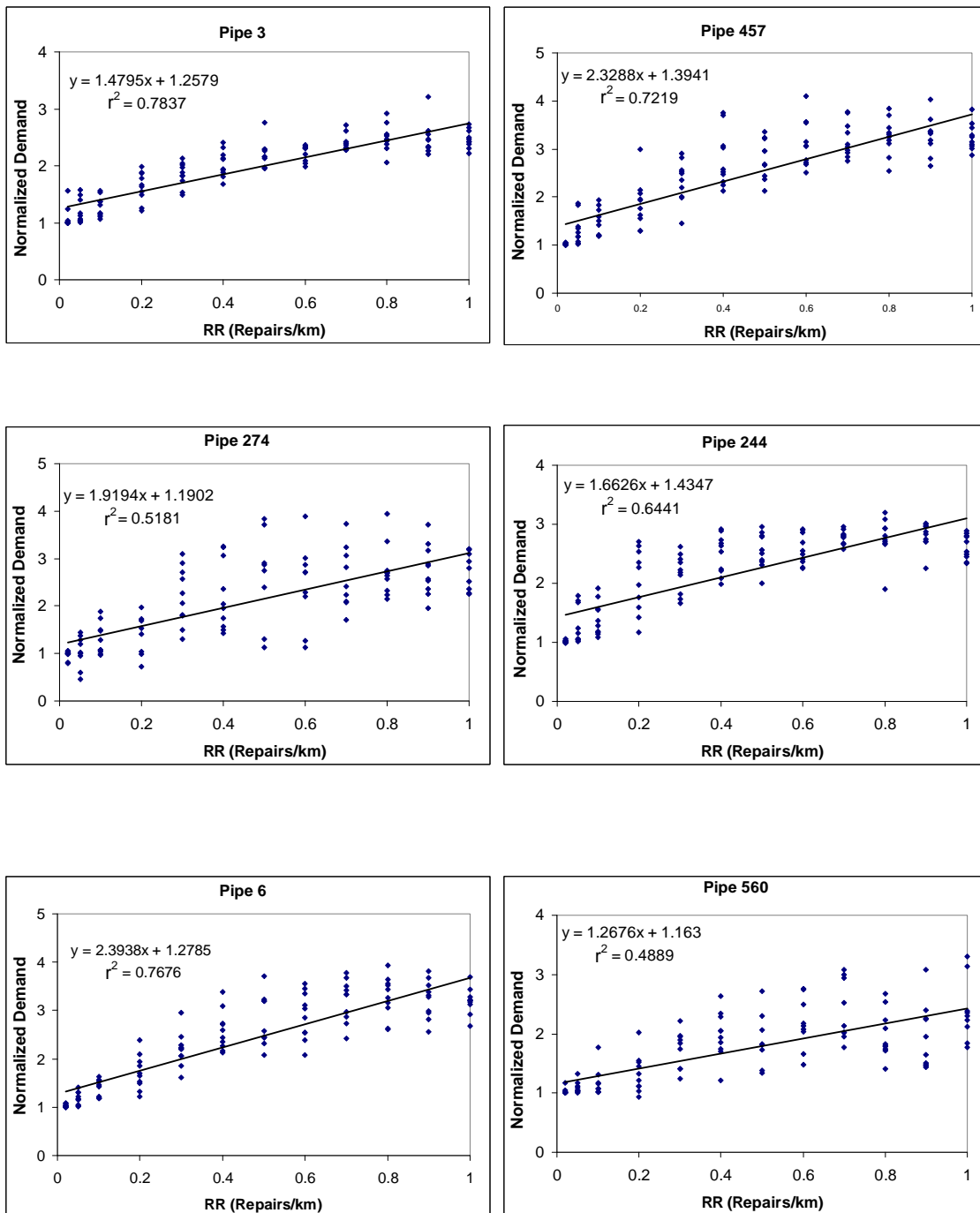
Figure B.6 Simulation Results for Monitored Pipes in Distribution System 205

APPENDIX C

LADWP TRUNK LINE DAMAGE SIMUALTIONS

This appendix describes the hydraulic simulations of the 67 locations of LADWP trunk line damage that occurred in the San Fernando Valley during the 1994 Northridge earthquake. The Granada Trunk Line (GTL), Rinaldi Trunk Line (RTL), and Roscoe Trunk Line sustained severe damage during the earthquake. In total, 49 locations of damage occurred in these three trunk lines. Damage simulations of the three trunk lines are described under the first three subheadings that follow. Simulations of the other 18 locations of damage are described under the fourth subheading.

C.1 GRANADA TRUNK LINE

The GTL is composed partly of welded steel and partly of prestressed concrete with a diameter ranging from 1220 (48) to 1257 mm (49.5 in.). It receives water from the Clearwell Tank in the Van Norman Complex and is located along the Balboa Boulevard, Rinaldi Street, and western rim of the San Fernando Valley.

The GTL was the most severely damaged trunk line during the 1994 Northridge earthquake. Figure C.1 shows the locations of damage in the GTL. The relevant damage details, including the location, pipe diameter, pipe material, damage descriptions, are summarized in Table C.1, based on information provided by LADWP (1996) and Davis (2003). Twenty-nine locations of damage were identified in the GTL after the earthquake. Among the 29 locations, 20 of them (Repairs 1 to 20) were
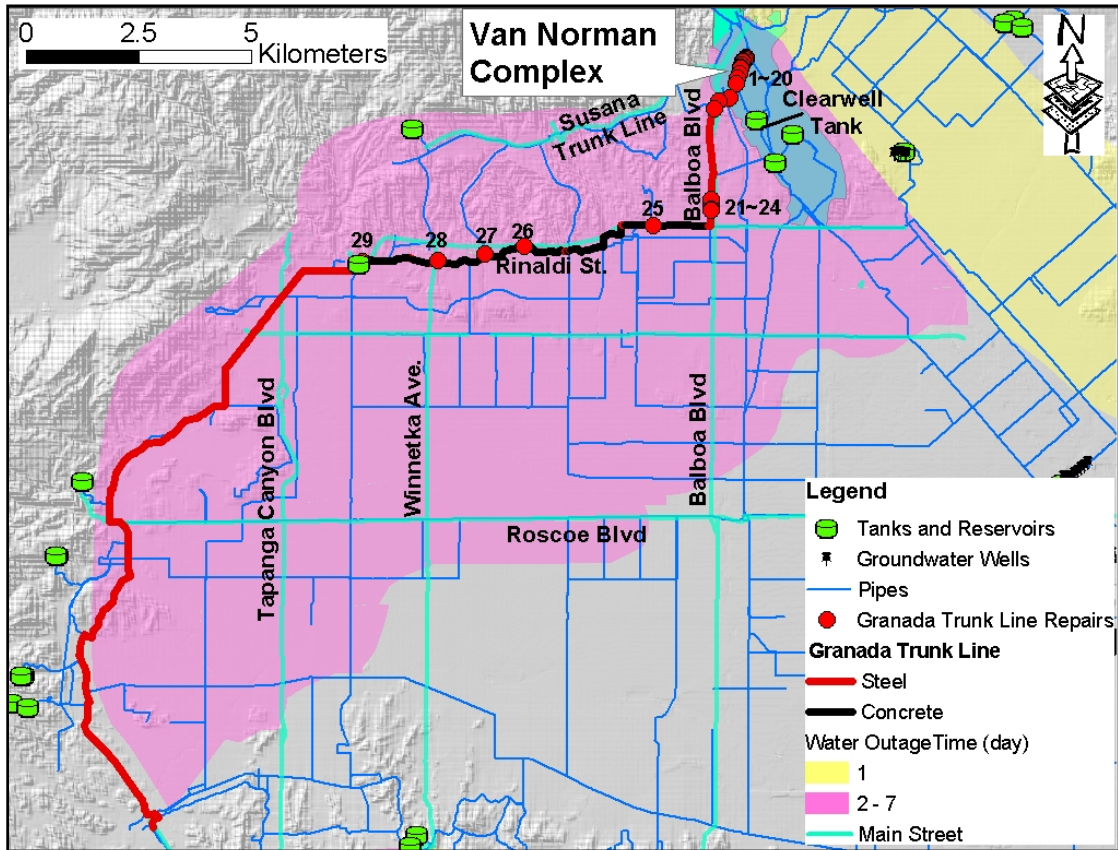
Figure C.1 Granada Trunk Line and Its Repairs

within or around the Van Norman Complex. Outside the Van Norman Complex, there were 4 repairs (Repairs 21 to 24) along Balboa Boulevard and 5 repairs (Repairs 25 to 29) along Rinaldi Street. Damage to the GTL in the Van Norman Complex was mainly in the form of compressive buckling at welded slip joints. Damage along Balboa Boulevard was mostly associated with the lateral ground displacement triggered by liquefaction.

Damage descriptions indicate that the GTL was pulled more than a half meter (20 in.) at Repair 23 in Balboa Boulevard. These descriptions are consistent with the field evidence that large ground deformation was generated by soil liquefaction in

Table C.1 Granada Trunk Line Damage Information Summary

ID	Trunk Line	Location	Dia. (mm)	Pipe Material	Damage Descriptions	Leak/ Break	Leak Dia. (mm)
1		Upper Debris Basin under Dike	1257	Steel	Crack at joint, approximate 300 mm long		
2		Upper Debris Basin under Dike	1257	Steel	Crack at joint, approximate 300 mm long Jagged tears, folded inward 76 mm, separated several tens mm, identified as major break by Davis (1999)		
3		Upper Debris Basin Sta. 3+68	1257	Steel	Jagged tears, folded inward 76 mm, separated several tens mm, identified as major break by Davis (1999)		
4		Upper Debris Basin Sta. 3+72	1257	Steel	Spigot flared inward 13 mm, compression		
5	Granada Trunk Line	Upper Debris Basin Sta. 6+21	1257	Steel	Folded inward and separated, identified as major break by Davis (1999) Jagged tears, folded inward 76 mm, separated several tens mm, identified as major break by Davis (1999)	Not modeled because Granada Trunk Line is completely disconnected downstream	N/A[1]
6		Upper Debris Basin Sta. 6+21	1257	Steel	Folded inward and separated 292 mm residual compressional displacement, coupling compressed 305 mm, slammed together, and separated 12 mm		
7		Upper Debris Basin Sta. 0+3.4 Relocated Line	1257	Steel	50 to 76 mm inside bulge, buckling at joint		
8		Upper Debris Basin Sta. 0+4.4 Relocated Line	1257	Steel	Crack at joint, approximate 300 mm long		
9		Utility Corridor, Sta 0+91.70	1257	Steel	Crack at joint, approximate 300 mm long		
10		Utility Corridor, Sta. 3+39 to 3+48	1257	Steel	Jagged tears, folded inward 76 mm, separated several tens mm, identified as major break by Davis (1999)		

Table C.1 (Continued)

ID	Trunk Line	Location	Dia. (mm)	Pipe Material	Damage Descriptions	Leak/Break	Leak Dia. (mm)
11	Granada Trunk Line	Utility Corridor, Sta. 3+60	1257	Steel	50 mm compressional displacement	Not modeled because Granada Trunk Line is completely disconnected down stream	N/A[1]
12		Utility Corridor, Sta. 5+40	1257	Steel	Cement mortar failure		
13		Utility Corridor, Sta. 6+98.4	1257	Steel	76 mm extensional displacement		
14		Utility Corridor, Sta. 9+68.4	1257	Steel	76 mm extensional displacement		
15		Utility Corridor, Sta. 13+28.5	1257	Steel	102 mm extensional displacement		
16		Utility Corridor, Sta. 16+49.9	1257	Steel	50 mm extensional displacement		
17		Utility Corridor, Sta. 17+40	1257	Steel	Cement mortar failure		
18		Utility Corridor, Sta. 26+89.18	1257	Steel	76 mm extensional displacement		
19		Utility Corridor, Sta. 39+60	1257	Steel	30 mm extensional displacement		
20		Balboa Blvd. at Valve between Woodley and Colvin	1257	Steel	Damaged and leaking, extensional movement		

Table C.1 (Continued)

ID	Trunk Line	Location	Dia. (mm)	Pipe Material	Damage Descriptions	Leak/ Break	Leak Dia. (mm)
21		17200 Balboa Blvd at Lorillard	1257	Steel	Joint fracture, extensional movement	**Break**	N/A[1]
22		Balboa Blvd. Sta. 115+80	1257	Steel	Separated joint, tension		
23		11661 Balboa Blvd.	1257	Steel	**Pulled apart 508 mm, extensional movement**		
24	Granada Trunk Line	Balboa Blvd. Sta. 129+56	1257	Steel	Pipe telescoped inside itself, compression		
25		East of Shoshone	1220	Concrete	Unknown	Leak	122 (Scenario 1)
26		Wilbur	1220	Concrete	Unknown	Leak	122 (Scenario 1)
27		Tampa Ave. at 118 Frwy	1220	Concrete	Joint fracture, joint fractured along side existing weld	Leak	122 (Scenario 1)
28		Between Melvin & Winnetka	1220	Concrete	Unknown	Leak	122 (Scenario 1)
29		Desoto Reservoir, North side	1220	Concrete	Joint fracture, joint fractured along side existing weld	Leak	122 (Scenario 1)

1: Not Applicable

Balboa Boulevard. The large ground deformation pulled several buried pipelines apart, and as a result, the Balboa Boulevard at that location was flooded after the earthquake. As such, Repair 23 was modeled as a break. The GTL receives water from the Clearwell Tank in the Van Normal Complex and transports water along Rinaldi Street and the western margin of San Fernando Valley. Downstream of Repair 23, the disconnection of the GTL in Balboa Boulevard cut off water from the source to its main demands. It is not significant in hydraulics to model the 20 repairs in the Van Norman Complex because the water losses from these repairs can be collectively modeled at Repair 23. Similarly, Repairs 21, 22, and 24 are in close proximity to Repair 23, and their effects can be represented by the break at Repair 23.

Limited damage descriptions are available for Repairs 25 to 29, and they indicate that damage most likely occurred as joint ruptures and disengagements. Each of these damage locations was modeled as a leak, characterized by annular disengagement, and orifice area calculated with Equation 5.11 developed in Section 5.4.4.1. The leak scenario and equivalent orifice diameter are listed in Table C.1. In summary, one break in Balboa Boulevard and five leaks in Rinaldi Street were modeled in the GTL.

C.2 RINALDI TRUNK LINE

The RTL is owned by the Metropolitan Water District (MWD) but operated by the LADWP. It originates at the Van Norman Complex and extends along Balboa Boulevard and Rinaldi Street in parallel with the GTL. The RTL consists of two major sections. One is composed of welded steel with a diameter of 1727 mm (68 in.) and runs from the Van Norman Complex to the intersection of Balboa Boulevard and
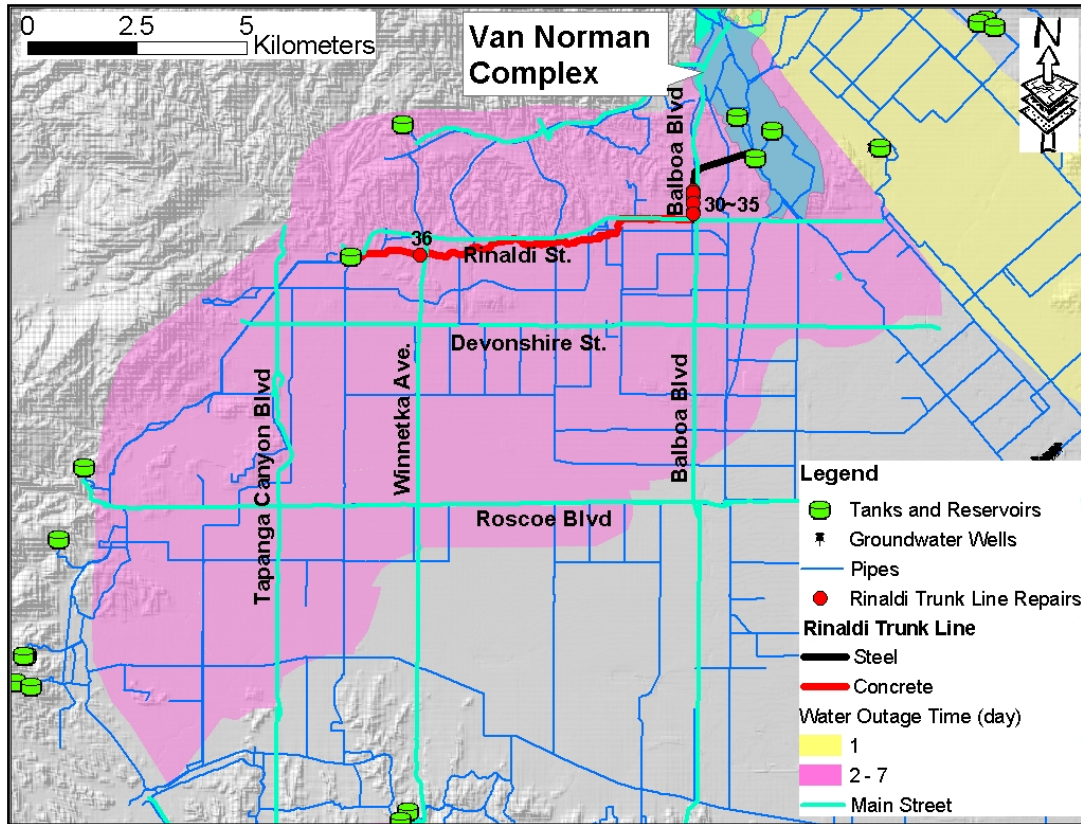
Figure C.2 Rinaldi Trunk Line and Its Repairs

Rinaldi Street. The other is composed of prestressed concrete with a diameter of 1372

mm (54 in.) and extends along Rinaldi Street. Figure C.2 shows the layout of the RTL

and its repairs after the Northridge earthquake.   Similar to the GTL, the 1994

Northridge earthquake caused severe damage to the RTL. The relevant repair details

are summarized in Table C.2.

Most of the damage locations occurred in the steel pipe section along Balboa

Boulevard, including 4 locations of joint pullout (Repairs 30 to 33), one location of

minor damage (Repair 34) with cement mortar cracking, and one location of

compressive failure (Repair 35). Multiple cracks also occurred in a 4.9-m(16-ft)-

length of concrete pipe section under Rinaldi Street (Repair 36). The damage to RTL

Table C.2 Rinaldi Trunk Line Damage Information Summary

Repair ID	Trunk Line	Location	Dia. (mm)	Pipe Material	Damage Descriptions	Leak/Break	Leak Dia. (mm)
30		Balboa Blvd. 91 m North of above	1727	Steel	Extensional movement		
31		11700 Balboa Blvd.	1727	Steel	**Pulled apart 508 mm, extensional movement**	**Break**	N/A[1]
32	Rinaldi Trunk Line	Balboa Blvd. Sta. 62+12	1727	Steel	13 mm separation, extensional movement		
33		Balboa Blvd. Sta. 63+72	1753	Steel	102 mm separation, extensional movement		
34		Balboa Blvd. Sta. 65+87	1727	Steel	Cement mortar failure		
35		11539 Balboa Blvd.	1727	Steel	Compression		
36		West of Winnetka St. Sta. 1219+10 (west of Melvin)	1372	Concrete	Multiple cracks in 4.9-m section of pipe, cracked at a cut-off wall	Leak	137 (Scenario 4)

1: Not Applicable

was attributed to the lateral ground displacement triggered by soil liquefaction, except for Repair 36. Similar to the GTL, the RTL lost its continuity due to the large ground deformation around the intersection of Balboa Boulevard and Rinaldi Street. Because locations of Repairs 30, 31, 32, 33, 34, and 35, are in close proximity, they were collectively modeled as a break at Repair 31. Repair 36 was modeled as a leak with local loss of pipe wall. The equivalent orifice area was calculated using Equation 5.22 developed in Section 5.4.4.4.

C.3   ROSCOE TRUNK LINE

The Roscoe Trunk Line is located in the central part of the San Fernando Valley and serves as a connector among the major trunk lines, such as the De Soto, Haskell and Hayvenhurst Trunk Lines. The Roscoe Trunk Line is composed partly of riveted steel and partly of welded steel with a diameter ranging from 914 mm (36 in.) to 1524 mm (60 in.). Figure C.3 shows the layout and material composition of the Roscoe Trunk Line together with its repairs. In total 13 repairs were made in Roscoe Trunk Line. The relevant details are summarized in Table C.3.

Repairs 37 to 42 occurred in the welded steel sections. As described in Section 4.4.5, the major damage mode to welded steel pipelines is compressive local buckling with an estimated 20% probability of causing leakage. As such, two leaks were modeled for the 6 repairs. One was modeled between Repairs 37 and 38 and the other was modeled between Repairs 39 and 42. The diameter of these leaks was calculated using Equation 5.26 developed in Section 5.4.4.5 by assuming each leak was a local tear of pipe wall.
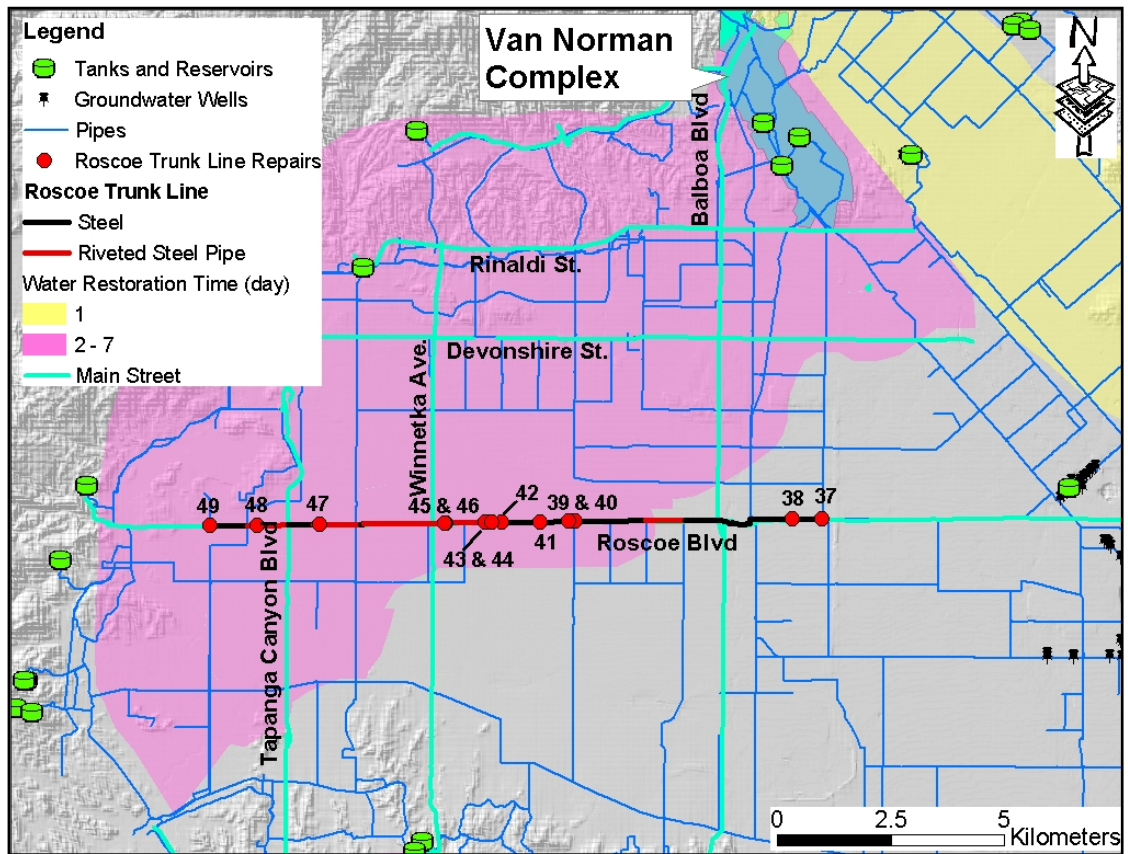
Figure C.3 Roscoe Trunk Line and Its Repairs

Repairs 43 to 49 occurred in the riveted steel section. Damage to riveted steel pipelines typically results from shear failure of rivets along the longitudinal and circumferential seams. Since Repairs 43 to 44 are very close to each other, they were modeled as one leak with its orifice area doubled. The same situation occurs at Repairs 45 and 46, which were modeled as one leak with its orifice area doubled. Each of Repairs 47, 48, and 49 was modeled as one leak, respectively. Due to the lack of information on the leak characteristics, it is difficult to decide on the type of leak that best represents the damage. From Section 5.4.5, three leak scenarios for riveted steel pipelines are possible, which are annular disengagement with a probability of 0.6, longitudinal crack with a probability of 0.3, and local loss of pipe wall with a

Table C.3 Roscoe Trunk Line Damage Information Summary

Repair ID	Trunk Line	Location	Dia. (mm)	Pipe Material	Damage Descriptions	Leak/Break	Leak Dia. (mm)
37		Haskel Ave	1524	Steel	Unknown	Leak	147 (Scenario 5)
38		Woodley Ave	1321	Steel	Unknown		
39		Reseda Blvd.	1016	Steel	No observable pipe movement	Leak	125 (Scenario 5)
40		Reseda Blvd., 140 m West, 18546 Roscoe Blvd	1016	Steel	No observable pipe movement		
41		Wilbur Ave. 53 m East 18844 Roscoe Blvd.	1016	Steel	No observable pipe movement		
42	Roscoe Trunk Line	Tampa	1016	Steel	No observable pipe movement		
43		Calvin	1016	Riveted Steel	No observable pipe movement	Leaks	251 (WA[1])
44		Shirley Ave. 46 m East	991	Riveted Steel	No observable pipe movement		
45		Oakdale, 18 m West	1067	Riveted Steel	No observable pipe movement	Leak	254 (WA[1])
46		Oakdale, 58 m West	1067	Riveted Steel	Unknown		
47		Canoga Ave	1295	Riveted Steel	Unknown	Leak	147 (WA[1])
48		Faralone Ave. 171 m West 22259 Roscoe Blvd.	1372	Riveted Steel	Unknown	Leak	150 (WA[1])
49		Fallbrook Ave. West Side	914	Riveted Steel	No observable pipe movement	Leak	100 (WA[1])

1 Weighted Average of Orifice Diameter from All Possible Leak Scenarios according to the Probability of Each Leak Scenario.

295

probability of 0.1. A weighted average of the equivalent orifice areas of the three leak scenarios with respect to their probabilities was calculated and assigned to each leak. The equivalent orifice diameter indicated as WA in Table C.3 means that this diameter was calculated from the weighted average of the equivalent orifice areas.

C.4   Other Trunk Lines

Besides the 49 repairs in the Granada, Rinaldi, and Roscoe Trunk Lines, there were 18 repairs in other trunk lines, which are shown in Figures C.4 and C.5 with expanded views. The relevant details on these repairs are provided in Tables C.4 and C.5. Among the 18 repairs, 12 occurred within or around the Van Norman Complex, as shown in Figure C.4 and Table C.4. Figure C.4 shows that 1 repair occurred in the LA City Trunk Line, 2 in the Stone Canyon Inlet, 1 in the Hayvenhurst Trunk Line, 4 in the Van Norman Pump Station Discharge Pipeline, 2 in the LA Reservoir Outlet, and 1 in the Susana Trunk Line. Field evidence indicated that a portion of the pipe wall of the LA City Trunk Line was torn apart and resulted in total loss of pipe function. As such, the repair at the LA City Trunk Line was modeled as a break. For other repairs, damage descriptions show no evidence of pipe breakage. Each repair was modeled as a leak except Repairs 56, 57, and 58 in the Van Norman Pump Station Discharge Line. Leaks were classified as annular disengagement based on the damage and repair descriptions. The equivalent orifice area was calculated using Equation 5.11 developed in Section 5.4.4.1. Damage at location of Repair 56 occurred at the pier supports of pipeline. Damage at locations of Repairs 57 and 58 occurred as compressive buckling of steel pipeline. These three locations of damage are unlikely to cause leakage and therefore they were not modeled as leaks.

296
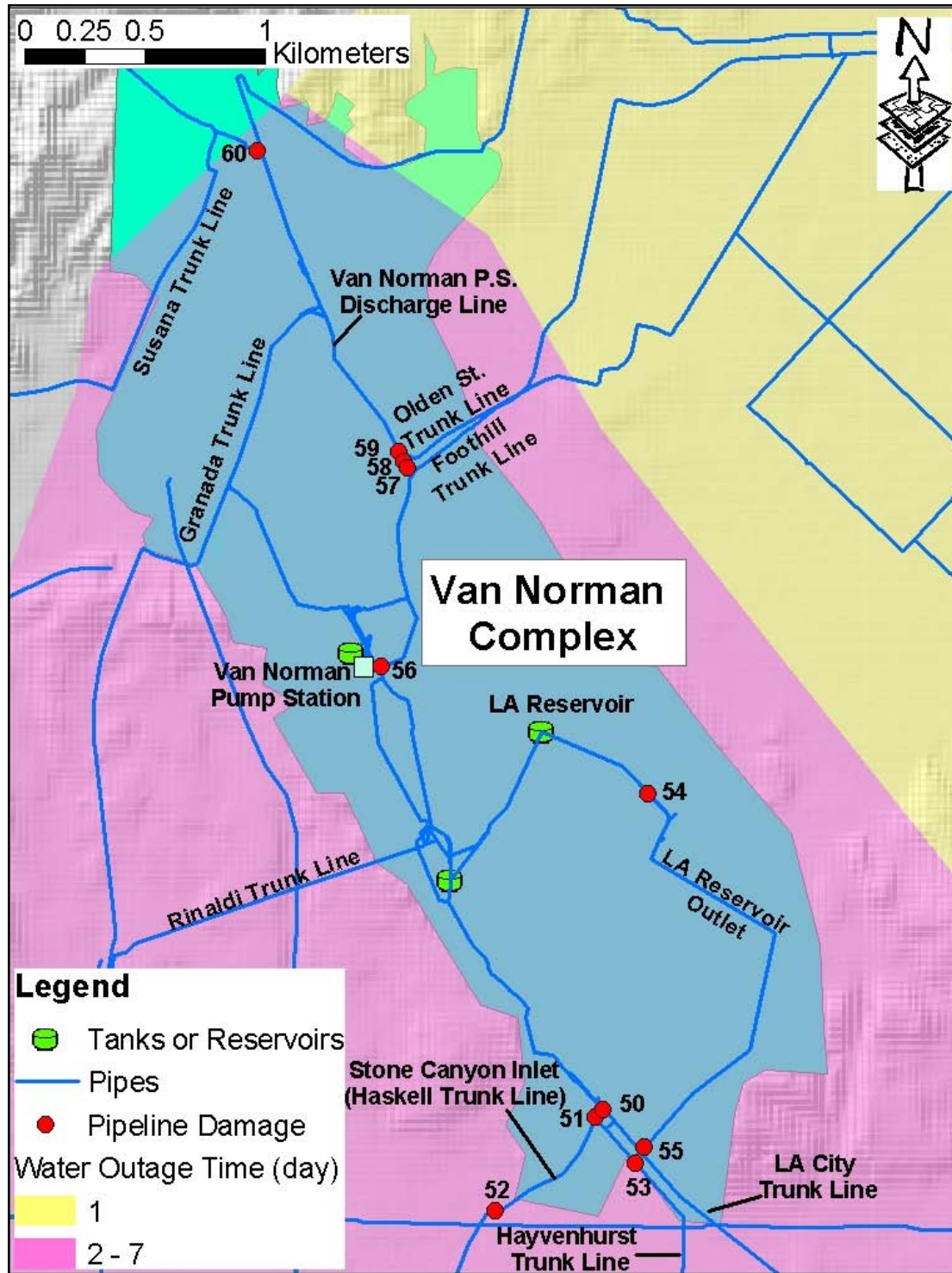
Figure C.4 Other Trunk Line Repairs in Van Norman Complex

Table C.4 Other Trunk Line Damage Information Summary 1

Repair ID	Trunk Line	Location	Dia. (mm)	Pipe Material	Damage Descriptions	Leak/Break	Leak Dia. (mm)
50	City Trunk Line	Lower San Fernando Dam	1829	Riveted Steel	**Tear at longitudinal seam**	**Break**	N/A
51	Stone Canyon Inlet	762-mm main at Hayvenhurst Trunk Line	1524	Steel	Leak at coupling, ruptured gasket	Leak	137 (Scenario 1)
52	Stone Canyon Inlet	1219-mm butterfly valve at LAR outlet	1524	Steel	Leak at coupling, ruptured gasket	Leak	137 (Scenario 1)
53	Hayvenhurst Trunk Line	Rinaldi & Woodley NE corner	1372	Riveted Steel	Sheared rivets, up to 25 mm compressional movement	Leak	130 (Scenario 1)
54	LA Reservoir Outlet	Butterfly valve at vault below dam	3048	Steel	Leak at coupling	Leak	193 (Scenario 1)
55	LA Reservoir Outlet	At City Trunk Line	3048	Steel	Leak at coupling, tear in gasket	Leak	193 (Scenario 1)
56	Van Norman P.S. Discharge Line	Pier supports	1372	Steel	Ring girder collapse, displaced pier supports, no damage to pipe connections, only pipe damage came from pipe falling on concrete pier after girder collapse	No leak/ No break	N/A
57	Van Norman P.S. Discharge Line	Between Foothill and Olden St. Trunk Line's	1372	Steel	Compression, bow, wrinkle and rip in gasket, pipe shell bowed	Leak	130 (Scenario 1)
58	Van Norman P.S. Discharge Line	Between Foothill and Olden St. Trunk Line's	305	Steel	Compression, shear	No leak/ No break	N/A
59	Van Norman P.S. Discharge Line	North of Olden St. Trunk Line	1372	Steel	Compression buckle, 50 mm lateral offset	No leak/ No break	N/A
60	Susana Trunk Line	Penstock Pump Station	1372	Steel	102 mm flange gasket tapped off	Leak	109 (Scenario 1)
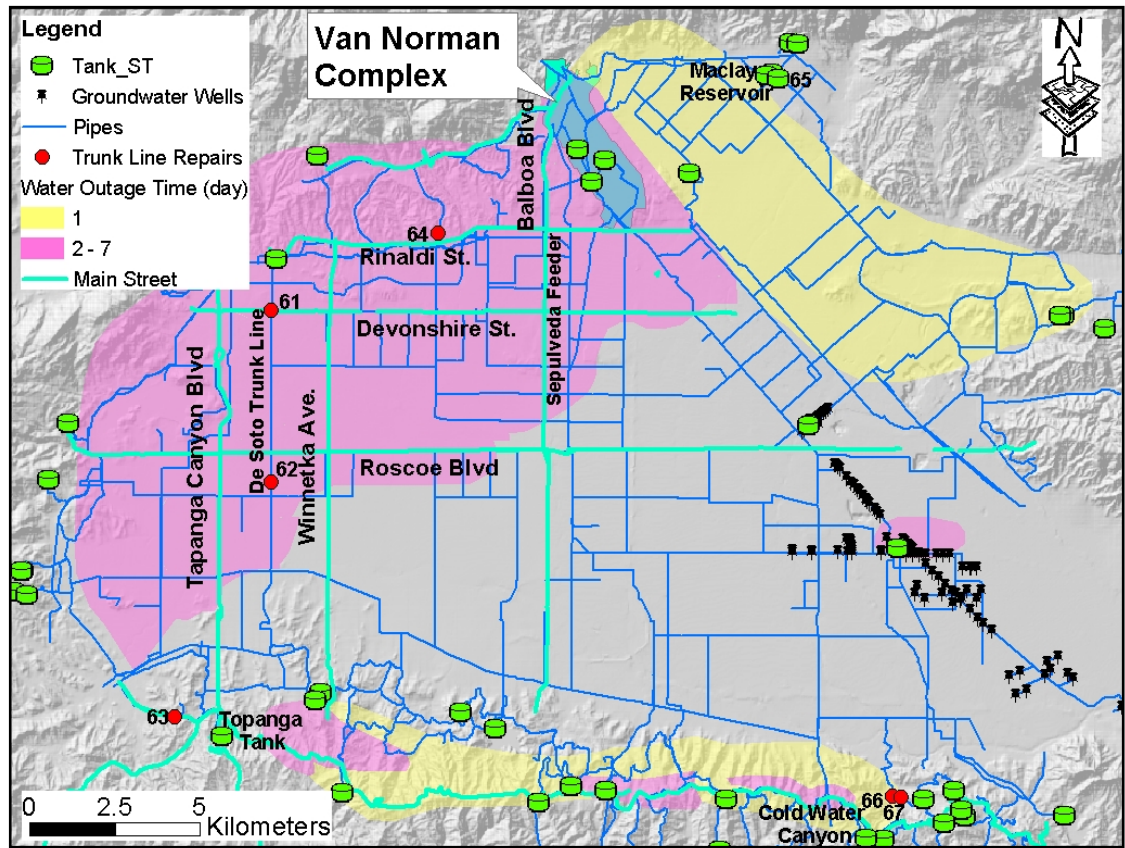
Figure C.5 Other Trunk Line Repairs outside Van Norman Complex

The 7 leaks outside the Van Norman Complex are shown in Figure C.5 and Table C.5. There is minimal damage description available for them. Each of them was modeled as a leak, with the equivalent orifice area calculated as the weighted average of the orifice areas of all possible leak scenarios. Because Repairs 66 and 67 are in the same pipeline and close to each other, the two leaks were combined into one leak with double orifice size.

Table C.5   Other Trunk Line Damage Information Summary 2

Repair ID	Trunk Line	Location	Dia. (mm)	Pipe Material	Damage Description	Leak/Break	Leak Dia. (mm)
61	Desoto Trunk Line	Ingomar	1067	Steel	Unknown	Leak	127 (WA[1])
62	Desoto Trunk Line	Devonshire	1372	Steel	Unknown	Leak	145 (WA[1])
63		Near Topanga Tank	914	Steel	Unknown	Leak	117 (WA[1])
64	Reseda Trunk Line	Asuncion St. (1.5 blocks North of Rinaldi)	762	Steel	Unknown	Leak	107 (WA[1])
65		Near Maclay Reservior	914	Ductile Iron?	Unknown	Leak	109 (WA[1])
66		Near Cold Water Canyon Tank	610	Ductile Iron?	Unknown		
67		Near Cold Water Canyon Tank	610	Ductile Iron?	Unknown	Leak	175 (WA[1])

1 Weighted Average of Orifice Diameter from All Possible Leak Scenarios according to the Probability of Each Leak Scenario

MCEER Technical Reports

MCEER publishes technical reports on a variety of subjects written by authors funded through MCEER. These reports are available from both MCEER Publications and the National Technical Information Service (NTIS). Requests for reports should be directed to MCEER Publications, MCEER, University at Buffalo, State University of New York, Red Jacket Quadrangle, Buffalo, New York 14261. Reports can also be requested through NTIS, 5285 Port Royal Road, Springfield, Virginia 22161. NTIS accession numbers are shown in parenthesis, if available.

NCEER-87-0001   "First-Year Program in Research, Education and Technology Transfer," 3/5/87, (PB88-134275, A04, MF-A01).

NCEER-87-0002   "Experimental Evaluation of Instantaneous Optimal Algorithms for Structural Control," by R.C. Lin, T.T. Soong and A.M. Reinhorn, 4/20/87, (PB88-134341, A04, MF-A01).

NCEER-87-0003   "Experimentation Using the Earthquake Simulation Facilities at University at Buffalo," by A.M. Reinhorn and R.L. Ketter, to be published.

NCEER-87-0004   "The System Characteristics and Performance of a Shaking Table," by J.S. Hwang, K.C. Chang and G.C. Lee, 6/1/87, (PB88-134259, A03, MF-A01). This report is available only through NTIS (see address given above).

NCEER-87-0005   "A Finite Element Formulation for Nonlinear Viscoplastic Material Using a Q Model," by O. Gyebi and G. Dasgupta, 11/2/87, (PB88-213764, A08, MF-A01).

NCEER-87-0006   "Symbolic Manipulation Program (SMP) - Algebraic Codes for Two and Three Dimensional Finite Element Formulations," by X. Lee and G. Dasgupta, 11/9/87, (PB88-218522, A05, MF-A01).

NCEER-87-0007   "Instantaneous Optimal Control Laws for Tall Buildings Under Seismic Excitations," by J.N. Yang, A. Akbarpour and P. Ghaemmaghami, 6/10/87, (PB88-134333, A06, MF-A01). This report is only available through NTIS (see address given above).

NCEER-87-0008   "IDARC: Inelastic Damage Analysis of Reinforced Concrete Frame - Shear-Wall Structures," by Y.J. Park, A.M. Reinhorn and S.K. Kunnath, 7/20/87, (PB88-134325, A09, MF-A01). This report is only available through NTIS (see address given above).

NCEER-87-0009   "Liquefaction Potential for New York State: A Preliminary Report on Sites in Manhattan and Buffalo," by M. Budhu, V. Vijayakumar, R.F. Giese and L. Baumgras, 8/31/87, (PB88-163704, A03, MF-A01). This report is available only through NTIS (see address given above).

NCEER-87-0010   "Vertical and Torsional Vibration of Foundations in Inhomogeneous Media," by A.S. Veletsos and K.W. Dotson, 6/1/87, (PB88-134291, A03, MF-A01). This report is only available through NTIS (see address given above).

NCEER-87-0011   "Seismic Probabilistic Risk Assessment and Seismic Margins Studies for Nuclear Power Plants," by Howard H.M. Hwang, 6/15/87, (PB88-134267, A03, MF-A01). This report is only available through NTIS (see address given above).

NCEER-87-0012   "Parametric Studies of Frequency Response of Secondary Systems Under Ground-Acceleration Excitations," by Y. Yong and Y.K. Lin, 6/10/87, (PB88-134309, A03, MF-A01). This report is only available through NTIS (see address given above).

NCEER-87-0013   "Frequency Response of Secondary Systems Under Seismic Excitation," by J.A. HoLung, J. Cai and Y.K. Lin, 7/31/87, (PB88-134317, A05, MF-A01). This report is only available through NTIS (see address given above).

NCEER-87-0014   "Modelling Earthquake Ground Motions in Seismically Active Regions Using Parametric Time Series Methods," by G.W. Ellis and A.S. Cakmak, 8/25/87, (PB88-134283, A08, MF-A01). This report is only available through NTIS (see address given above).

NCEER-87-0015   "Detection and Assessment of Seismic Structural Damage," by E. DiPasquale and A.S. Cakmak, 8/25/87, (PB88-163712, A05, MF-A01). This report is only available through NTIS (see address given above).

NCEER-87-0016 "Pipeline Experiment at Parkfield, California," by J. Isenberg and E. Richardson, 9/15/87, (PB88-163720, A03, MF-A01). This report is available only through NTIS (see address given above).

NCEER-87-0017 "Digital Simulation of Seismic Ground Motion," by M. Shinozuka, G. Deodatis and T. Harada, 8/31/87, (PB88-155197, A04, MF-A01). This report is available only through NTIS (see address given above).

NCEER-87-0018 "Practical Considerations for Structural Control: System Uncertainty, System Time Delay and Truncation of Small Control Forces," J.N. Yang and A. Akbarpour, 8/10/87, (PB88-163738, A08, MF-A01). This report is only available through NTIS (see address given above).

NCEER-87-0019 "Modal Analysis of Nonclassically Damped Structural Systems Using Canonical Transformation," by J.N. Yang, S. Sarkani and F.X. Long, 9/27/87, (PB88-187851, A04, MF-A01).

NCEER-87-0020 "A Nonstationary Solution in Random Vibration Theory," by J.R. Red-Horse and P.D. Spanos, 11/3/87, (PB88-163746, A03, MF-A01).

NCEER-87-0021 "Horizontal Impedances for Radially Inhomogeneous Viscoelastic Soil Layers," by A.S. Veletsos and K.W. Dotson, 10/15/87, (PB88-150859, A04, MF-A01).

NCEER-87-0022 "Seismic Damage Assessment of Reinforced Concrete Members," by Y.S. Chung, C. Meyer and M. Shinozuka, 10/9/87, (PB88-150867, A05, MF-A01). This report is available only through NTIS (see address given above).

NCEER-87-0023 "Active Structural Control in Civil Engineering," by T.T. Soong, 11/11/87, (PB88-187778, A03, MF-A01).

NCEER-87-0024 "Vertical and Torsional Impedances for Radially Inhomogeneous Viscoelastic Soil Layers," by K.W. Dotson and A.S. Veletsos, 12/87, (PB88-187786, A03, MF-A01).

NCEER-87-0025 "Proceedings from the Symposium on Seismic Hazards, Ground Motions, Soil-Liquefaction and Engineering Practice in Eastern North America," October 20-22, 1987, edited by K.H. Jacob, 12/87, (PB88-188115, A23, MF-A01). This report is available only through NTIS (see address given above).

NCEER-87-0026 "Report on the Whittier-Narrows, California, Earthquake of October 1, 1987," by J. Pantelic and A. Reinhorn, 11/87, (PB88-187752, A03, MF-A01). This report is available only through NTIS (see address given above).

NCEER-87-0027 "Design of a Modular Program for Transient Nonlinear Analysis of Large 3-D Building Structures," by S. Srivastav and J.F. Abel, 12/30/87, (PB88-187950, A05, MF-A01). This report is only available through NTIS (see address given above).

NCEER-87-0028 "Second-Year Program in Research, Education and Technology Transfer," 3/8/88, (PB88-219480, A04, MF-A01).

NCEER-88-0001 "Workshop on Seismic Computer Analysis and Design of Buildings With Interactive Graphics," by W. McGuire, J.F. Abel and C.H. Conley, 1/18/88, (PB88-187760, A03, MF-A01). This report is only available through NTIS (see address given above).

NCEER-88-0002 "Optimal Control of Nonlinear Flexible Structures," by J.N. Yang, F.X. Long and D. Wong, 1/22/88, (PB88-213772, A06, MF-A01).

NCEER-88-0003 "Substructuring Techniques in the Time Domain for Primary-Secondary Structural Systems," by G.D. Manolis and G. Juhn, 2/10/88, (PB88-213780, A04, MF-A01).

NCEER-88-0004 "Iterative Seismic Analysis of Primary-Secondary Systems," by A. Singhal, L.D. Lutes and P.D. Spanos, 2/23/88, (PB88-213798, A04, MF-A01).

NCEER-88-0005 "Stochastic Finite Element Expansion for Random Media," by P.D. Spanos and R. Ghanem, 3/14/88, (PB88-213806, A03, MF-A01).

NCEER-88-0006   "Combining Structural Optimization and Structural Control," by F.Y. Cheng and C.P. Pantelides, 1/10/88, (PB88-213814, A05, MF-A01).

NCEER-88-0007   "Seismic Performance Assessment of Code-Designed Structures," by H.H-M. Hwang, J-W. Jaw and H-J. Shau, 3/20/88, (PB88-219423, A04, MF-A01). This report is only available through NTIS (see address given above).

NCEER-88-0008   "Reliability Analysis of Code-Designed Structures Under Natural Hazards," by H.H-M. Hwang, H. Ushiba and M. Shinozuka, 2/29/88, (PB88-229471, A07, MF-A01). This report is only available through NTIS (see address given above).

NCEER-88-0009   "Seismic Fragility Analysis of Shear Wall Structures," by J-W Jaw and H.H-M. Hwang, 4/30/88, (PB89-102867, A04, MF-A01).

NCEER-88-0010   "Base Isolation of a Multi-Story Building Under a Harmonic Ground Motion - A Comparison of Performances of Various Systems," by F-G Fan, G. Ahmadi and I.G. Tadjbakhsh, 5/18/88, (PB89-122238, A06, MF-A01). This report is only available through NTIS (see address given above).

NCEER-88-0011   "Seismic Floor Response Spectra for a Combined System by Green's Functions," by F.M. Lavelle, L.A. Bergman and P.D. Spanos, 5/1/88, (PB89-102875, A03, MF-A01).

NCEER-88-0012   "A New Solution Technique for Randomly Excited Hysteretic Structures," by G.Q. Cai and Y.K. Lin, 5/16/88, (PB89-102883, A03, MF-A01).

NCEER-88-0013   "A Study of Radiation Damping and Soil-Structure Interaction Effects in the Centrifuge," by K. Weissman, supervised by J.H. Prevost, 5/24/88, (PB89-144703, A06, MF-A01).

NCEER-88-0014   "Parameter Identification and Implementation of a Kinematic Plasticity Model for Frictional Soils," by J.H. Prevost and D.V. Griffiths, to be published.

NCEER-88-0015   "Two- and Three- Dimensional Dynamic Finite Element Analyses of the Long Valley Dam," by D.V. Griffiths and J.H. Prevost, 6/17/88, (PB89-144711, A04, MF-A01).

NCEER-88-0016   "Damage Assessment of Reinforced Concrete Structures in Eastern United States," by A.M. Reinhorn, M.J. Seidel, S.K. Kunnath and Y.J. Park, 6/15/88, (PB89-122220, A04, MF-A01). This report is only available through NTIS (see address given above).

NCEER-88-0017   "Dynamic Compliance of Vertically Loaded Strip Foundations in Multilayered Viscoelastic Soils," by S. Ahmad and A.S.M. Israil, 6/17/88, (PB89-102891, A04, MF-A01).

NCEER-88-0018   "An Experimental Study of Seismic Structural Response With Added Viscoelastic Dampers," by R.C. Lin, Z. Liang, T.T. Soong and R.H. Zhang, 6/30/88, (PB89-122212, A05, MF-A01). This report is available only through NTIS (see address given above).

NCEER-88-0019   "Experimental Investigation of Primary - Secondary System Interaction," by G.D. Manolis, G. Juhn and A.M. Reinhorn, 5/27/88, (PB89-122204, A04, MF-A01).

NCEER-88-0020   "A Response Spectrum Approach For Analysis of Nonclassically Damped Structures," by J.N. Yang, S. Sarkani and F.X. Long, 4/22/88, (PB89-102909, A04, MF-A01).

NCEER-88-0021   "Seismic Interaction of Structures and Soils: Stochastic Approach," by A.S. Veletsos and A.M. Prasad, 7/21/88, (PB89-122196, A04, MF-A01). This report is only available through NTIS (see address given above).

NCEER-88-0022   "Identification of the Serviceability Limit State and Detection of Seismic Structural Damage," by E. DiPasquale and A.S. Cakmak, 6/15/88, (PB89-122188, A05, MF-A01). This report is available only through NTIS (see address given above).

NCEER-88-0023   "Multi-Hazard Risk Analysis: Case of a Simple Offshore Structure," by B.K. Bhartia and E.H. Vanmarcke, 7/21/88, (PB89-145213, A05, MF-A01).

NCEER-88-0024   "Automated Seismic Design of Reinforced Concrete Buildings," by Y.S. Chung, C. Meyer and M. Shinozuka, 7/5/88, (PB89-122170, A06, MF-A01). This report is available only through NTIS (see address given above).

NCEER-88-0025   "Experimental Study of Active Control of MDOF Structures Under Seismic Excitations," by L.L. Chung, R.C. Lin, T.T. Soong and A.M. Reinhorn, 7/10/88, (PB89-122600, A04, MF-A01).

NCEER-88-0026   "Earthquake Simulation Tests of a Low-Rise Metal Structure," by J.S. Hwang, K.C. Chang, G.C. Lee and R.L. Ketter, 8/1/88, (PB89-102917, A04, MF-A01).

NCEER-88-0027   "Systems Study of Urban Response and Reconstruction Due to Catastrophic Earthquakes," by F. Kozin and H.K. Zhou, 9/22/88, (PB90-162348, A04, MF-A01).

NCEER-88-0028   "Seismic Fragility Analysis of Plane Frame Structures," by H.H-M. Hwang and Y.K. Low, 7/31/88, (PB89-131445, A06, MF-A01).

NCEER-88-0029   "Response Analysis of Stochastic Structures," by A. Kardara, C. Bucher and M. Shinozuka, 9/22/88, (PB89-174429, A04, MF-A01).

NCEER-88-0030   "Nonnormal Accelerations Due to Yielding in a Primary Structure," by D.C.K. Chen and L.D. Lutes, 9/19/88, (PB89-131437, A04, MF-A01).

NCEER-88-0031   "Design Approaches for Soil-Structure Interaction," by A.S. Veletsos, A.M. Prasad and Y. Tang, 12/30/88, (PB89-174437, A03, MF-A01). This report is available only through NTIS (see address given above).

NCEER-88-0032   "A Re-evaluation of Design Spectra for Seismic Damage Control," by C.J. Turkstra and A.G. Tallin, 11/7/88, (PB89-145221, A05, MF-A01).

NCEER-88-0033   "The Behavior and Design of Noncontact Lap Splices Subjected to Repeated Inelastic Tensile Loading," by V.E. Sagan, P. Gergely and R.N. White, 12/8/88, (PB89-163737, A08, MF-A01).

NCEER-88-0034   "Seismic Response of Pile Foundations," by S.M. Mamoon, P.K. Banerjee and S. Ahmad, 11/1/88, (PB89-145239, A04, MF-A01).

NCEER-88-0035   "Modeling of R/C Building Structures With Flexible Floor Diaphragms (IDARC2)," by A.M. Reinhorn, S.K. Kunnath and N. Panahshahi, 9/7/88, (PB89-207153, A07, MF-A01).

NCEER-88-0036   "Solution of the Dam-Reservoir Interaction Problem Using a Combination of FEM, BEM with Particular Integrals, Modal Analysis, and Substructuring," by C-S. Tsai, G.C. Lee and R.L. Ketter, 12/31/88, (PB89-207146, A04, MF-A01).

NCEER-88-0037   "Optimal Placement of Actuators for Structural Control," by F.Y. Cheng and C.P. Pantelides, 8/15/88, (PB89-162846, A05, MF-A01).

NCEER-88-0038   "Teflon Bearings in Aseismic Base Isolation: Experimental Studies and Mathematical Modeling," by A. Mokha, M.C. Constantinou and A.M. Reinhorn, 12/5/88, (PB89-218457, A10, MF-A01). This report is available only through NTIS (see address given above).

NCEER-88-0039   "Seismic Behavior of Flat Slab High-Rise Buildings in the New York City Area," by P. Weidlinger and M. Ettouney, 10/15/88, (PB90-145681, A04, MF-A01).

NCEER-88-0040   "Evaluation of the Earthquake Resistance of Existing Buildings in New York City," by P. Weidlinger and M. Ettouney, 10/15/88, to be published.

NCEER-88-0041   "Small-Scale Modeling Techniques for Reinforced Concrete Structures Subjected to Seismic Loads," by W. Kim, A. El-Attar and R.N. White, 11/22/88, (PB89-189625, A05, MF-A01).

NCEER-88-0042   "Modeling Strong Ground Motion from Multiple Event Earthquakes," by G.W. Ellis and A.S. Cakmak, 10/15/88, (PB89-174445, A03, MF-A01).

NCEER-88-0043   "Nonstationary Models of Seismic Ground Acceleration," by M. Grigoriu, S.E. Ruiz and E. Rosenblueth, 7/15/88, (PB89-189617, A04, MF-A01).

NCEER-88-0044   "SARCF User's Guide: Seismic Analysis of Reinforced Concrete Frames," by Y.S. Chung, C. Meyer and M. Shinozuka, 11/9/88, (PB89-174452, A08, MF-A01).

NCEER-88-0045   "First Expert Panel Meeting on Disaster Research and Planning," edited by J. Pantelic and J. Stoyle, 9/15/88, (PB89-174460, A05, MF-A01).

NCEER-88-0046   "Preliminary Studies of the Effect of Degrading Infill Walls on the Nonlinear Seismic Response of Steel Frames," by C.Z. Chrysostomou, P. Gergely and J.F. Abel, 12/19/88, (PB89-208383, A05, MF-A01).

NCEER-88-0047   "Reinforced Concrete Frame Component Testing Facility - Design, Construction, Instrumentation and Operation," by S.P. Pessiki, C. Conley, T. Bond, P. Gergely and R.N. White, 12/16/88, (PB89-174478, A04, MF-A01).

NCEER-89-0001   "Effects of Protective Cushion and Soil Compliancy on the Response of Equipment Within a Seismically Excited Building," by J.A. HoLung, 2/16/89, (PB89-207179, A04, MF-A01).

NCEER-89-0002   "Statistical Evaluation of Response Modification Factors for Reinforced Concrete Structures," by H.H-M. Hwang and J-W. Jaw, 2/17/89, (PB89-207187, A05, MF-A01).

NCEER-89-0003   "Hysteretic Columns Under Random Excitation," by G-Q. Cai and Y.K. Lin, 1/9/89, (PB89-196513, A03, MF-A01).

NCEER-89-0004   "Experimental Study of `Elephant Foot Bulge' Instability of Thin-Walled Metal Tanks," by Z-H. Jia and R.L. Ketter, 2/22/89, (PB89-207195, A03, MF-A01).

NCEER-89-0005   "Experiment on Performance of Buried Pipelines Across San Andreas Fault," by J. Isenberg, E. Richardson and T.D. O'Rourke, 3/10/89, (PB89-218440, A04, MF-A01). This report is available only through NTIS (see address given above).

NCEER-89-0006   "A Knowledge-Based Approach to Structural Design of Earthquake-Resistant Buildings," by M. Subramani, P. Gergely, C.H. Conley, J.F. Abel and A.H. Zaghw, 1/15/89, (PB89-218465, A06, MF-A01).

NCEER-89-0007   "Liquefaction Hazards and Their Effects on Buried Pipelines," by T.D. O'Rourke and P.A. Lane, 2/1/89, (PB89-218481, A09, MF-A01).

NCEER-89-0008   "Fundamentals of System Identification in Structural Dynamics," by H. Imai, C-B. Yun, O. Maruyama and M. Shinozuka, 1/26/89, (PB89-207211, A04, MF-A01).

NCEER-89-0009   "Effects of the 1985 Michoacan Earthquake on Water Systems and Other Buried Lifelines in Mexico," by A.G. Ayala and M.J. O'Rourke, 3/8/89, (PB89-207229, A06, MF-A01).

NCEER-89-R010   "NCEER Bibliography of Earthquake Education Materials," by K.E.K. Ross, Second Revision, 9/1/89, (PB90-125352, A05, MF-A01). This report is replaced by NCEER-92-0018.

NCEER-89-0011   "Inelastic Three-Dimensional Response Analysis of Reinforced Concrete Building Structures (IDARC-3D), Part I - Modeling," by S.K. Kunnath and A.M. Reinhorn, 4/17/89, (PB90-114612, A07, MF-A01). This report is available only through NTIS (see address given above).

NCEER-89-0012   "Recommended Modifications to ATC-14," by C.D. Poland and J.O. Malley, 4/12/89, (PB90-108648, A15, MF-A01).

NCEER-89-0013   "Repair and Strengthening of Beam-to-Column Connections Subjected to Earthquake Loading," by M. Corazao and A.J. Durrani, 2/28/89, (PB90-109885, A06, MF-A01).

NCEER-89-0014   "Program EXKAL2 for Identification of Structural Dynamic Systems," by O. Maruyama, C-B. Yun, M. Hoshiya and M. Shinozuka, 5/19/89, (PB90-109877, A09, MF-A01).

NCEER-89-0015   "Response of Frames With Bolted Semi-Rigid Connections, Part I - Experimental Study and Analytical Predictions," by P.J. DiCorso, A.M. Reinhorn, J.R. Dickerson, J.B. Radziminski and W.L. Harper, 6/1/89, to be published.

NCEER-89-0016   "ARMA Monte Carlo Simulation in Probabilistic Structural Analysis," by P.D. Spanos and M.P. Mignolet, 7/10/89, (PB90-109893, A03, MF-A01).

NCEER-89-P017   "Preliminary Proceedings from the Conference on Disaster Preparedness - The Place of Earthquake Education in Our Schools," Edited by K.E.K. Ross, 6/23/89, (PB90-108606, A03, MF-A01).

NCEER-89-0017   "Proceedings from the Conference on Disaster Preparedness - The Place of Earthquake Education in Our Schools," Edited by K.E.K. Ross, 12/31/89, (PB90-207895, A012, MF-A02). This report is available only through NTIS (see address given above).

NCEER-89-0018   "Multidimensional Models of Hysteretic Material Behavior for Vibration Analysis of Shape Memory Energy Absorbing Devices, by E.J. Graesser and F.A. Cozzarelli, 6/7/89, (PB90-164146, A04, MF-A01).

NCEER-89-0019   "Nonlinear Dynamic Analysis of Three-Dimensional Base Isolated Structures (3D-BASIS)," by S. Nagarajaiah, A.M. Reinhorn and M.C. Constantinou, 8/3/89, (PB90-161936, A06, MF-A01). This report has been replaced by NCEER-93-0011.

NCEER-89-0020   "Structural Control Considering Time-Rate of Control Forces and Control Rate Constraints," by F.Y. Cheng and C.P. Pantelides, 8/3/89, (PB90-120445, A04, MF-A01).

NCEER-89-0021   "Subsurface Conditions of Memphis and Shelby County," by K.W. Ng, T-S. Chang and H-H.M. Hwang, 7/26/89, (PB90-120437, A03, MF-A01).

NCEER-89-0022   "Seismic Wave Propagation Effects on Straight Jointed Buried Pipelines," by K. Elhmadi and M.J. O'Rourke, 8/24/89, (PB90-162322, A10, MF-A02).

NCEER-89-0023   "Workshop on Serviceability Analysis of Water Delivery Systems," edited by M. Grigoriu, 3/6/89, (PB90-127424, A03, MF-A01).

NCEER-89-0024   "Shaking Table Study of a 1/5 Scale Steel Frame Composed of Tapered Members," by K.C. Chang, J.S. Hwang and G.C. Lee, 9/18/89, (PB90-160169, A04, MF-A01).

NCEER-89-0025   "DYNA1D: A Computer Program for Nonlinear Seismic Site Response Analysis - Technical Documentation," by Jean H. Prevost, 9/14/89, (PB90-161944, A07, MF-A01). This report is available only through NTIS (see address given above).

NCEER-89-0026   "1:4 Scale Model Studies of Active Tendon Systems and Active Mass Dampers for Aseismic Protection," by A.M. Reinhorn, T.T. Soong, R.C. Lin, Y.P. Yang, Y. Fukao, H. Abe and M. Nakai, 9/15/89, (PB90-173246, A10, MF-A02). This report is available only through NTIS (see address given above).

NCEER-89-0027   "Scattering of Waves by Inclusions in a Nonhomogeneous Elastic Half Space Solved by Boundary Element Methods," by P.K. Hadley, A. Askar and A.S. Cakmak, 6/15/89, (PB90-145699, A07, MF-A01).

NCEER-89-0028   "Statistical Evaluation of Deflection Amplification Factors for Reinforced Concrete Structures," by H.H.M. Hwang, J-W. Jaw and A.L. Ch'ng, 8/31/89, (PB90-164633, A05, MF-A01).

NCEER-89-0029   "Bedrock Accelerations in Memphis Area Due to Large New Madrid Earthquakes," by H.H.M. Hwang, C.H.S. Chen and G. Yu, 11/7/89, (PB90-162330, A04, MF-A01).

NCEER-89-0030   "Seismic Behavior and Response Sensitivity of Secondary Structural Systems," by Y.Q. Chen and T.T. Soong, 10/23/89, (PB90-164658, A08, MF-A01).

NCEER-89-0031   "Random Vibration and Reliability Analysis of Primary-Secondary Structural Systems," by Y. Ibrahim, M. Grigoriu and T.T. Soong, 11/10/89, (PB90-161951, A04, MF-A01).

NCEER-89-0032   "Proceedings from the Second U.S. - Japan Workshop on Liquefaction, Large Ground Deformation and Their Effects on Lifelines, September 26-29, 1989," Edited by T.D. O'Rourke and M. Hamada, 12/1/89, (PB90-209388, A22, MF-A03).

NCEER-89-0033   "Deterministic Model for Seismic Damage Evaluation of Reinforced Concrete Structures," by J.M. Bracci, A.M. Reinhorn, J.B. Mander and S.K. Kunnath, 9/27/89, (PB91-108803, A06, MF-A01).

NCEER-89-0034   "On the Relation Between Local and Global Damage Indices," by E. DiPasquale and A.S. Cakmak, 8/15/89, (PB90-173865, A05, MF-A01).

NCEER-89-0035   "Cyclic Undrained Behavior of Nonplastic and Low Plasticity Silts," by A.J. Walker and H.E. Stewart, 7/26/89, (PB90-183518, A10, MF-A01).

NCEER-89-0036   "Liquefaction Potential of Surficial Deposits in the City of Buffalo, New York," by M. Budhu, R. Giese and L. Baumgrass, 1/17/89, (PB90-208455, A04, MF-A01).

NCEER-89-0037   "A Deterministic Assessment of Effects of Ground Motion Incoherence," by A.S. Veletsos and Y. Tang, 7/15/89, (PB90-164294, A03, MF-A01).

NCEER-89-0038   "Workshop on Ground Motion Parameters for Seismic Hazard Mapping," July 17-18, 1989, edited by R.V. Whitman, 12/1/89, (PB90-173923, A04, MF-A01).

NCEER-89-0039   "Seismic Effects on Elevated Transit Lines of the New York City Transit Authority," by C.J. Costantino, C.A. Miller and E. Heymsfield, 12/26/89, (PB90-207887, A06, MF-A01).

NCEER-89-0040   "Centrifugal Modeling of Dynamic Soil-Structure Interaction," by K. Weissman, Supervised by J.H. Prevost, 5/10/89, (PB90-207879, A07, MF-A01).

NCEER-89-0041   "Linearized Identification of Buildings With Cores for Seismic Vulnerability Assessment," by I-K. Ho and A.E. Aktan, 11/1/89, (PB90-251943, A07, MF-A01).

NCEER-90-0001   "Geotechnical and Lifeline Aspects of the October 17, 1989 Loma Prieta Earthquake in San Francisco," by T.D. O'Rourke, H.E. Stewart, F.T. Blackburn and T.S. Dickerman, 1/90, (PB90-208596, A05, MF-A01).

NCEER-90-0002   "Nonnormal Secondary Response Due to Yielding in a Primary Structure," by D.C.K. Chen and L.D. Lutes, 2/28/90, (PB90-251976, A07, MF-A01).

NCEER-90-0003   "Earthquake Education Materials for Grades K-12," by K.E.K. Ross, 4/16/90, (PB91-251984, A05, MF-A05). This report has been replaced by NCEER-92-0018.

NCEER-90-0004   "Catalog of Strong Motion Stations in Eastern North America," by R.W. Busby, 4/3/90, (PB90-251984, A05, MF-A01).

NCEER-90-0005   "NCEER Strong-Motion Data Base: A User Manual for the GeoBase Release (Version 1.0 for the Sun3)," by P. Friberg and K. Jacob, 3/31/90 (PB90-258062, A04, MF-A01).

NCEER-90-0006   "Seismic Hazard Along a Crude Oil Pipeline in the Event of an 1811-1812 Type New Madrid Earthquake," by H.H.M. Hwang and C-H.S. Chen, 4/16/90, (PB90-258054, A04, MF-A01).

NCEER-90-0007   "Site-Specific Response Spectra for Memphis Sheahan Pumping Station," by H.H.M. Hwang and C.S. Lee, 5/15/90, (PB91-108811, A05, MF-A01).

NCEER-90-0008   "Pilot Study on Seismic Vulnerability of Crude Oil Transmission Systems," by T. Ariman, R. Dobry, M. Grigoriu, F. Kozin, M. O'Rourke, T. O'Rourke and M. Shinozuka, 5/25/90, (PB91-108837, A06, MF-A01).

NCEER-90-0009   "A Program to Generate Site Dependent Time Histories: EQGEN," by G.W. Ellis, M. Srinivasan and A.S. Cakmak, 1/30/90, (PB91-108829, A04, MF-A01).

NCEER-90-0010   "Active Isolation for Seismic Protection of Operating Rooms," by M.E. Talbott, Supervised by M. Shinozuka, 6/8/9, (PB91-110205, A05, MF-A01).

NCEER-90-0011   "Program LINEARID for Identification of Linear Structural Dynamic Systems," by C-B. Yun and M. Shinozuka, 6/25/90, (PB91-110312, A08, MF-A01).

NCEER-90-0012   "Two-Dimensional Two-Phase Elasto-Plastic Seismic Response of Earth Dams," by A.N. Yiagos, Supervised by J.H. Prevost, 6/20/90, (PB91-110197, A13, MF-A02).

NCEER-90-0013   "Secondary Systems in Base-Isolated Structures: Experimental Investigation, Stochastic Response and Stochastic Sensitivity," by G.D. Manolis, G. Juhn, M.C. Constantinou and A.M. Reinhorn, 7/1/90, (PB91-110320, A08, MF-A01).

NCEER-90-0014   "Seismic Behavior of Lightly-Reinforced Concrete Column and Beam-Column Joint Details," by S.P. Pessiki, C.H. Conley, P. Gergely and R.N. White, 8/22/90, (PB91-108795, A11, MF-A02).

NCEER-90-0015   "Two Hybrid Control Systems for Building Structures Under Strong Earthquakes," by J.N. Yang and A. Danielians, 6/29/90, (PB91-125393, A04, MF-A01).

NCEER-90-0016   "Instantaneous Optimal Control with Acceleration and Velocity Feedback," by J.N. Yang and Z. Li, 6/29/90, (PB91-125401, A03, MF-A01).

NCEER-90-0017   "Reconnaissance Report on the Northern Iran Earthquake of June 21, 1990," by M. Mehrain, 10/4/90, (PB91-125377, A03, MF-A01).

NCEER-90-0018   "Evaluation of Liquefaction Potential in Memphis and Shelby County," by T.S. Chang, P.S. Tang, C.S. Lee and H. Hwang, 8/10/90, (PB91-125427, A09, MF-A01).

NCEER-90-0019   "Experimental and Analytical Study of a Combined Sliding Disc Bearing and Helical Steel Spring Isolation System," by M.C. Constantinou, A.S. Mokha and A.M. Reinhorn, 10/4/90, (PB91-125385, A06, MF-A01). This report is available only through NTIS (see address given above).

NCEER-90-0020   "Experimental Study and Analytical Prediction of Earthquake Response of a Sliding Isolation System with a Spherical Surface," by A.S. Mokha, M.C. Constantinou and A.M. Reinhorn, 10/11/90, (PB91-125419, A05, MF-A01).

NCEER-90-0021   "Dynamic Interaction Factors for Floating Pile Groups," by G. Gazetas, K. Fan, A. Kaynia and E. Kausel, 9/10/90, (PB91-170381, A05, MF-A01).

NCEER-90-0022   "Evaluation of Seismic Damage Indices for Reinforced Concrete Structures," by S. Rodriguez-Gomez and A.S. Cakmak, 9/30/90, PB91-171322, A06, MF-A01).

NCEER-90-0023   "Study of Site Response at a Selected Memphis Site," by H. Desai, S. Ahmad, E.S. Gazetas and M.R. Oh, 10/11/90, (PB91-196857, A03, MF-A01).

NCEER-90-0024   "A User's Guide to Strongmo: Version 1.0 of NCEER's Strong-Motion Data Access Tool for PCs and Terminals," by P.A. Friberg and C.A.T. Susch, 11/15/90, (PB91-171272, A03, MF-A01).

NCEER-90-0025   "A Three-Dimensional Analytical Study of Spatial Variability of Seismic Ground Motions," by L-L. Hong and A.H.-S. Ang, 10/30/90, (PB91-170399, A09, MF-A01).

NCEER-90-0026   "MUMOID User's Guide - A Program for the Identification of Modal Parameters," by S. Rodriguez-Gomez and E. DiPasquale, 9/30/90, (PB91-171298, A04, MF-A01).

NCEER-90-0027   "SARCF-II User's Guide - Seismic Analysis of Reinforced Concrete Frames," by S. Rodriguez-Gomez, Y.S. Chung and C. Meyer, 9/30/90, (PB91-171280, A05, MF-A01).

NCEER-90-0028   "Viscous Dampers: Testing, Modeling and Application in Vibration and Seismic Isolation," by N. Makris and M.C. Constantinou, 12/20/90 (PB91-190561, A06, MF-A01).

NCEER-90-0029   "Soil Effects on Earthquake Ground Motions in the Memphis Area," by H. Hwang, C.S. Lee, K.W. Ng and T.S. Chang, 8/2/90, (PB91-190751, A05, MF-A01).

NCEER-91-0001   "Proceedings from the Third Japan-U.S. Workshop on Earthquake Resistant Design of Lifeline Facilities and Countermeasures for Soil Liquefaction, December 17-19, 1990," edited by T.D. O'Rourke and M. Hamada, 2/1/91, (PB91-179259, A99, MF-A04).

NCEER-91-0002   "Physical Space Solutions of Non-Proportionally Damped Systems," by M. Tong, Z. Liang and G.C. Lee, 1/15/91, (PB91-179242, A04, MF-A01).

NCEER-91-0003   "Seismic Response of Single Piles and Pile Groups," by K. Fan and G. Gazetas, 1/10/91, (PB92-174994, A04, MF-A01).

NCEER-91-0004   "Damping of Structures: Part 1 - Theory of Complex Damping," by Z. Liang and G. Lee, 10/10/91, (PB92-197235, A12, MF-A03).

NCEER-91-0005   "3D-BASIS - Nonlinear Dynamic Analysis of Three Dimensional Base Isolated Structures: Part II," by S. Nagarajaiah, A.M. Reinhorn and M.C. Constantinou, 2/28/91, (PB91-190553, A07, MF-A01). This report has been replaced by NCEER-93-0011.

NCEER-91-0006   "A Multidimensional Hysteretic Model for Plasticity Deforming Metals in Energy Absorbing Devices," by E.J. Graesser and F.A. Cozzarelli, 4/9/91, (PB92-108364, A04, MF-A01).

NCEER-91-0007   "A Framework for Customizable Knowledge-Based Expert Systems with an Application to a KBES for Evaluating the Seismic Resistance of Existing Buildings," by E.G. Ibarra-Anaya and S.J. Fenves, 4/9/91, (PB91-210930, A08, MF-A01).

NCEER-91-0008   "Nonlinear Analysis of Steel Frames with Semi-Rigid Connections Using the Capacity Spectrum Method," by G.G. Deierlein, S-H. Hsieh, Y-J. Shen and J.F. Abel, 7/2/91, (PB92-113828, A05, MF-A01).

NCEER-91-0009   "Earthquake Education Materials for Grades K-12," by K.E.K. Ross, 4/30/91, (PB91-212142, A06, MF-A01). This report has been replaced by NCEER-92-0018.

NCEER-91-0010   "Phase Wave Velocities and Displacement Phase Differences in a Harmonically Oscillating Pile," by N. Makris and G. Gazetas, 7/8/91, (PB92-108356, A04, MF-A01).

NCEER-91-0011   "Dynamic Characteristics of a Full-Size Five-Story Steel Structure and a 2/5 Scale Model," by K.C. Chang, G.C. Yao, G.C. Lee, D.S. Hao and Y.C. Yeh," 7/2/91, (PB93-116648, A06, MF-A02).

NCEER-91-0012   "Seismic Response of a 2/5 Scale Steel Structure with Added Viscoelastic Dampers," by K.C. Chang, T.T. Soong, S-T. Oh and M.L. Lai, 5/17/91, (PB92-110816, A05, MF-A01).

NCEER-91-0013   "Earthquake Response of Retaining Walls; Full-Scale Testing and Computational Modeling," by S. Alampalli and A-W.M. Elgamal, 6/20/91, to be published.

NCEER-91-0014   "3D-BASIS-M: Nonlinear Dynamic Analysis of Multiple Building Base Isolated Structures," by P.C. Tsopelas, S. Nagarajaiah, M.C. Constantinou and A.M. Reinhorn, 5/28/91, (PB92-113885, A09, MF-A02).

NCEER-91-0015   "Evaluation of SEAOC Design Requirements for Sliding Isolated Structures," by D. Theodossiou and M.C. Constantinou, 6/10/91, (PB92-114602, A11, MF-A03).

NCEER-91-0016   "Closed-Loop Modal Testing of a 27-Story Reinforced Concrete Flat Plate-Core Building," by H.R. Somaprasad, T. Toksoy, H. Yoshiyuki and A.E. Aktan, 7/15/91, (PB92-129980, A07, MF-A02).

NCEER-91-0017   "Shake Table Test of a 1/6 Scale Two-Story Lightly Reinforced Concrete Building," by A.G. El-Attar, R.N. White and P. Gergely, 2/28/91, (PB92-222447, A06, MF-A02).

NCEER-91-0018   "Shake Table Test of a 1/8 Scale Three-Story Lightly Reinforced Concrete Building," by A.G. El-Attar, R.N. White and P. Gergely, 2/28/91, (PB93-116630, A08, MF-A02).

NCEER-91-0019   "Transfer Functions for Rigid Rectangular Foundations," by A.S. Veletsos, A.M. Prasad and W.H. Wu, 7/31/91, to be published.

NCEER-91-0020   "Hybrid Control of Seismic-Excited Nonlinear and Inelastic Structural Systems," by J.N. Yang, Z. Li and A. Danielians, 8/1/91, (PB92-143171, A06, MF-A02).

NCEER-91-0021   "The NCEER-91 Earthquake Catalog: Improved Intensity-Based Magnitudes and Recurrence Relations for U.S. Earthquakes East of New Madrid," by L. Seeber and J.G. Armbruster, 8/28/91, (PB92-176742, A06, MF-A02).

NCEER-91-0022   "Proceedings from the Implementation of Earthquake Planning and Education in Schools: The Need for Change - The Roles of the Changemakers," by K.E.K. Ross and F. Winslow, 7/23/91, (PB92-129998, A12, MF-A03).

NCEER-91-0023   "A Study of Reliability-Based Criteria for Seismic Design of Reinforced Concrete Frame Buildings," by H.H.M. Hwang and H-M. Hsu, 8/10/91, (PB92-140235, A09, MF-A02).

NCEER-91-0024   "Experimental Verification of a Number of Structural System Identification Algorithms," by R.G. Ghanem, H. Gavin and M. Shinozuka, 9/18/91, (PB92-176577, A18, MF-A04).

NCEER-91-0025   "Probabilistic Evaluation of Liquefaction Potential," by H.H.M. Hwang and C.S. Lee," 11/25/91, (PB92-143429, A05, MF-A01).

NCEER-91-0026   "Instantaneous Optimal Control for Linear, Nonlinear and Hysteretic Structures - Stable Controllers," by J.N. Yang and Z. Li, 11/15/91, (PB92-163807, A04, MF-A01).

NCEER-91-0027   "Experimental and Theoretical Study of a Sliding Isolation System for Bridges," by M.C. Constantinou, A. Kartoum, A.M. Reinhorn and P. Bradford, 11/15/91, (PB92-176973, A10, MF-A03).

NCEER-92-0001   "Case Studies of Liquefaction and Lifeline Performance During Past Earthquakes, Volume 1: Japanese Case Studies," Edited by M. Hamada and T. O'Rourke, 2/17/92, (PB92-197243, A18, MF-A04).

NCEER-92-0002   "Case Studies of Liquefaction and Lifeline Performance During Past Earthquakes, Volume 2: United States Case Studies," Edited by T. O'Rourke and M. Hamada, 2/17/92, (PB92-197250, A20, MF-A04).

NCEER-92-0003   "Issues in Earthquake Education," Edited by K. Ross, 2/3/92, (PB92-222389, A07, MF-A02).

NCEER-92-0004   "Proceedings from the First U.S. - Japan Workshop on Earthquake Protective Systems for Bridges," Edited by I.G. Buckle, 2/4/92, (PB94-142239, A99, MF-A06).

NCEER-92-0005   "Seismic Ground Motion from a Haskell-Type Source in a Multiple-Layered Half-Space," A.P. Theoharis, G. Deodatis and M. Shinozuka, 1/2/92, to be published.

NCEER-92-0006   "Proceedings from the Site Effects Workshop," Edited by R. Whitman, 2/29/92, (PB92-197201, A04, MF-A01).

NCEER-92-0007   "Engineering Evaluation of Permanent Ground Deformations Due to Seismically-Induced Liquefaction," by M.H. Baziar, R. Dobry and A-W.M. Elgamal, 3/24/92, (PB92-222421, A13, MF-A03).

NCEER-92-0008   "A Procedure for the Seismic Evaluation of Buildings in the Central and Eastern United States," by C.D. Poland and J.O. Malley, 4/2/92, (PB92-222439, A20, MF-A04).

NCEER-92-0009   "Experimental and Analytical Study of a Hybrid Isolation System Using Friction Controllable Sliding Bearings," by M.Q. Feng, S. Fujii and M. Shinozuka, 5/15/92, (PB93-150282, A06, MF-A02).

NCEER-92-0010   "Seismic Resistance of Slab-Column Connections in Existing Non-Ductile Flat-Plate Buildings," by A.J. Durrani and Y. Du, 5/18/92, (PB93-116812, A06, MF-A02).

NCEER-92-0011   "The Hysteretic and Dynamic Behavior of Brick Masonry Walls Upgraded by Ferrocement Coatings Under Cyclic Loading and Strong Simulated Ground Motion," by H. Lee and S.P. Prawel, 5/11/92, to be published.

NCEER-92-0012   "Study of Wire Rope Systems for Seismic Protection of Equipment in Buildings," by G.F. Demetriades, M.C. Constantinou and A.M. Reinhorn, 5/20/92, (PB93-116655, A08, MF-A02).

NCEER-92-0013   "Shape Memory Structural Dampers: Material Properties, Design and Seismic Testing," by P.R. Witting and F.A. Cozzarelli, 5/26/92, (PB93-116663, A05, MF-A01).

NCEER-92-0014   "Longitudinal Permanent Ground Deformation Effects on Buried Continuous Pipelines," by M.J. O'Rourke, and C. Nordberg, 6/15/92, (PB93-116671, A08, MF-A02).

NCEER-92-0015   "A Simulation Method for Stationary Gaussian Random Functions Based on the Sampling Theorem," by M. Grigoriu and S. Balopoulou, 6/11/92, (PB93-127496, A05, MF-A01).

NCEER-92-0016   "Gravity-Load-Designed Reinforced Concrete Buildings: Seismic Evaluation of Existing Construction and Detailing Strategies for Improved Seismic Resistance," by G.W. Hoffmann, S.K. Kunnath, A.M. Reinhorn and J.B. Mander, 7/15/92, (PB94-142007, A08, MF-A02).

NCEER-92-0017   "Observations on Water System and Pipeline Performance in the Limón Area of Costa Rica Due to the April 22, 1991 Earthquake," by M. O'Rourke and D. Ballantyne, 6/30/92, (PB93-126811, A06, MF-A02).

NCEER-92-0018   "Fourth Edition of Earthquake Education Materials for Grades K-12," Edited by K.E.K. Ross, 8/10/92, (PB93-114023, A07, MF-A02).

NCEER-92-0019   "Proceedings from the Fourth Japan-U.S. Workshop on Earthquake Resistant Design of Lifeline Facilities and Countermeasures for Soil Liquefaction," Edited by M. Hamada and T.D. O'Rourke, 8/12/92, (PB93-163939, A99, MF-E11).

NCEER-92-0020   "Active Bracing System: A Full Scale Implementation of Active Control," by A.M. Reinhorn, T.T. Soong, R.C. Lin, M.A. Riley, Y.P. Wang, S. Aizawa and M. Higashino, 8/14/92, (PB93-127512, A06, MF-A02).

NCEER-92-0021   "Empirical Analysis of Horizontal Ground Displacement Generated by Liquefaction-Induced Lateral Spreads," by S.F. Bartlett and T.L. Youd, 8/17/92, (PB93-188241, A06, MF-A02).

NCEER-92-0022   "IDARC Version 3.0: Inelastic Damage Analysis of Reinforced Concrete Structures," by S.K. Kunnath, A.M. Reinhorn and R.F. Lobo, 8/31/92, (PB93-227502, A07, MF-A02).

NCEER-92-0023   "A Semi-Empirical Analysis of Strong-Motion Peaks in Terms of Seismic Source, Propagation Path and Local Site Conditions, by M. Kamiyama, M.J. O'Rourke and R. Flores-Berrones, 9/9/92, (PB93-150266, A08, MF-A02).

NCEER-92-0024   "Seismic Behavior of Reinforced Concrete Frame Structures with Nonductile Details, Part I: Summary of Experimental Findings of Full Scale Beam-Column Joint Tests," by A. Beres, R.N. White and P. Gergely, 9/30/92, (PB93-227783, A05, MF-A01).

NCEER-92-0025   "Experimental Results of Repaired and Retrofitted Beam-Column Joint Tests in Lightly Reinforced Concrete Frame Buildings," by A. Beres, S. El-Borgi, R.N. White and P. Gergely, 10/29/92, (PB93-227791, A05, MF-A01).

NCEER-92-0026   "A Generalization of Optimal Control Theory: Linear and Nonlinear Structures," by J.N. Yang, Z. Li and S. Vongchavalitkul, 11/2/92, (PB93-188621, A05, MF-A01).

NCEER-92-0027   "Seismic Resistance of Reinforced Concrete Frame Structures Designed Only for Gravity Loads: Part I - Design and Properties of a One-Third Scale Model Structure," by J.M. Bracci, A.M. Reinhorn and J.B. Mander, 12/1/92, (PB94-104502, A08, MF-A02).

NCEER-92-0028   "Seismic Resistance of Reinforced Concrete Frame Structures Designed Only for Gravity Loads: Part II - Experimental Performance of Subassemblages," by L.E. Aycardi, J.B. Mander and A.M. Reinhorn, 12/1/92, (PB94-104510, A08, MF-A02).

NCEER-92-0029   "Seismic Resistance of Reinforced Concrete Frame Structures Designed Only for Gravity Loads: Part III - Experimental Performance and Analytical Study of a Structural Model," by J.M. Bracci, A.M. Reinhorn and J.B. Mander, 12/1/92, (PB93-227528, A09, MF-A01).

NCEER-92-0030   "Evaluation of Seismic Retrofit of Reinforced Concrete Frame Structures: Part I - Experimental Performance of Retrofitted Subassemblages," by D. Choudhuri, J.B. Mander and A.M. Reinhorn, 12/8/92, (PB93-198307, A07, MF-A02).

NCEER-92-0031   "Evaluation of Seismic Retrofit of Reinforced Concrete Frame Structures: Part II - Experimental Performance and Analytical Study of a Retrofitted Structural Model," by J.M. Bracci, A.M. Reinhorn and J.B. Mander, 12/8/92, (PB93-198315, A09, MF-A03).

NCEER-92-0032   "Experimental and Analytical Investigation of Seismic Response of Structures with Supplemental Fluid Viscous Dampers," by M.C. Constantinou and M.D. Symans, 12/21/92, (PB93-191435, A10, MF-A03). This report is available only through NTIS (see address given above).

NCEER-92-0033   "Reconnaissance Report on the Cairo, Egypt Earthquake of October 12, 1992," by M. Khater, 12/23/92, (PB93-188621, A03, MF-A01).

NCEER-92-0034   "Low-Level Dynamic Characteristics of Four Tall Flat-Plate Buildings in New York City," by H. Gavin, S. Yuan, J. Grossman, E. Pekelis and K. Jacob, 12/28/92, (PB93-188217, A07, MF-A02).

NCEER-93-0001   "An Experimental Study on the Seismic Performance of Brick-Infilled Steel Frames With and Without Retrofit," by J.B. Mander, B. Nair, K. Wojtkowski and J. Ma, 1/29/93, (PB93-227510, A07, MF-A02).

NCEER-93-0002   "Social Accounting for Disaster Preparedness and Recovery Planning," by S. Cole, E. Pantoja and V. Razak, 2/22/93, (PB94-142114, A12, MF-A03).

NCEER-93-0003   "Assessment of 1991 NEHRP Provisions for Nonstructural Components and Recommended Revisions," by T.T. Soong, G. Chen, Z. Wu, R-H. Zhang and M. Grigoriu, 3/1/93, (PB93-188639, A06, MF-A02).

NCEER-93-0004   "Evaluation of Static and Response Spectrum Analysis Procedures of SEAOC/UBC for Seismic Isolated Structures," by C.W. Winters and M.C. Constantinou, 3/23/93, (PB93-198299, A10, MF-A03).

NCEER-93-0005   "Earthquakes in the Northeast - Are We Ignoring the Hazard? A Workshop on Earthquake Science and Safety for Educators," edited by K.E.K. Ross, 4/2/93, (PB94-103066, A09, MF-A02).

NCEER-93-0006   "Inelastic Response of Reinforced Concrete Structures with Viscoelastic Braces," by R.F. Lobo, J.M. Bracci, K.L. Shen, A.M. Reinhorn and T.T. Soong, 4/5/93, (PB93-227486, A05, MF-A02).

NCEER-93-0007   "Seismic Testing of Installation Methods for Computers and Data Processing Equipment," by K. Kosar, T.T. Soong, K.L. Shen, J.A. HoLung and Y.K. Lin, 4/12/93, (PB93-198299, A07, MF-A02).

NCEER-93-0008   "Retrofit of Reinforced Concrete Frames Using Added Dampers," by A. Reinhorn, M. Constantinou and C. Li, to be published.

NCEER-93-0009   "Seismic Behavior and Design Guidelines for Steel Frame Structures with Added Viscoelastic Dampers," by K.C. Chang, M.L. Lai, T.T. Soong, D.S. Hao and Y.C. Yeh, 5/1/93, (PB94-141959, A07, MF-A02).

NCEER-93-0010   "Seismic Performance of Shear-Critical Reinforced Concrete Bridge Piers," by J.B. Mander, S.M. Waheed, M.T.A. Chaudhary and S.S. Chen, 5/12/93, (PB93-227494, A08, MF-A02).

NCEER-93-0011   "3D-BASIS-TABS: Computer Program for Nonlinear Dynamic Analysis of Three Dimensional Base Isolated Structures," by S. Nagarajaiah, C. Li, A.M. Reinhorn and M.C. Constantinou, 8/2/93, (PB94-141819, A09, MF-A02).

NCEER-93-0012   "Effects of Hydrocarbon Spills from an Oil Pipeline Break on Ground Water," by O.J. Helweg and H.H.M. Hwang, 8/3/93, (PB94-141942, A06, MF-A02).

NCEER-93-0013   "Simplified Procedures for Seismic Design of Nonstructural Components and Assessment of Current Code Provisions," by M.P. Singh, L.E. Suarez, E.E. Matheu and G.O. Maldonado, 8/4/93, (PB94-141827, A09, MF-A02).

NCEER-93-0014   "An Energy Approach to Seismic Analysis and Design of Secondary Systems," by G. Chen and T.T. Soong, 8/6/93, (PB94-142767, A11, MF-A03).

NCEER-93-0015   "Proceedings from School Sites: Becoming Prepared for Earthquakes - Commemorating the Third Anniversary of the Loma Prieta Earthquake," Edited by F.E. Winslow and K.E.K. Ross, 8/16/93, (PB94-154275, A16, MF-A02).

NCEER-93-0016   "Reconnaissance Report of Damage to Historic Monuments in Cairo, Egypt Following the October 12, 1992 Dahshur Earthquake," by D. Sykora, D. Look, G. Croci, E. Karaesmen and E. Karaesmen, 8/19/93, (PB94-142221, A08, MF-A02).

NCEER-93-0017   "The Island of Guam Earthquake of August 8, 1993," by S.W. Swan and S.K. Harris, 9/30/93, (PB94-141843, A04, MF-A01).

NCEER-93-0018   "Engineering Aspects of the October 12, 1992 Egyptian Earthquake," by A.W. Elgamal, M. Amer, K. Adalier and A. Abul-Fadl, 10/7/93, (PB94-141983, A05, MF-A01).

NCEER-93-0019   "Development of an Earthquake Motion Simulator and its Application in Dynamic Centrifuge Testing," by I. Krstelj, Supervised by J.H. Prevost, 10/23/93, (PB94-181773, A-10, MF-A03).

NCEER-93-0020   "NCEER-Taisei Corporation Research Program on Sliding Seismic Isolation Systems for Bridges: Experimental and Analytical Study of a Friction Pendulum System (FPS)," by M.C. Constantinou, P. Tsopelas, Y-S. Kim and S. Okamoto, 11/1/93, (PB94-142775, A08, MF-A02).

NCEER-93-0021   "Finite Element Modeling of Elastomeric Seismic Isolation Bearings," by L.J. Billings, Supervised by R. Shepherd, 11/8/93, to be published.

NCEER-93-0022   "Seismic Vulnerability of Equipment in Critical Facilities: Life-Safety and Operational Consequences," by K. Porter, G.S. Johnson, M.M. Zadeh, C. Scawthorn and S. Eder, 11/24/93, (PB94-181765, A16, MF-A03).

NCEER-93-0023   "Hokkaido Nansei-oki, Japan Earthquake of July 12, 1993, by P.I. Yanev and C.R. Scawthorn, 12/23/93, (PB94-181500, A07, MF-A01).

NCEER-94-0001   "An Evaluation of Seismic Serviceability of Water Supply Networks with Application to the San Francisco Auxiliary Water Supply System," by I. Markov, Supervised by M. Grigoriu and T. O'Rourke, 1/21/94, (PB94-204013, A07, MF-A02).

NCEER-94-0002   "NCEER-Taisei Corporation Research Program on Sliding Seismic Isolation Systems for Bridges: Experimental and Analytical Study of Systems Consisting of Sliding Bearings, Rubber Restoring Force Devices and Fluid Dampers," Volumes I and II, by P. Tsopelas, S. Okamoto, M.C. Constantinou, D. Ozaki and S. Fujii, 2/4/94, (PB94-181740, A09, MF-A02 and PB94-181757, A12, MF-A03).

NCEER-94-0003   "A Markov Model for Local and Global Damage Indices in Seismic Analysis," by S. Rahman and M. Grigoriu, 2/18/94, (PB94-206000, A12, MF-A03).

NCEER-94-0004   "Proceedings from the NCEER Workshop on Seismic Response of Masonry Infills," edited by D.P. Abrams, 3/1/94, (PB94-180783, A07, MF-A02).

NCEER-94-0005   "The Northridge, California Earthquake of January 17, 1994: General Reconnaissance Report," edited by J.D. Goltz, 3/11/94, (PB94-193943, A10, MF-A03).

NCEER-94-0006   "Seismic Energy Based Fatigue Damage Analysis of Bridge Columns: Part I - Evaluation of Seismic Capacity," by G.A. Chang and J.B. Mander, 3/14/94, (PB94-219185, A11, MF-A03).

NCEER-94-0007   "Seismic Isolation of Multi-Story Frame Structures Using Spherical Sliding Isolation Systems," by T.M. Al-Hussaini, V.A. Zayas and M.C. Constantinou, 3/17/94, (PB94-193745, A09, MF-A02).

NCEER-94-0008   "The Northridge, California Earthquake of January 17, 1994: Performance of Highway Bridges," edited by I.G. Buckle, 3/24/94, (PB94-193851, A06, MF-A02).

NCEER-94-0009   "Proceedings of the Third U.S.-Japan Workshop on Earthquake Protective Systems for Bridges," edited by I.G. Buckle and I. Friedland, 3/31/94, (PB94-195815, A99, MF-A06).

NCEER-94-0010   "3D-BASIS-ME: Computer Program for Nonlinear Dynamic Analysis of Seismically Isolated Single and Multiple Structures and Liquid Storage Tanks," by P.C. Tsopelas, M.C. Constantinou and A.M. Reinhorn, 4/12/94, (PB94-204922, A09, MF-A02).

NCEER-94-0011   "The Northridge, California Earthquake of January 17, 1994: Performance of Gas Transmission Pipelines," by T.D. O'Rourke and M.C. Palmer, 5/16/94, (PB94-204989, A05, MF-A01).

NCEER-94-0012   "Feasibility Study of Replacement Procedures and Earthquake Performance Related to Gas Transmission Pipelines," by T.D. O'Rourke and M.C. Palmer, 5/25/94, (PB94-206638, A09, MF-A02).

NCEER-94-0013   "Seismic Energy Based Fatigue Damage Analysis of Bridge Columns: Part II - Evaluation of Seismic Demand," by G.A. Chang and J.B. Mander, 6/1/94, (PB95-18106, A08, MF-A02).

NCEER-94-0014   "NCEER-Taisei Corporation Research Program on Sliding Seismic Isolation Systems for Bridges: Experimental and Analytical Study of a System Consisting of Sliding Bearings and Fluid Restoring Force/Damping Devices," by P. Tsopelas and M.C. Constantinou, 6/13/94, (PB94-219144, A10, MF-A03).

NCEER-94-0015   "Generation of Hazard-Consistent Fragility Curves for Seismic Loss Estimation Studies," by H. Hwang and J-R. Huo, 6/14/94, (PB95-181996, A09, MF-A02).

NCEER-94-0016   "Seismic Study of Building Frames with Added Energy-Absorbing Devices," by W.S. Pong, C.S. Tsai and G.C. Lee, 6/20/94, (PB94-219136, A10, A03).

NCEER-94-0017   "Sliding Mode Control for Seismic-Excited Linear and Nonlinear Civil Engineering Structures," by J. Yang, J. Wu, A. Agrawal and Z. Li, 6/21/94, (PB95-138483, A06, MF-A02).

NCEER-94-0018   "3D-BASIS-TABS Version 2.0: Computer Program for Nonlinear Dynamic Analysis of Three Dimensional Base Isolated Structures," by A.M. Reinhorn, S. Nagarajaiah, M.C. Constantinou, P. Tsopelas and R. Li, 6/22/94, (PB95-182176, A08, MF-A02).

NCEER-94-0019   "Proceedings of the International Workshop on Civil Infrastructure Systems: Application of Intelligent Systems and Advanced Materials on Bridge Systems," Edited by G.C. Lee and K.C. Chang, 7/18/94, (PB95-252474, A20, MF-A04).

NCEER-94-0020   "Study of Seismic Isolation Systems for Computer Floors," by V. Lambrou and M.C. Constantinou, 7/19/94, (PB95-138533, A10, MF-A03).

NCEER-94-0021   "Proceedings of the U.S.-Italian Workshop on Guidelines for Seismic Evaluation and Rehabilitation of Unreinforced Masonry Buildings," Edited by D.P. Abrams and G.M. Calvi, 7/20/94, (PB95-138749, A13, MF-A03).

NCEER-94-0022   "NCEER-Taisei Corporation Research Program on Sliding Seismic Isolation Systems for Bridges: Experimental and Analytical Study of a System Consisting of Lubricated PTFE Sliding Bearings and Mild Steel Dampers," by P. Tsopelas and M.C. Constantinou, 7/22/94, (PB95-182184, A08, MF-A02).

NCEER-94-0023   "Development of Reliability-Based Design Criteria for Buildings Under Seismic Load," by Y.K. Wen, H. Hwang and M. Shinozuka, 8/1/94, (PB95-211934, A08, MF-A02).

NCEER-94-0024   "Experimental Verification of Acceleration Feedback Control Strategies for an Active Tendon System," by S.J. Dyke, B.F. Spencer, Jr., P. Quast, M.K. Sain, D.C. Kaspari, Jr. and T.T. Soong, 8/29/94, (PB95-212320, A05, MF-A01).

NCEER-94-0025   "Seismic Retrofitting Manual for Highway Bridges," Edited by I.G. Buckle and I.F. Friedland, published by the Federal Highway Administration (PB95-212676, A15, MF-A03).

NCEER-94-0026   "Proceedings from the Fifth U.S.-Japan Workshop on Earthquake Resistant Design of Lifeline Facilities and Countermeasures Against Soil Liquefaction," Edited by T.D. O'Rourke and M. Hamada, 11/7/94, (PB95-220802, A99, MF-E08).

NCEER-95-0001 "Experimental and Analytical Investigation of Seismic Retrofit of Structures with Supplemental Damping: Part 1 - Fluid Viscous Damping Devices," by A.M. Reinhorn, C. Li and M.C. Constantinou, 1/3/95, (PB95-266599, A09, MF-A02).

NCEER-95-0002 "Experimental and Analytical Study of Low-Cycle Fatigue Behavior of Semi-Rigid Top-And-Seat Angle Connections," by G. Pekcan, J.B. Mander and S.S. Chen, 1/5/95, (PB95-220042, A07, MF-A02).

NCEER-95-0003 "NCEER-ATC Joint Study on Fragility of Buildings," by T. Anagnos, C. Rojahn and A.S. Kiremidjian, 1/20/95, (PB95-220026, A06, MF-A02).

NCEER-95-0004 "Nonlinear Control Algorithms for Peak Response Reduction," by Z. Wu, T.T. Soong, V. Gattulli and R.C. Lin, 2/16/95, (PB95-220349, A05, MF-A01).

NCEER-95-0005 "Pipeline Replacement Feasibility Study: A Methodology for Minimizing Seismic and Corrosion Risks to Underground Natural Gas Pipelines," by R.T. Eguchi, H.A. Seligson and D.G. Honegger, 3/2/95, (PB95-252326, A06, MF-A02).

NCEER-95-0006 "Evaluation of Seismic Performance of an 11-Story Frame Building During the 1994 Northridge Earthquake," by F. Naeim, R. DiSulio, K. Benuska, A. Reinhorn and C. Li, to be published.

NCEER-95-0007 "Prioritization of Bridges for Seismic Retrofitting," by N. Basöz and A.S. Kiremidjian, 4/24/95, (PB95-252300, A08, MF-A02).

NCEER-95-0008 "Method for Developing Motion Damage Relationships for Reinforced Concrete Frames," by A. Singhal and A.S. Kiremidjian, 5/11/95, (PB95-266607, A06, MF-A02).

NCEER-95-0009 "Experimental and Analytical Investigation of Seismic Retrofit of Structures with Supplemental Damping: Part II - Friction Devices," by C. Li and A.M. Reinhorn, 7/6/95, (PB96-128087, A11, MF-A03).

NCEER-95-0010 "Experimental Performance and Analytical Study of a Non-Ductile Reinforced Concrete Frame Structure Retrofitted with Elastomeric Spring Dampers," by G. Pekcan, J.B. Mander and S.S. Chen, 7/14/95, (PB96-137161, A08, MF-A02).

NCEER-95-0011 "Development and Experimental Study of Semi-Active Fluid Damping Devices for Seismic Protection of Structures," by M.D. Symans and M.C. Constantinou, 8/3/95, (PB96-136940, A23, MF-A04).

NCEER-95-0012 "Real-Time Structural Parameter Modification (RSPM): Development of Innervated Structures," by Z. Liang, M. Tong and G.C. Lee, 4/11/95, (PB96-137153, A06, MF-A01).

NCEER-95-0013 "Experimental and Analytical Investigation of Seismic Retrofit of Structures with Supplemental Damping: Part III - Viscous Damping Walls," by A.M. Reinhorn and C. Li, 10/1/95, (PB96-176409, A11, MF-A03).

NCEER-95-0014 "Seismic Fragility Analysis of Equipment and Structures in a Memphis Electric Substation," by J-R. Huo and H.H.M. Hwang, 8/10/95, (PB96-128087, A09, MF-A02).

NCEER-95-0015 "The Hanshin-Awaji Earthquake of January 17, 1995: Performance of Lifelines," Edited by M. Shinozuka, 11/3/95, (PB96-176383, A15, MF-A03).

NCEER-95-0016 "Highway Culvert Performance During Earthquakes," by T.L. Youd and C.J. Beckman, available as NCEER-96-0015.

NCEER-95-0017 "The Hanshin-Awaji Earthquake of January 17, 1995: Performance of Highway Bridges," Edited by I.G. Buckle, 12/1/95, to be published.

NCEER-95-0018 "Modeling of Masonry Infill Panels for Structural Analysis," by A.M. Reinhorn, A. Madan, R.E. Valles, Y. Reichmann and J.B. Mander, 12/8/95, (PB97-110886, MF-A01, A06).

NCEER-95-0019 "Optimal Polynomial Control for Linear and Nonlinear Structures," by A.K. Agrawal and J.N. Yang, 12/11/95, (PB96-168737, A07, MF-A02).

NCEER-95-0020 "Retrofit of Non-Ductile Reinforced Concrete Frames Using Friction Dampers," by R.S. Rao, P. Gergely and R.N. White, 12/22/95, (PB97-133508, A10, MF-A02).

NCEER-95-0021 "Parametric Results for Seismic Response of Pile-Supported Bridge Bents," by G. Mylonakis, A. Nikolaou and G. Gazetas, 12/22/95, (PB97-100242, A12, MF-A03).

NCEER-95-0022 "Kinematic Bending Moments in Seismically Stressed Piles," by A. Nikolaou, G. Mylonakis and G. Gazetas, 12/23/95, (PB97-113914, MF-A03, A13).

NCEER-96-0001 "Dynamic Response of Unreinforced Masonry Buildings with Flexible Diaphragms," by A.C. Costley and D.P. Abrams," 10/10/96, (PB97-133573, MF-A03, A15).

NCEER-96-0002 "State of the Art Review: Foundations and Retaining Structures," by I. Po Lam, to be published.

NCEER-96-0003 "Ductility of Rectangular Reinforced Concrete Bridge Columns with Moderate Confinement," by N. Wehbe, M. Saiidi, D. Sanders and B. Douglas, 11/7/96, (PB97-133557, A06, MF-A02).

NCEER-96-0004 "Proceedings of the Long-Span Bridge Seismic Research Workshop," edited by I.G. Buckle and I.M. Friedland, to be published.

NCEER-96-0005 "Establish Representative Pier Types for Comprehensive Study: Eastern United States," by J. Kulicki and Z. Prucz, 5/28/96, (PB98-119217, A07, MF-A02).

NCEER-96-0006 "Establish Representative Pier Types for Comprehensive Study: Western United States," by R. Imbsen, R.A. Schamber and T.A. Osterkamp, 5/28/96, (PB98-118607, A07, MF-A02).

NCEER-96-0007 "Nonlinear Control Techniques for Dynamical Systems with Uncertain Parameters," by R.G. Ghanem and M.I. Bujakov, 5/27/96, (PB97-100259, A17, MF-A03).

NCEER-96-0008 "Seismic Evaluation of a 30-Year Old Non-Ductile Highway Bridge Pier and Its Retrofit," by J.B. Mander, B. Mahmoodzadegan, S. Bhadra and S.S. Chen, 5/31/96, (PB97-110902, MF-A03, A10).

NCEER-96-0009 "Seismic Performance of a Model Reinforced Concrete Bridge Pier Before and After Retrofit," by J.B. Mander, J.H. Kim and C.A. Ligozio, 5/31/96, (PB97-110910, MF-A02, A10).

NCEER-96-0010 "IDARC2D Version 4.0: A Computer Program for the Inelastic Damage Analysis of Buildings," by R.E. Valles, A.M. Reinhorn, S.K. Kunnath, C. Li and A. Madan, 6/3/96, (PB97-100234, A17, MF-A03).

NCEER-96-0011 "Estimation of the Economic Impact of Multiple Lifeline Disruption: Memphis Light, Gas and Water Division Case Study," by S.E. Chang, H.A. Seligson and R.T. Eguchi, 8/16/96, (PB97-133490, A11, MF-A03).

NCEER-96-0012 "Proceedings from the Sixth Japan-U.S. Workshop on Earthquake Resistant Design of Lifeline Facilities and Countermeasures Against Soil Liquefaction, Edited by M. Hamada and T. O'Rourke, 9/11/96, (PB97-133581, A99, MF-A06).

NCEER-96-0013 "Chemical Hazards, Mitigation and Preparedness in Areas of High Seismic Risk: A Methodology for Estimating the Risk of Post-Earthquake Hazardous Materials Release," by H.A. Seligson, R.T. Eguchi, K.J. Tierney and K. Richmond, 11/7/96, (PB97-133565, MF-A02, A08).

NCEER-96-0014 "Response of Steel Bridge Bearings to Reversed Cyclic Loading," by J.B. Mander, D-K. Kim, S.S. Chen and G.J. Premus, 11/13/96, (PB97-140735, A12, MF-A03).

NCEER-96-0015 "Highway Culvert Performance During Past Earthquakes," by T.L. Youd and C.J. Beckman, 11/25/96, (PB97-133532, A06, MF-A01).

NCEER-97-0001 "Evaluation, Prevention and Mitigation of Pounding Effects in Building Structures," by R.E. Valles and A.M. Reinhorn, 2/20/97, (PB97-159552, A14, MF-A03).

NCEER-97-0002 "Seismic Design Criteria for Bridges and Other Highway Structures," by C. Rojahn, R. Mayes, D.G. Anderson, J. Clark, J.H. Hom, R.V. Nutt and M.J. O'Rourke, 4/30/97, (PB97-194658, A06, MF-A03).

NCEER-97-0003   "Proceedings of the U.S.-Italian Workshop on Seismic Evaluation and Retrofit," Edited by D.P. Abrams and G.M. Calvi, 3/19/97, (PB97-194666, A13, MF-A03).

NCEER-97-0004   "Investigation of Seismic Response of Buildings with Linear and Nonlinear Fluid Viscous Dampers," by A.A. Seleemah and M.C. Constantinou, 5/21/97, (PB98-109002, A15, MF-A03).

NCEER-97-0005   "Proceedings of the Workshop on Earthquake Engineering Frontiers in Transportation Facilities," edited by G.C. Lee and I.M. Friedland, 8/29/97, (PB98-128911, A25, MR-A04).

NCEER-97-0006   "Cumulative Seismic Damage of Reinforced Concrete Bridge Piers," by S.K. Kunnath, A. El-Bahy, A. Taylor and W. Stone, 9/2/97, (PB98-108814, A11, MF-A03).

NCEER-97-0007   "Structural Details to Accommodate Seismic Movements of Highway Bridges and Retaining Walls," by R.A. Imbsen, R.A. Schamber, E. Thorkildsen, A. Kartoum, B.T. Martin, T.N. Rosser and J.M. Kulicki, 9/3/97, (PB98-108996, A09, MF-A02).

NCEER-97-0008   "A Method for Earthquake Motion-Damage Relationships with Application to Reinforced Concrete Frames," by A. Singhal and A.S. Kiremidjian, 9/10/97, (PB98-108988, A13, MF-A03).

NCEER-97-0009   "Seismic Analysis and Design of Bridge Abutments Considering Sliding and Rotation," by K. Fishman and R. Richards, Jr., 9/15/97, (PB98-108897, A06, MF-A02).

NCEER-97-0010   "Proceedings of the FHWA/NCEER Workshop on the National Representation of Seismic Ground Motion for New and Existing Highway Facilities," edited by I.M. Friedland, M.S. Power and R.L. Mayes, 9/22/97, (PB98-128903, A21, MF-A04).

NCEER-97-0011   "Seismic Analysis for Design or Retrofit of Gravity Bridge Abutments," by K.L. Fishman, R. Richards, Jr. and R.C. Divito, 10/2/97, (PB98-128937, A08, MF-A02).

NCEER-97-0012   "Evaluation of Simplified Methods of Analysis for Yielding Structures," by P. Tsopelas, M.C. Constantinou, C.A. Kircher and A.S. Whittaker, 10/31/97, (PB98-128929, A10, MF-A03).

NCEER-97-0013   "Seismic Design of Bridge Columns Based on Control and Repairability of Damage," by C-T. Cheng and J.B. Mander, 12/8/97, (PB98-144249, A11, MF-A03).

NCEER-97-0014   "Seismic Resistance of Bridge Piers Based on Damage Avoidance Design," by J.B. Mander and C-T. Cheng, 12/10/97, (PB98-144223, A09, MF-A02).

NCEER-97-0015   "Seismic Response of Nominally Symmetric Systems with Strength Uncertainty," by S. Balopoulou and M. Grigoriu, 12/23/97, (PB98-153422, A11, MF-A03).

NCEER-97-0016   "Evaluation of Seismic Retrofit Methods for Reinforced Concrete Bridge Columns," by T.J. Wipf, F.W. Klaiber and F.M. Russo, 12/28/97, (PB98-144215, A12, MF-A03).

NCEER-97-0017   "Seismic Fragility of Existing Conventional Reinforced Concrete Highway Bridges," by C.L. Mullen and A.S. Cakmak, 12/30/97, (PB98-153406, A08, MF-A02).

NCEER-97-0018   "Loss Asssessment of Memphis Buildings," edited by D.P. Abrams and M. Shinozuka, 12/31/97, (PB98-144231, A13, MF-A03).

NCEER-97-0019   "Seismic Evaluation of Frames with Infill Walls Using Quasi-static Experiments," by K.M. Mosalam, R.N. White and P. Gergely, 12/31/97, (PB98-153455, A07, MF-A02).

NCEER-97-0020   "Seismic Evaluation of Frames with Infill Walls Using Pseudo-dynamic Experiments," by K.M. Mosalam, R.N. White and P. Gergely, 12/31/97, (PB98-153430, A07, MF-A02).

NCEER-97-0021   "Computational Strategies for Frames with Infill Walls: Discrete and Smeared Crack Analyses and Seismic Fragility," by K.M. Mosalam, R.N. White and P. Gergely, 12/31/97, (PB98-153414, A10, MF-A02).

NCEER-97-0022 "Proceedings of the NCEER Workshop on Evaluation of Liquefaction Resistance of Soils," edited by T.L. Youd and I.M. Idriss, 12/31/97, (PB98-155617, A15, MF-A03).

MCEER-98-0001 "Extraction of Nonlinear Hysteretic Properties of Seismically Isolated Bridges from Quick-Release Field Tests," by Q. Chen, B.M. Douglas, E.M. Maragakis and I.G. Buckle, 5/26/98, (PB99-118838, A06, MF-A01).

MCEER-98-0002 "Methodologies for Evaluating the Importance of Highway Bridges," by A. Thomas, S. Eshenaur and J. Kulicki, 5/29/98, (PB99-118846, A10, MF-A02).

MCEER-98-0003 "Capacity Design of Bridge Piers and the Analysis of Overstrength," by J.B. Mander, A. Dutta and P. Goel, 6/1/98, (PB99-118853, A09, MF-A02).

MCEER-98-0004 "Evaluation of Bridge Damage Data from the Loma Prieta and Northridge, California Earthquakes," by N. Basoz and A. Kiremidjian, 6/2/98, (PB99-118861, A15, MF-A03).

MCEER-98-0005 "Screening Guide for Rapid Assessment of Liquefaction Hazard at Highway Bridge Sites," by T. L. Youd, 6/16/98, (PB99-118879, A06, not available on microfiche).

MCEER-98-0006 "Structural Steel and Steel/Concrete Interface Details for Bridges," by P. Ritchie, N. Kauhl and J. Kulicki, 7/13/98, (PB99-118945, A06, MF-A01).

MCEER-98-0007 "Capacity Design and Fatigue Analysis of Confined Concrete Columns," by A. Dutta and J.B. Mander, 7/14/98, (PB99-118960, A14, MF-A03).

MCEER-98-0008 "Proceedings of the Workshop on Performance Criteria for Telecommunication Services Under Earthquake Conditions," edited by A.J. Schiff, 7/15/98, (PB99-118952, A08, MF-A02).

MCEER-98-0009 "Fatigue Analysis of Unconfined Concrete Columns," by J.B. Mander, A. Dutta and J.H. Kim, 9/12/98, (PB99-123655, A10, MF-A02).

MCEER-98-0010 "Centrifuge Modeling of Cyclic Lateral Response of Pile-Cap Systems and Seat-Type Abutments in Dry Sands," by A.D. Gadre and R. Dobry, 10/2/98, (PB99-123606, A13, MF-A03).

MCEER-98-0011 "IDARC-BRIDGE: A Computational Platform for Seismic Damage Assessment of Bridge Structures," by A.M. Reinhorn, V. Simeonov, G. Mylonakis and Y. Reichman, 10/2/98, (PB99-162919, A15, MF-A03).

MCEER-98-0012 "Experimental Investigation of the Dynamic Response of Two Bridges Before and After Retrofitting with Elastomeric Bearings," by D.A. Wendichansky, S.S. Chen and J.B. Mander, 10/2/98, (PB99-162927, A15, MF-A03).

MCEER-98-0013 "Design Procedures for Hinge Restrainers and Hinge Sear Width for Multiple-Frame Bridges," by R. Des Roches and G.L. Fenves, 11/3/98, (PB99-140477, A13, MF-A03).

MCEER-98-0014 "Response Modification Factors for Seismically Isolated Bridges," by M.C. Constantinou and J.K. Quarshie, 11/3/98, (PB99-140485, A14, MF-A03).

MCEER-98-0015 "Proceedings of the U.S.-Italy Workshop on Seismic Protective Systems for Bridges," edited by I.M. Friedland and M.C. Constantinou, 11/3/98, (PB2000-101711, A22, MF-A04).

MCEER-98-0016 "Appropriate Seismic Reliability for Critical Equipment Systems: Recommendations Based on Regional Analysis of Financial and Life Loss," by K. Porter, C. Scawthorn, C. Taylor and N. Blais, 11/10/98, (PB99-157265, A08, MF-A02).

MCEER-98-0017 "Proceedings of the U.S. Japan Joint Seminar on Civil Infrastructure Systems Research," edited by M. Shinozuka and A. Rose, 11/12/98, (PB99-156713, A16, MF-A03).

MCEER-98-0018 "Modeling of Pile Footings and Drilled Shafts for Seismic Design," by I. PoLam, M. Kapuskar and D. Chaudhuri, 12/21/98, (PB99-157257, A09, MF-A02).

MCEER-99-0001   "Seismic Evaluation of a Masonry Infilled Reinforced Concrete Frame by Pseudodynamic Testing," by S.G. Buonopane and R.N. White, 2/16/99, (PB99-162851, A09, MF-A02).

MCEER-99-0002   "Response History Analysis of Structures with Seismic Isolation and Energy Dissipation Systems: Verification Examples for Program SAP2000," by J. Scheller and M.C. Constantinou, 2/22/99, (PB99-162869, A08, MF-A02).

MCEER-99-0003   "Experimental Study on the Seismic Design and Retrofit of Bridge Columns Including Axial Load Effects," by A. Dutta, T. Kokorina and J.B. Mander, 2/22/99, (PB99-162877, A09, MF-A02).

MCEER-99-0004   "Experimental Study of Bridge Elastomeric and Other Isolation and Energy Dissipation Systems with Emphasis on Uplift Prevention and High Velocity Near-source Seismic Excitation," by A. Kasalanati and M. C. Constantinou, 2/26/99, (PB99-162885, A12, MF-A03).

MCEER-99-0005   "Truss Modeling of Reinforced Concrete Shear-flexure Behavior," by J.H. Kim and J.B. Mander, 3/8/99, (PB99-163693, A12, MF-A03).

MCEER-99-0006   "Experimental Investigation and Computational Modeling of Seismic Response of a 1:4 Scale Model Steel Structure with a Load Balancing Supplemental Damping System," by G. Pekcan, J.B. Mander and S.S. Chen, 4/2/99, (PB99-162893, A11, MF-A03).

MCEER-99-0007   "Effect of Vertical Ground Motions on the Structural Response of Highway Bridges," by M.R. Button, C.J. Cronin and R.L. Mayes, 4/10/99, (PB2000-101411, A10, MF-A03).

MCEER-99-0008   "Seismic Reliability Assessment of Critical Facilities: A Handbook, Supporting Documentation, and Model Code Provisions," by G.S. Johnson, R.E. Sheppard, M.D. Quilici, S.J. Eder and C.R. Scawthorn, 4/12/99, (PB2000-101701, A18, MF-A04).

MCEER-99-0009   "Impact Assessment of Selected MCEER Highway Project Research on the Seismic Design of Highway Structures," by C. Rojahn, R. Mayes, D.G. Anderson, J.H. Clark, D'Appolonia Engineering, S. Gloyd and R.V. Nutt, 4/14/99, (PB99-162901, A10, MF-A02).

MCEER-99-0010   "Site Factors and Site Categories in Seismic Codes," by R. Dobry, R. Ramos and M.S. Power, 7/19/99, (PB2000-101705, A08, MF-A02).

MCEER-99-0011   "Restrainer Design Procedures for Multi-Span Simply-Supported Bridges," by M.J. Randall, M. Saiidi, E. Maragakis and T. Isakovic, 7/20/99, (PB2000-101702, A10, MF-A02).

MCEER-99-0012   "Property Modification Factors for Seismic Isolation Bearings," by M.C. Constantinou, P. Tsopelas, A. Kasalanati and E. Wolff, 7/20/99, (PB2000-103387, A11, MF-A03).

MCEER-99-0013   "Critical Seismic Issues for Existing Steel Bridges," by P. Ritchie, N. Kauhl and J. Kulicki, 7/20/99, (PB2000-101697, A09, MF-A02).

MCEER-99-0014   "Nonstructural Damage Database," by A. Kao, T.T. Soong and A. Vender, 7/24/99, (PB2000-101407, A06, MF-A01).

MCEER-99-0015   "Guide to Remedial Measures for Liquefaction Mitigation at Existing Highway Bridge Sites," by H.G. Cooke and J. K. Mitchell, 7/26/99, (PB2000-101703, A11, MF-A03).

MCEER-99-0016   "Proceedings of the MCEER Workshop on Ground Motion Methodologies for the Eastern United States," edited by N. Abrahamson and A. Becker, 8/11/99, (PB2000-103385, A07, MF-A02).

MCEER-99-0017   "Quindío, Colombia Earthquake of January 25, 1999: Reconnaissance Report," by A.P. Asfura and P.J. Flores, 10/4/99, (PB2000-106893, A06, MF-A01).

MCEER-99-0018   "Hysteretic Models for Cyclic Behavior of Deteriorating Inelastic Structures," by M.V. Sivaselvan and A.M. Reinhorn, 11/5/99, (PB2000-103386, A08, MF-A02).

MCEER-99-0019   "Proceedings of the 7th U.S.- Japan Workshop on Earthquake Resistant Design of Lifeline Facilities and Countermeasures Against Soil Liquefaction," edited by T.D. O'Rourke, J.P. Bardet and M. Hamada, 11/19/99, (PB2000-103354, A99, MF-A06).

MCEER-99-0020   "Development of Measurement Capability for Micro-Vibration Evaluations with Application to Chip Fabrication Facilities," by G.C. Lee, Z. Liang, J.W. Song, J.D. Shen and W.C. Liu, 12/1/99, (PB2000-105993, A08, MF-A02).

MCEER-99-0021   "Design and Retrofit Methodology for Building Structures with Supplemental Energy Dissipating Systems," by G. Pekcan, J.B. Mander and S.S. Chen, 12/31/99, (PB2000-105994, A11, MF-A03).

MCEER-00-0001   "The Marmara, Turkey Earthquake of August 17, 1999: Reconnaissance Report," edited by C. Scawthorn; with major contributions by M. Bruneau, R. Eguchi, T. Holzer, G. Johnson, J. Mander, J. Mitchell, W. Mitchell, A. Papageorgiou, C. Scaethorn, and G. Webb, 3/23/00, (PB2000-106200, A11, MF-A03).

MCEER-00-0002   "Proceedings of the MCEER Workshop for Seismic Hazard Mitigation of Health Care Facilities," edited by G.C. Lee, M. Ettouney, M. Grigoriu, J. Hauer and J. Nigg, 3/29/00, (PB2000-106892, A08, MF-A02).

MCEER-00-0003   "The Chi-Chi, Taiwan Earthquake of September 21, 1999: Reconnaissance Report," edited by G.C. Lee and C.H. Loh, with major contributions by G.C. Lee, M. Bruneau, I.G. Buckle, S.E. Chang, P.J. Flores, T.D. O'Rourke, M. Shinozuka, T.T. Soong, C-H. Loh, K-C. Chang, Z-J. Chen, J-S. Hwang, M-L. Lin, G-Y. Liu, K-C. Tsai, G.C. Yao and C-L. Yen, 4/30/00, (PB2001-100980, A10, MF-A02).

MCEER-00-0004   "Seismic Retrofit of End-Sway Frames of Steel Deck-Truss Bridges with a Supplemental Tendon System: Experimental and Analytical Investigation," by G. Pekcan, J.B. Mander and S.S. Chen, 7/1/00, (PB2001-100982, A10, MF-A02).

MCEER-00-0005   "Sliding Fragility of Unrestrained Equipment in Critical Facilities," by W.H. Chong and T.T. Soong, 7/5/00, (PB2001-100983, A08, MF-A02).

MCEER-00-0006   "Seismic Response of Reinforced Concrete Bridge Pier Walls in the Weak Direction," by N. Abo-Shadi, M. Saiidi and D. Sanders, 7/17/00, (PB2001-100981, A17, MF-A03).

MCEER-00-0007   "Low-Cycle Fatigue Behavior of Longitudinal Reinforcement in Reinforced Concrete Bridge Columns," by J. Brown and S.K. Kunnath, 7/23/00, (PB2001-104392, A08, MF-A02).

MCEER-00-0008   "Soil Structure Interaction of Bridges for Seismic Analysis," I. PoLam and H. Law, 9/25/00, (PB2001-105397, A08, MF-A02).

MCEER-00-0009   "Proceedings of the First MCEER Workshop on Mitigation of Earthquake Disaster by Advanced Technologies (MEDAT-1), edited by M. Shinozuka, D.J. Inman and T.D. O'Rourke, 11/10/00, (PB2001-105399, A14, MF-A03).

MCEER-00-0010   "Development and Evaluation of Simplified Procedures for Analysis and Design of Buildings with Passive Energy Dissipation Systems, Revision 01," by O.M. Ramirez, M.C. Constantinou, C.A. Kircher, A.S. Whittaker, M.W. Johnson, J.D. Gomez and C. Chrysostomou, 11/16/01, (PB2001-105523, A23, MF-A04).

MCEER-00-0011   "Dynamic Soil-Foundation-Structure Interaction Analyses of Large Caissons," by C-Y. Chang, C-M. Mok, Z-L. Wang, R. Settgast, F. Waggoner, M.A. Ketchum, H.M. Gonnermann and C-C. Chin, 12/30/00, (PB2001-104373, A07, MF-A02).

MCEER-00-0012   "Experimental Evaluation of Seismic Performance of Bridge Restrainers," by A.G. Vlassis, E.M. Maragakis and M. Saiid Saiidi, 12/30/00, (PB2001-104354, A09, MF-A02).

MCEER-00-0013   "Effect of Spatial Variation of Ground Motion on Highway Structures," by M. Shinozuka, V. Saxena and G. Deodatis, 12/31/00, (PB2001-108755, A13, MF-A03).

MCEER-00-0014   "A Risk-Based Methodology for Assessing the Seismic Performance of Highway Systems," by S.D. Werner, C.E. Taylor, J.E. Moore, II, J.S. Walton and S. Cho, 12/31/00, (PB2001-108756, A14, MF-A03).

MCEER-01-0001	"Experimental Investigation of P-Delta Effects to Collapse During Earthquakes," by D. Vian and M. Bruneau, 6/25/01, (PB2002-100534, A17, MF-A03).

MCEER-01-0002	"Proceedings of the Second MCEER Workshop on Mitigation of Earthquake Disaster by Advanced Technologies (MEDAT-2)," edited by M. Bruneau and D.J. Inman, 7/23/01, (PB2002-100434, A16, MF-A03).

MCEER-01-0003	"Sensitivity Analysis of Dynamic Systems Subjected to Seismic Loads," by C. Roth and M. Grigoriu, 9/18/01, (PB2003-100884, A12, MF-A03).

MCEER-01-0004	"Overcoming Obstacles to Implementing Earthquake Hazard Mitigation Policies: Stage 1 Report," by D.J. Alesch and W.J. Petak, 12/17/01, (PB2002-107949, A07, MF-A02).

MCEER-01-0005	"Updating Real-Time Earthquake Loss Estimates: Methods, Problems and Insights," by C.E. Taylor, S.E. Chang and R.T. Eguchi, 12/17/01, (PB2002-107948, A05, MF-A01).

MCEER-01-0006	"Experimental Investigation and Retrofit of Steel Pile Foundations and Pile Bents Under Cyclic Lateral Loadings," by A. Shama, J. Mander, B. Blabac and S. Chen, 12/31/01, (PB2002-107950, A13, MF-A03).

MCEER-02-0001	"Assessment of Performance of Bolu Viaduct in the 1999 Duzce Earthquake in Turkey" by P.C. Roussis, M.C. Constantinou, M. Erdik, E. Durukal and M. Dicleli, 5/8/02, (PB2003-100883, A08, MF-A02).

MCEER-02-0002	"Seismic Behavior of Rail Counterweight Systems of Elevators in Buildings," by M.P. Singh, Rildova and L.E. Suarez, 5/27/02. (PB2003-100882, A11, MF-A03).

MCEER-02-0003	"Development of Analysis and Design Procedures for Spread Footings," by G. Mylonakis, G. Gazetas, S. Nikolaou and A. Chauncey, 10/02/02, (PB2004-101636, A13, MF-A03, CD-A13).

MCEER-02-0004	"Bare-Earth Algorithms for Use with SAR and LIDAR Digital Elevation Models," by C.K. Huyck, R.T. Eguchi and B. Houshmand, 10/16/02, (PB2004-101637, A07, CD-A07).

MCEER-02-0005	"Review of Energy Dissipation of Compression Members in Concentrically Braced Frames," by K.Lee and M. Bruneau, 10/18/02, (PB2004-101638, A10, CD-A10).

MCEER-03-0001	"Experimental Investigation of Light-Gauge Steel Plate Shear Walls for the Seismic Retrofit of Buildings" by J. Berman and M. Bruneau, 5/2/03, (PB2004-101622, A10, MF-A03, CD-A10).

MCEER-03-0002	"Statistical Analysis of Fragility Curves," by M. Shinozuka, M.Q. Feng, H. Kim, T. Uzawa and T. Ueda, 6/16/03, (PB2004-101849, A09, CD-A09).

MCEER-03-0003	"Proceedings of the Eighth U.S.-Japan Workshop on Earthquake Resistant Design f Lifeline Facilities and Countermeasures Against Liquefaction," edited by M. Hamada, J.P. Bardet and T.D. O'Rourke, 6/30/03, (PB2004-104386, A99, CD-A99).

MCEER-03-0004	"Proceedings of the PRC-US Workshop on Seismic Analysis and Design of Special Bridges," edited by L.C. Fan and G.C. Lee, 7/15/03, (PB2004-104387, A14, CD-A14).

MCEER-03-0005	"Urban Disaster Recovery: A Framework and Simulation Model," by S.B. Miles and S.E. Chang, 7/25/03, (PB2004-104388, A07, CD-A07).

MCEER-03-0006	"Behavior of Underground Piping Joints Due to Static and Dynamic Loading," by R.D. Meis, M. Maragakis and R. Siddharthan, 11/17/03, (PB2005-102194, A13, MF-A03, CD-A00).

MCEER-04-0001	"Experimental Study of Seismic Isolation Systems with Emphasis on Secondary System Response and Verification of Accuracy of Dynamic Response History Analysis Methods," by E. Wolff and M. Constantinou, 1/16/04 (PB2005-102195, A99, MF-E08, CD-A00).

MCEER-04-0002	"Tension, Compression and Cyclic Testing of Engineered Cementitious Composite Materials," by K. Kesner and S.L. Billington, 3/1/04, (PB2005-102196, A08, CD-A08).

MCEER-04-0003 "Cyclic Testing of Braces Laterally Restrained by Steel Studs to Enhance Performance During Earthquakes," by O.C. Celik, J.W. Berman and M. Bruneau, 3/16/04, (PB2005-102197, A13, MF-A03, CD-A00).

MCEER-04-0004 "Methodologies for Post Earthquake Building Damage Detection Using SAR and Optical Remote Sensing: Application to the August 17, 1999 Marmara, Turkey Earthquake," by C.K. Huyck, B.J. Adams, S. Cho, R.T. Eguchi, B. Mansouri and B. Houshmand, 6/15/04, (PB2005-104888, A10, CD-A00).

MCEER-04-0005 "Nonlinear Structural Analysis Towards Collapse Simulation: A Dynamical Systems Approach," by M.V. Sivaselvan and A.M. Reinhorn, 6/16/04, (PB2005-104889, A11, MF-A03, CD-A00).

MCEER-04-0006 "Proceedings of the Second PRC-US Workshop on Seismic Analysis and Design of Special Bridges," edited by G.C. Lee and L.C. Fan, 6/25/04, (PB2005-104890, A16, CD-A00).

MCEER-04-0007 "Seismic Vulnerability Evaluation of Axially Loaded Steel Built-up Laced Members," by K. Lee and M. Bruneau, 6/30/04, (PB2005-104891, A16, CD-A00).

MCEER-04-0008 "Evaluation of Accuracy of Simplified Methods of Analysis and Design of Buildings with Damping Systems for Near-Fault and for Soft-Soil Seismic Motions," by E.A. Pavlou and M.C. Constantinou, 8/16/04, (PB2005-104892, A08, MF-A02, CD-A00).

MCEER-04-0009 "Assessment of Geotechnical Issues in Acute Care Facilities in California," by M. Lew, T.D. O'Rourke, R. Dobry and M. Koch, 9/15/04, (PB2005-104893, A08, CD-A00).

MCEER-04-0010 "Scissor-Jack-Damper Energy Dissipation System," by A.N. Sigaher-Boyle and M.C. Constantinou, 12/1/04 (PB2005-108221).

MCEER-04-0011 "Seismic Retrofit of Bridge Steel Truss Piers Using a Controlled Rocking Approach," by M. Pollino and M. Bruneau, 12/20/04 (PB2006-105795).

MCEER-05-0001 "Experimental and Analytical Studies of Structures Seismically Isolated with an Uplift-Restraint Isolation System," by P.C. Roussis and M.C. Constantinou, 1/10/05 (PB2005-108222).

MCEER-05-0002 "A Versatile Experimentation Model for Study of Structures Near Collapse Applied to Seismic Evaluation of Irregular Structures," by D. Kusumastuti, A.M. Reinhorn and A. Rutenberg, 3/31/05 (PB2006-101523).

MCEER-05-0003 "Proceedings of the Third PRC-US Workshop on Seismic Analysis and Design of Special Bridges," edited by L.C. Fan and G.C. Lee, 4/20/05, (PB2006-105796).

MCEER-05-0004 "Approaches for the Seismic Retrofit of Braced Steel Bridge Piers and Proof-of-Concept Testing of an Eccentrically Braced Frame with Tubular Link," by J.W. Berman and M. Bruneau, 4/21/05 (PB2006-101524).

MCEER-05-0005 "Simulation of Strong Ground Motions for Seismic Fragility Evaluation of Nonstructural Components in Hospitals," by A. Wanitkorkul and A. Filiatrault, 5/26/05 (PB2006-500027).

MCEER-05-0006 "Seismic Safety in California Hospitals: Assessing an Attempt to Accelerate the Replacement or Seismic Retrofit of Older Hospital Facilities," by D.J. Alesch, L.A. Arendt and W.J. Petak, 6/6/05 (PB2006-105794).

MCEER-05-0007 "Development of Seismic Strengthening and Retrofit Strategies for Critical Facilities Using Engineered Cementitious Composite Materials," by K. Kesner and S.L. Billington, 8/29/05 (PB2006-111701).

MCEER-05-0008 "Experimental and Analytical Studies of Base Isolation Systems for Seismic Protection of Power Transformers," by N. Murota, M.Q. Feng and G-Y. Liu, 9/30/05 (PB2006-111702).

MCEER-05-0009 "3D-BASIS-ME-MB: Computer Program for Nonlinear Dynamic Analysis of Seismically Isolated Structures," by P.C. Tsopelas, P.C. Roussis, M.C. Constantinou, R. Buchanan and A.M. Reinhorn, 10/3/05 (PB2006-111703).

MCEER-05-0010 "Steel Plate Shear Walls for Seismic Design and Retrofit of Building Structures," by D. Vian and M. Bruneau, 12/15/05 (PB2006-111704).

MCEER-05-0011 "The Performance-Based Design Paradigm," by M.J. Astrella and A. Whittaker, 12/15/05 (PB2006-111705).

MCEER-06-0001 "Seismic Fragility of Suspended Ceiling Systems," H. Badillo-Almaraz, A.S. Whittaker, A.M. Reinhorn and G.P. Cimellaro, 2/4/06 (PB2006-111706).

MCEER-06-0002 "Multi-Dimensional Fragility of Structures," by G.P. Cimellaro, A.M. Reinhorn and M. Bruneau, 3/1/06 (PB2007-106974, A09, MF-A02, CD A00).

MCEER-06-0003 "Built-Up Shear Links as Energy Dissipators for Seismic Protection of Bridges," by P. Dusicka, A.M. Itani and I.G. Buckle, 3/15/06 (PB2006-111708).

MCEER-06-0004 "Analytical Investigation of the Structural Fuse Concept," by R.E. Vargas and M. Bruneau, 3/16/06 (PB2006-111709).

MCEER-06-0005 "Experimental Investigation of the Structural Fuse Concept," by R.E. Vargas and M. Bruneau, 3/17/06 (PB2006-111710).

MCEER-06-0006 "Further Development of Tubular Eccentrically Braced Frame Links for the Seismic Retrofit of Braced Steel Truss Bridge Piers," by J.W. Berman and M. Bruneau, 3/27/06 (PB2007-105147).

MCEER-06-0007 "REDARS Validation Report," by S. Cho, C.K. Huyck, S. Ghosh and R.T. Eguchi, 8/8/06 (PB2007-106983).

MCEER-06-0008 "Review of Current NDE Technologies for Post-Earthquake Assessment of Retrofitted Bridge Columns," by J.W. Song, Z. Liang and G.C. Lee, 8/21/06 (PB2007-106984).

MCEER-06-0009 "Liquefaction Remediation in Silty Soils Using Dynamic Compaction and Stone Columns," by S. Thevanayagam, G.R. Martin, R. Nashed, T. Shenthan, T. Kanagalingam and N. Ecemis, 8/28/06 (PB2007-106985).

MCEER-06-0010 "Conceptual Design and Experimental Investigation of Polymer Matrix Composite Infill Panels for Seismic Retrofitting," by W. Jung, M. Chiewanichakorn and A.J. Aref, 9/21/06 (PB2007-106986).

MCEER-06-0011 "A Study of the Coupled Horizontal-Vertical Behavior of Elastomeric and Lead-Rubber Seismic Isolation Bearings," by G.P. Warn and A.S. Whittaker, 9/22/06 (PB2007-108679).

MCEER-06-0012 "Proceedings of the Fourth PRC-US Workshop on Seismic Analysis and Design of Special Bridges: Advancing Bridge Technologies in Research, Design, Construction and Preservation," Edited by L.C. Fan, G.C. Lee and L. Ziang, 10/12/06 (PB2007-109042).

MCEER-06-0013 "Cyclic Response and Low Cycle Fatigue Characteristics of Plate Steels," by P. Dusicka, A.M. Itani and I.G. Buckle, 11/1/06 06 (PB2007-106987).

MCEER-06-0014 "Proceedings of the Second US-Taiwan Bridge Engineering Workshop," edited by W.P. Yen, J. Shen, J-Y. Chen and M. Wang, 11/15/06 (PB2008-500041).

MCEER-06-0015 "User Manual and Technical Documentation for the REDARS^{TM} Import Wizard," by S. Cho, S. Ghosh, C.K. Huyck and S.D. Werner, 11/30/06 (PB2007-114766).

MCEER-06-0016 "Hazard Mitigation Strategy and Monitoring Technologies for Urban and Infrastructure Public Buildings: Proceedings of the China-US Workshops," edited by X.Y. Zhou, A.L. Zhang, G.C. Lee and M. Tong, 12/12/06 (PB2008-500018).

MCEER-07-0001 "Static and Kinetic Coefficients of Friction for Rigid Blocks," by C. Kafali, S. Fathali, M. Grigoriu and A.S. Whittaker, 3/20/07 (PB2007-114767).

MCEER-07-0002 "Hazard Mitigation Investment Decision Making: Organizational Response to Legislative Mandate," by L.A. Arendt, D.J. Alesch and W.J. Petak, 4/9/07 (PB2007-114768).

MCEER-07-0003 "Seismic Behavior of Bidirectional-Resistant Ductile End Diaphragms with Unbonded Braces in Straight or Skewed Steel Bridges," by O. Celik and M. Bruneau, 4/11/07 (PB2008-105141).

MCEER-07-0004   "Modeling Pile Behavior in Large Pile Groups Under Lateral Loading," by A.M. Dodds and G.R. Martin, 4/16/07(PB2008-105142).

MCEER-07-0005   "Experimental Investigation of Blast Performance of Seismically Resistant Concrete-Filled Steel Tube Bridge Piers," by S. Fujikura, M. Bruneau and D. Lopez-Garcia, 4/20/07 (PB2008-105143).

MCEER-07-0006   "Seismic Analysis of Conventional and Isolated Liquefied Natural Gas Tanks Using Mechanical Analogs," by I.P. Christovasilis and A.S. Whittaker, 5/1/07.

MCEER-07-0007   "Experimental Seismic Performance Evaluation of Isolation/Restraint Systems for Mechanical Equipment – Part 1: Heavy Equipment Study," by S. Fathali and A. Filiatrault, 6/6/07 (PB2008-105144).

MCEER-07-0008   "Seismic Vulnerability of Timber Bridges and Timber Substructures," by A.A. Sharma, J.B. Mander, I.M. Friedland and D.R. Allicock, 6/7/07 (PB2008-105145).

MCEER-07-0009   "Experimental and Analytical Study of the XY-Friction Pendulum (XY-FP) Bearing for Bridge Applications," by C.C. Marin-Artieda, A.S. Whittaker and M.C. Constantinou, 6/7/07 (PB2008-105191).

MCEER-07-0010   "Proceedings of the PRC-US Earthquake Engineering Forum for Young Researchers," Edited by G.C. Lee and X.Z. Qi, 6/8/07.

MCEER-07-0011   "Design Recommendations for Perforated Steel Plate Shear Walls," by R. Purba and M. Bruneau, 6/18/07, (PB2008-105192).

MCEER-07-0012   "Performance of Seismic Isolation Hardware Under Service and Seismic Loading," by M.C. Constantinou, A.S. Whittaker, Y. Kalpakidis, D.M. Fenz and G.P. Warn, 8/27/07, (PB2008-105193).

MCEER-07-0013   "Experimental Evaluation of the Seismic Performance of Hospital Piping Subassemblies," by E.R. Goodwin, E. Maragakis and A.M. Itani, 9/4/07, (PB2008-105194).

MCEER-07-0014   "A Simulation Model of Urban Disaster Recovery and Resilience: Implementation for the 1994 Northridge Earthquake," by S. Miles and S.E. Chang, 9/7/07, (PB2008-106426).

MCEER-07-0015   "Statistical and Mechanistic Fragility Analysis of Concrete Bridges," by M. Shinozuka, S. Banerjee and S-H. Kim, 9/10/07, (PB2008-106427).

MCEER-07-0016   "Three-Dimensional Modeling of Inelastic Buckling in Frame Structures," by M. Schachter and AM. Reinhorn, 9/13/07, (PB2008-108125).

MCEER-07-0017   "Modeling of Seismic Wave Scattering on Pile Groups and Caissons," by I. Po Lam, H. Law and C.T. Yang, 9/17/07 (PB2008-108150).

MCEER-07-0018   "Bridge Foundations: Modeling Large Pile Groups and Caissons for Seismic Design," by I. Po Lam, H. Law and G.R. Martin (Coordinating Author), 12/1/07 (PB2008-111190).

MCEER-07-0019   "Principles and Performance of Roller Seismic Isolation Bearings for Highway Bridges," by G.C. Lee, Y.C. Ou, Z. Liang, T.C. Niu and J. Song, 12/10/07.

MCEER-07-0020   "Centrifuge Modeling of Permeability and Pinning Reinforcement Effects on Pile Response to Lateral Spreading," by L.L Gonzalez-Lagos, T. Abdoun and R. Dobry, 12/10/07 (PB2008-111191).

MCEER-07-0021   "Damage to the Highway System from the Pisco, Perú Earthquake of August 15, 2007," by J.S. O'Connor, L. Mesa and M. Nykamp, 12/10/07, (PB2008-108126).

MCEER-07-0022   "Experimental Seismic Performance Evaluation of Isolation/Restraint Systems for Mechanical Equipment – Part 2: Light Equipment Study," by S. Fathali and A. Filiatrault, 12/13/07 (PB2008-111192).

MCEER-07-0023   "Fragility Considerations in Highway Bridge Design," by M. Shinozuka, S. Banerjee and S.H. Kim, 12/14/07 (PB2008-111193).

MCEER-07-0024   "Performance Estimates for Seismically Isolated Bridges," by G.P. Warn and A.S. Whittaker, 12/30/07 (PB2008-112230).

MCEER-08-0001   "Seismic Performance of Steel Girder Bridge Superstructures with Conventional Cross Frames," by L.P. Carden, A.M. Itani and I.G. Buckle, 1/7/08, (PB2008-112231).

MCEER-08-0002   "Seismic Performance of Steel Girder Bridge Superstructures with Ductile End Cross Frames with Seismic Isolators," by L.P. Carden, A.M. Itani and I.G. Buckle, 1/7/08 (PB2008-112232).

MCEER-08-0003   "Analytical and Experimental Investigation of a Controlled Rocking Approach for Seismic Protection of Bridge Steel Truss Piers," by M. Pollino and M. Bruneau, 1/21/08 (PB2008-112233).

MCEER-08-0004   "Linking Lifeline Infrastructure Performance and Community Disaster Resilience: Models and Multi-Stakeholder Processes," by S.E. Chang, C. Pasion, K. Tatebe and R. Ahmad, 3/3/08 (PB2008-112234).

MCEER-08-0005   "Modal Analysis of Generally Damped Linear Structures Subjected to Seismic Excitations," by J. Song, Y-L. Chu, Z. Liang and G.C. Lee, 3/4/08 (PB2009-102311).

MCEER-08-0006   "System Performance Under Multi-Hazard Environments," by C. Kafali and M. Grigoriu, 3/4/08 (PB2008-112235).

MCEER-08-0007   "Mechanical Behavior of Multi-Spherical Sliding Bearings," by D.M. Fenz and M.C. Constantinou, 3/6/08 (PB2008-112236).

MCEER-08-0008   "Post-Earthquake Restoration of the Los Angeles Water Supply System," by T.H.P. Tabucchi and R.A. Davidson, 3/7/08 (PB2008-112237).

MCEER-08-0009   "Fragility Analysis of Water Supply Systems," by A. Jacobson and M. Grigoriu, 3/10/08.

MCEER-08-0010   "Experimental Investigation of Full-Scale Two-Story Steel Plate Shear Walls with Reduced Beam Section Connections," by B. Qu, M. Bruneau, C-H. Lin and K-C. Tsai, 3/17/08.

MCEER-08-0011   "Seismic Evaluation and Rehabilitation of Critical Components of Electrical Power Systems," S. Ersoy, B. Feizi, A. Ashrafi and M. Ala Saadeghvaziri, 3/17/08.

MCEER-08-0012   "Seismic Behavior and Design of Boundary Frame Members of Steel Plate Shear Walls," by B. Qu and M. Bruneau, 4/26/08.

MCEER-08-0013   "Development and Appraisal of a Numerical Cyclic Loading Protocol for Quantifying Building System Performance," by A. Filiatrault, A. Wanitkorkul and M. Constantinou, 4/27/08.

MCEER-08-0014   "Structural and Nonstructural Earthquake Design: The Challenge of Integrating Specialty Areas in Designing Complex, Critical Facilities," by W.J. Petak and D.J. Alesch, 4/30/08.

MCEER-08-0015   "Seismic Performance Evaluation of Water Systems," by Y. Wang and T.D. O'Rourke, 5/5/08.

MCEER-08-0016   "Seismic Response Modeling of Water Supply Systems," by P. Shi and T.D. O'Rourke, 5/5/08.